

ENERGY STORAGE SYSTEM OPERATION AND CONTROL FOR GRID  
RESILIENCY AND ENHANCING RENEWABLE ENERGY PENETRATION

by

Sherif Abdelmageed Elsadek Abdelrazek

A dissertation submitted to the faculty of  
The University of North Carolina at Charlotte  
in partial fulfillment of the requirements  
for the degree of Doctor of Philosophy in  
Electrical Engineering

Charlotte

2015

Approved by:

---

Dr. Sukumar Kamalasan

---

Dr. Johan Enslin

---

Dr. Valentina Cecchi

---

Dr. Brett Tempest



## ABSTRACT

SHERIF ABDELMAGEED ABDELRAZEK. Energy storage system operation and control for grid resiliency and enhancing renewable energy penetration. (Under the direction of DR. SUKUMAR KAMALASADAN)

This research aims to examine the potential value of Energy Storage Systems (ESSs) to different sects of the electrical power system through the various applications in which it could be utilized. The different storage technologies are reviewed in light of the sector of the grid (generation, transmission and distribution) where the value they hold is most desired. Further, energy storage technologies' feasible renewable energy applications as well as ancillary services applications are closely examined. Efforts to quantify the value that such applications hold to power producers, grid operators and consumers are reviewed and presented. A complete battery energy storage management scheme to maximize potential value that can be brought forth to medium voltage feeders is presented. In general, the potential performance benefits produced by possible energy storage applications include improved system reliability, dynamic stability, enhanced power quality, transmission capacity enhancement and area protection. Hence, a unique control algorithm is introduced. This algorithm comprises three main storage applications. An ancillary services application (voltage support), Energy Time Shift (ETS) and PV Capacity Firming (PVCF) are presented. Designs are tested on EMTP simulation platforms and implemented on a practical feeder.

## DEDICATION

This dissertation is dedicated to my mother, Howida Omar (هويدا مجد الدين عمر) who continuous to be a beacon of support, love and belief. It is her strength, knowledge and prayers that paved the way for this study. This dissertation is also dedicated to my loving father, Abdelmageed Elsadek (عبدالمجيد الصادق عبدالرازق), who's teachings, guidance and support inspired the strength to complete this research. His example will continue to be my guide in my contribution to society.

## ACKNOWLEDGMENTS

First, the author would like to thank Allah the merciful (الْحَمْدُ لِلَّهِ رَبِّ الْعَالَمِينَ) for the blessings bestowed upon him to complete this research. Second, the author would like to greatly thank and express gratitude in his acknowledgement of the support and guidance presented by Dr. Sukumar Kamalasan. The author would also like to extend his gratitude to committee members Dr. Johan Enslin and Dr. Valentina Cecchi for the support they presented throughout this research. The author would also like to extend his thanks to his fellow students in the Power Energy and Intelligent Systems Laboratory (PEISL) and ECE department for providing a great learning environment. The graduate assistantships provided by Dr. Sukumar Kamalasan, The graduate school and funded by Duke Energy and the Energy Production and Infrastructure Center (EPIC) are greatly and sincerely appreciated. The author would also like to thank Duke Energy' New and Emerging Technologies team for the practical data provided, without which this work could not have been done. Finally, I would like to thank my parents, brother (Mahmoud Abdelmageed) and sisters (Lobna Abdelmageed and Rabab Abdelmageed) whose love and support made it all possible.

## TABLE OF CONTENTS

LIST OF TABLES	x
LIST OF FIGURES	xi
CHAPTER 1: INTRODUCTION	1
1.1. Introduction	1
1.2. Energy Storage Technologies	2
1.2.1. Flywheel Energy Storage (FES)	3
1.2.2. Pumped Hydro Energy Storage	6
1.2.3. Compressed Air Energy Storage (CAES)	8
1.2.4. Battery Energy Storage (BES)	10
1.3. Energy Storage Applications	12
1.3.1. Renewables Capacity Firming	12
1.3.2. Voltage Support	16
1.3.3. Electrical Energy Time Shift	18
1.4. Conclusion	20
1.5. Research Contributions	21
CHAPTER 2: BATTERY ENERGY STORAGE AND MANAGEMENT SYSTEM	23
2.1. Introduction	23
2.2. Battery Energy Storage System (BESS)	24
2.2.1. Battery Pack	25
2.2.2. Battery Management System (BMS)	38
2.3. Storage Management System (SMS)	38
2.3.1. Storage Management System Architecture	39
2.3.2. Storage Management System Design and Modeling	41
2.3.3. SMS Operation & Model Validation	63

2.4. Medium Voltage Distribution Feeder Specifications	68
2.5. Conclusion	70
CHAPTER 3: PV STATION MODELING	71
3.1. Introduction	71
3.2. Practical PV Station Specifications	72
3.3. Modeled PV Station Specifications	74
3.4. PV Station Model Design	75
3.4.1. PV Module Model	76
3.4.2. Aggregated PV Array Model	86
3.4.3. Buck Converter Model Design	87
3.4.4. Inverter Model Design	96
3.4.5. Full System Control Methodology & Validation	99
3.5. Overall Distributed Energy System Architecture	100
3.6. Conclusion	103
CHAPTER 4: PV STATION CAPACITY FIRING APPLICATION	104
4.1. Introduction	104
4.2. Algorithm Methodology	104
4.2.1. Firming Reference Calculation	104
4.2.2. Intermittency Detection	111
4.2.3. State of Charge Constraint	113
4.3. Simulation Results	117
4.3.1. Simulation Results without SoC Constraint	118
4.3.2. Simulation Results with SoC Constraint	120
4.4. PVCF Implementation	122
4.4.1. PVCF Implementation Results without SoC Constraint	124
4.4.2. PVCF Implementation Results with SoC Constraint	131
4.5. Conclusion	134

CHAPTER 5: ENERGY TIME SHIFT APPLICATION	135
5.1. Introduction	135
5.2. System Setup	136
5.3. Energy Time Shift Algorithm	136
5.3.1. Predication Algorithm	137
5.3.2. ESS Power Dispatch Algorithm	160
5.4. ETS application Simulation Results	162
5.4.1. Standalone ETS Application Simulation Results	162
5.4.2. ETS Application Synergy with PVCF Application	163
5.5. Combined ETS & PVCF (SoC Constrained) Implementation Results	163
5.6. Conclusion	172
CHAPTER 6: CLOUD STATE PATTERN RECOGNITION AIDED PV CAPACITY FIRING OPTIMIZATION	173
6.1. Introduction	173
6.2. PV Capacity Firing Methodology	175
6.2.1. Characteristic PV Curve Calculation	176
6.2.2. Firing Reference Calculation	180
6.2.3. Intermittency Detection	184
6.3. Firing Maximization	186
6.3.1. Optimization Parameters	187
6.3.2. Single Day Optimization Methodology	189
6.4. Multiple Day Optimization Framework	194
6.4.1. Daily Cloud State Classification	195
6.4.2. Day Type Identification Criteria	197
6.4.3. Optimal Value Determination	198
6.4.4. Forecasting and Optimal Value Utilization	200
6.5. Implementation Results	201

6.6. Conclusion	206
CHAPTER 7: VOLTAGE SUPPORT APPLICATION	207
7.1. Introduction	207
7.2. Model Based Voltage Support (MBVS)	208
7.2.1. Methodology	208
7.2.2. Simulation Results	210
7.2.3. Implementation Results	215
7.3. Sensor Based Voltage Support (SBVS)	221
7.3.1. Methodology	221
7.3.2. Implementation Results	224
7.4. Conclusion	228
CHAPTER 8: CONCLUSION	230
8.1. Introduction	230
8.2. Conclusion	231
8.3. Future Work	232
8.3.1. Economic Value Evaluation	233
8.3.2. Controller Productization	233
8.3.3. Grid Ramp Rate Control	233
REFERENCES	235

## LIST OF TABLES

Table 2.1	Battery Pack Specifications	26
Table 2.2	Discharge Buck Converter required characteristics	42
Table 2.3	Inverter Specifications	52
Table 2.4	Rectifier specifications	54
Table 2.5	Charge Buck Converter specifications	56
Table 2.6	BESMS capability limits	66
Table 2.7	Distribution Feeder Specifications	71
Table 3.1	Module specifications of practical PV station arrays	75
Table 3.2	Array specifications of practical PV station	76
Table 3.3	Inverter specifications of practical PV station arrays	76
Table 3.4	Specifications of aggregated PV station model	77
Table 3.5	PV Station Buck Converter specifications	89
Table 3.6	Inverter Specifications	99
Table 5.1	Days types based on clouds states	201
Table 5.2	Optimal value lookup table for sample day types	206
Table 6.1	MBVS Simulation results summary	221
Table 6.2	Voltage regulator tap operations comparison	227
Table 6.3	Regulators operation summary targeting Line Regulator 2	234
Table 6.4	Regulators operation summary targeting Line Regulator 2	234

## LIST OF FIGURES

FIGURE 1.1: Beacon Power flywheel energy storage system [29]	3
FIGURE 1.2: Pumped hydro energy storage system [30]	6
FIGURE 1.3: Compressed air energy storage system [32]	9
FIGURE 2.1: BESMS Architecture	24
FIGURE 2.2: BESS electrical circuit	25
FIGURE 2.3: Battery discharge model [18]	27
FIGURE 2.4: Battery Manufacturer Discharge Curve for SLPB120216216	28
FIGURE 2.5: Matlab battery model discharge curve	33
FIGURE 2.6: Modeled cell discharge curve versus manufacturer discharge curve	33
FIGURE 2.7: PSCAD battery pack description	34
FIGURE 2.8: PSCAD battery cell model validation circuit	35
FIGURE 2.9: Constant current load model	35
FIGURE 2.10: PSCAD battery model discharge curve	36
FIGURE 2.11: PSCAD and matlab battery models discharge curves	36
FIGURE 2.12: Battery voltage, current and SoC during discharge curve evaluation	37
FIGURE 2.13: Storage Management System Architecture	39
FIGURE 2.14: DC-DC Buck converter basic electrical circuit	41
FIGURE 2.15: Voltage and current wave forms per converter cycle	42
FIGURE 2.16: Discharge buck converter PSCAD model	44
FIGURE 2.17: Inductor current and output voltage ripples of discharge converter	45
FIGURE 2.18: Uncompensated discharge buck converter bode plot	46
FIGURE 2.19: Discharge converter PD compensator bode plot	48
FIGURE 2.20: Compensated discharge converter system bode plot	49
FIGURE 2.21: Step response of compensated discharge buck converter	50

FIGURE 2.22: Discharge buck converter control circuit model	50
FIGURE 2.23: Inverter PSCAD model	51
FIGURE 2.24: Inverter PWM control circuit model	52
FIGURE 2.25: Three phase full wave rectifier PSCAD model	53
FIGURE 2.26: Rectifier voltage and current plots at rated power	54
FIGURE 2.27: Charge converter PSCAD model	56
FIGURE 2.28: Charge converter PSCAD model voltage and current ripples	56
FIGURE 2.29: Uncompensated charge buck converter bode plot	58
FIGURE 2.30: Charge converter PD compensator bode plot	60
FIGURE 2.31: Compensated charge converter system bode plot	61
FIGURE 2.32: Step response of compensated discharge buck converter	62
FIGURE 2.33: Discharge buck converter control circuit model	62
FIGURE 2.34: BESMS model	63
FIGURE 2.35: Desired BESMS output capabilities	65
FIGURE 2.36: BESMS output for max discharge and ramped reactive power(1 <sup>st</sup> & 2 <sup>nd</sup> quad)	66
FIGURE 2.37: BESMS output for max charge and ramped reactive power(3 <sup>rd</sup> & 4 <sup>th</sup> quad)	66
FIGURE 2.38: BESMS output for capacitive reactive power and ramped active power (1 <sup>st</sup> & 2 <sup>nd</sup> quad)	67
FIGURE 2.39: BESMS output for inductive reactive power and ramped active power (3 <sup>rd</sup> & 4 <sup>th</sup> quad)	67
FIGURE 2.40: Simulation test results compilation in P-Q axis	68
FIGURE 2.41: Practical 720 node distribution feeder with substation and BESS location shown	69
FIGURE 2.42: EMT aggregated model of distribution feeder	70
FIGURE 3.1: Practical PV station schematic	73
FIGURE 3.2: (a) Practical PV station Architecture (b) Modeled PV station Architecture	76

FIGURE 3.3: Solar photovoltaic cell model	77
FIGURE 3.4: PSCAD PV module model I-V curve	84
FIGURE 3.5: PSCAD PV module model P-V curve	84
FIGURE 3.6: PSCAD PV cell model	86
FIGURE 3.7: PSCAD aggregated PV array model parameters	87
FIGURE 3.8: PV station buck converter PSCAD model	89
FIGURE 3.9: Inductor current and output voltage ripples of PV station buck converter model	90
FIGURE 3.10: Uncompensated PV station buck converter bode plot	91
FIGURE 3.11: PV station buck converter PD compensator bode plot	93
FIGURE 3.12: Compensated PV buck converter system bode plot	94
FIGURE 3.13: Step response of compensated discharge buck converter	95
FIGURE 3.14: PV Station buck converter control circuit model	96
FIGURE 3.15: Inverter PSCAD model	96
FIGURE 3.16: Inverter PWM control circuit model	98
FIGURE 3.17: Full aggregated PV station model	99
FIGURE 3.18: PSCAD PV station model output active power plotted against input irradiance	100
FIGURE 3.19: Distributed generation system setup	101
FIGURE 3.20: BESMS active and reactive power supplying capabilities.	102
FIGURE 4.1: Comparison between consecutive days output powers (Day 1 & Day 2)	105
FIGURE 4.2: Comparison between consecutive days output powers (Day 3 & Day 4)	105
FIGURE 4.3: Comparison between consecutive days output powers (Day 5 & Day 6)	106
FIGURE 4.4: Comparison between consecutive days output powers (Day 7 & Day 8)	106
FIGURE 4.5: Comparison between eight consecutive days output powers	108

FIGURE 4.6 Characteristic Maximum Power Curve	108
FIGURE 4.7: Smoothed Characteristic Maximum Power Curve (SCMP)	109
FIGURE 4.8: Optimal Power Reference Curve and the limits of PV firming (smoothing) region	110
FIGURE 4.9: Firming range compared to day 9 output power	111
FIGURE 4.10 Intermittency detection algorithm PSCAD model	112
FIGURE 4.11: Intermittency detection algorithm output in response to power swing	113
FIGURE 4.12: $m_e$ calculation for energy oriented firming reference power	115
FIGURE 4.13: Dynamic BESS energy oriented reference power firming region	116
FIGURE 4.14: Weighing factor $m_e(t)$ and SoC variation for example PV day	116
FIGURE 4.15: Day 9 PV power compared to algorithm firming optimal power reference	117
FIGURE 4.16: ESS power output for firming of day 9	117
FIGURE 4.17: The point of common coupling output power compared to that of PV station	118
FIGURE 4.18: PVCF simulation results without SoC constraint. (a) PV power output compared to OPR. (b) BESS output power with battery SoC plotted on the second y-axis. (c) PCC active power output after PVCF compared to PV power output.	120
FIGURE 4.19: PVCF simulation results with SoC constraint. (a) PV power output compared to OPR. (b) BESS output power with battery SoC plotted on the second y-axis. (c) PCC active power output after PVCF compared to PV power output.	122
FIGURE 4.20: Field testing communication infrastructure	123
FIGURE 4.21: PV power compared to reference power, algorithm set-point compared to BESS dispatched power and SoC, respectively for November 16th, 2014 PVCF	124
FIGURE 4.22: Intermittency detection algorithm output for November 16th, 2014 PVCF	125
FIGURE 4.23: Result of PVCF application shown in the PCC power compared to that of the PV station for November 16th, 2014 PVCF	126
FIGURE 4.24: Firming index for November 16th, 2014 PVCF	126

FIGURE 4.25: PV power compared to reference power, algorithm set-point compared to BESS dispatched power and SoC, respectively for January 11th, 2015 PVCF	128
FIGURE 4.26: Intermittency detection algorithm output for January 11th, 2015 PVCF	129
FIGURE 4.27: Result of PVCF application shown in the PCC power compared to that of the PV station for January 11th, 2015 PVCF	129
FIGURE 4.28: Firming index for January 11th, 2015 PVCF	130
FIGURE 4.29: PV power compared to reference power, algorithm set-point compared to BESS dispatched power and SoC, respectively for January 9th, 2015 PVCF	131
FIGURE 4.30: Intermittency detection algorithm output for January 9th, 2015 PVCF	132
FIGURE 4.31: Result of PVCF application shown in the PCC power compared to that of the PV station for January 9th, 2015 PVCF	133
FIGURE 4.32: Firming index for January 9th, 2015 PVCF	133
FIGURE 5.1: Distributed generation system setup	136
FIGURE 5.2: Feeder load curve of 27th of October 2014	138
FIGURE 5.3: Feeder peak loads versus look-back days of October 28th, 2014	143
FIGURE 5.4: Time of feeder peak loads plotted against look-back days of October 28th, 2014	144
FIGURE 5.5: Feeder peak load values plotted versus time of peak loads of run day October 28th, 2014	144
FIGURE 5.6: Daily peak load magnitude prediction using averaged historical data method	148
FIGURE 5.7: Daily peak load time prediction using averaged historical data method	148
FIGURE 5.8: Averaged historical data prediction method percent errors	150
FIGURE 5.9: Daily peak load magnitude prediction using moving average method	154
FIGURE 5.10: Daily peak load time prediction using moving average method	154
FIGURE 5.11: Moving average prediction method percent errors	155

FIGURE 5.12: Average daily prediction percent error plotted verses the moving average time interval used	158
FIGURE 5.13: Moving average peak power magnitude prediction for M=1	159
FIGURE 5.14: Moving average peak power time prediction for M=14	160
FIGURE 5.15 Load curves of a practical feeder in a residential area for the week of September 21st, 2012	161
FIGURE 5.16: Energy time shift algorithm results for a residential feeder on Tuesday of the week of September 21st, 2012	162
FIGURE 5.17: PV power compared to reference power, algorithm set-point compared to actual BESS dispatched power and SoC, respectively for July 27th, 2014 PVCF & ETS	164
FIGURE 5.18: Intermittency detection algorithm output for July 27th, 2014 PVCF	165
FIGURE 5.19: Firming index for July 27th, 2014 PVCF	166
FIGURE 5.20: ETS application shown in the feeder active power load compared to substation generation for July 27th, 2014	166
FIGURE 5.21: PV power compared to reference power, algorithm set-point compared to BESS dispatched power and SoC, respectively for July 29th, 2014 PVCF	167
FIGURE 5.22: Firming index for July 29th, 2014 PVCF	168
FIGURE 5.23: ETS application results shown in feeder active power load compared to substation generation for July 29th, 2014	168
FIGURE 5.24: PV power compared to reference power, algorithm set-point compared to BESS dispatched power and SoC, respectively for August 5th, 2014 PVCF	169
FIGURE 5.25: Firming index for August 5th, 2014 PVCF	170
FIGURE 5.26: ETS application results shown in feeder active power load compared to substation generation for August 5th, 2014	170
FIGURE 5.27: PVCF & ETS results without SoC optimization	171
FIGURE 5.28: PVCF & ETS results with SoC optimization	171
FIGURE 6.1: BESS operation in response to output PV power and reference power values	176
FIGURE 6.2: Characteristic maximum PV curve	177

FIGURE 6.3: Smoothed characteristic maximum PV power	178
FIGURE 6.4: 1MW PV station sixth order polynomial rate of change and maximum ramp rate identification	179
FIGURE 6.5: Smoothed characteristic maximum PV curve for a 1MW PV station	180
FIGURE 6.6: BESS firming region	183
FIGURE 6.7: IDA operation for typical PV station output	185
FIGURE 6.8: Unfirming Energy for sample hour given reference power	187
FIGURE 6.9: PVCF algorithm simulation result for sample day with arbitrarily chosen values for SoCst and $m \cdot dCap$ (Feb 28th, 2015)	188
FIGURE 6.10: Upper and lower firming limits for deduced algorithm reference power and the resulting unfirming energy	189
FIGURE 6.11: Dynamic programming optimization flow chart to identify optimal PVCF algorithm parameter values for single day	191
FIGURE 6.12: Surface plot for unfirming energy ( $A_t$ ) plotted versus full search ranges of SoCst & $m \cdot dCap$	192
FIGURE 6.13: Contour plot showing the optimal values for SoCst & $m \cdot dCap$ , satisfying maximum firming	193
FIGURE 6.14: Firming results for sample day utilizing optimal algorithm parameters	194
FIGURE 6.15: PV power output for two days for clear, partially cloudy and overcast cloud states	195
FIGURE 6.16: Flow chart to identify periodical cloud states based on PV station power output	197
FIGURE 6.17: Flow chart showing to deduce average optimal values for different day types utilizing mass historical data	199
FIGURE 6.18: Practical firming results utilizing generic values for SoCst & $m \cdot dCap$	202
FIGURE 6.19: Firming index for practical firming case adopting generic values for SoCst & $m \cdot dCap$	203
FIGURE 6.20: Simulation firming results utilizing optimal values for SoCst & $m \cdot dCap$ as found in the lookup table	204

FIGURE 6.21: Firming index for optimized firming adopting optimal values of SoCst & m•dCap as found in the lookup table	205
FIGURE 6.22: Optimization routine run for May 15th showing minimum attainable unfirmed energy for search of SoCst & m•dCap	205
FIGURE 7.1: Two bus system to depict reactive power transmission.	209
FIGURE 7.2: Aggregated model of a medium voltage feeder	209
FIGURE 7.3: PSCAD distribution feeder model	211
FIGURE 7.4: Feeder loads and generation. (a)Active power output of substation & ESS, plotted with feeder active power load. (b)Reactive power output of substation & ESS, plotted with feeder reactive power load	212
FIGURE 7.5: Voltage profile at PCC with and without MBVS	213
FIGURE 7.6: Voltage profile at substation with and without MBVS	213
FIGURE 7.7: Voltage Regulator 1 tap operations	214
FIGURE 7.8: Voltage Regulator 2 tap operations	214
FIGURE 7.9: Voltage Regulator 3 tap operations	215
FIGURE 7.10: Field testing communication infrastructure	216
FIGURE 7.11: Voltage support parameters for day with MBVS application on (January 26th, 2015)	217
FIGURE 7.12: Voltage support parameters for day with MBVS application off (January 27th, 2015)	218
FIGURE 7.13: Feeder voltage regulators tap operations for day with MBVS application off (January 26th, 2015)	219
FIGURE 7.14: Feeder voltage regulators tap operations for day with MBVS application on (January 27th, 2015)	220
FIGURE 7.15: SBVS algorithm methodology	222
FIGURE 7.16: Unexecuted tap change identification criteria	223
FIGURE 7.17: Substation Regulator (Reg 1) states during SBVS	225
FIGURE 7.18: Line Regulator 1 (Reg 2) states during SBVS	226
FIGURE 7.19: Line Regulator 2 (Reg 3) states during SBVS	227

## CHAPTER 1: INTRODUCTION

### 1.1. Introduction

The applications in which energy storage systems are used hold considerable value to energy producers, grid operators and in turn, energy consumers. Energy storage systems can provide efficient solutions for various issues in modern electrical networks including micro grids. Reference [1] discuss different applications where different technologies of energy storage can be used. These applications include electric energy time shift, electric supply capacity, load following, area regulation, electric supply reserve capacity, voltage support, transmission support, transmission congestion relief, transmission and distribution upgrade deferral, substation on-site power, time of use energy cost management, demand change management, electric service reliability, electric service power quality, renewable energy time shift, renewable capacity firming [2,3] and wind generation grid integration. [2] Also discusses the value of using energy storage systems in flexible AC systems (FACS) and high voltage DC transmission (HVDC).

It has been identified that there is a concurrent need to quantify the “value” of storage in the various services it provides to the grid, individually and in multiple or “stacked” services, where a single storage system has the potential to capture several revenue streams to achieve economic viability. This is important now and as the cost of storage systems decline to economically attractive levels [16]. Reference [17] discusses

tools for evaluating BESS multiple functions value based on various applications and battery technologies. The ability to evaluate applications and technologies provides greater value for grid level energy storage. However, it is important to develop multiple control functions for storage management system considering grid level value and economic benefits for a given storage technology. Such control architecture should interact with grid and provide command signals to storage management systems for the appropriate set points and applications that provide maximum benefit at a given time.

The problem to which an energy storage system is aimed to solve, dictates the energy storage technology to be applied. Applications that require power sources that are able to provide a wide range of power levels for a relatively short period of time (in the order of seconds or minutes) use different storage technologies than applications that require energy sources that are able to supply limited power levels for a considerably long period of time (in the order of hours). Applications that require power sources use storage technologies that can bare relatively low amounts of energy per rated power output. These storage technologies include flywheels, capacitors, super conducting magnetic energy storage systems (SCMES) and some electrochemical battery types. Applications that require energy sources use storage technologies with high energy baring capability per rated power output. These storage technologies include thermal energy storage, pumped hydro, compressed air energy storage and most battery types [1].

## 1.2. Energy Storage Technologies

We will examine and discuss energy storage technologies according to degree of maturity. The US department of energy grid energy storage 2013 report declares

flywheel, pumped hydro, compressed air and battery energy storage systems as most mature or “deployed”.

### 1.2.1. Flywheel Energy Storage (FES)

#### 1.2.1.1. Theory of Operation

As elaborated in [11], today’s modern flywheel energy storage systems are comprised mainly of giant rotating cylinders. As shown in FIGURE 1.1, these giant cylinders are mounted on stators using magnetically levitated bearings that minimize mechanical friction and contribute to increasing system life time and eliminate bearing wear. The flywheel cylinder rotates in an air vacuumed housing that allows for a minimal drag environment. A motor/generator is mechanically coupled to the flywheel cylinder shaft. The motor/generator set is responsible for charging and discharging the flywheel energy storage system at the desired power rates. Energy is stored in the FES system through motor operation which allows the rotor to gain kinetic energy. This kinetic energy can be discharged from the rotor through generator operation.

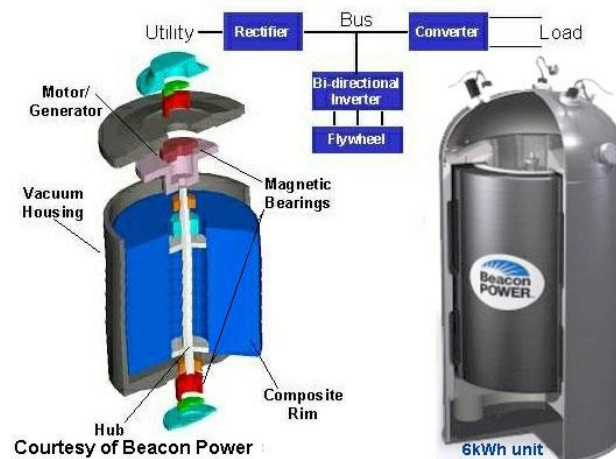


FIGURE 1.1: Beacon Power flywheel energy storage system [29]

### 1.2.1.2. Power Capacity and Energy Storage Capability

The peak power transfer ratings are dependent only on the ratings of the power electronic converters and electric machines used [2]. The energy storage capability of fly wheel energy storage systems is proportional to the moment of inertia ( $I$ ) of the rotor and square of its rotational velocity ( $\omega$ ) as shown in equation (1.2). The rotor moment of inertia relies on the mass, radius and height of the rotor as shown in (1.1).

FES systems utilize two main energy storage capacity design concepts [2]:-

- Increasing rotor inertia by increasing rotor mass ( $m$ ) (using high density materials like steel) and radius ( $r$ ). This design concept allows rotational velocities up to approximately 10,000 rpm
- Allowing for high rotational speeds ( $\omega$ ) while maintaining rotor weight light. This design concept allows rotational velocities up to approximately 100,000 rpm. This design concept allows FES systems to be small and light. Nevertheless, challenges arise in the form of bearing friction and drag which can be solved through utilizing magnetic bearings and vacuumed housings as shown in FIGURE 1.1

$$I = m r^2 \frac{h}{2} \quad (1.1)$$

$$E = \frac{1}{2} I \omega^2 \quad (1.2)$$

FESs can be practically sized between 100kW and 1650 kW and can be used for durations of 1 hour or less [26]. The largest available flywheel energy storage system is 1.6 MVA weighing approximately 10 tons [2].

#### 1.2.1.3. Technology Advantages

- Long life time 20 years (Tens of Thousands of cycles)[33]
- High power densities (5-10 times that of batteries). FESs require much less space to store a comparable amount of power [26]
- Fast response time (4 ms)
- High peak power without overheating concerns [16]
- High round trip energy efficiency [16]

#### 1.2.1.4. Technology Disadvantages

- Practically, able only to provide energy for short duration, rendering this technology not suitable for large scale grid support applications [26].
- Limitations appear due to rotor tensile strength [16]

#### 1.2.1.5. Applications

Flywheel energy storage technologies are suitable for applications that address dynamic stability [4], transient stability [5], voltage support [6] and power quality improvement [7,19,20]. Nevertheless, FES cannot present value for transmission capability improvement [2].

Reference [16] names the following primary FES applications:-

- Load leveling
- Frequency regulation
- Peak shaving and off peak storage
- Transient stability

According to [26], the cost and efficiency of using FES technology for fast frequency regulation and renewable integration is 1950-2200 \$/kW & 7800-8800 \$/kWh with efficiency at 85-87% and lifetime cycles greater than 100,000 cycle.

## 1.2.2. Pumped Hydro Energy Storage

### 1.2.2.1. Theory of Operation

Pumped hydro energy storage utilizes the difference in potential energy between elevated and depressed grounds. Such useful altitude differences are apparent in mountains located close to ocean or sea shores. In most cases, the depressed ground is a lake, sea or ocean. The elevated ground is (in most cases) naturally vacant from water. It is used after human intervention as an elevated water reservoir which represents the amount of stored energy. As shown in FIGURE 1.2, pumped hydro energy storage systems are charged by utilizing motors to pump water from depressed grounds to elevated grounds and are discharged by switching the process and allowing elevated water to flow back to depressed grounds while operating hydraulic turbines in the process allowing power generation.

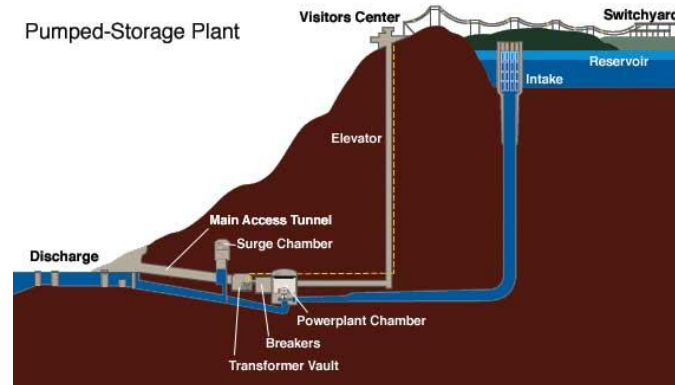


FIGURE 1.2: Pumped hydro energy storage system [30]

#### 1.2.2.2. Power Capacity and Energy Storage Capability

- Power Capacity: The power capacity of pumped hydro energy storage systems is limited by maximum intake water volumetric flow capability and hydraulic turbine and generator capacities.
- Energy Capacity: The energy capacity of pumped hydro energy storage systems is proportional to the product of the total water volume in the elevated reservoir and difference in height between reservoirs.
- The largest pumped hydro energy storage site in the U.S. is at Raccoon Mountain in Tennessee. The site energy capacity is 34 GWh with head 300 m and 1.53 GW installed capacity. The reservoir lake water volume is  $45 \times 10^6 \text{ m}^3$  and covers a total area of  $2.14 \text{ km}^2$
- The global capacity of pumped hydro storage plants is 95 GW with approximately 20 GW in the U.S. [33]

#### 1.2.2.3. Technology Advantages

- Developed and mature technology [16]
- Currently most cost effective form of storage [16]
- Largest energy storage capacity technology available

#### 1.2.2.4. Technology Disadvantages

- Long construction cost and requirement of large areas of land [31]
- Geographically limited [16]
- Large environmental impacts
- High overall project cost [16]

#### 1.2.2.5. Applications

Reference [16] names the following primary pumped hydro energy storage applications:-

- Energy management
- Backup and seasonal reserves
- Regulation service through variable speed pumps
- Peak shaving and off peak storage

According to [26], the cost and efficiency of using pumped hydro energy storage technology for bulk energy storage to support system and renewable integration applications is:-

- 2500-4300 \$/kW & 420-430 \$/kWh for 280MW-530MW (1680MWh-5300MWh) projects
- 1500-2700 \$/kW & 250-270 \$/kWh for 900MW-1400MW (5400MWh-14,000MWh) projects
- Efficiency is averaged at 80-82% and lifetime cycles greater than 13,000 cycle

#### 1.2.3. Compressed Air Energy Storage (CAES)

##### 1.2.3.1. Theory of Operation

Compressed air energy storage (CAES) systems utilize motors and air compressors to pressurize air into underground reservoirs (salt caverns, hard rock mine, or aquifer) during off peak hours. The pressurized air is then released during power system peak load daytime hours to power a turbine/generator for power production. This technology substitutes the low-cost power from an off-peak base-load facility for the

more expensive gas turbine-produced power to compress the air for combustion. In a gas turbine, roughly two thirds of the energy produced is used to pressurize the air. Since CAES facilities have no need for air compressors tied to the turbines, they can produce two to three times as much power as conventional gas turbines for the same amount of fuel. [31]

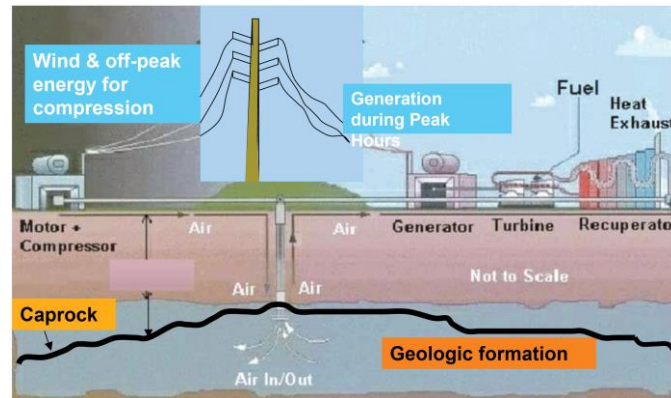


FIGURE 1.3: Compressed air energy storage system [32]

#### 1.2.3.2. Power Capacity and Energy Storage Capability

- Compressed air energy storage technology matches pumped-hydro energy storage technology in its ability to provide very-large system power capacity in the order of 100MW for a single unit. [31]
- There is two significant CAES plants. One in Huntorf, Germany with a power capacity of 290 MW. The second plant is a 110 MW unit built in McIntosh, Alabama. Both facilities utilize salt caverns for their underground air reservoir. The third will be a 2,700 MW facility (when fully built out) in Norton, OH that will use an abandoned limestone mine as the reservoir.[31]

#### 1.2.3.3. Technology Advantages

- Developed and mature technology [16]

- Relatively low cost for capacity
- Better ramp rates than gas turbine plants [16]

#### 1.2.3.4. Technology Disadvantages

- Lower efficiency due to round trip conversion [16]
- Geographically limited [16]
- Large environmental impacts [16]
- Slower response time than FES and BESSs [16]

#### 1.2.3.5. Applications

Reference [16] names the following primary CAES applications:-

- Energy management
- Backup and seasonal reserves
- Renewable integration

According to [26], the cost of using commercial CAES technology for bulk energy storage to support system and renewable integration applications is given by:-

- 1000 \$/kW & 125 \$/kWh for 1080MW (135MWh) projects
- 1250 \$/kW & 60 \$/kWh for 2700MW (135MWh) projects
- Lifetime cycles are estimated greater than 13,000 cycle.

### 1.2.4. Battery Energy Storage (BES)

#### 1.2.4.1. Theory of Operation

Battery cells are generally composed of two electrodes separated by an electrolyte. Discharge occurs when ions migrate from the anode into the electrolyte and deposit oxides on the cathode. The battery cell is charged when the said chemical reaction is reversed. [31]

Battery energy storage systems are comprised of the said cells connected together to form modules. Said modules are in turn connected together to form racks which are in turn connected to for the required BES system. All the mentioned connections are either series or parallel depending on the desired system electrical properties.

#### 1.2.4.2. Power Capacity and Energy Storage Capability

Batteries are one of the most cost-effective energy storage technologies available in which energy is stored electrochemically. Lead acid batteries can be designed for bulk energy storage or for rapid charge/discharge. Their only downside is their low energy density and limited cycle life [2].

Batteries cannot operate at high power levels for long time periods due to the chemical dynamics involved which cause rise in temperatures. Also, rapid discharges may lead to shortening battery lifetime. [2]

There are a number of relatively high power and energy capacity installations existing. One of which is a 10MW (40MWh) installation in Chino, CA. [31]

#### 1.2.4.3. Technology Advantages

- High energy density, High energy capability, Cycling capability & life span and initial cost [6]
- High charge/discharge efficiency [16]

#### 1.2.4.4. Technology Disadvantages

- Environmental concerns due to toxic gas emissions during charge and discharge [2].
- Disposal of hazardous battery materials presents some challenges for some battery types [2]

- Intolerance to deep discharge [16]

#### 1.2.4.5. Applications

battery energy storage systems are suitable for applications that improve dynamic stability [8,9,21], transient stability [10,11,21,22], voltage support [12, 21], area control/frequency regulation [13,14], transmission capability [13,14,23] and power quality [5,15,24,25].

Also, it was calculated in [26] that the cost utilizing BES technologies for frequency regulation and renewables integration applications is as follows:-

- Li-ion BESS: 1085-1550 \$/kW & 4340-6200 \$/kWh

Therefore, BESS was found to be the most feasible and economically viable energy storage technology for the intended applications.

### 1.3. Energy Storage Applications

#### 1.3.1. Renewables Capacity Firming

Renewables capacity firming using energy storage units involves supplying (discharging) and consuming (Charging) power in a manner that will make the combined output of the renewable energy source and the energy storage system constant to some extent. As mentioned in [1], “The resulting firmed capacity offsets the need to purchase or ‘rent’ additional dispatchable (capacity) electric supply resources. Depending on location, firmed renewable energy output may also offset the need for transmission and/or distribution equipment. Renewables capacity firming is especially valuable when peak demand occurs.” [3] Discusses capacity firming for a large wind farm. It focuses on developing a control strategy for optimal use of BESS for wind capacity firming. It was concluded in that publication that capacity firming is achievable for the presence of a

BESS with relatively high charge/discharge frequency and proper size (20% to 30% of wind farm capacity). The case of PV station's output power also presents a clear example of intermittent power (due to clouds) that requires firming. Similar to [3]'s conclusion, PV capacity firming applications requires a power source capable of supplying power at rapidly changing pace to cope with intermittencies that are sudden in nature. Suitable energy storage technologies for firming include BESS and SCMESs.

#### 1.3.1.1. State of Charge Optimization in Firming

Reference [34] attempts to design a capacity firming algorithm for a hybrid wind and photovoltaic (PV) system utilizing battery energy storage. It proposes a control strategy for smoothing wind and PV power fluctuations by means of feedback control of SOC and a large scale BESS. In this publication, the firming problem is formulated based on the power fluctuation rate. The power fluctuation rate is considered as an assessment indicator for PV and wind power generation equipment that is connected to the power grid. The power fluctuations rates over the investigated time period are used to evaluate the control effect of PV and wind power firming both with and without the BESS. The general ideology in this publication is to design a PV and wind power system firming strategy while taking into consideration the BESS SoC to avoid forced shutdown of the BESS due to overcharge or over-discharge. Simulation results demonstrate that the proposed control strategy can manage BESS power and SoC within a specified target region while firming PV and wind power generation systems.

Successive to what has been done in [34], it is proposed for my work to consider the SoC of the BESS an objective function rather than a constraint. This allows for the ability to perform several energy storage applications in a single day. Rather than having

a depleted BESS SoC (fully charged or fully discharged) at the end of the daily firming period, it would be possible to perform an optimized firming routine and at the same have a BESS SoC level at a suitable level to perform other storage applications. This leads to the boosting of energy storage system value to operating facilities and allows for single storage systems the potential to capture several revenue streams. Such value would be able to contribute to the effort to make investments in battery energy storage systems economically viable.

#### 1.3.1.2. Hybrid Energy Storage System Firming

A hybrid energy storage system is used in [35] to smooth the PV power output of a 1MW grid connected solar plant. The Hybrid Energy Storage System (HESS) is comprised of a Vanadium Redox Battery (VRB) and a Super Capacitor Bank (SCB). The proposed PV station power management algorithm in this publication is a heuristic rule-based algorithm. The heuristic control rules are developed based on the Australian rules for semischeduled generation [36] and the rating constraints of VRB and SCB. Specifically, the Australian grid code requires the PV power plant to generate a constant power below in every 5 min dispatch interval.

In this publication, the first stage of the power management algorithm handles the power sharing between the VRB and the SCB. The power reference of the HESS is divided into two parts: VRB power reference and SCB power reference. In order to reduce the operating points of VRB, the VRB reference is regulated to several incremental steps. The value is kept constant until the difference between the HESS and VRB reference powers is higher than one incremental step. This leads to VRB power being constant during each interval while the SCB handles the oscillating power. [35]

Successive to the described work, the research to be conducted will aim to determine the technical and economical traits of utilizing combinations of different storage technologies for renewable capacity firming. The impact of firming applications on storage systems' life times will be studied and sought to be maximized using different storage technology combinations. Accomplishing this would contribute to maximizing energy storage system value through increasing investment period and thus, decreasing cost. This would also contribute to the effort to make investments in battery energy storage systems economically viable.

#### 1.3.1.3. Renewables Power Output Prediction

Reference [37] proposes a practical approach for the prediction of photovoltaic power generation using solar irradiance as a single input. Solar irradiance is modeled as the sum of a deterministic component and a Gaussian noise component. The solar irradiance on a partly cloudy day is forecasted by Kalman filtering. The shaping filter for the Gaussian noise is calculated using spectral analysis and an autoregressive moving average (ARMA) model. The results of the two approaches are compared with the measured irradiance at a practical PV generating facility. The results show that more accurate estimates are obtained using spectral analysis than those obtained with the ARMA model, particularly for lower sampling rates. [37]

Energy storage system response time during firming was practically found to be a crucial factor of the efficiency of the renewables capacity firming application. It is therefore sought to predict renewables output power. Weather forecast as well as kalman filtering will be used to design a sub-hourly and hourly prediction algorithm for PV

power output. This will allow for a buffer time period in which communication time delays and storage management systems' response time delays are covered.

### 1.3.2. Voltage Support

One of the main and most important concerns for utilities and grid operators is maintaining the voltage within permissible levels. Radial networks exhibit voltage depression as the distance from the substation increases. Utilities invest considerable amounts of money on capacitor banks and static VAR compensators to keep voltage levels steady within the permissible band. These devices generate reactive power to counter effect reactive power sinks represented in feeder lines and poor power factor loads connected to the grid like fans, air conditioning systems, washers and dryers. Utilities also invest in numerous voltage regulators (VRs) and load tap changers (LTCs) per feeder. These devices vary the number of turns connected to their primary or secondary winding in order either to buck or boost the voltage depending on the need. Unfortunately, each tap change for such devices decreases their remaining life time which forces utilities to invest in new VRs and LTCs after a shorter period of time. Since VRs and LTCs operate relatively slower than VAR compensators, BESS can be used to compensate for reactive power which in turn, will lead to a decreased total number of regulator operations and tap changes.

As mentioned in [1, 27, 28], "BESS voltage support is an application for which distributed storage may be especially attractive because reactive power cannot be transmitted efficaciously over long distances. Notably, many major power outages are at least partially attributable to problems related to transmitting reactive power to load

centers. So, distributed storage – located within load centers where most reactance occurs – provides especially helpful voltage support.”

In reference [38], an architecture for voltage regulation in distribution networks is proposed. This architecture relies on controlling reactive power injections provided by distributed energy resources (DERs). Amongst these distributed energy sources could be BESSs. In this publication’s setup, a local controller on each bus of the network monitors the bus voltage. Whenever there is a voltage violation, it uses locally available information to estimate the amount of reactive power that needs to be injected into the bus in order to correct the violation. If the DERs connected to the bus can collectively provide the reactive power estimated by the local controller, they are instructed to do so. Otherwise, the local controller initiates a request for additional reactive power support from other controllers at neighboring buses through a distributed algorithm that relies on a local exchange of information among neighboring controllers. It is shown in this publication that the proposed architecture helps prevent voltage violations and shapes the voltage profile in radial distribution networks, even in the presence of considerable penetration of variable generation and loads.

It can be concluded from the referenced publications that in order to attain an efficient voltage support strategy, the following points must be fulfilled:-

- The constant knowledge of the degree of reactive power compensation at BESS point of common coupling in order to attain a required voltage level.
- The determination of the optimal value of voltage magnitude at a certain bus to attain a better voltage profile and minimize voltage regulator tap changes across the feeder.

- The presence of real time data streams from different points on the targeted feeder

The main challenges complicating the performance of voltage support on medium voltage distribution feeders are represented in the scarcity of buses with metering of local loads, voltage magnitude and phase in real time. Also, expense of Phase Measurement Units (PMUs) hinders utility efforts to monitor phase angles across different points on their distribution feeders. This dictates devising state estimation based routines to account for missing system states. The validity of state estimation solutions in comparison to exact solutions will be studied and verified. The approach followed to devise a voltage support algorithm with minimal required system state information relies on comparing results attained from two solutions; the first solution assumes the presence of all system parameters and states which gives exact value for the required reactive power for voltage support at a specific bus. The second solution uses state estimation values and approximations using data that is most likely available for a proposed practical controller.

### 1.3.3. Electrical Energy Time Shift

Electrical Energy Time Shift (ETS) aims to minimize power system peak loads through utilizing battery energy stored during times of off peak loads. Since time of peak load represents the time during which price of energy is most expensive, the prediction of feeder peak load value and time represents the most important aspect of ETS storage applications.

Further, Electric energy time-shift involves acquiring low-cost electric energy, available during minimal distribution feeder load, to charge the energy storage system in order to be able to use the stored energy during times of peak feeder load when price of

energy is at its peak. As stated in [1], “this application tends to involve purchase of inexpensive energy from the *wholesale* electric energy market for storage charging. When the energy is discharged, it could be resold via the wholesale market, or it may offset the need to purchase wholesale energy and/or to generate energy to serve end users’ needs.”

For storage plants of large energy bearing capacity like CAES and pumped hydro energy storage, the plant storage discharge duration is determined based on the incremental benefit associated with being able to make additional buy low – sell high transaction during the year versus the incremental cost for additional energy storage (discharge duration). [1]

The standard assumption value for storage minimum discharge duration for this application is two hours. The upper boundary for discharge duration is defined by potential CAES or pumped hydroelectric facilities. For storage types that have a high incremental cost to increase the amount of energy that can be stored, the upper boundary is probably five or six hours, the typical duration of a utility’s daily peak demand period. Both storage variable operating cost and storage efficiency are especially important for this application because electric energy time-shift involves many possible transactions whose economic merit is based on the difference between the cost to purchase, store and discharge energy (discharging cost) and the benefit derived when the energy is discharged. Any increase in variable operating cost or reduction of efficiency reduces the number of transactions for which the benefit exceeds the cost. That number of transactions is quite sensitive to the discharge cost, so a modest increase may reduce the number of viable transactions considerably. [1]

A simple auto-regressive moving average algorithm will be used to predict the time and magnitude of distribution feeder peak loads.

#### 1.4. Conclusion

In conclusion, the versatility of different energy storage technologies was investigated. We were able to confidently name Li-ion and lithium polymer battery energy storage systems as the most versatile energy storage technologies for the energy storage applications discussed. Efforts to combine different storage applications in single controllers were discussed and found highly beneficial for battery energy storage economic viability. These controllers work with Storage Management Systems to enhance active power capabilities and at the same time evaluate the need and requirement of distribution feeders. Photo Voltaic Capacity Firming (PVCF), ETS and voltage support were studied individually as well as collectively in order to study function coordination for the sole purpose of maximizing value.

## 1.5. Research Contributions

Main research contributions are presented in TABLE 1.1.

TABLE 1.1: Research contributions

Contribution Topic	Description	Section
Battery Energy Storage System (BESS) modeling	<p>A practical utility scale 250kW/750kWh lithium polymer battery energy storage system was modeled in PSCAD. Battery cell parameters were deduced utilizing Matlab. Cell charge/discharge characteristics were matched to the manufacturer's data sheet and practical operation data.</p> <p>The BESS inverter, referred to here as the Storage Management System (SMS), was modeled utilizing a unique electronic switch architecture allowing reactive power supply and absorption during both charge and discharge battery operations. The designed architecture performance was validated using practical system data.</p>	2.2 and 2.3
PV station modeling	<p>A 1.25MVA utility scale PV station consisting of six arrays was modeled in PSCAD. PV cell parameters were deduced utilizing Matlab solvers. Matlab I-V curves were matched to that of manufacturer. PSCAD PV cell models were matched to both Matlab models and manufacturer data sheet. Solar inverter model was designed utilizing a buck converter/three leg voltage source inverter combination in PSCAD. Inverter model was validated with practical system data (Irradiance as input and injected power as system output)</p>	3.4
PV Station Capacity Firming (PVCF) Algorithm design	<p>Two main PVCF algorithms were designed. The first algorithm aims to minimize PV output power swings regardless of any other system parameter. The second algorithm relies on monitoring battery SoC to allow multiple application operation daily. Simulation and implementation results performed display the algorithms' effectiveness</p>	4.2 - 4.4

Energy Time Shift (ETS) Algorithm design	An ETS algorithm was designed to effectively predict the time and value of feeder peak load. Further, the optimal time of ETS full battery discharge was deduced in the methodology to allow operation of parallel storage applications.	5.3
Cloud state pattern recognition aided PVCF design	A PVCF algorithm was designed to utilize cloud state pattern recognitions and predictions. A dynamic programming optimization routine was designed to maximize the BESS's capacity firming efficiency using forecasted cloud state patterns.	6.2 - 6.4
Model based Voltage Support Algorithm design	A voltage support algorithm was designed relying on model based architecture to define the value of VARs to be injected or absorbed at the point of common coupling.	7.2
Sensor based Voltage Support Algorithm design	A sensor based voltage support algorithm was designed to utilize distribution level voltage regulator sensors to deduce the VAR value to be injected or absorbed at the point of common coupling.	7.3

## CHAPTER 2: BATTERY ENERGY STORAGE AND MANAGEMENT SYSTEM

### 2.1. Introduction

In this chapter, the detailed architecture, design and modeling of the Battery Energy Storage and Management System (BESMS) is studied. In section 2.2, the details of the studied storage technology, namely, Battery Energy Storage Systems (BESS) are discussed. This section discusses the full details of specifications, model evaluation and validation of the studied practical BESS. Section 2.3 studies the Storage Management System (SMS) responsible for the protection, stability, control and operation of the BESS. Each device of the SMS is designed and modeled according to the specifications of the studied practical SMS. The chapter is concluded in section 2.5.

Further, in the studied practical setup, the BESMS is connected to a 12.475 kV distribution feeder. As shown in FIGURE 2.1, the BESMS is comprised of the BESS and the Storage Management System (SMS). The BESS is comprised of the actual battery pack and Battery Management System (BMS). The BESS battery pack consists of a series of lithium battery cells connected in modules and racks. The SMS is connected to the BESS and is responsible for its operation and control. It handles connection and synchronization between the DC side BESS and the AC side distribution feeder. It also, controls active and reactive power supplied and absorbed from the distribution feeder.

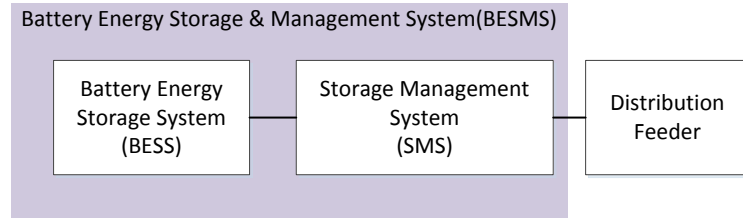


FIGURE 2.1: BESMS Architecture

## 2.2. Battery Energy Storage System (BESS)

The studied practical BESS is a product of Kokam. It has an energy storing capacity of 750 kWh and a power capacity of 250 kW. The BESS is mainly comprised of the battery pack and the Battery Management System (BMS) responsible for management, protection and operation of the battery pack's cells, modules and racks.

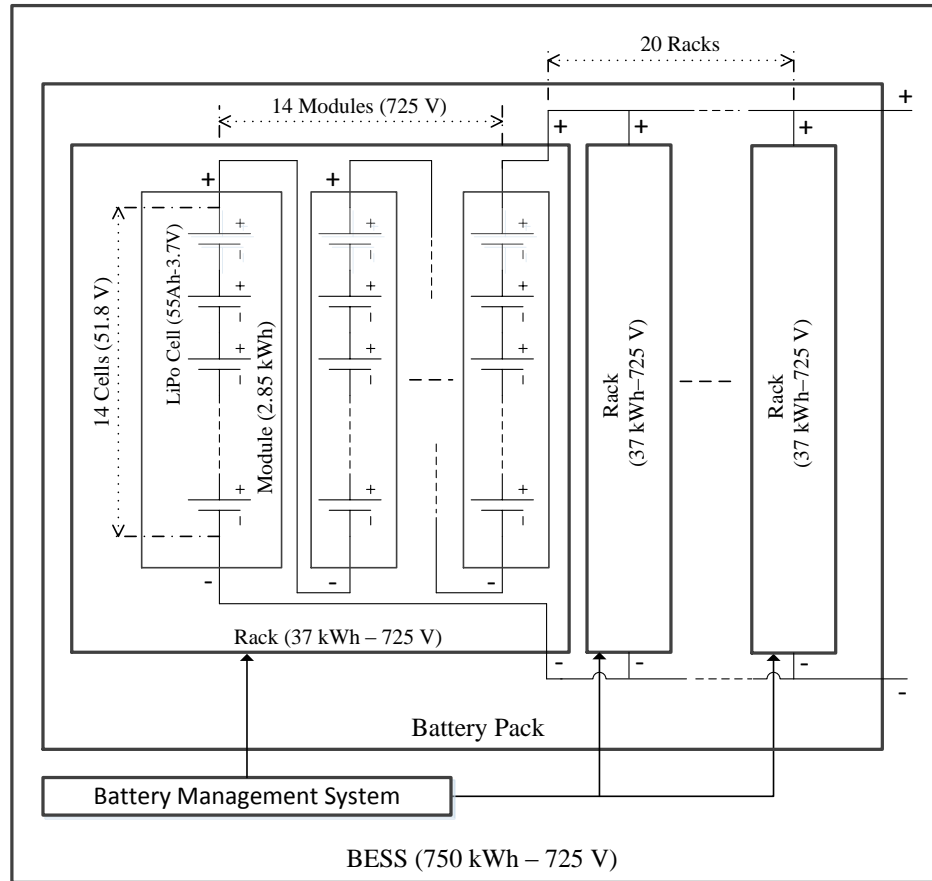


FIGURE 2.2: BESS electrical circuit

### 2.2.1. Battery Pack

#### 2.2.1.1. Battery Pack Specifications:-

The battery pack in study is constructed of lithium polymer (LiPo) cells. Lithium cells offer great advantageous in size and weight characteristics when compared to other battery storage technologies. Lithium cells have an average specific energy of 200 Wh/kg and an average energy density of 350 Wh/L which is more than double that of Nickel Cadmium cells for both aspects. As shown in FIGURE 2.2, each module is comprised of 14 LiPo cells connected in series. Fourteen 51.8 volt Modules are in turn connected in series amongst each other to form a single rack of a nominal voltage of 725V. The ESS is

comprised of 20 of the specified racks connected in parallel. The exact specifications for cells, modules and racks forming the BESS are summarized in TABLE 2.1.

TABLE 2.1: Battery Pack Specifications

	Parameter	Value
<b>Cell</b>	Type	Lithium Polymer
	Internal Resistance	0.7 mΩ
	Capacity	55 Ah
	Nominal Voltage	3.7 V
	Operational Voltage Range	2.7 V-4.2 V
<b>Module</b>	Connection Type	Series
	Number of Cells per Module	14
	Nominal Voltage	51.8 V
	Capacity	2.85 kWh
<b>Rack</b>	Connection Type	Parallel
	Number of Modules per Rack	14
	Nominal Voltage	725 V
	Operational Voltage Range	645-815 V
	Capacity	37 kWh
<b>Battery Pack</b>	Connection Type	Parallel
	Number of Racks in ESS	20
	Nominal Voltage	725 V
	Operational Voltage Range	645-815 V
	Capacity	750 kWh
	Maximum Charge & Discharge Power	250 kW

#### 2.2.1.2. Battery Pack Model:-

The battery model used in the described Energy Storage System (ESS) is modeled with the same methods used in [18] for Lithium batteries.

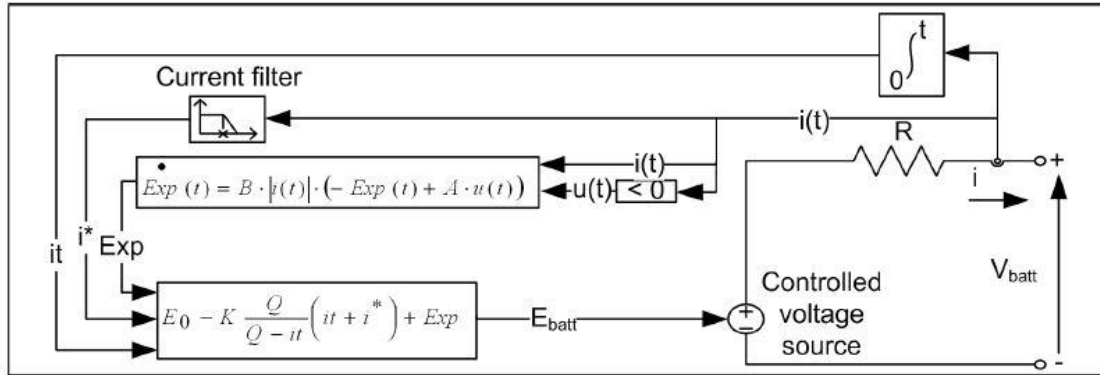


FIGURE 2.3: Battery discharge model [18]

In the described model the voltage at battery terminal is governed based on the case of the battery being charging or discharging as follows:-

- Discharge

$$V_{batt} = E_0 - K \frac{Q}{Q - it} \cdot (it + i^*) - R \cdot i + A e^{-B \cdot it} \quad (2.1)$$

- Charge

The charge model is similar to the discharge model shown in FIGURE 2.3 with only the equation of  $E_{batt}$  different.

$$V_{batt} = E_0 - R \cdot i - K \frac{Q}{it - 0.1Q} \cdot i^* - K \frac{Q}{Q - it} \cdot it + A e^{-B \cdot it} \quad (2.2)$$

Where:-

$V_{batt}$  = battery voltage (V)

$E_0$  = battery constant voltage (V)

$K$  = polarisation constant (V/(Ah)) or polarization resistance ( $\Omega$ )

$Q$  = battery capacity (Ah)

$it$  = actual battery charge (Ah)

$A$  = exponential zone amplitude (V)

$B$  = exponential zone time constant inverse (Ah)<sup>-1</sup>

$R$  = internal resistance ( $\Omega$ )

$i$  = battery current (A)

$i^*$  = filtered current (A)

### 2.2.1.3. Model Parameters Evaluation:-

The battery cell used in our setup is Kokam's SLPB100255255HR2. The discharge curve of SLPB120216216 was attainable. This cell is 53 Ah rather than 55 Ah and has an internal resistance of 0.9 m $\Omega$  rather than 0.7 m $\Omega$ . The curve shown in FIGURE 2.4 will be used as an approximation.

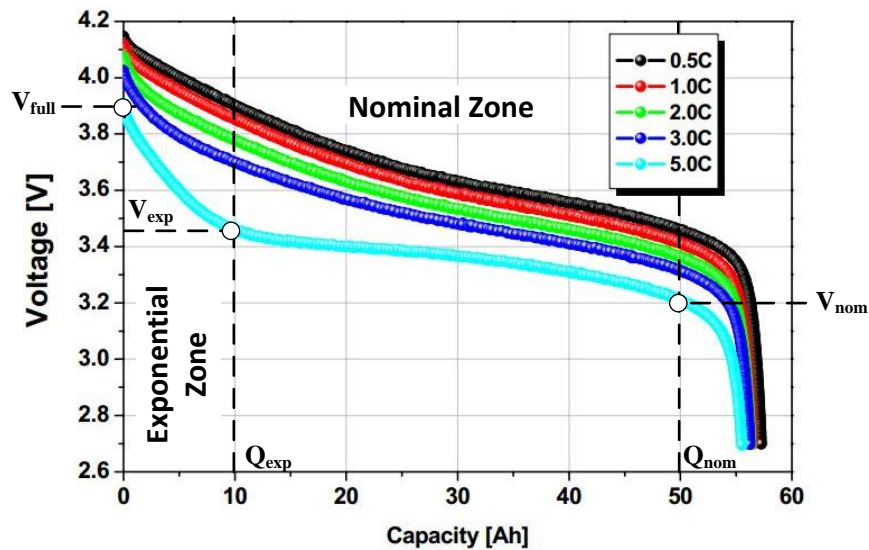


FIGURE 2.4: Battery Manufacturer Discharge Curve for SLPB120216216

Using the method described in [18] to calculate the parameters of the described model, three points of the manufacturers discharge curve are required. These three points can be extracted from the discharge curve shown in FIGURE 2.4. The first point is the point at which the cell is fully charged. At this point, the battery voltage is denoted by ( $V_{full}$ ), extracted charge is zero ( $it=0$ ) and filtered current is zero ( $i^*=0$ ). The second point is represented by the end of the exponential zone ( $Q_{exp}$ ,  $V_{exp}$ ). The third point is represented by the end of the nominal zone ( $Q_{nom}$ ,  $V_{nom}$ ).

Substituting with values of the first point in (2.1), we attain (2.3)

$$V_{full} = E_0 - R \cdot i + A \quad (2.3)$$

As applied in [18], the factor B can be approximated to ( $3/Q_{exp}$ ) for the second point (end of exponential zone) since the energy of the exponential term is approximately 5% after 3 time constants. Also, the filtered current ( $i^*$ ) is equal to ( $i$ ) since it is in steady state. Applying this to (2.1), we attain equation (2.4)

$$V_{exp} = E_0 - K \frac{Q}{Q - Q_{exp}} \cdot (Q_{exp} + i) - R \cdot i + A e^{-\frac{3}{Q_{exp}} \cdot Q_{exp}} \quad (2.4)$$

For the third point, namely, the end of the nominal zone, equation (2.1) becomes:-

$$V_{nom} = E_0 - K \frac{Q}{Q - Q_{nom}} \cdot (Q_{nom} + i) - R \cdot i + A e^{-\frac{3}{Q_{exp}} \cdot Q_{nom}} \quad (2.5)$$

Using the 5C discharge rate ( $i = 275A$ ), the three discussed points can be extracted from the manufacturer discharge curve shown in FIGURE 2.4 as follows,

$$V_{full} = 3.9 V$$

$$Q_{exp} = 10 \text{ Ah} \qquad V_{exp} = 3.45 \text{ V}$$

$$Q_{nom} = 50 \text{ Ah} \qquad V_{nom} = 3.2 \text{ V}$$

$$R = 0.7 \text{ m}\Omega \qquad i = 275 \text{ A (5C)}$$

The following matlab code is used to deduce  $A$ ,  $B$ ,  $K$  and  $E_o$  :-

```

clc
clear all

%% Battery Model Parameters Evaluation

syms Vbatt Eo K Q it istar A B R i

Eo=Vbatt+K*(Q/(Q-it))*(it+istar)-A*exp(-B*it)+i*R ;

%% Discharge Curve Data (Discharge Rate: 0.5C)

Qcell=55;      %Ah
Vfull=3.9;    %Volts
Qexp=10;      %Ah
Vexp=3.45;   %Volts
Qnom=50;      %Ah
Vnom=3.2;    %Volts
R=0.0007;    %Ohm
itest=275;   %A (0.5C)

%% Full Cell Charge Equation

Vbatt=Vfull;
Q=Qcell;
it=0;
istar=0;

Eo1=vpa(subs(Eo))

%% Exponential Region Equation

Vbatt=Vexp;
it=Qexp;
istar=itest;
i=itest;
B=3/Qexp;

Eo2=vpa(subs(Eo),5)

```

```
%% Nominal Region Equation
```

```
Vbatt=Vnom;
it=Qnom;
istar=itest;
i=itest;
B=3/Qexp;

Eo3=vpa(subs(Eo),5)
```

This matlab code outputs the following equations:-

```
Eo1 = 4.0925 - 1.0*A
Eo2 = 348.33*K - 0.049787*A + 3.6425
Eo3 = 3575.0*K - 3.059e-7*A + 3.3925
```

Solving these three equations in matlab :-

```
%% Solving The Three Deduced Equations for A, K, Eo

syms A K Eo

[A,K,Eo] = solve(Eo==Vfull+i*R-A, Eo == Vexp + K*(Q/(Q-Qexp))*(Qexp+i)
+ i*R - A*exp(-3), Eo == Vnom + K*(Q/(Q-Qnom))*(Qnom+i) + i*R -
A*exp((-3/Qexp)*Qnom) ,A,K,Eo);

A=vpa(A,4)
B
K=vpa(K,4)
Eo=vpa(Eo,4)

%% Battery Cell Voltage Equation

syms it Vbatt i
Vbatt=Eo-K*(Q/(Q-it))*(it+istar)+A*exp(-B*it)-i*R
```

The values of  $A$ ,  $B$ ,  $K$  and  $E_o$  are given by:-

```

A =0.4477

B =0.3000

K =7.057e-5

Eo =3.645

Vbatt =0.4477*exp(-(3*it)/10) - (7*i)/10000 + (0.0039*(istar +
it))/(it - 55) + 3.6448

```

Substituting the calculated  $A$ ,  $B$ ,  $K$  and  $E_o$  values in (2.1), the battery model voltage equation becomes:-

$$V_{batt} = 3.645 - 7.057 \times 10^{-5} \frac{55}{55 - it} \cdot (it + i^*) - 0.0007 \cdot i + 0.4477 e^{-0.3 \cdot it} \quad (2.6)$$

Plotting the discharge curve of the deduced model:-

```

%% Plotting Discharge Curve of Model
istar=275;
i=itest;
n=0;
for it=0:54.9
    n=n+1;
    x(n)=it;
    V(n)=vpa(subs(Vbatt));
end

figure (1)
plot(x,V)
grid on
xlabel('Capacity (AH)')
ylabel('Voltage (V)')

```

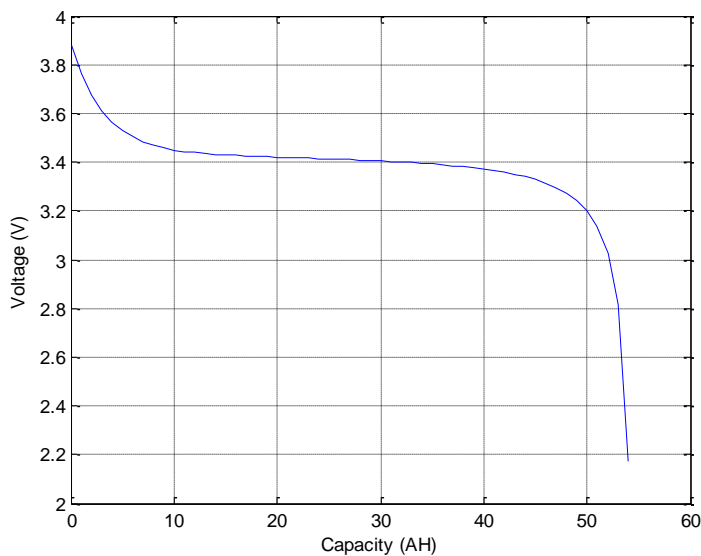


FIGURE 2.5: Matlab battery model discharge curve

FIGURE 2.5 shows the discharge curve of the matlab battery model for a 5C ( $i=275A$ ) discharge rate. The comparison of the modeled battery discharge curve to that of the manufacturer's is shown in FIGURE 2.6.

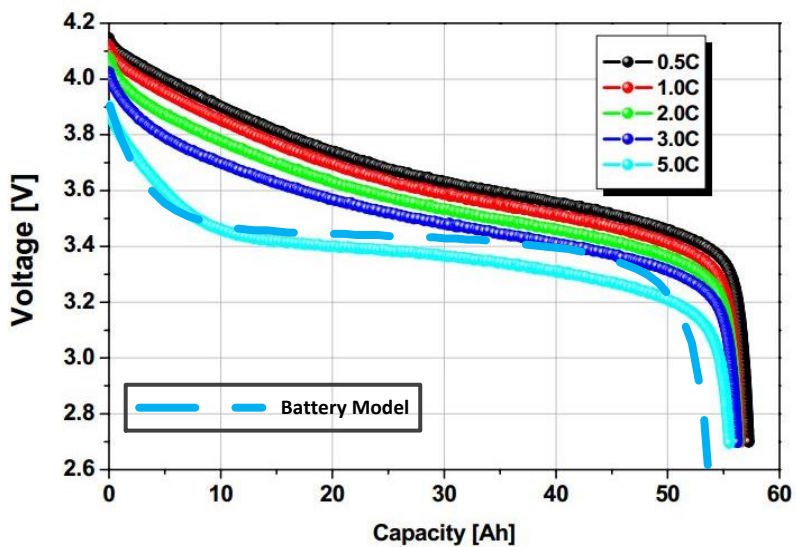


FIGURE 2.6: Modeled cell discharge curve versus manufacturer discharge curve

The comparison shows fairly close characteristics between both. It is now safe to use the deduced battery cell parameters ( $A$ ,  $B$ ,  $K$  &  $E_o$ ) in PSCAD as the building block of total battery pack.

#### 2.2.1.4. PSCAD Model Validation:-

The parameters evaluated in the previous section are used to model the battery cell in PSCAD. Battery pack specifications are filled in the PSCAD description dialog to apply the use of one battery cell as shown in FIGURE 2.7.

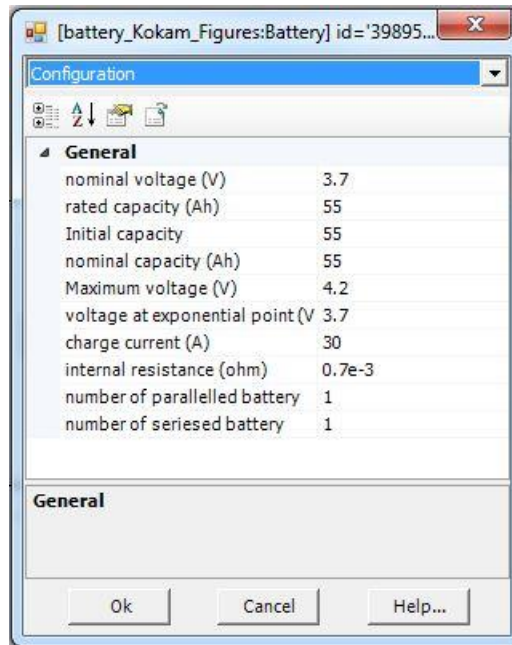


FIGURE 2.7: PSCAD battery pack description

The circuit shown in FIGURE 2.8 is constructed to test the PSCAD model discharge cycle. A constant current load is used to conduct the test at a discharge current level of (5C) which is equivalent to 275A. This is the same discharge rate used to evaluate the battery model parameters.

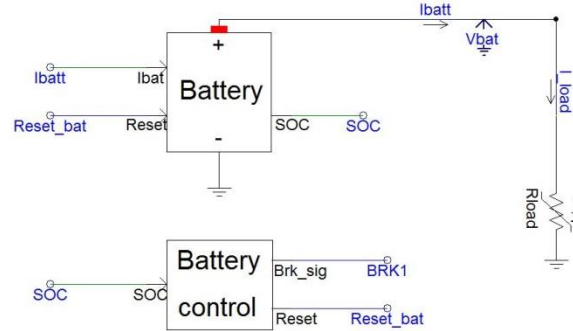


FIGURE 2.8: PSCAD battery cell model validation circuit

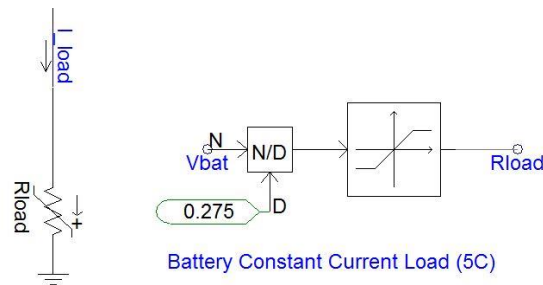


FIGURE 2.9: Constant current load model

As shown in FIGURE 2.9, a simple variable resistance ( $R_{load}$ ) is used to model a constant current load. The hard limiter shown is used to avoid a short circuit at the beginning of the simulation.

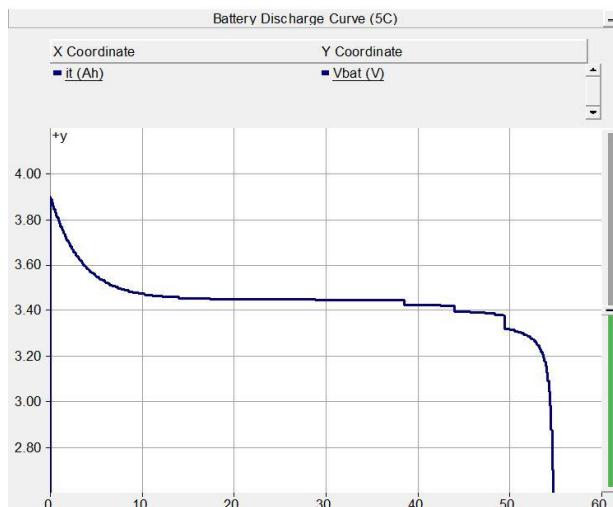


FIGURE 2.10: PSCAD battery model discharge curve

FIGURE 2.10 shows the discharge curve of the PSCAD model after running the simulation and monitoring the discharged battery energy and the corresponding battery voltage. The PSCAD battery model discharge curve is plotted with the matlab discharge curve in a single plot shown in FIGURE 2.11

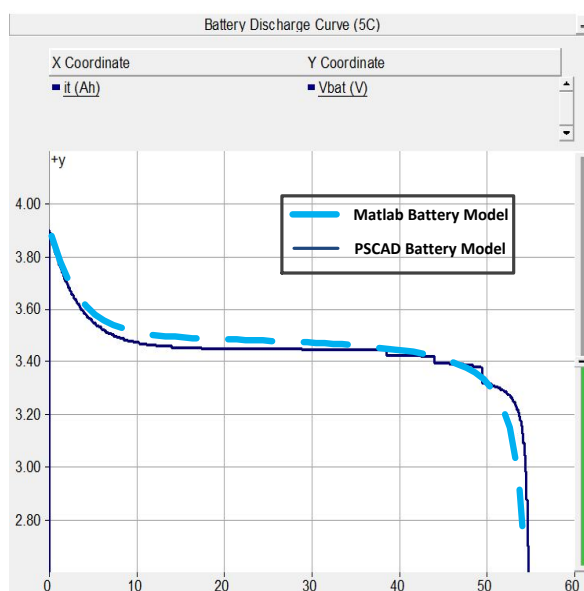


FIGURE 2.11: PSCAD and matlab battery models discharge curves

It is also important to validate the PSCAD battery cell model discharge time under the same test condition of constant discharge current (5C). FIGURE 2.12 shows the battery voltage, current and State of Charge (SoC) during the discharge test. Since the used battery cell has an energy capacity ( $Q=55\text{Ah}$ ), and the test is conducted at  $i_{batt}=5C$ , the time in which the battery SoC goes from 100% to 0% should be one fifth of an hour (720sec). It is clear in FIGURE 2.12 that this discharge period is in fact 720 seconds. It is also clear that the battery is discharging at a constant rate 275A (5C).

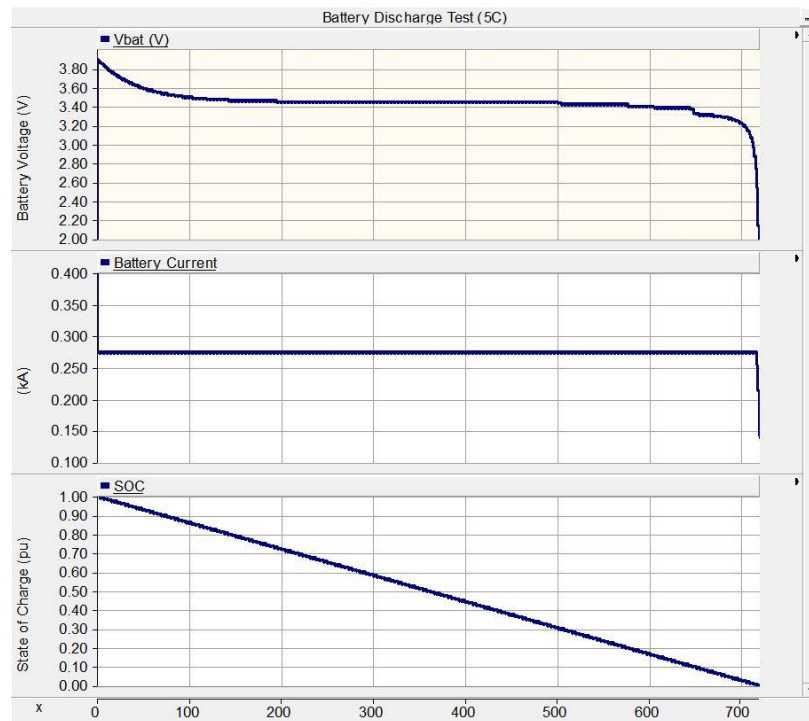


FIGURE 2.12: Battery voltage, current and SoC during discharge curve evaluation

### 2.2.2. Battery Management System (BMS)

The battery management system installed on the practical system studied manages the temperature of each battery cell in the system to provide protection against overheating. It also predicts when cells, modules and racks should be replaced before device issues occur. It also insures safe system operation by dictating maximum charge and discharge rates of the BESS by setting the Charge Current Limit (CCL) and Discharge Current Limit (DCL).

Some of the issues being monitored and managed practically by BMSs, Namely, cell temperature, battery life time, total operating time since first use, total energy delivered since first use and total number of cycles are not modeled in the applied PSCAD & matlab models since they are specific to practical operation of the BESS. Other parameters like CCL and DCL are managed and controlled in PSCAD models by the Storage Managements System (SMS) model.

### 2.3. Storage Management System (SMS)

The main purpose of the SMS is to provide a stable and reliable system to convey electrical energy from and to the battery fulfilling the following goals:-

- Convert DC voltage at battery terminal to AC voltage
- Provide an AC voltage magnitude and phase at SMS terminals suitable for the amount of reactive and active power desirable for dispatch
- Provide a grid synchronized AC voltage wave at SMS terminals
- Provide the ability to have reactive power dispatch independent of battery charge/discharge case. i.e. The SMS should be able to provide or

absorb reactive power from the feeder whether the battery is discharging or charging

- Provide the capability to control the rate of charge and discharge of the battery
- Maintain battery operation in respect to the BMS set CCL and DCL

### 2.3.1. Storage Management System Architecture

The studied SMS topology is connected on its DC side to the lithium polymer battery which was modeled and validated in the previous section. The SMS topology is constructed to allow operation in the four PQ power quadrants. In other words, reactive power supply and consumption is possible during both charge and discharge states of the battery. This would not be achievable with conventional bidirectional inverter topologies.

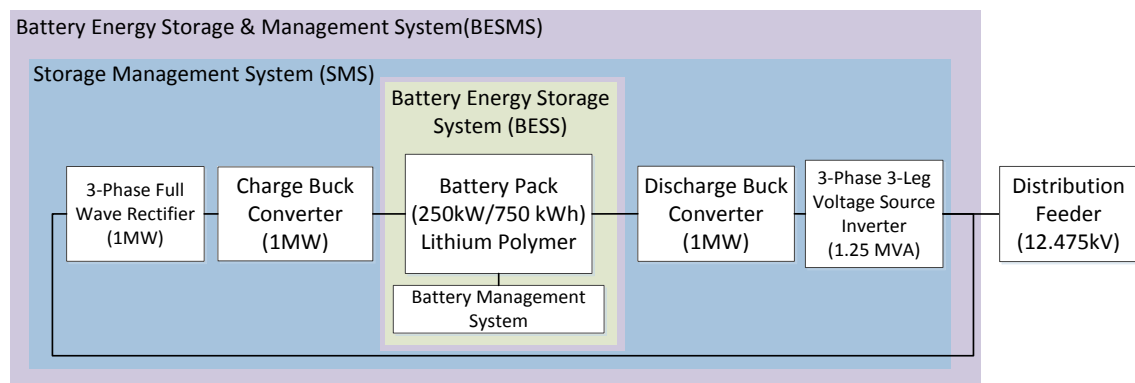


FIGURE 2.13: Storage Management System Architecture

The Storage Management System shown in FIGURE 2.13 is constructed of the following devices:-

#### 2.3.1.1. Discharge DC-DC Buck Converter

The Discharge Buck Converter is connected at its input to the battery pack terminals at a maximum DC voltage level of 815V. Converter duty cycle is controlled to

maintain DC link voltage at 700V. Converter elements are designed to maintain continuous mode operation with a maximum of 5% voltage and current ripple level. This converter is designed to operate at 250 kW with a maximum capacity of 1MW.

#### 2.3.1.2. Inverter

The SMS inverter is designed to operate at 1.25MVA. It is connected on its DC side to the output of the discharge buck converter which has the DC link voltage set to 700V. The output of the inverter is set at a nominal voltage level of 480V (line to line, RMS). Current and voltage filtering is performed by a series inductor and parallel capacitor. The parallel capacitor is sized for harmonic removal and reactive power support. The output is connected to the grid through a step up transformer (0.48/29.4kV). Output active and reactive power is controlled by phase and magnitude control respectively, of PWM reference signal controlling inverter switches.

#### 2.3.1.3. Three Phase Full Wave Rectifier

The three phase full wave rectifier is uncontrolled and operates at 250 kW and has a maximum capacity of 1 MW. It is connected on its AC side to the grid through a 24.9/1 kV, 1MW delta-delta transformer. The rectifier DC side voltage is 1.85 kV.

#### 2.3.1.4. Charge DC-DC Buck Converter

The charge Buck Converter is connected at its input to the output of the rectifier at a DC voltage level of 1.85 kV. The output is connected to the battery terminals. The output voltage is controlled according to the desired battery charge rate. A 5% converter voltage and current ripple level is allowed. This converter is designed to operate at 250 kW with a maximum capacity of 1MW.

### 2.3.2. Storage Management System Design and Modeling

The different converters forming the SMS are hereafter, designed in matlab and modeled in PSCAD.

#### 2.3.2.1. Discharge DC-DC Buck Converter

The discharge buck converter is responsible for holding the inverter DC link voltage constant at 700V regardless of the rate of discharge.

- Discharge Buck Converter Specifications

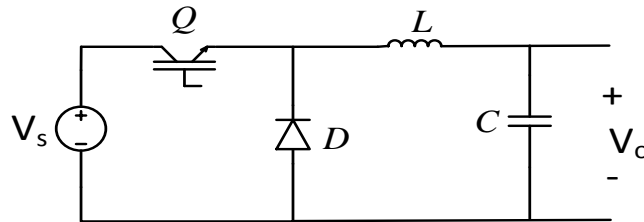


FIGURE 2.14: DC-DC Buck converter basic electrical circuit

The discharge buck converter to be designed in this section has the following specifications:-

TABLE 2.2: Discharge Buck Converter required characteristics

Parameter	Value
Input Voltage Range	700V-815V
Output Voltage	700V
Manufacturer Capacity	1 MW
Maximum Voltage Ripple	5% (35V)
Maximum Current Ripple	5% (71A)
Switching Frequency	500Hz

- Discharge Buck Converter Element Design

Let us find expressions relating the output current and voltage of buck converters to the filter elements described.

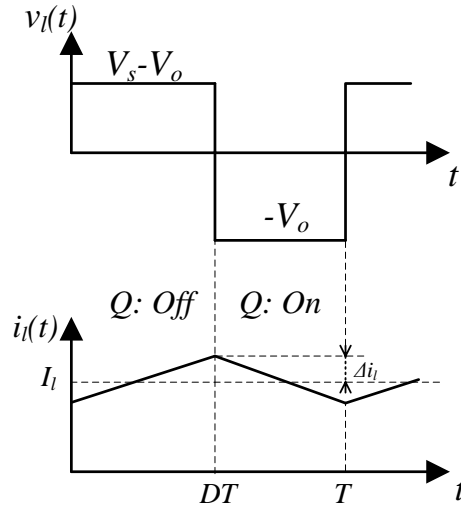


FIGURE 2.15: Voltage and current wave forms per converter cycle

As shown in FIGURE 2.15, the inductor carries a voltage  $(V_s - V_o)$  when  $(Q)$  is on. Where  $(V_o)$  represents the averaged voltage of the converter output. The inductor has a voltage of  $(-V_o)$  when  $(Q)$  is off. This leads us to the following equations.

During on period:-

$$v_l = L \frac{di_l}{dt} = V_s - V_o \quad (2.7)$$

During off period:-

$$v_l = L \frac{di_l}{dt} = -V_o \quad (2.8)$$

Total current ripple:-

$$i_{ripple} = 2 \Delta i = DT \frac{di_l}{dt} \quad (2.9)$$

From equations (2.7) and (2.9):-

$$L = DT \frac{V_s - V_o}{i_{ripple}} \quad (2.10)$$

The inductor value indicated in equation (2.10) represents the minimum inductance that will satisfy the allowed current ripple percentage (5% in our case). It is favorable to choose an inductor 25% greater than that calculated value.

Similarly, the capacitor value is specified by the following equation:-

$$C = \frac{\Delta i_l T_s}{8\Delta v_c} \quad (2.11)$$

The following matlab code is written to deduce the values of L & C:-

```

clc
clear all

%%Element specification: For 1MW Buck Converter
Vs = 815;
Vout = 700;
P = 1000e3;
D_prime = Vs/Vout;
D = 1/D_prime;
Iin = P/Vs;
Iout=P/Vout;
IL = Iout;
Fsw= 500;
T = 1/Fsw;
R = Vout^2/P;
i_ripple = 5/100*Iout; % 5% ripple in output current
v_ripple = 5/100*Vout; % 5% ripple in output voltage

%%Element Design:
Ldesign = D*T*(Vs-Vout)/i_ripple
Cdesign= (i_ripple*T)/(8*v_ripple)

```

The design values of the converter inductor and capacitor are as follows:-

```

Ldesign = 0.0028 (Henry)
Cdesign = 5.1020e-04 (Farad)

```

In order to assure operation within voltage and current ripple limits, the following inductor values are chosen:-

$$L_l = 3.5 \text{ mH}$$

$$C_l = 600 \text{ } \mu\text{F}$$

The attained values are used to model the discharge converter in PSCAD as shown in FIGURE 2.16. An 815V DC voltage source is used as converter input. The switch duty cycle is set to obtain an output voltage of 700V.

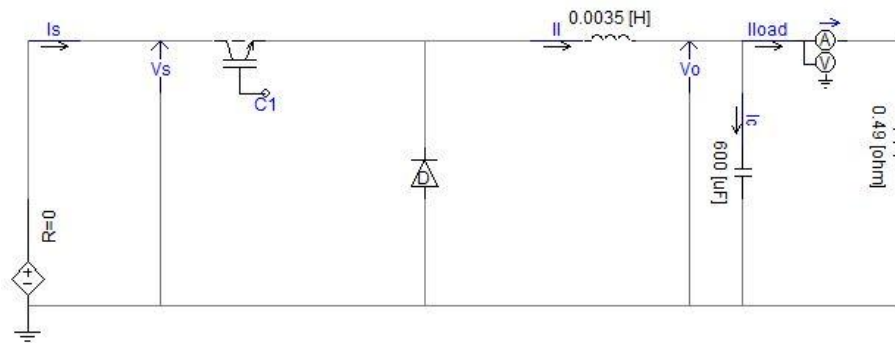


FIGURE 2.16: Discharge buck converter PSCAD model

As shown in FIGURE 2.17, the peak to peak current ripples are found to be 25A which represents 1.7% of rated inductor current. This satisfies the applied design characteristics. Also, the peak to peak output voltage ripples are found to be 3.7V which represents 0.5% of rated voltage output. This satisfies the applied design characteristics.

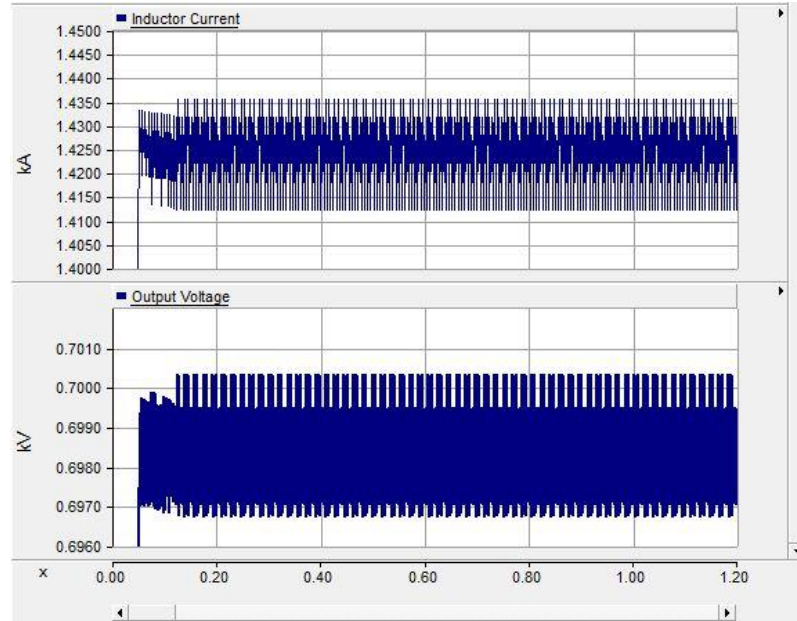


FIGURE 2.17: Inductor current and output voltage ripples of discharge converter

- Discharge Buck Converter Controller Design

The transfer function of the system is evaluated in the following matlab code. The system is perturbed with duty cycle as a single input and output voltage as single output.

```

%% PD Controller Design

L = 1.25* Ldesign;      %Ldesign= 2.4 mH
C=600e-6;              %Cdesign = 510.2 uF

%%Perturbation from duty ratio to the output voltage:
num0 = [(Vout/D)];
den0 = [(L*C) (L/R) 1];
sys0 = tf(num0,den0)

figure(1);
margin(sys0);
[Gm0,Pm0,Wgm0,Wpm0]=margin(sys0);

Gdo=Vout/D             % System gain
Wo=1/(sqrt(L*C))      % System Corner frequency

```

This code outputs the following:-

```

sys0 =

          815
-----
2.074e-06 s^2 + 0.007055 s + 1

Continuous-time transfer function.

Gdc = 815.0000
Wc = 694.3385

```

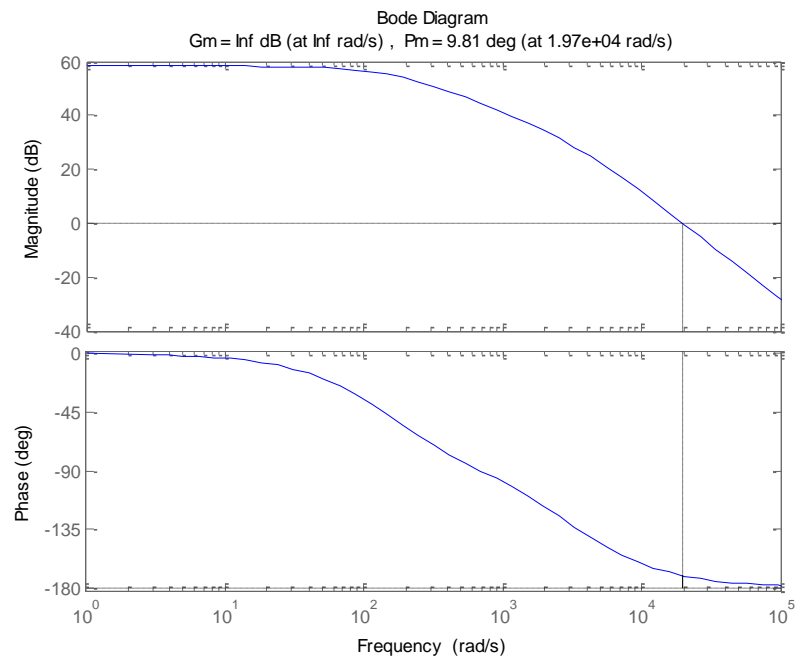


FIGURE 2.18: Uncompensated discharge buck converter bode plot

As shown in FIGURE 2.18, the phase margin of the uncompensated system is  $9.81^\circ$ . We will design a PD controller to obtain a bandwidth of 30,000 rad/sec and a phase margin of  $52^\circ$ .

```

%% Required Closed Loop System Characteristics PM=52degree , Wc=30,000
rad/sec

```

```

BW_req=30000; %in rad/sec
PM_req=52; %in degrees

[magx,phasex] = bode(sys0,BW_req);
PM_bw=180+phasex
PM_adj=PM_req-PM_bw %in degrees

% Controller gain, zero and pole evaluation

Wz=BW_req*sqrt((1-sin(degtorad(PM_adj)))/(1+sin(degtorad(PM_adj))))
Wp=BW_req*sqrt((1+sin(degtorad(PM_adj)))/(1-sin(degtorad(PM_adj))))
Gco=((BW_req/Wo)^2)*(1/Gdo)*sqrt(Wz/Wp)

% PD Compensator Bode Plot & Margins
numc=[(1/Wz) 1];
denc=[(1/Wp) 1];
Gc=Gco*tf(numc,denc)
figure(2);
margin(Gc);

```

The controller gain, zero and pole is given by the following values

```

PM_bw =
    6.4719
PM_adj =
    45.5281
Wz =
    1.2265e+04
Wp =
    7.3381e+04
Gco =
    0.9364

Gc =

    7.635e-05 s + 0.9364
    -----
    1.363e-05 s + 1

Continuous-time transfer function.

```

The designed PD controller ( $G_c$ ) is shown in the matlab output shown above. The controller bode plot is shown in FIGURE 2.19.

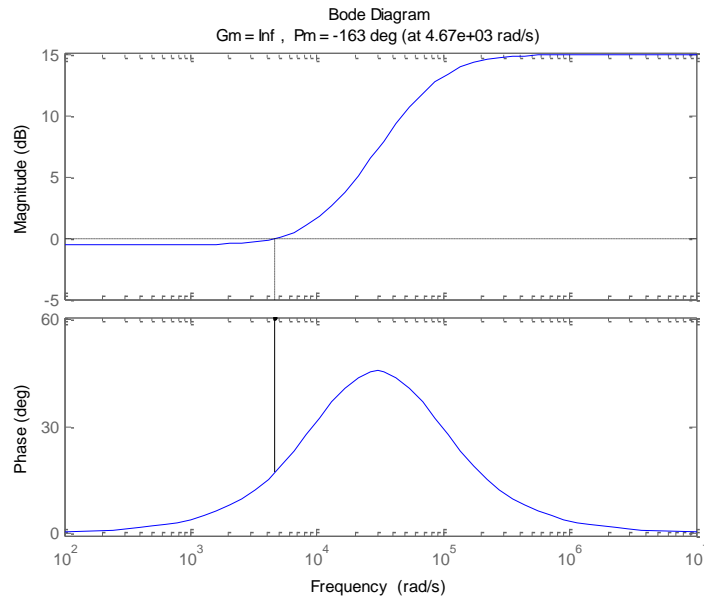


FIGURE 2.19: Discharge converter PD compensator bode plot

The designed PD controller is implemented into the system loop with unity feedback.

```

%% Compensated system
Tol=Gc*sys0
figure(3);
margin(Tol);

% Step Response
H = 1; %Unity gain feedback;
Tcl = feedback(Tol,H) % Unity Feedback system

figure(5)
step(Tcl)

```

The open and closed loop transfer functions are as follows

```

Tol =
-----
          0.06223 s + 642.8
-----
2.381e-11 s^3 + 2.155e-06 s^2 + 0.007067 s + 1

```

Continuous-time transfer function.

Tcl =

$$\frac{0.06223 s + 642.8}{2.381e-11 s^3 + 2.155e-06 s^2 + 0.06929 s + 643.8}$$

Continuous-time transfer function.

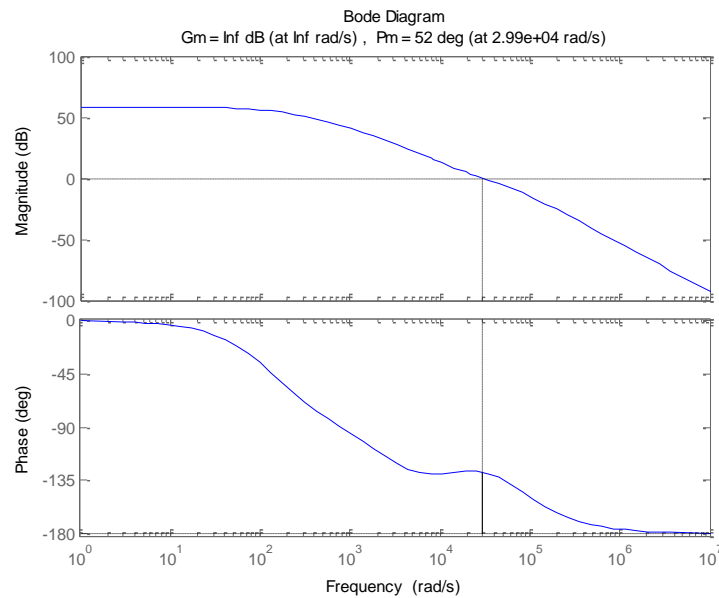


FIGURE 2.20: Compensated discharge converter system bode plot

As shown in FIGURE 2.20, the compensated system bandwidth and phase margin is 30,000 rad/sec and 52°, respectively. The attained values satisfy the margins we have set for the compensated system.

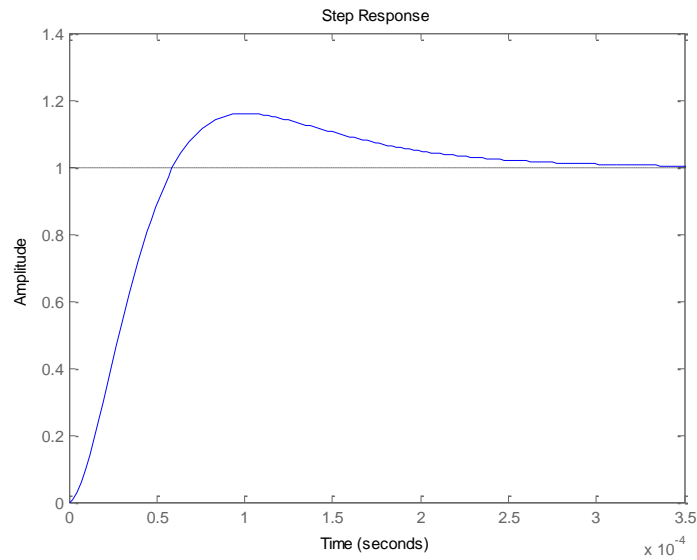


FIGURE 2.21: Step response of compensated discharge buck converter

As shown in FIGURE 2.21, the steady state time response of the compensated system is 350  $\mu\text{s}$ . This represents a good response time for a 1MW converter. The deduced PD controller values are implemented in the PSCAD converter model and used to control the discharge buck converter as shown in FIGURE 2.22.

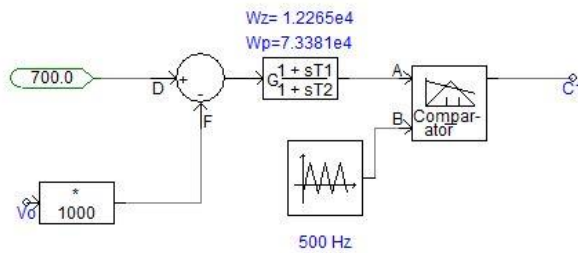


FIGURE 2.22: Discharge buck converter control circuit model

### 2.3.2.2. Inverter

- Inverter Specifications

TABLE 2.3: Inverter Specifications

Parameter	Value
DC Link Voltage	700V
AC Output Voltage (L-L, rms)	480V
Capacity	1.25 MVA
Switching Frequency	500Hz

- Inverter Modeling

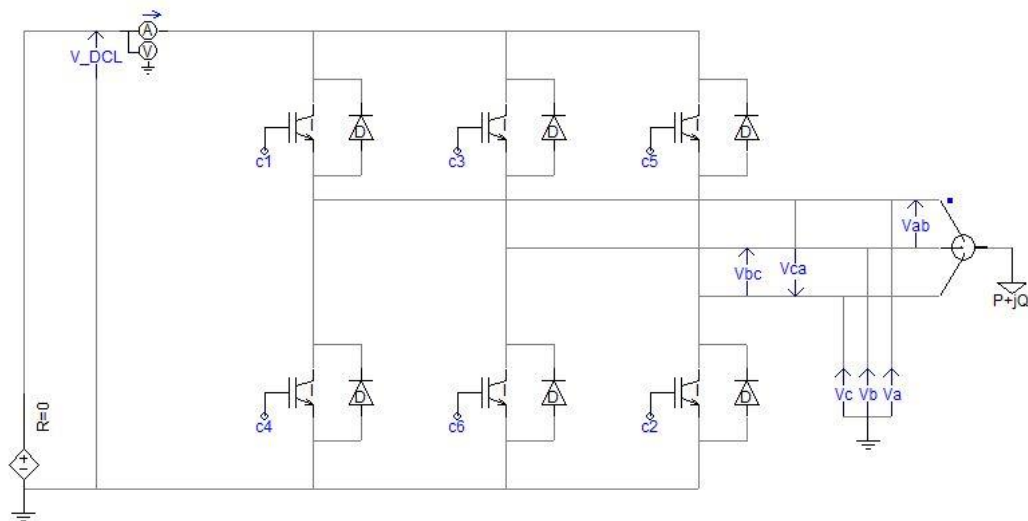


FIGURE 2.23: Inverter PSCAD model

The SMS inverter is modeled in PSCAD as shown in FIGURE 2.23. IGBT electronic switches models are used as switching elements. As shown in FIGURE 2.24, a PQ control scheme is used to manage output active and reactive power of the inverter. The phase and modulation index of the reference sine wave signal is controlled with PI controllers to vary inverter output active and reactive power, respectively. The Active

Power Reference signal (APR) in this inverter is used to control the discharge rate of the battery only whereas the Reactive Power Reference signal (RPR) is used to control the full range of reactive power capabilities of the SMS.

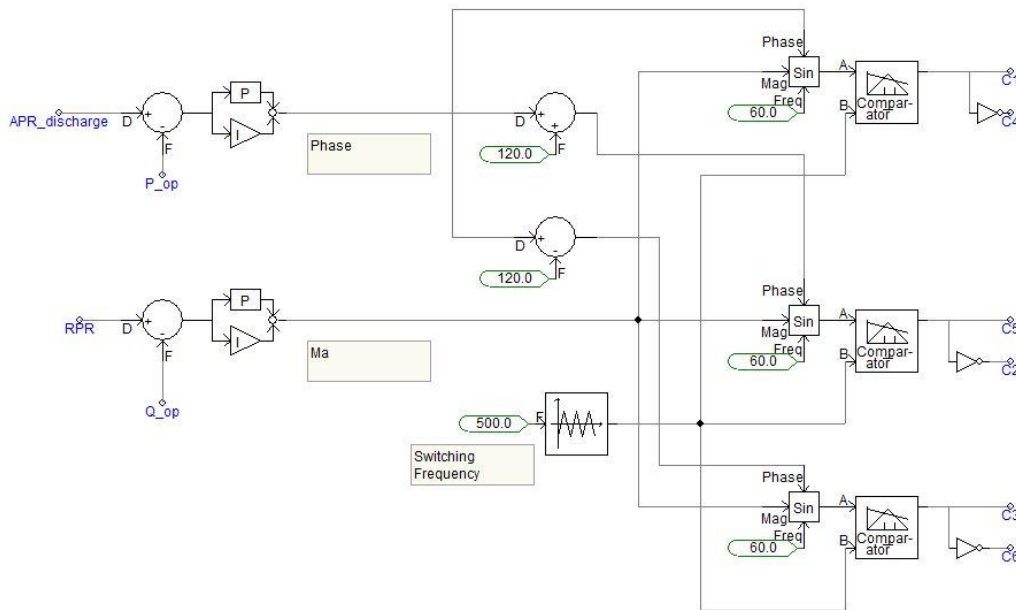


FIGURE 2.24: Inverter PWM control circuit model

2.3.2.3. Three Phase Full Wave Rectifier

- Rectifier Specifications

TABLE 2.4: Rectifier specifications

Parameter	Value
Input AC Voltage	1 kV
DC Output Voltage	1.3 kV
Manufacturer Capacity	1 MW
Maximum Voltage Ripple	5% (65V)
Maximum Current Ripple	5% (38A)

- Rectifier Modeling

The rectifier model shown in FIGURE 2.25 is designed in order to maintain a 1.3kV DC voltage at charge buck converter input. The smoothing capacitor is designed such that output voltage ripples are minimized below 5% of the nominal output voltage. Equation (2.13) is used to determine the smoothing capacitor value.

$$C_R = \frac{V_{Rec}}{6 \times f \times 0.05 \times V_{Rec}} = 0.03 \text{ Farad} \quad (2.12)$$

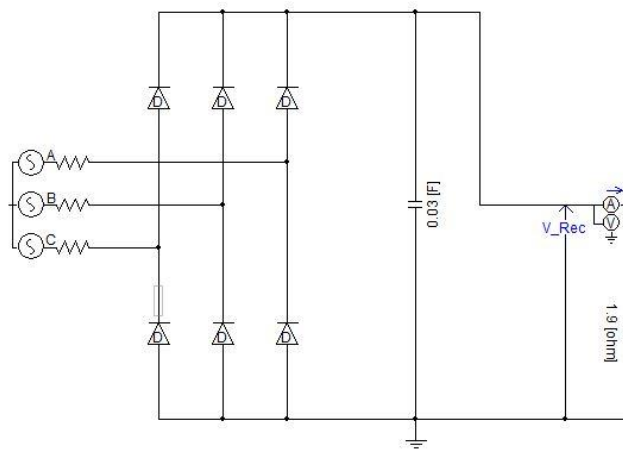


FIGURE 2.25: Three phase full wave rectifier PSCAD model

The chosen capacitor value ( $C_R=0.03F$ ) is found sufficient to suppress voltage ripples below our 5% limit. As shown in FIGURE 2.26, the peak to peak voltage ripple value is 50 volts which is 3.8% of nominal output voltage.

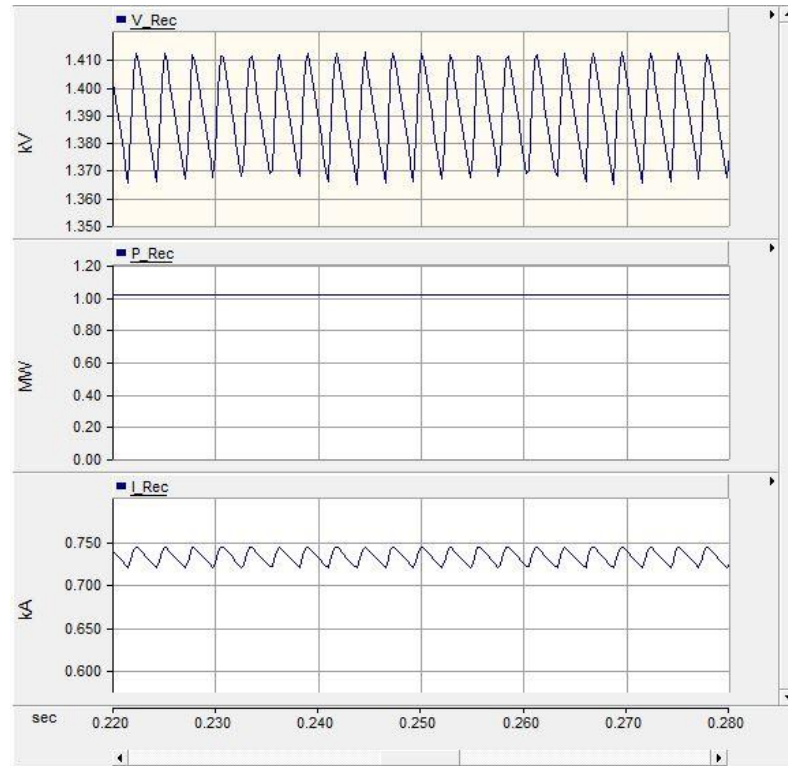


FIGURE 2.26: Rectifier voltage and current plots at rated power

#### 2.3.2.4. Charge DC-DC Buck Converter

The charge buck converter is responsible for controlling the charge rate of the BESS through controlling the output voltage level according to the desired charge rate.

- Charge Buck Converter Specifications

The specifications of the discharge buck converter are as follows:-

TABLE 2.5: Charge Buck Converter specifications

Parameter	Value
Input Voltage Range	1.3 kV
Maximum Output Voltage	850 V
Manufacturer Capacity	1 MW
Maximum Voltage Ripple	5% (42.5V)
Maximum Current Ripple	5% (59A)
Switching Frequency	500Hz

- Charge Buck Converter Element Design

Similar to the steps in section 2.3.2.1, the following matlab code is written to determine converter elements.

```

clc
clear all

%%Element specification: For 1MW Buck Converter
Vs = 1300;
Vout = 850;
P = 1000e3;
D_prime = Vs/Vout;
D = 1/D_prime;
Iin = P/Vs;
Iout=P/Vout;
IL = Iout;
Fsw= 500;
T = 1/Fsw;
R = Vout^2/P;
i_ripple = 5/100*Iout; % 5% ripple in output current
v_ripple = 5/100*Vout; % 5% ripple in output voltage

%%Element Design:

Ldesign = D*T*(Vs-Vout)/i_ripple
Cdesign= (i_ripple*T)/(8*v_ripple)

```

The design values of the converter inductor and capacitor are as follows:-

```

Ldesign = 0.0100 (Henry)
Cdesign = 3.4602e-04 (Farad)

```

In order to assure operation within voltage and current ripple limits, the following inductor values are chosen:-

$$L_2 = 12.5 \text{ mH (125\% of } L_{design})$$

$$C_2 = 400 \text{ } \mu\text{F}$$

The attained values are used to model the charge converter in PSCAD as shown in FIGURE 2.27. A 1.3 kV DC voltage source is used as converter input. The switch duty cycle is set to obtain an output voltage of 850V.

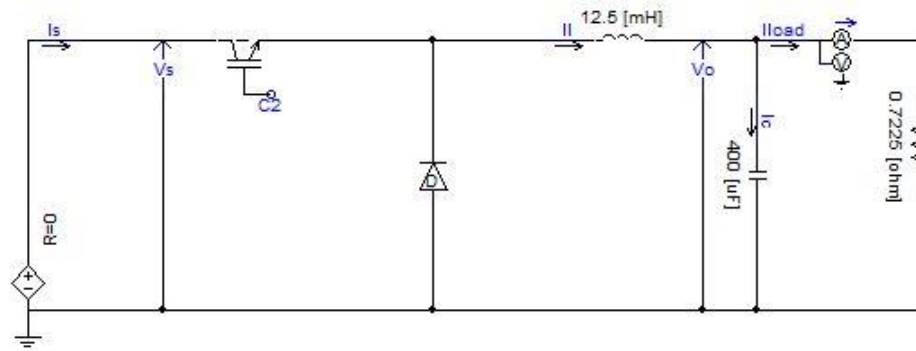


FIGURE 2.27: Charge converter PSCAD model

As shown in FIGURE 2.28, the peak to peak current ripples are found to be 14A which represents 1.2% of rated inductor current. This satisfies the applied design characteristics. Also, the peak to peak output voltage ripples are found to be 3.5V which represents 0.41% of rated voltage output. This satisfies the applied design characteristics.

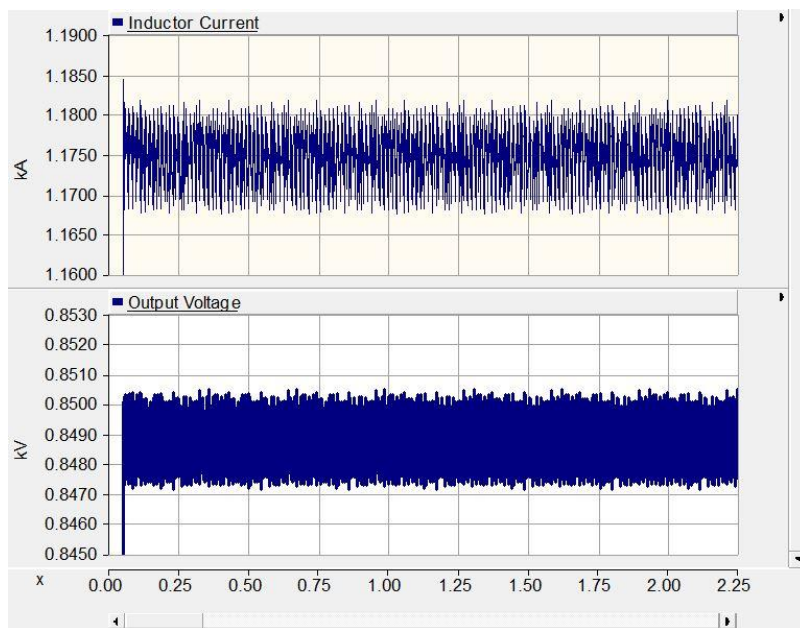


FIGURE 2.28: Charge converter PSCAD model voltage and current ripples

- Charge Buck Converter Controller Design

The transfer function of the system is evaluated in the following matlab code. The system is perturbed with duty cycle as a single input and output voltage as single output.

```
%% PD Controller Design

L = 1.25* Ldesign;      %Ldesign= 1 mH
C=400e-6;              %Cdesign = 346.02 uF

%%Perturbation from duty ratio to the output voltage:
num0 = [(Vout/D)];
den0 = [(L*C) (L/R) 1];
sys0 = tf(num0,den0)

figure(1);
margin(sys0);
[Gm0,Pm0,Wgm0,Wpm0]=margin(sys0);

Gdo=Vout/D           % System gain
Wo=1/(sqrt(L*C))     % System Corner frequency
```

This code outputs the following:-

```
sys0 =

          1300
-----
5.002e-06 s^2 + 0.01731 s + 1

Continuous-time transfer function.

Gdo = 1300
Wo = 447.1276
```

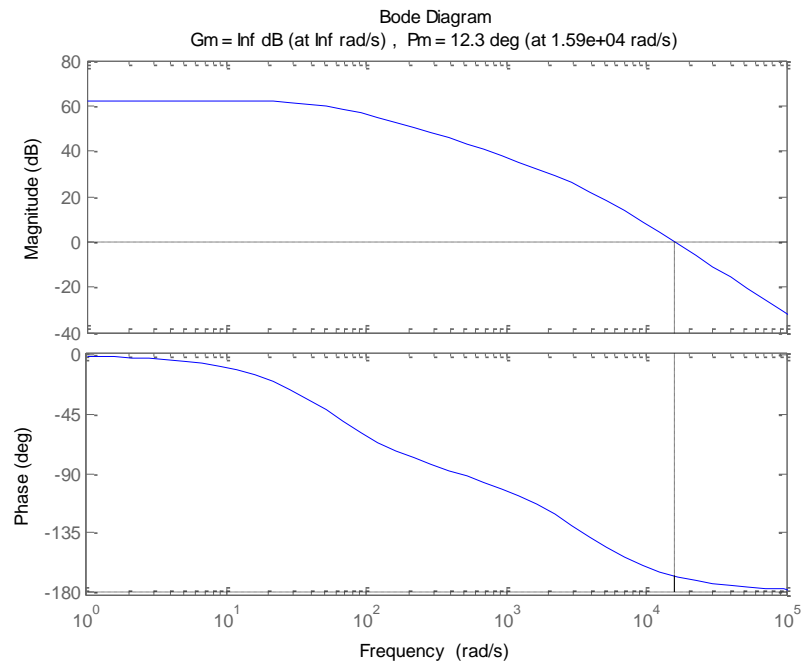


FIGURE 2.29: Uncompensated charge buck converter bode plot

As shown in FIGURE 2.29, the phase margin of the uncompensated system is  $12.3^\circ$ . We will design a PD controller to obtain a bandwidth of 30,000 rad/sec and a phase margin of  $52^\circ$ .

```

%% Required Closed Loop System Characteristics PM=52degree , Wc=30,000
rad/sec
BW_req=30000; %in rad/sec
PM_req=52; %in degrees

[magx,phases] = bode(sys0,BW_req);
PM_bw=180+phases
PM_adj=PM_req-PM_bw %in degrees

% Controller gain, zero and pole evaluation

Wz=BW_req*sqrt((1-sin(degtorad(PM_adj)))/(1+sin(degtorad(PM_adj))))
Wp=BW_req*sqrt((1+sin(degtorad(PM_adj)))/(1-sin(degtorad(PM_adj))))
Gco=((BW_req/Wo)^2)*(1/Gdo)*sqrt(Wz/Wp)

```

```
% PD Compensator Bode Plot & Margins
numc=[(1/Wz) 1];
denc=[(1/Wp) 1];
Gc=Gco*tf(numc,denc)
figure(2);
margin(Gc);
```

The controller gain, zero and pole is given by the following values

```
PM_bw =
    6.5809
PM_adj =
    45.4191
Wz =
    1.2298e+04
Wp =
    7.3182e+04
Gco =
    1.4196

Gc =

    0.0001154 s + 1.42
    -----
    1.366e-05 s + 1
```

The designed PD controller ( $G_c$ ) is shown in the matlab output shown above. The controller bode plot is shown in FIGURE 2.30.

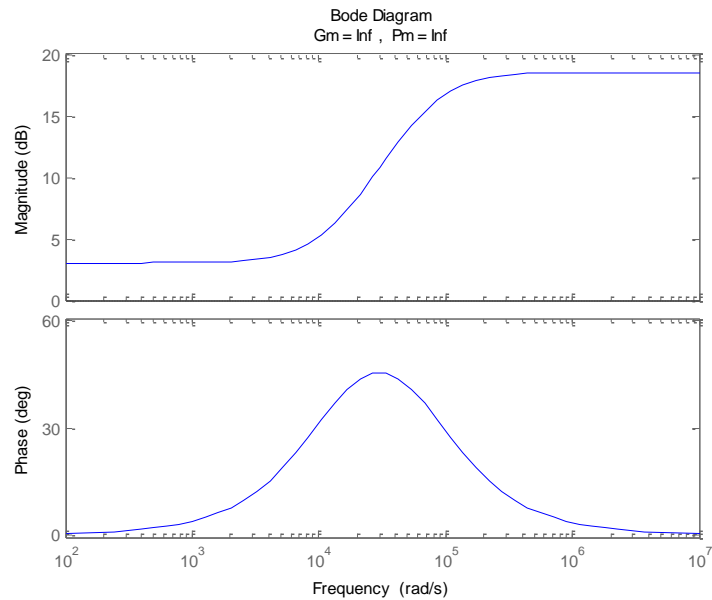


FIGURE 2.30: Charge converter PD compensator bode plot

The designed PD controller is implemented into the system loop with unity feedback.

```

%% Compensated system
Tol=Gc*sys0
figure(3);
margin(Tol);

% Step Response
H = 1; %Unity gain feedback;
Tcl = feedback(Tol,H) % Unity Feedback system
figure(4)
step(Tcl)

```

The open and closed loop transfer functions are as follows

```

Tol =
      0.1501 s + 1845
-----
6.835e-11 s^3 + 5.238e-06 s^2 + 0.01732 s + 1

```

```

Continuous-time transfer function.

Tcl =

          0.1501 s + 1845
-----
6.835e-11 s^3 + 5.238e-06 s^2 + 0.1674 s + 1846

Continuous-time transfer function.

```

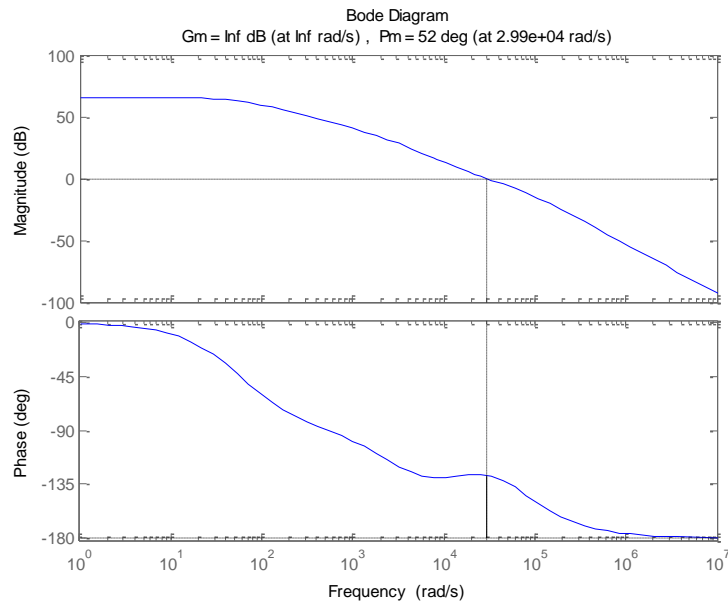


FIGURE 2.31: Compensated charge converter system bode plot

As shown in FIGURE 2.31, the compensated system bandwidth and phase margin is 30,000 rad/sec and 52°, respectively. The attained values satisfy the margins we have set for the compensated system.

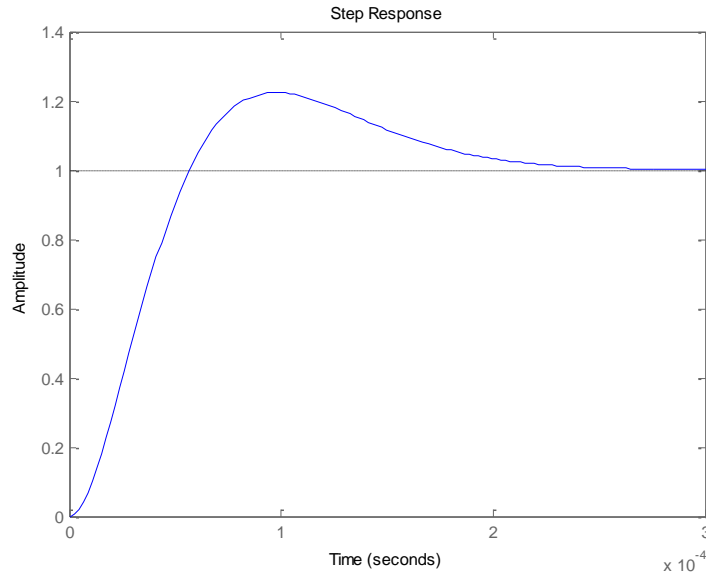


FIGURE 2.32: Step response of compensated discharge buck converter

As shown in FIGURE 2.21, the steady state time response of the compensated system is 350  $\mu$ s. This represents a good response time for a 1MW converter. The deduced PD controller values are implemented in the PSCAD converter model and used to control the charge buck converter model.

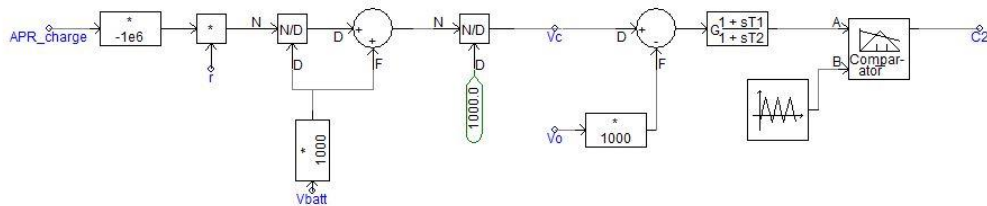


FIGURE 2.33: Discharge buck converter control circuit model

The output voltage reference of the charge buck converter is deduced from the required  $APR_{charge}$  signal, battery voltage and internal resistance. The deduced value

shown in equation (2.13) is used as the reference voltage signal for the PD controller of the charge buck converter as shown in FIGURE 2.33

$$V_c = \frac{APR_{charge} \times r}{V_{Battery}} + V_{Batt} \quad (2.13)$$

### 2.3.3. SMS Operation & Model Validation

The converter, inverter and rectifier design values deduced in the previous section are used in SMS model shown in FIGURE 2.34. The BESS model is connected at the output of the charge converter and at the input of the discharge converter.

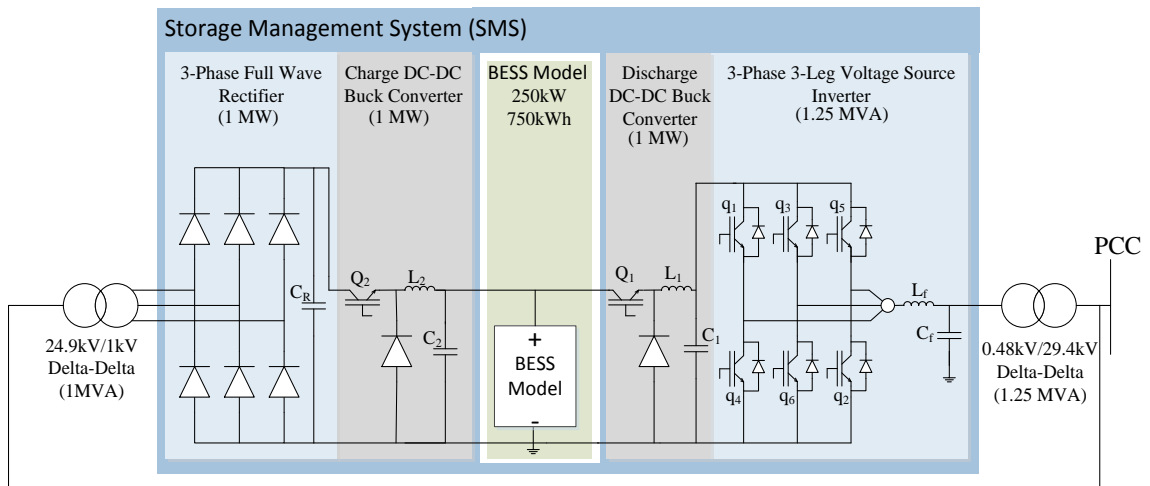


FIGURE 2.34: BESMS model

### 2.3.3.1. Storage Management System Operation

- Discharge Cycle

During battery discharge cycle, switch ( $Q_1$ ) shown in FIGURE 2.34 is controlled to hold the DC link voltage to a set value. Switch ( $Q_2$ ) remains open during discharge period. Inverter switches are controlled by pulse width modulation (PWM). Modulation index is set according to the reactive power required to be supplied or consumed from the feeder ( $Q_{ESSr}$ ). The phase of the PWM reference signal controls the active power output and is set by the reference active power signal ( $P_{ESSr}$ ). During the discharge cycle, the charge converter switch is off and current flows to the grid through the discharge converter and inverter only.

- Charge Cycle

During charge cycle, Power is provided to the battery through the 3-phase full wave rectifier and the charge buck converter. The rectifier sets the voltage at the charge DC link. Switch ( $Q_2$ ) shown in FIGURE 2.34 is controlled to buck the rectified voltage at the rectifier output to the required voltage value for the required battery charge rate. The voltage ( $V_c$ ) required to charge the battery is calculated from the desired charge rate ( $APR_{Charge}$ ). Switch ( $Q_2$ ) duty cycle is controlled according to voltage ( $V_c$ ). The rectifier is uncontrolled and battery charge rate is controlled solely by the charge buck converter.

### 2.3.3.2. SMS Model Validation

In this section we will validate the operational limits of the designed SMS model. The desired SMS apparent power operational limit is shown. The power limits shown in FIGURE 2.35 are as follows:-

TABLE 2.6: BESMS capability limits

Symbol	Description	Value
$P_{ESS}^{dm}$	Maximum ESS discharge active power	250kW
$P_{ESS}^{cm}$	Maximum ESS charge active power	-250kW
$Q_{SMS}^{Capm}$	Maximum ESS output capacitive reactive power	1MVAR
$Q_{SMS}^{Indm}$	Maximum ESS output inductive reactive power	1MVAR
$S_1$	Maximum BESMS (discharge-capacitive) apparent power	1.03MVA
$S_2$	Maximum BESMS (charge-capacitive) apparent power	1.03MVA
$S_3$	Maximum BESMS (charge-inductive) apparent power	1.03MVA
$S_4$	Maximum BESMS (discharge-inductive) apparent power	1.03MVA

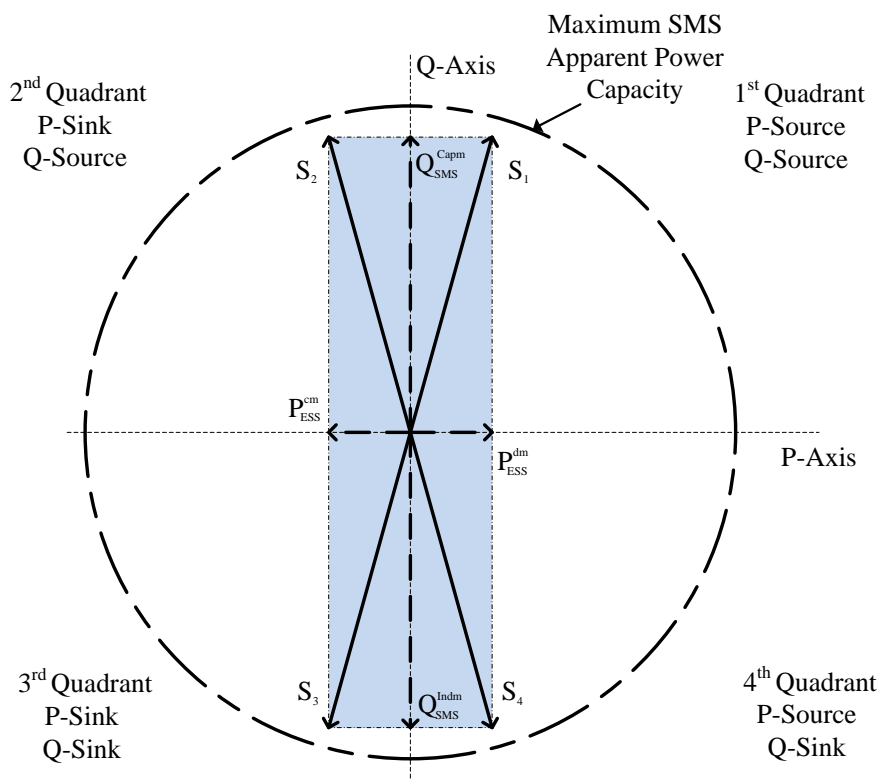


FIGURE 2.35: Desired BESMS output capabilities

The values shown in TABLE 2.6 are validated through PSCAD simulation results, presented hereafter

- Active power set to  $P_{ESS}^{dm}$  and ramped reactive power

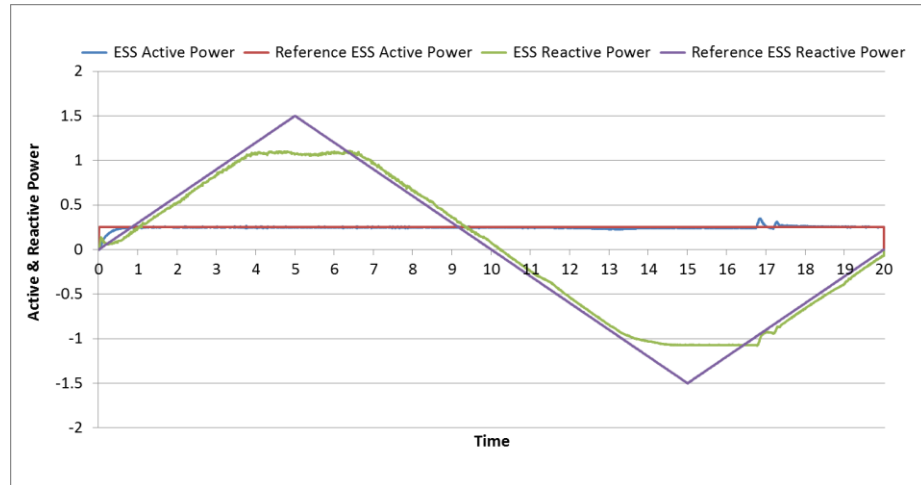


FIGURE 2.36: BESMS output for max discharge and ramped reactive power(1<sup>st</sup> & 2<sup>nd</sup> quad)

- Active power set to  $P_{ESS}^{cm}$  and ramped reactive power

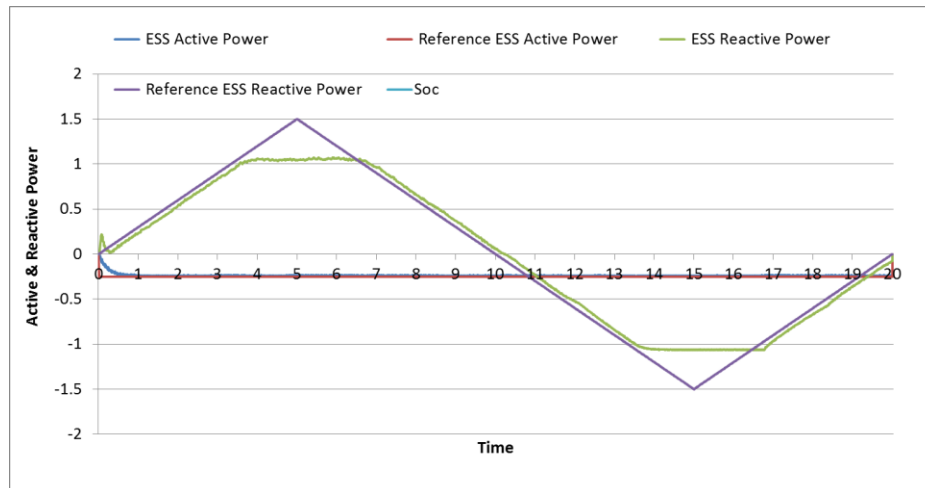


FIGURE 2.37: BESMS output for max charge and ramped reactive power(3<sup>rd</sup> & 4<sup>th</sup> quad)

- Ramped active power and reactive power set to  $Q_{SMS}^{Capm}$

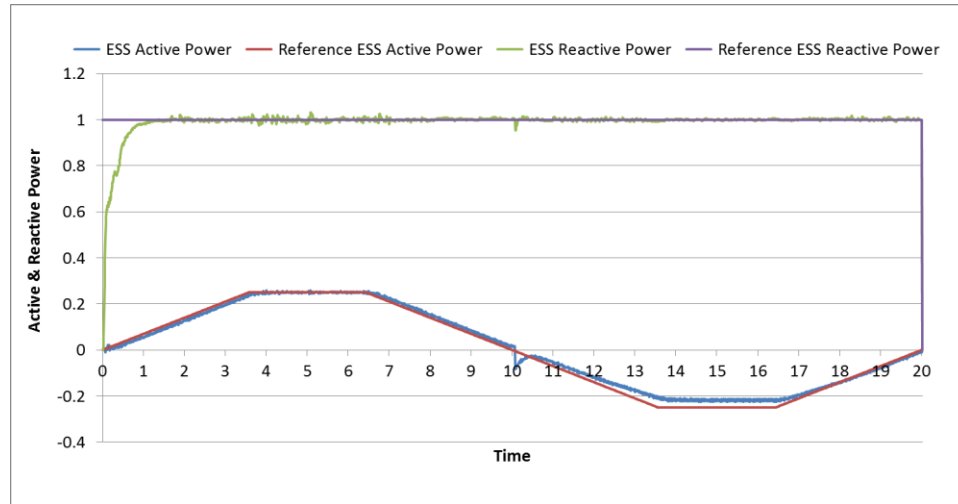


FIGURE 2.38: BESMS output for capacitive reactive power and ramped active power (1<sup>st</sup> & 2<sup>nd</sup> quad)

- Ramped active power and reactive power set to  $Q_{SMS}^{Indm}$

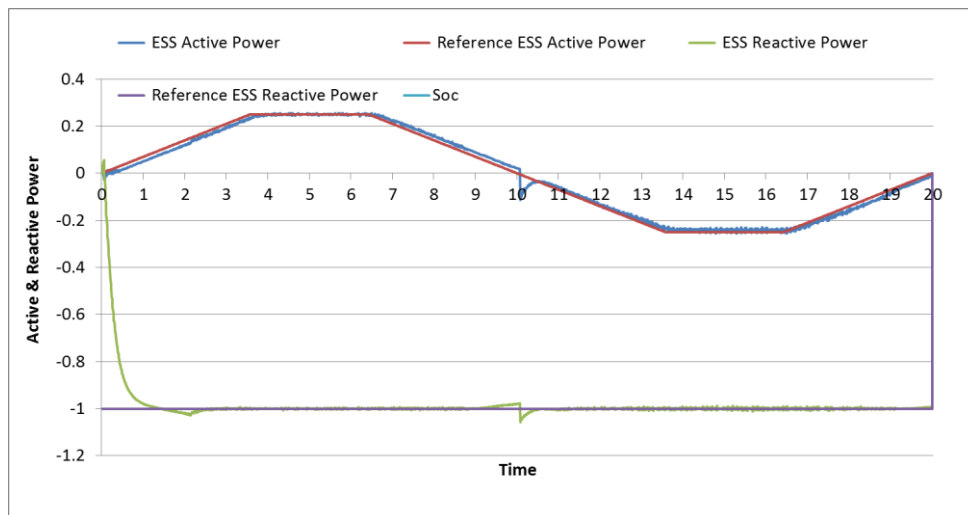


FIGURE 2.39: BESMS output for inductive reactive power and ramped active power (3<sup>rd</sup> & 4<sup>th</sup> quad)

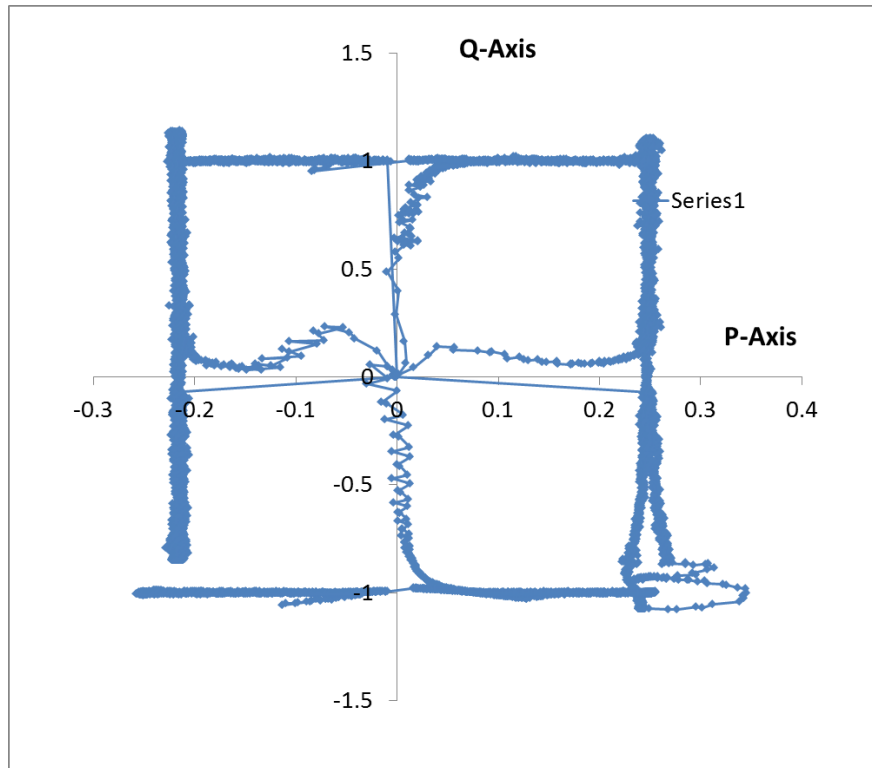


FIGURE 2.40: Simulation test results compilation in P-Q axis

Comparing results shown in FIGURE 2.40 & FIGURE 2.35, we can conclude that the BESMS is operating efficiently within the desired range.

#### 2.4. Medium Voltage Distribution Feeder Specifications

The distribution feeder shown in FIGURE 2.41 is a partially aggregated CYME model of the 720 node practical 12.475 kV distribution feeder that is hosting the described BESMS. The BESMS is connected in conjunction with a 1.25MVA PV station at the same point of common coupling.

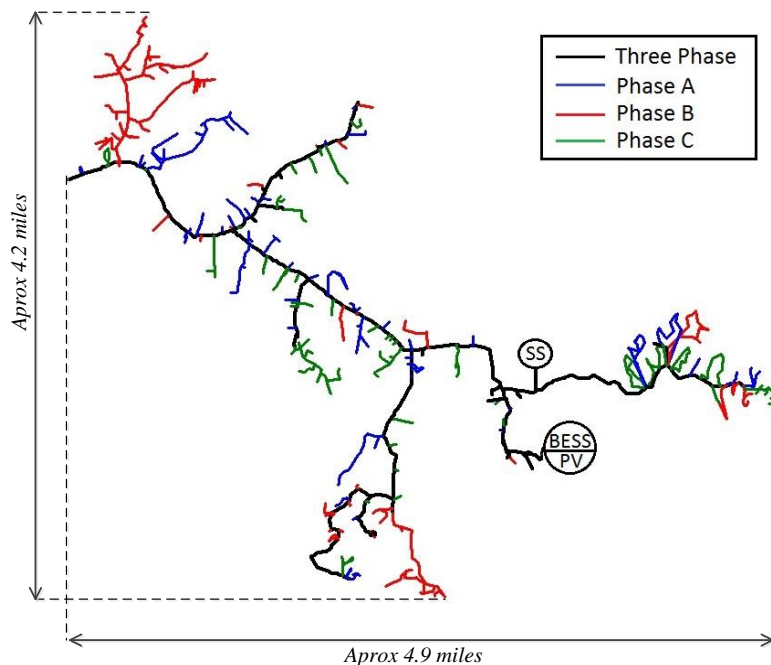


FIGURE 2.41: Practical 720 node distribution feeder with substation and BESS location shown

The PCC is practically located at one of the terminals of the radial distribution feeder in question. TABLE 2.7 summarizes distribution feeder specifications.

TABLE 2.7: Distribution Feeder Specifications

Aspect	Value
Number of Nodes	720
Voltage	12.475 kV
VAR Compensation	Three Static Capacitor Banks
Load Category	Residential
Load Types	Various (Constant Power, Impedance & Current)
Number of Line Regulators	Two Three-Phase Line Regulators
Station Regulator	One Three-Phase Station Regulator

As presented in FIGURE 2.42, feeder load is modeled utilizing three spot loads across the feeder. The circuit impedances shown are aggregations of total feeder impedances across the practical feeder. These impedance values are calculated utilizing

practical feeder data. The validity of the aggregation of the 720 node feeder to the 16 bus model shown below was performed through the comparison of short circuit currents. This was satisfied in previous works.

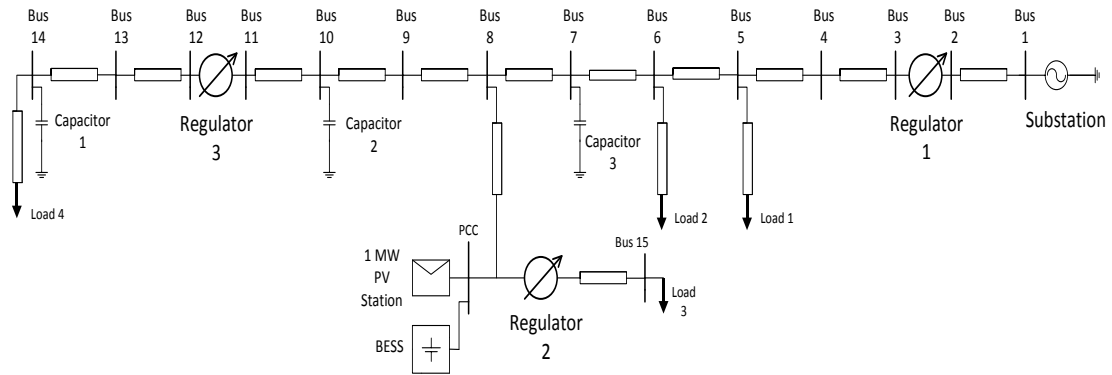


FIGURE 2.42: EMT aggregated model of distribution feeder

## 2.5. Conclusion

It can be concluded in this chapter that the BESMS model efficiently mimics the described practical system. In the next chapters, the different storage applications in which battery energy storage systems can be utilized will be studied. Also, the value which these applications can offer to medium voltage feeders will be analyzed.

## CHAPTER 3: PV STATION MODELING

### 3.1. Introduction

In the previous chapter, the practical and model specifications of the BESMS were thoroughly discussed. In this chapter we will study the control methodology of the BESMS and formulate a PV Capacity Firming (PVCF) algorithm capable of minimizing large power swings caused by clouds passing above large PV stations.

Renewables capacity firming using energy storage units involves supplying (discharging) and consuming (Charging) power in a manner that will make the combined output of the renewable energy source and the energy storage system constant to some extent. As mentioned in [1], “The resulting firmed capacity offsets the need to purchase or ‘rent’ additional dispatchable (capacity) electric supply resources. Depending on location, firmed renewable energy output may also offset the need for transmission and/or distribution equipment. Renewables capacity firming is especially valuable when peak demand occurs.” [3] Discusses capacity firming for a large wind farm. It focuses on developing a control strategy for optimal use of BESMS for wind capacity firming. It was concluded in that paper that capacity firming is achievable for the presence of a BESS with relatively high charge/discharge frequency and proper size (20% to 30% of wind farm capacity). The case of PV station’s output power also presents a clear example of intermittent power (due to clouds) that requires firming. Similar to [3]’s conclusion, PV capacity firming applications requires a power source capable of supplying power at

rapidly changing pace to cope with intermittencies that are sudden in nature. Suitable energy storage technologies for firming include battery energy storage systems and superconducting magnetic energy storage systems.

### 3.2. Practical PV Station Specifications

The PV station studied hereafter is practically implemented in Mooresville, North Carolina. It consists of six individual arrays. Each array has a different module type and size. Also, each array is fixated with its own inverter. These inverters are coupled together on the AC side as shown in FIGURE 3.1.

Due to the computational limitation that would be encountered if each of the six arrays is modeled individually, the full PV station will be aggregated into a single array with a single inverter. The power capacity of the aggregated PV station model is equal to that of the combined power capacity of the individual arrays. Also, the PV module to be modeled in the aggregated model is the module with greatest significance amongst the six practical arrays.

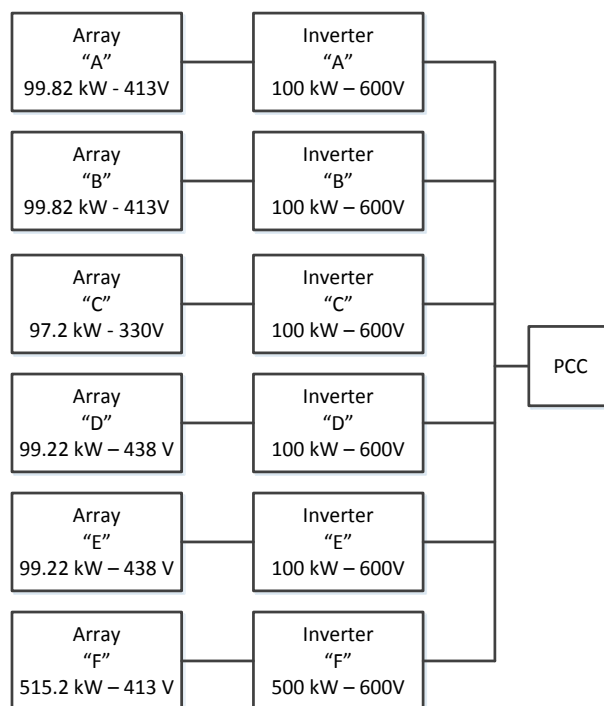


FIGURE 3.1: Practical PV station schematic

Each array in the practical PV station is built using a single module type. There is no array with more than one module type. The module brands and models as well as number of modules per string and number of strings per array are presented in TABLE 3.1 Also, the brand and specifications of inverters used in each array is shown below in TABLE 3.2.

Module Specifications:-

TABLE 3.1: Module specifications of practical PV station arrays

Array	Brand & Model	$V_{mp}$ (V)	$I_{mp}$ (A)	$V_{oc}$ (V)	$I_{sc}$ (V)
A	Yingli (YL-230P-29B)	29.5	7.8	37	8.4
B	Yingli (YL-230P-29B)	29.5	7.8	37	8.4
C	ENN (EST-120)	110	1.1	141	1.32
D	Sun Power (SPR-318)	54.7	5.82	64.7	6.2

E	Sun Power (SPR-318)	54.7	5.82	64.7	6.2
F	Yingli (YL-230P-29B)	29.5	7.8	37	8.4

#### Array Specifications:-

TABLE 3.2: Array specifications of practical PV station

Array	DC String Voltage (V)	Maximum Power (kW)	Number of Modules per String ( $N_{M/S}$ )	Number of Strings Per Array ( $N_{S/A}$ )
A	413	99.82	14	31
B	413	99.82	14	31
C	330	97.2	3	270
D	438	99.216	8	39
E	438	99.216	8	39
F	413	515.2	14	160

#### Inverter Specifications:-

TABLE 3.3: Inverter specifications of practical PV station arrays

Inverter	Brand & Model	Maximum DC Voltage	Maximum Power (kW)	AC voltage
A	Satcon (PVS-100)	600	100	480
B	Satcon (PVS-100)	600	100	480
C	Satcon (PVS-100)	600	100	480
D	Satcon (PVS-100)	600	100	480
E	Satcon (PVS-100)	600	100	480
F	Satcon (PVS-500)	600	500	480

### 3.3. Modeled PV Station Specifications

As shown in the previous section, Arrays A, B & F are built using Yingli PV modules. The combined power of these arrays is 714.84 kW which represents 71% of the total PV station capacity. This leads us to choose Yingli's YL-230P-29B for the aggregated PV station module.

Since all array inverters have a DC link maximum voltage as 600V, this value will be assumed for the aggregated PV station model. The capacity of the aggregated station inverter will be modeled as the total practical station capacity which is 1MW.

Also, since the string voltages of the arrays in which Yingli modules and Satcon inverters are used are equal and have a value of 413 Volts, this is the string voltage value used for the aggregated PV station. This also dictates the number of modules per string for the aggregated model to be 14.

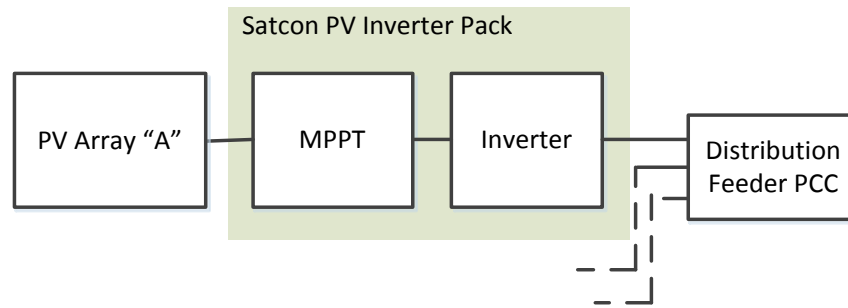
The aggregated PV station specifications can be summarized as follows in:-

TABLE 3.4: Specifications of aggregated PV station model

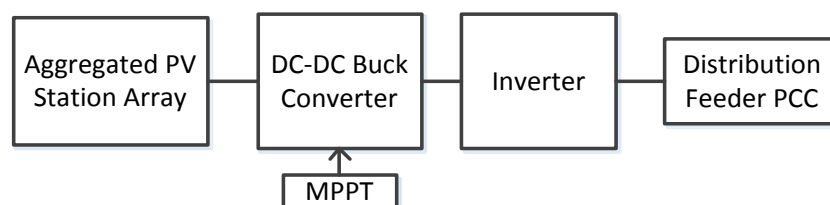
Module					Array			
Brand & Model	$V_{mp}$ (V)	$I_{mp}$ (A)	$V_{oc}$ (V)	$I_{sc}$ (A)	$V_{DCStr}$ (V)	$P_{max}$ (kW)	$N_{M/S}$	$N_{S/A}$
Yingli (YL-230P-29B)	29.5	7.8	37	8.4	413	1010	14	314

### 3.4. PV Station Model Design

The specifications shown in the previous section are modeled in PSCAD in this section. Practically, PV inverter manufacturers include Maximum Power Point Trackers (MPPTs) and their actuating power electronic devices within the inverter pack. This is the case with the inverter used for all practical system arrays at hand. Alternatively, to model this, the MPPT is modeled using a buck converter controlled by an incremental conductance MPPT algorithm.



(a)



(b)

FIGURE 3.2: (a) Practical PV station Architecture (b) Modeled PV station Architecture

### 3.4.1. PV Module Model

The PV module model is assumed to consist of several strings of PV cells connected in parallel, where each string can consist of a number of PV cells connected in series. All PV cells in the array are assumed identical. The PV cell model presented hereafter is based on [39]. A solar cell can be represented using the electrical equivalent circuit shown in FIGURE 3.3.

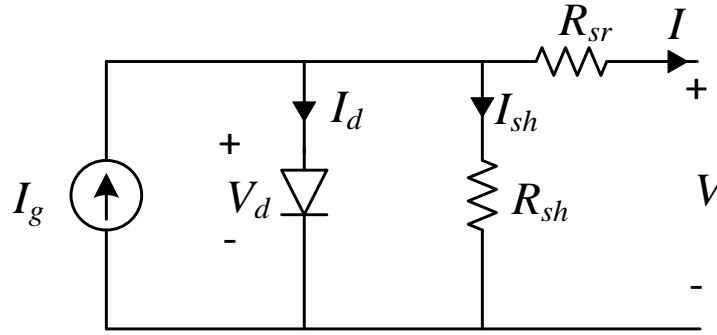


FIGURE 3.3: Solar photovoltaic cell model

The photo current,  $I_g$ , generated when the cell is exposed to light, varies linearly with solar irradiance. The current  $I_d$  through the anti-parallel diode is largely responsible for producing the nonlinear I-V characteristics of the PV cell.

Application of the Kirchhoff's current law to the circuit gives:

$$I = I_g - I_d - I_{sh} \quad (3.1)$$

Substitution of relevant expressions for the diode current  $I_d$  and the shunt branch current  $I_{sh}$  yields:

$$I = I_g - I_0 \left( e^{\frac{q(V+IR_{sr})}{nkT_c}} - 1 \right) - \frac{V + IR_{sr}}{R_{sh}} \quad (3.2)$$

In equation (3.2),  $I_g$  is the photo current and it is a function of the solar radiation on the plane of the solar cell ( $G$ ) and the cell temperature ( $T_c$ ):

$$I_g = I_{scr} \frac{G}{G_r} [1 + \alpha_t (T_c - T_{cr})] \quad (3.3)$$

Where  $I_{scr}$  is the short circuit current at the reference solar radiation  $G_R$  and the reference cell temperature  $T_{cr}$ . The parameter  $\alpha_T$  is the temperature coefficient of photo current (for Silicon solar cells  $\alpha_T = 0.0017$  A/K).

The current  $I_o$  in equation (3.4) is called the dark (saturation) current, a function of cell temperature, and given by:

$$I_o = I_{or} \frac{T_c^3}{T_{cr}^3} e^{\left(\frac{1}{T_{cr}} - \frac{1}{T_c}\right) \frac{q e_g}{nk}} \quad (3.4)$$

The other parameters appearing in equations (3.1) to (3.4) are defined as follows:-

$q$ : electron charge

$k$ : the Boltzmann constant,

$e_g$ : the band-gap energy of the solar cell material

$n$ : diode ideality factor (typically 1.3 for silicon solar cells)

$I_{or}$ : dark current at the reference temperature.

$G$ : Instantaneous value of solar radiation on the panel (W/m<sup>2</sup>).

$T$ : Instantaneous value of cell operating temperature (°C).

The following matlab code is implemented to deduce model parameters, namely,  $I_{or}$ ,  $R_{sr}$  and  $R_{sh}$ .

```

clc
clear all

%% Yingli PV Module Parameters (polycrystalline silicon PV cells)

Ncs=60;           % Number of cells in series per module
Ncp=1;           % Number of cell strings in parallel per module
G=1000;          % Irradiance
Gr=1000;         % Reference Irradiance
Tc=24+273.15;    % Temperature
Tcr=25+273.15;   % Reference Temperature
k=1.3806488e-23; % Boltzman Constant
n=1.3;           % Diode ideality factor

```

```

eg=1.12;           % Band gap energy of the solar material (1.12 eV
for cristalline Si, 1.03 eV for CIS, 1.7 eV for amorphous silicon,
1.5 eV for CdTe)
Iscr=8.4/Ncp;      % Short Circuit Current at Reference Temp
AlphaT=0.0017;    % Temperature coefficient of photo current (0.0017
A/K for silicon solar cells)
q=1.60217657e-19; % Electron charge

%% PV Cell Model Equations

syms I V Io Ish Z Rsr Rsh Ior

Ig= Iscr*(G/Gr)*(1+AlphaT*(Tc-Tcr));
Io=(Ior*((Tc^3)/(Tcr^3))*exp((1/Tcr)-(1/Tc))*q*eg*(1/(n*k))));
Id=Io*((exp((V+I*Rsr)/(n*k*Tc/q))-1));
Ish=(V+I*Rsr)/Rsh;

Ix= vpa(Ig-Id-Ish-I,3) %Ix=0

```

This code outputs the PV cell model equation as output current a function of voltage with parameters  $I_{or}$ ,  $R_{sr}$  and  $R_{sh}$  unknown.

$$I = 8.34 - 0.884 * I_{or} * (\exp(30.0 * V + 30.0 * I * R_{sr}) - 1.0) - (1.0 * (V + I * R_{sr})) / R_{sh}$$

Now, we can substitute with three known points on the modules I-V curve to deduce the three unknown model parameters as follows:-

```

%% Short Circuit Current Equation

I1=8.4/Ncp;
V1=0;
I=I1;
V=V1;

Ix1=vpa(subs(Ix),3)

%% Open Circuit Voltage Equation

I2=0;
V2=37/Ncs;
I=I2;

```

```
V=V2;
Ix2=vpa(subs(Ix),3)

%% Maximum Power point Equation

I3=7.8/Ncp;
V3=29.5/Ncs;
I=I3;
V=V3;

Ix3=vpa(subs(Ix),3)
```

This code outputs the following three equations:-

```
- 0.884*Ior*(exp(252.0*Rsr) - 1.0) - (8.4*Rsr)/Rsh - 0.0562 = 0

8.34 - 0.617/Rsh - 9.82e7*Ior = 0

0.544 - 0.884*Ior*(exp(234.0*Rsr + 14.8) - 1.0) - (1.0*(7.8*Rsr +
0.492))/Rsh = 0
```

Solving the three equations above is a challenging ordeal since two of the three equations are nonlinear. Therefore, an iterative method based on an initial guess of  $I_{or}$ ,  $R_{sr}$  and  $R_{sh}$  values must be applied.

```
function F = myfun(x,y)

F= [- 0.884*x(1)*(exp(252.0*x(2)) - 1.0) - (8.4*x(2))/x(3) - 1.69;
    6.71 - 0.617/x(3) - 9.82e7*x(1);
    -(1.0*(7.8*x(2)+0.492))/x(3)-0.884*x(1)*(exp(234.0*x(2)+14.8)-1.0)
    - 1.09];

x0 = [1e-7;0.1;1000];
options = optimoptions('fsolve','Display','iter');
[x,fval] = fsolve(@myfun,x0,options) % Call solver
```

As shown, the initial guesses are as follows:-

$$I_{or} = 1 \times 10^{-7}$$

$$R_{sr} = 0.1$$

$$R_{sh} = 1000$$

This gives:-

Iteration	Func-count	f(x)	Norm of step	First-order optimality	Trust-region radius
0	4	1.18768e+19		1.19e+26	1
1	8	73.1921	1e-07	6.52e+16	1
2	12	69.6136		1.44e+15	1
3	16	69.6118	2.5	4.68e+13	2.5
4	20	69.6117	6.25	1.4e+14	6.25
5	24	69.6117	6.25	1.41e+14	6.25
6	28	69.6116	6.25	1.24e+14	6.25
7	32	69.6116	6.25	1.07e+14	6.25
8	36	69.6115	6.25	9.26e+13	6.25
9	40	69.6114	6.25	7.99e+13	6.25
10	44	69.6113	6.25	6.9e+13	6.25
11	48	69.6113	6.25	5.96e+13	6.25
12	52	69.6112	6.25	5.15e+13	6.25
13	56	69.6111	6.25	4.45e+13	6.25
14	60	69.6111	6.25	3.84e+13	6.25
15	64	69.6111	6.25	3.31e+13	6.25
16	68	69.6109	6.25	2.86e+13	6.25
17	72	69.6108	6.25	2.47e+13	6.25
18	76	69.6107	6.25	2.13e+13	6.25
19	80	69.6107	6.25	1.84e+13	6.25
20	84	69.6106	6.25	1.59e+13	6.25
21	88	69.6105	6.25	1.37e+13	6.25
22	92	69.6104	6.25	1.19e+13	6.25
23	96	69.6103	6.25	1.02e+13	6.25
24	100	69.6103	6.25	8.84e+12	6.25
25	104	69.6102	6.25	7.63e+12	6.25
26	108	69.6101	6.25	6.59e+12	6.25
27	112	69.61	6.25	5.69e+12	6.25
28	116	69.6099	6.25	4.91e+12	6.25
29	120	69.6098	6.25	4.24e+12	6.25
30	124	69.6097	6.25	3.66e+12	6.25
31	128	69.6096	6.25	3.16e+12	6.25
32	132	69.6095	6.25	2.73e+12	6.25
33	136	69.6094	6.25	2.36e+12	6.25
34	140	69.6093	6.25	2.03e+12	6.25
35	144	69.6092	6.25	1.76e+12	6.25
36	148	69.6091	6.25	1.52e+12	6.25
37	152	69.609	6.25	1.31e+12	6.25
38	156	69.6089	6.25	1.13e+12	6.25
39	160	69.6088	6.25	9.76e+11	6.25
40	164	69.6087	6.25	8.42e+11	6.25
41	168	69.6086	6.25	7.27e+11	6.25
42	172	69.6085	6.25	6.28e+11	6.25
43	176	69.6084	6.25	5.42e+11	6.25
44	180	69.6082	6.25	4.68e+11	6.25
45	184	69.6081	6.25	4.04e+11	6.25
46	188	69.608	6.25	3.49e+11	6.25
47	192	69.6079	6.25	3.01e+11	6.25
48	196	69.6077	6.25	2.6e+11	6.25
49	200	69.6076	6.25	2.24e+11	6.25
50	204	69.6075	6.25	1.94e+11	6.25
51	208	69.6073	6.25	1.67e+11	6.25
52	212	69.6072	6.25	1.44e+11	6.25
53	216	69.6071	6.25	1.25e+11	6.25
54	220	69.6069	6.25	1.08e+11	6.25
55	224	69.6068	6.25	9.3e+10	6.25
56	228	69.6066	6.25	8.03e+10	6.25
57	232	69.6065	6.25	6.93e+10	6.25
58	236	69.6063	6.25	5.99e+10	6.25
59	240	69.6061	6.25	5.17e+10	6.25
60	244	69.606	6.25	4.46e+10	6.25
61	248	69.6058	6.25	3.86e+10	6.25
62	252	69.6056	6.25	3.33e+10	6.25
63	256	69.6054	6.25	2.88e+10	6.25
64	260	69.6052	6.25	2.49e+10	6.25
65	264	69.605	6.25	2.15e+10	6.25
66	268	69.6048	6.25	1.86e+10	6.25
67	272	69.6046	6.25	1.6e+10	6.25
68	276	69.6043	6.25	1.39e+10	6.25
69	280	69.6041	6.25	1.2e+10	6.25
70	284	69.6038	6.25	1.04e+10	6.25
71	288	69.6035	6.25	8.97e+09	6.25
72	289	69.6035	15.625	8.97e+09	15.6
73	293	69.6033	3.90625	3.62e+09	3.91
74	297	69.603	9.76563	1.36e+10	9.77
75	301	69.6025	9.76563	1.24e+10	9.77

Solver stopped prematurely.

fsolve stopped because it exceeded the function evaluation limit, options.MaxFunEvals = 300 (the default value).

x =  
0.0000

```

0.0546
548.0625
fval =
-0.0570
8.3426
0.0141

```

As shown, an exact solution was not reached. Nevertheless, the value of the shunt resistance deduced could be used to plot the module I-V curve. Then trial and error method could be applied to fit the curve to manufacturer curve by varying the series resistance value and also that of dark's current at reference temperature.

The following code is implemented to attain the I-V curve with generic module parameter values.

```

clc
clear all

%% Yingli PV Module Parameters (polycrystalline silicon PV cells)

Ncs=60; % number of cells in series per module
Ncp=1;% number of cell strings in parallel per module
G=1000; % Irradiance 1000
Gr=1000; % Reference Irradiance
Tc=25+273.15; %20
Tcr=25+273.15;
k=1.3806488e-23; %Boltzman Constant
eg=1.12; % Band gap energy of the solar material (1.12 eV for
crystalline Si, 1.03 eV for CIS, 1.7 eV for amorphous silicon, 1.5 eV
for CdTe)
Iscr=8.4/Ncp; % Short Circuit Current at Reference Temp
AlphaT=0.0017; % Temperature coefficient of photo current (0.0017 A/K
for silicon solar cells)
q=1.60217657e-19; % electron charge

%% Trial & Error Values

n=1.05; % diode ideality factor
Rsr=0.00689;
Rsh=548;
Ior=1e-9;

%% Equations
syms I V Io Ish Z

```

```

Ig= Iscr*(G/Gr)*(1+AlphaT*(Tc-Tcr));
Io=(Ior*((Tc^3)/(Tcr^3))*exp((1/Tcr)-(1/Tc))*q*eg*(1/(n*k))));
Id=Io*((exp((V+I*Rsr)/(n*k*Tc/q))-1);
Ish=(V+I*Rsr)/Rsh);

Ix= vpa(Ig-Id-Ish-I,3)

f = @(i,v)8.4 - 0.00182*v - 1.0e-9*exp(0.255*i + 37.1*v) - 1.0*i;
v = 0:.01:0.82;
i0 = 1;
[i,fval] = arrayfun(@(v)fzero(@(i)f(i,v),i0), v);

figure(5)
plot(Ncs*v,Ncp*i);
grid on
xlabel('Voltage (V)')
ylabel('Current (A)')
title('Yingli YL-230P-29B Model I-V Curve');
xlim([0 40])
ylim([0 9])

P=v.*i;
figure(6)
plot(Ncs*v,Ncp*Ncs*P);
grid on
xlabel('Voltage (V)')
ylabel('Power (W)')
title('Yingli YL-230P-29B Model Power-Voltage Curve');
ylim([0 250])

```

This code outputs the following I-V and P-V curves:-

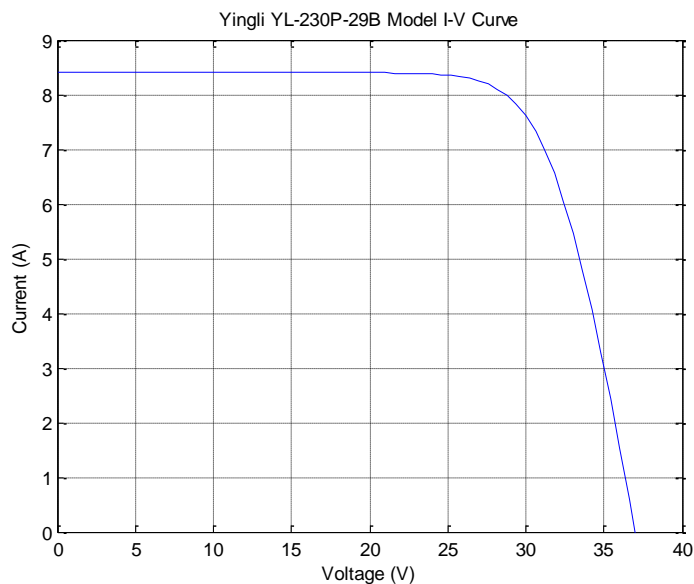


FIGURE 3.4: PSCAD PV module model I-V curve

Analyzing the curve shown in FIGURE 3.4, it can be noticed that the model short circuit current and open circuit voltage match with that provided by the manufacturer for this specific module series (YL230-29b).

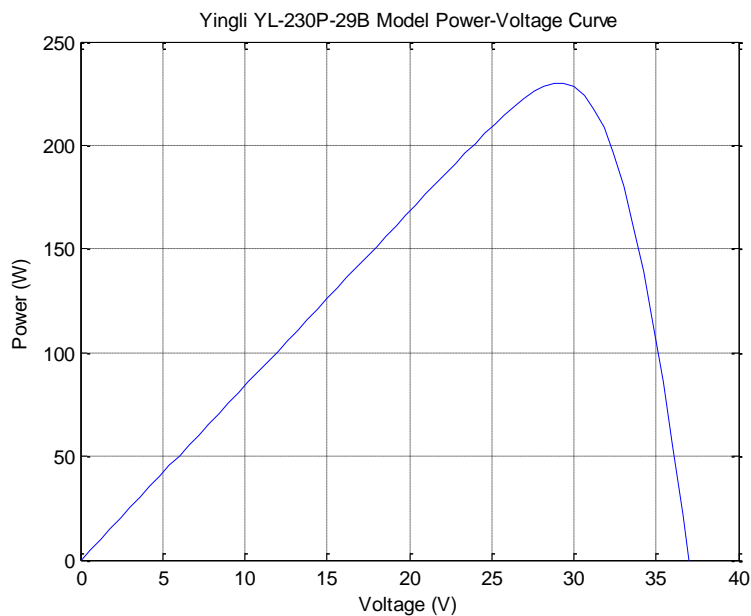


FIGURE 3.5: PSCAD PV module model P-V curve

Also, we can see that the maximum power of the PSCAD model shown in FIGURE 3.5 matches with manufacturer specifications. Therefore, the final model parameters to be used in the PSCAD model are as follows:-

$N_{cs}=60$	(number of cells in series per module)
$N_{cp}=1$	(number of cell strings in parallel per module)
$e_g=1.12$ eV	(Band gap energy of the solar material)
$I_{scr}=8.4$ A	(Short Circuit Current at Reference Temp)
$V_{ocr}=37V$	
$\alpha_T = 0.0017$	(Temperature coefficient of photo current)
$n=1.05$	(diode ideality factor)
$R_{sr}=0.00689$ Ohm	
$R_{sh}=548$ Ohm	
$I_{or}=1e-9$ A	(darks current at reference temperature)

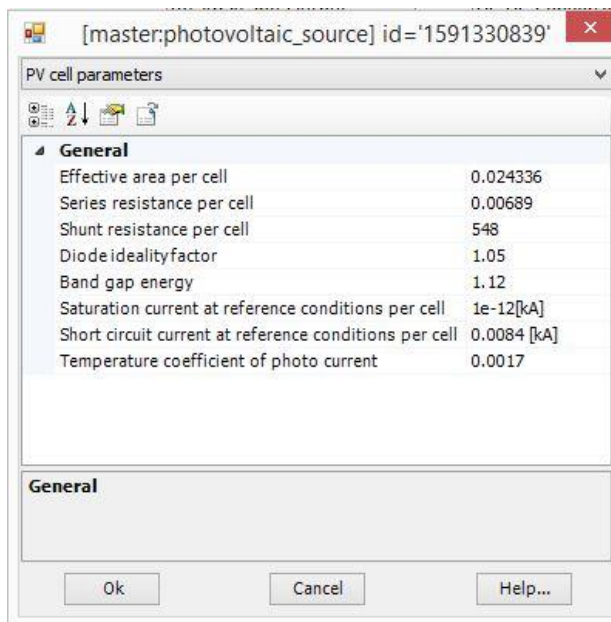


FIGURE 3.6: PSCAD PV cell model

The parameters shown above are filled in the PSCAD PV cell dialog shown in FIGURE 3.6

### 3.4.2. Aggregated PV Array Model

The PV module modeled above is utilized to construct the aggregated PV station model in PSCAD. The modeled array specifications in PSCAD are as shown below in FIGURE 3.7 :-

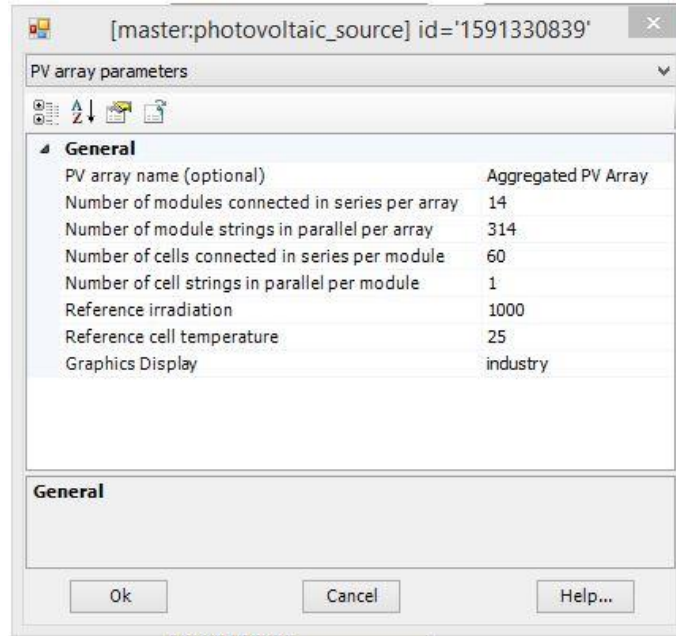


FIGURE 3.7: PSCAD aggregated PV array model parameters

### 3.4.3. Buck Converter Model Design

#### 3.4.3.1. PV Station Buck Converter Specifications

The PV station buck converter model is connected at the output of the aggregated PV station. Its purpose is to maintain PV station terminal voltage at a value that would maintain maximum PV power extraction. This voltage is calculated by an incremental conductance based MPPT algorithm. The buck converter to be designed is based on the following specifications:-

TABLE 3.5: PV Station Buck Converter specifications

Parameter	Value
Input Voltage at Maximum Power & at Standard Conditions	413 kV
Output Voltage	350 V
Capacity	1 MW
Maximum Voltage Ripple	5% (17.5)
Maximum Current Ripple	5% (142.5A)
Switching Frequency	500Hz

### 3.4.3.2. PV Station Buck Converter Element Design

The PV station buck converter elements, namely L and C are designed to maintain voltage and current ripples less than 5% of their rated values. The following matlab code is used to find proper inductor and capacitor values:-

```

clc
clear all

%%Element specification: For 1MW PV station Buck Converter
Vs = 413;
Vout = 350;
P = 1000e3;
D_prime = Vs/Vout;
D = 1/D_prime;
Iin = P/Vs;
Iout=P/Vout;
IL = Iout;
Fsw= 500;
T = 1/Fsw;
R = Vout^2/P;
i_ripple = 5/100*Iout; % 5% ripple in output current
v_ripple = 5/100*Vout; % 5% ripple in output voltage

%%Element Design:

Ldesign = D*T*(Vs-Vout)/i_ripple
Cdesign= (i_ripple*T)/(8*v_ripple)

```

The design values of the converter inductor and capacitor are as follows:-

```

Ldesign = 7.4746e-004 (Henry)
Cdesign = 0.0020 (Farad)

```

In order to assure operation within voltage and current ripple limits, the following inductor values are chosen:-

$$L_l = 1 \text{ mH}$$

$$C_l = 2.6 \text{ mF}$$

The attained values are used to model the discharge converter in PSCAD as shown in FIGURE 3.8. A 413V DC voltage source is used as converter input. The switch duty cycle is set to obtain an output voltage of 350V. The circuit load is to the rated converter value, 1MW.

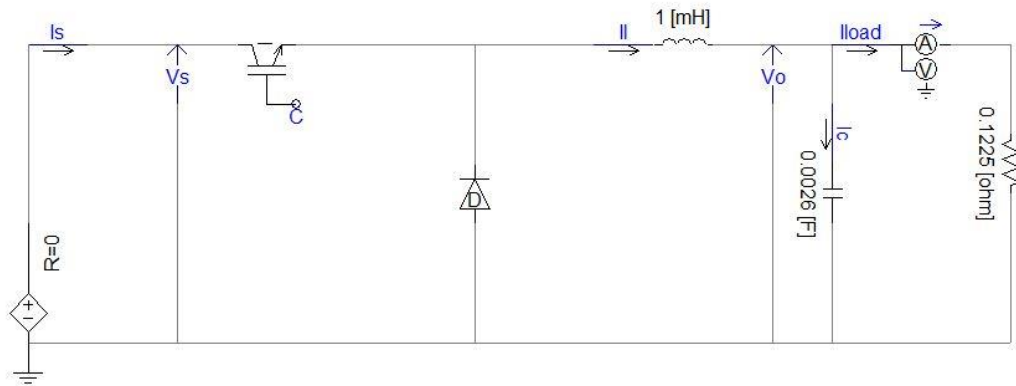


FIGURE 3.8: PV station buck converter PSCAD model

As shown in FIGURE 3.9, the peak to peak current ripples are found to be 25A which represents 1% of rated inductor current. This satisfies the applied design characteristics. Also, the peak to peak output voltage ripples are found to be 5V which represents 1.5% of rated voltage output. This satisfies the applied design characteristics.

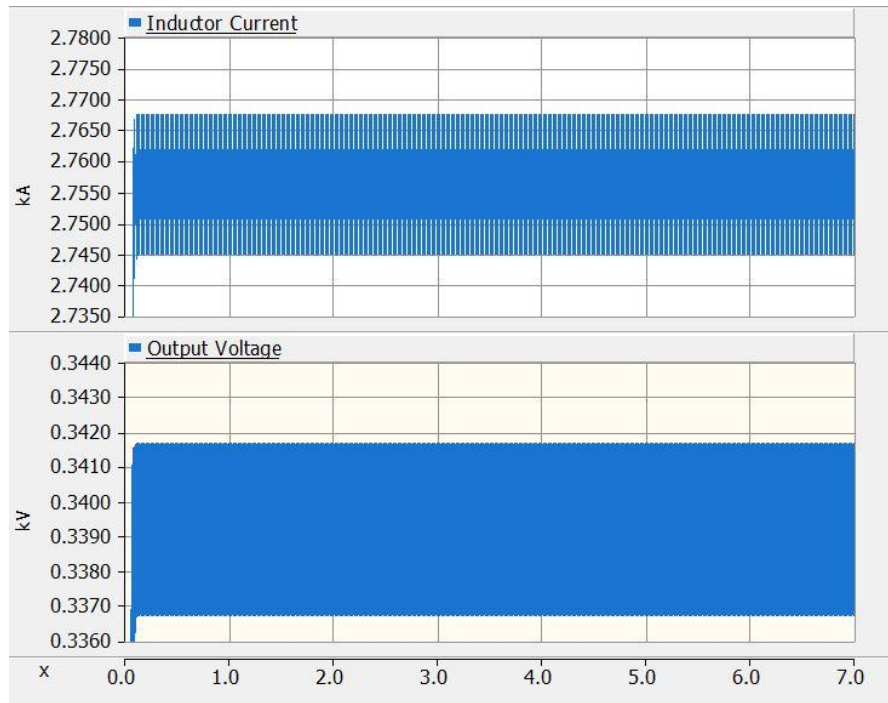


FIGURE 3.9: Inductor current and output voltage ripples of PV station buck converter model

#### 3.4.3.3. PV Station Buck Converter Controller Design

The transfer function of the system is evaluated in the following matlab code. The system is perturbed with duty cycle as a single input and converter input voltage as single output.

```

%% PD Controller Design

L = 1.25* Ldesign;      %Ldesign= 1 mH
C = 1.25*Cdesign;      %Cdesign = 2 mF

%%Perturbation from duty ratio to the converter input voltage:
num0 = [(Vout/D)];
den0 = [(L*C) (L/R) 1];
sys0 = tf(num0,den0)

figure(1);
margin(sys0);
[Gm0, Pm0, Wgm0, Wpm0]=margin(sys0);

Gdo=Vout/D           % System gain

```

```
Wo=1/(sqrt(L*C)) % System Corner frequency
```

This code outputs the following:-

```
sys0 =
      413
-----
 2.383e-06 s^2 + 0.007627 s + 1
Continuous-time transfer function.
Gdc = 413.0000
Wo = 647.7311
```

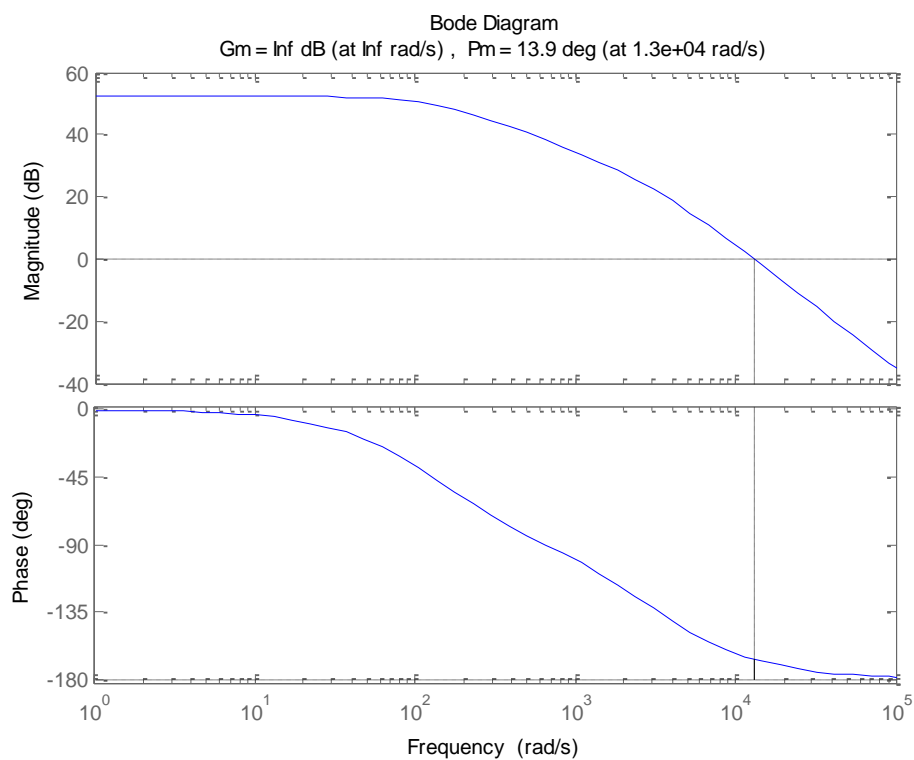


FIGURE 3.10: Uncompensated PV station buck converter bode plot

As shown in FIGURE 2.18, the phase margin of the uncompensated system is 13.9°. We will design a PD controller to obtain a bandwidth of 30,000 rad/sec and a phase margin of 52°.

```

%% Required Closed Loop System Characteristics PM=52degree , Wc=30,000
rad/sec
BW_req=30000; %in rad/sec
PM_req=52; %in degrees

[magx,phasex] = bode(sys0,BW_req);
PM_bw=180+phasex
PM_adj=PM_req-PM_bw %in degrees

% Controller gain, zero and pole evaluation

Wz=BW_req*sqrt((1-sin(degtorad(PM_adj)))/(1+sin(degtorad(PM_adj))))
Wp=BW_req*sqrt((1+sin(degtorad(PM_adj)))/(1-sin(degtorad(PM_adj))))
Gco=((BW_req/Wo)^2)*(1/Gdo)*sqrt(Wz/Wp)

% PD Compensator Bode Plot & Margins
numc=[(1/Wz) 1];
denc=[(1/Wp) 1];
Gc=Gco*tf(numc,denc)
figure(2);
margin(Gc);

```

The controller gain, zero and pole is given by the following values

```

PM_bw =
    6.0913
PM_adj =
    45.9087
Wz =
    1.2149e+04
Wp =
    7.4083e+04
Gco =
    2.1033

Gc =

    0.0001731 s + 2.103
    -----
    1.35e-05 s + 1

Continuous-time transfer function.

```

The designed PD controller ( $G_c$ ) is shown in the matlab output shown above. The controller bode plot is shown in FIGURE 2.19.

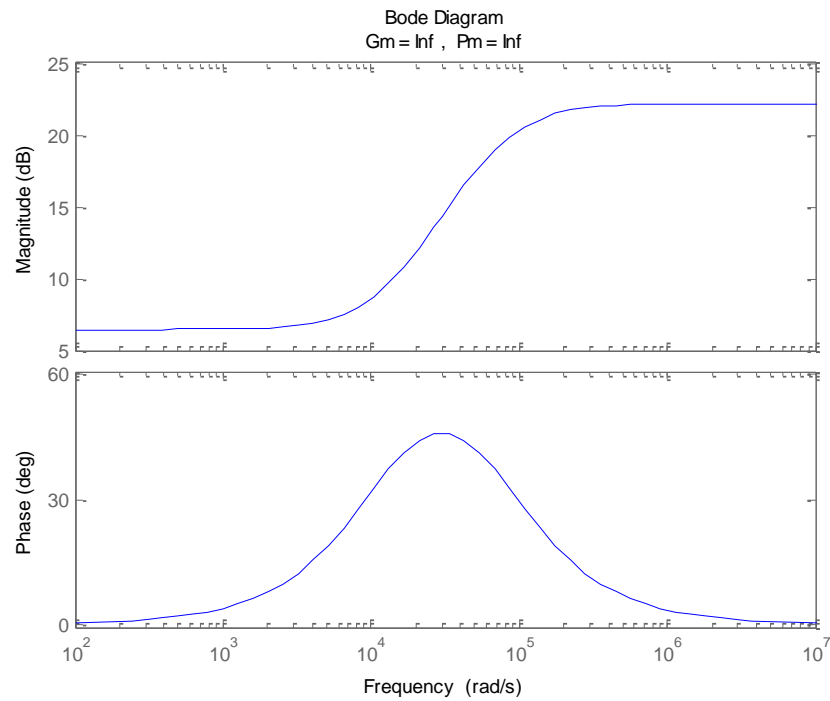


FIGURE 3.11: PV station buck converter PD compensator bode plot

The designed PD controller is implemented into the system loop with unity feedback.

```

%% Compensated system
Tol=Gc*sys0
figure(3);
margin(Tol);

% Step Response
H = 1; %Unity gain feedback;
Tcl = feedback(Tol,H) % Unity Feedback system
figure(4)
step(Tcl)

```

The open and closed loop transfer functions are as follows

Tol =

$$\frac{0.0715 s + 868.7}{3.217e-11 s^3 + 2.486e-06 s^2 + 0.007641 s + 1}$$

Continuous-time transfer function.

Tcl =

$$\frac{0.0715 s + 868.7}{3.217e-11 s^3 + 2.486e-06 s^2 + 0.07914 s + 869.7}$$

Continuous-time transfer function.

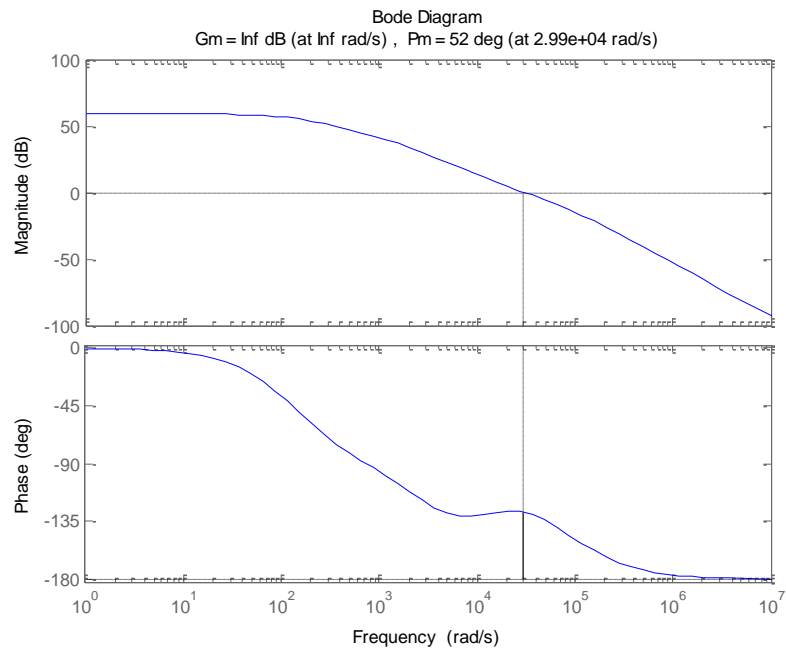


FIGURE 3.12: Compensated PV buck converter system bode plot

As shown in FIGURE 2.20, the compensated system bandwidth and phase margin is 30,000 rad/sec and  $52^\circ$ , respectively. The attained values satisfy the margins we have set for the compensated system.

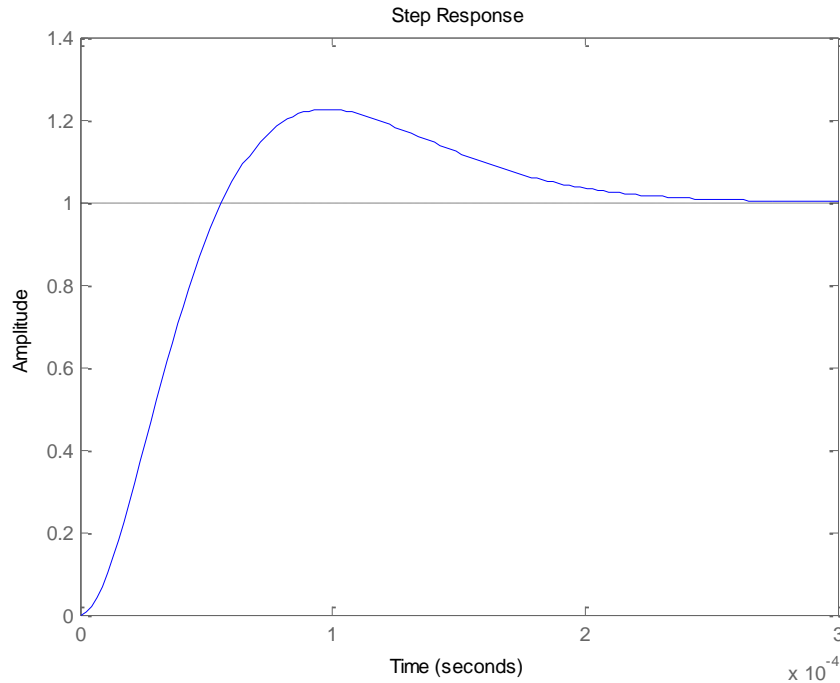


FIGURE 3.13: Step response of compensated discharge buck converter

As shown in FIGURE 2.21, the steady state time response of the compensated system is 300  $\mu$ s. This represents a good response time for a 1MW converter. The deduced PD controller values are implemented in the PSCAD converter model and used to control the PV station buck converter input voltage according to the MPPT algorithm calculated voltage value.

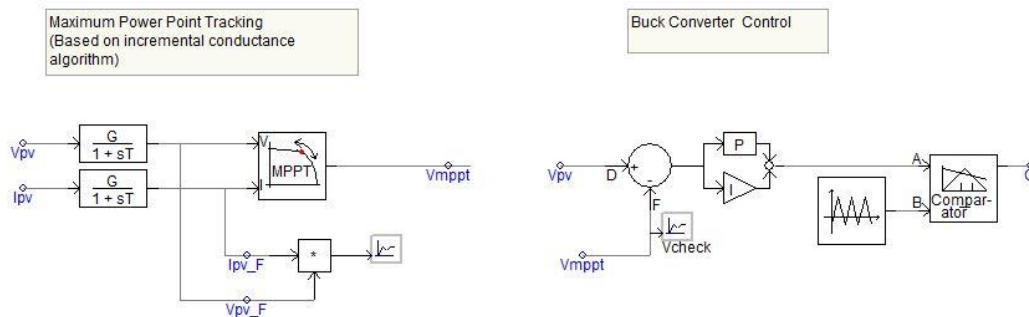


FIGURE 3.14: PV Station buck converter control circuit model

### 3.4.4. Inverter Model Design

#### 3.4.4.1. Inverter Specifications

TABLE 3.6: Inverter Specifications

Parameter	Value
DC Link Voltage	350V
AC Output Voltage (L-L, rms)	230V
Capacity	1 MW
Switching Frequency	500Hz

#### 3.4.4.2. Inverter Modeling

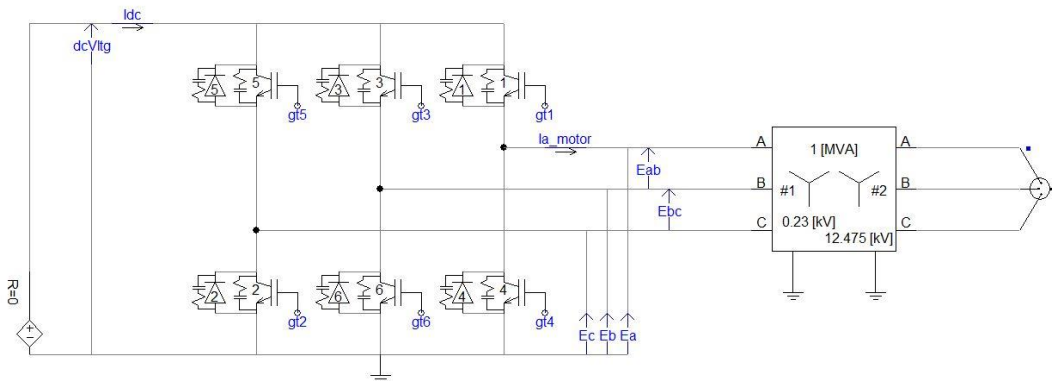
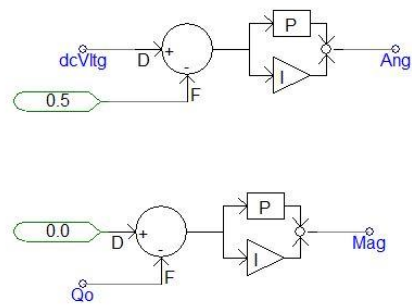


FIGURE 3.15: Inverter PSCAD model

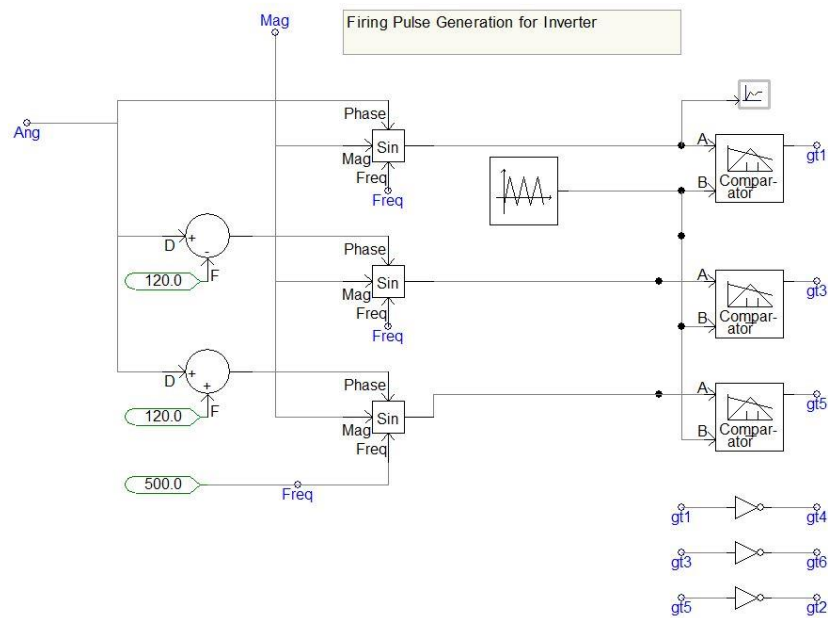
The SMS inverter is modeled in PSCAD as shown in FIGURE 2.23. IGBT electronic switches models are used as switching elements. The inverter operation is tested with a 350V DC voltage source.

As shown in FIGURE 2.24, a PQ control scheme is used to manage output active and reactive power of the inverter. Two PI controllers are used to control the angle and magnitude of the reference sine wave in this PWM scheme. The output active power of the inverter is controlled by the angle of the reference signal. This angle is set by maintaining the DC link voltage constant. This forces current output of the inverter to follow that of the PV array. In other words, inverter power output is controlled by PV station array power. The reactive power output of the inverter is maintained by controlling the magnitude of the PWM reference signal. The reference value for the reactive power is set to zero.

Simple P and Q regulation (Inverter control)



(a)



(b)

FIGURE 3.16: Inverter PWM control circuit model

### 3.4.5. Full System Control Methodology & Validation

As shown in FIGURE 3.17, The PV array model is connected to the input of the MPPT DC buck converter which is in turn connected to the inverter.

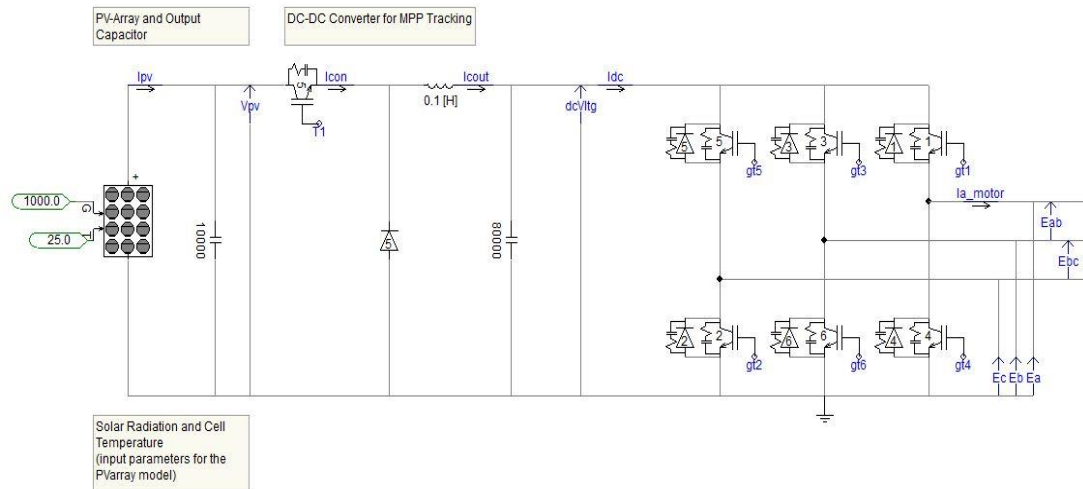


FIGURE 3.17: Full aggregated PV station model

The control methodology applied here is a backward control scheme where the DC buck converter is used to vary its input voltage ( PV array output voltage) according to the MPPT algorithm set value for that instant. This allows the power output from the PV station to be maximized since the voltage value set by the MPPT algorithm corresponds to the maximum power point on the full array I-V curve.

Inverter active power control is based on setting a constant value for the DC link voltage (Buck converter output voltage). This allows the PV array output power to be conveyed through the converter inverter set according to the irradiance and temperature level at the input of the PV array model shown above.

The control methodology stated above is applied to the system model described. The input irradiance signal is varied according actual irradiance values at a site in North

Carolina. The model response to irradiance changes is monitored to verify model validity.

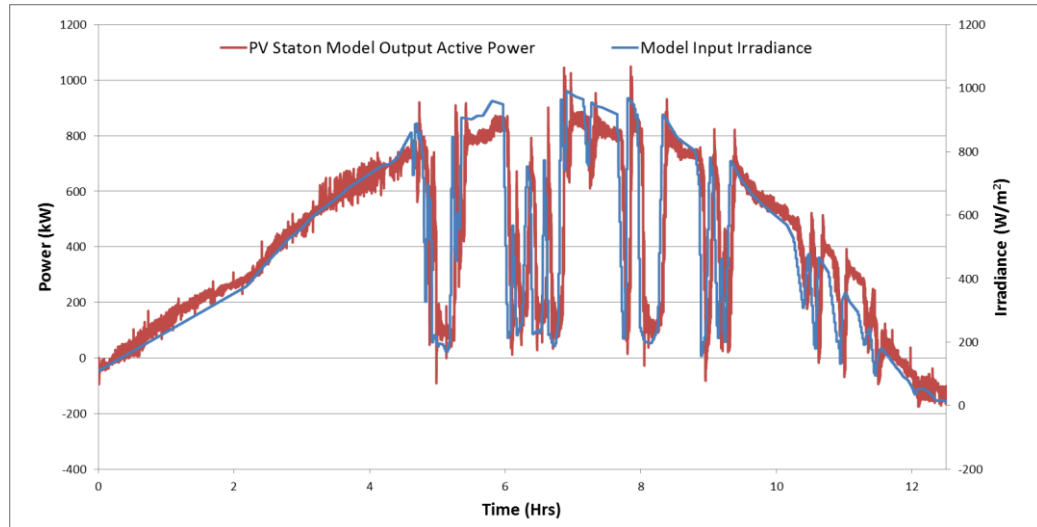


FIGURE 3.18: PSCAD PV station model output active power plotted against input irradiance

In order to confirm the validity of the PSCAD PV station model, a simulation is run where the model input irradiance signal is varied according to an irradiance log text file. The output of the PV station model in response to said irradiance values is recorded as shown in FIGURE 3.18

### 3.5. Overall Distributed Energy System Architecture

The system is setup as shown in

FIGURE 3.19. The designed aggregated PV station model is connected in conjunction with the BESMS. The main purpose of this section is to allow the BESMS to intervene with the value of  $P_{ess}$  in such a way to counteract large power swings of  $P_{pv}$ . This will allow the active power output at the point of common coupling to be firmed and

clear from large power swings. This in turn reduces the feeder's perception of large PV power swings which eventually would allow greater PV penetration on the same feeder.

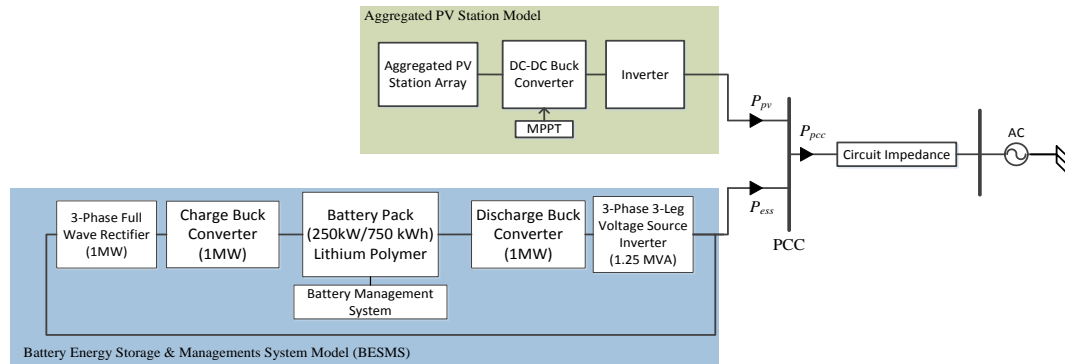


FIGURE 3.19: Distributed generation system setup

Like most PV installations, the PV station model is controlled to operate at unity power factor. In other words, the reactive power contribution of the PV station is set to zero. The Battery pack capacity is 0.25 MW and the inverter capacity 1.25MVA. FIGURE 3.20 shows the regions of ESS controllability.

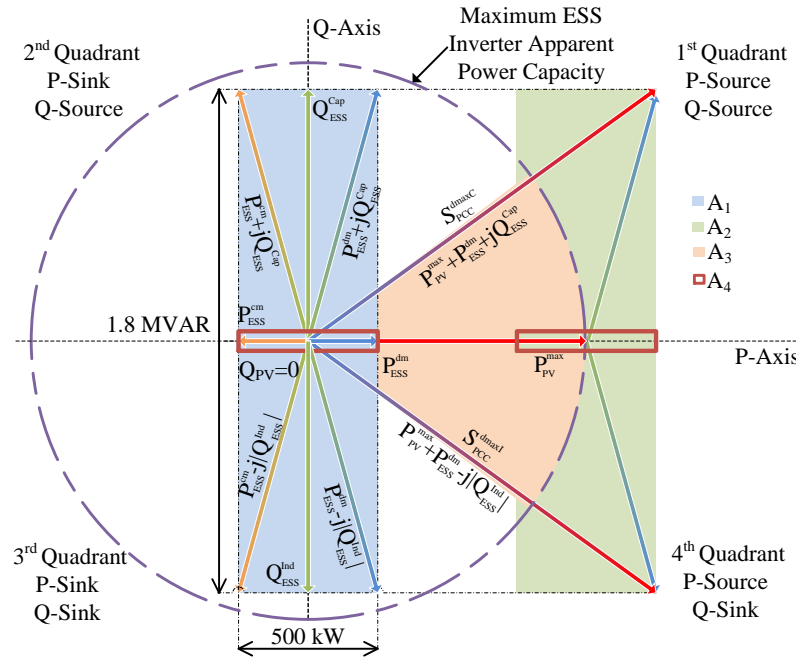


FIGURE 3.20: BESMS active and reactive power supplying capabilities.

For the proposed design, The BESS active power output varies between the maximum discharge power  $P_{ESS}^{dm} = 250kW$  and maximum charge power  $P_{ESS}^{cm} = -250kW$ . Area  $A_1$  in FIGURE 3.20 shows the ESS controllable output region. This is also the power output region for zero active power output from the PV station installed at the point of common coupling (PCC). As the PV station output increases, the controllable region is shifted to the right till it becomes  $A_2$  at maximum (PV) output. So, areas ( $A_1$ ) & ( $A_2$ ) represent the controllable regions for minimum and maximum PV station output, respectively.  $A_4$  shows the control regions used during PV capacity firming (PVCF) application.

### 3.6. Conclusion

In this chapter, a 1.25MVA utility scale PV station consisting of six arrays was modeled in PSCAD. PV cell parameters were deduced utilizing Matlab solvers. Matlab I-V curves were matched to that of manufacturer. PSCAD PV cell models were matched to both Matlab models and manufacturer data sheet. Solar inverter model was designed utilizing a buck converter/three leg voltage source inverter combination in PSCAD. Inverter model was validated with practical system data (Irradiance as input and injected power as system output)

## CHAPTER 4: PV STATION CAPACITY FIRING APPLICATION

### 4.1. Introduction

The described PV firming algorithm relies to a great extent on the fact that maximum irradiation levels at a certain location are constant to some extent for the same time of the day in a single season. For example, the irradiation at a location in North Carolina for a summer day at 11:00am will be almost equal to the irradiation of the preceding day at the same time and location provided the absence of clouds on both days. The impact of temperature on maximum output power is present but not significant since we are interested only in drastic power swings for PV firming. Temperature daily variations are not as drastic as the effect of clouds that dramatically impact insolation which in turn affects PV stations' output power.

### 4.2. Algorithm Methodology

The PVCF algorithm methodology is presented in the sections below. First, a firming reference calculation methodology is sought. Second, a PV power intermittency detection algorithm is designed. Third, BESS SoC is taken into consideration.

#### 4.2.1. Firming Reference Calculation

Since the output active power of a PV station is proportional to the irradiation levels, we can compare the output of a 1MW PV Station for several consecutive days to prove our hypothesis about irradiation.

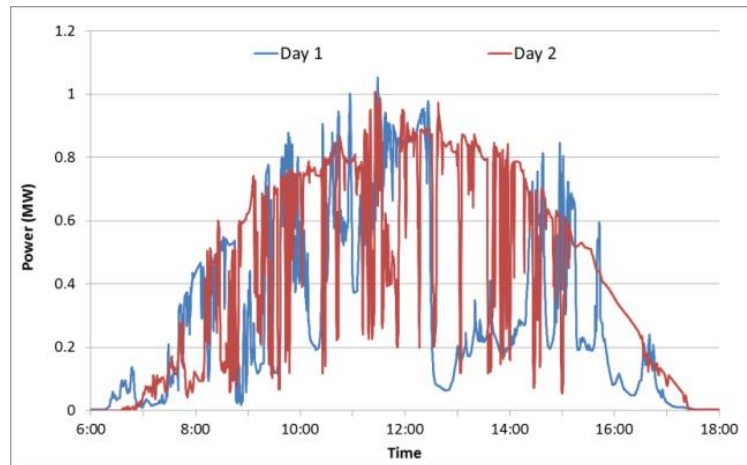


FIGURE 4.1: Comparison between consecutive days output powers (Day 1 & Day 2)

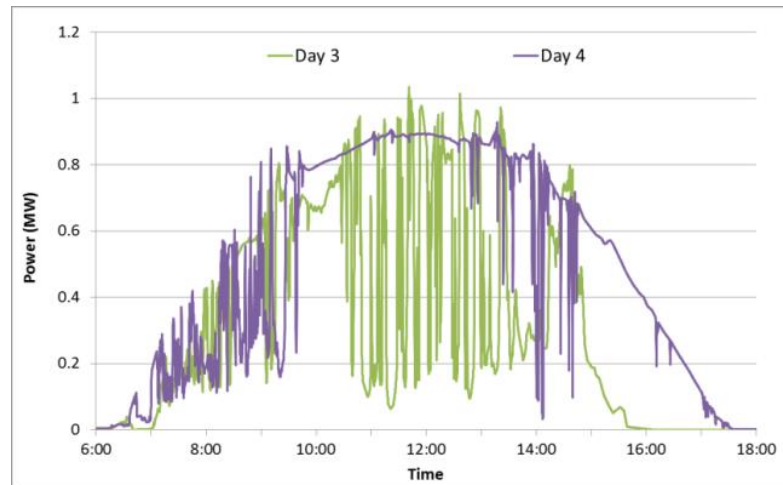


FIGURE 4.2: Comparison between consecutive days output powers (Day 3 & Day 4)

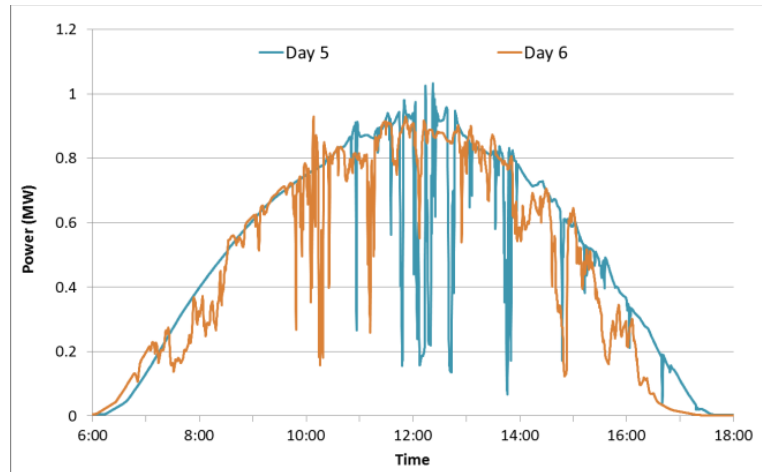


FIGURE 4.3: Comparison between consecutive days output powers (Day 5 & Day 6)

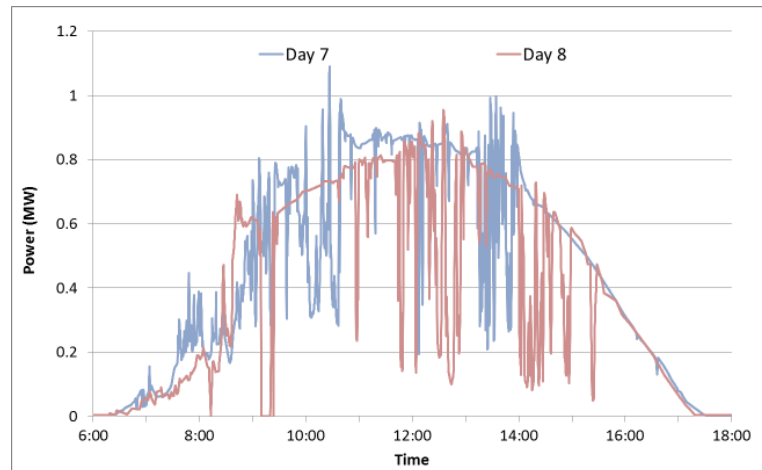


FIGURE 4.4: Comparison between consecutive days output powers (Day 7 & Day 8)

FIGURE 4.1 to FIGURE 4.4 show the comparison of four day pairs. As we can see, in the absence of intermittency (caused by clouds), the output power levels are almost equal. The relatively small differences that appear are attributed to temperature differences. The spikes in the characteristic maximum curve are smoothed and the smoothed characteristic PV curve is obtained.

Based on the mentioned fact, the described algorithm stacks the output power of the previous days and compares the most recent  $n$  days to obtain the characteristic

maximum PV curve for the PV station location at that time of year. This characteristic maximum PV curve varies from season to another and from location to another. Let us consider the shown 8 consecutive days to obtain our characteristic maximum PV curve. FIGURE 4.5 shows our 8 days plotted against each other. FIGURE 4.6 shows the 8 consecutive day's characteristic maximum PV curve.

The characteristic maximum PV curve is given by:

$$P_m(t) = \max(P_1(t), P_2(t), P_3(t) \dots P_n(t)) \quad (4.1)$$

Where  $P_k(t)$  is the daily output power of the PV station.  $k$  Signifies the day;  $k = 1, 2, 3, 4, \dots, n$

The smoothed characteristic maximum power curve (SCMPC) is defined as follows in equation (4.2):-

$$P_{SCMP}(t) = \begin{cases} P_m(t) & \text{for } L_l < \frac{\Delta P_m(t)}{\Delta t} < U_l \\ U_l \Delta t + P_m(t - \Delta t) & \text{for } \frac{\Delta P_m(t)}{\Delta t} > U_l \\ L_l \Delta t + P_m(t - \Delta t) & \text{for } \frac{\Delta P_m(t)}{\Delta t} < L_l \end{cases} \quad (4.2)$$

$$P_{OPR}(t) = m \times P_{SCMP}(t) \quad (4.3)$$

Where  $\Delta t$  is the sampling time of PV power output measurement in our case it is 30 sec.

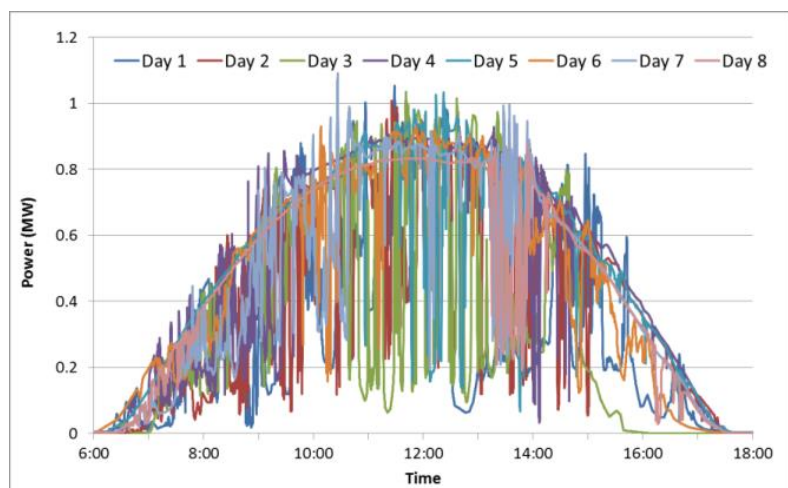


FIGURE 4.5: Comparison between eight consecutive days output powers

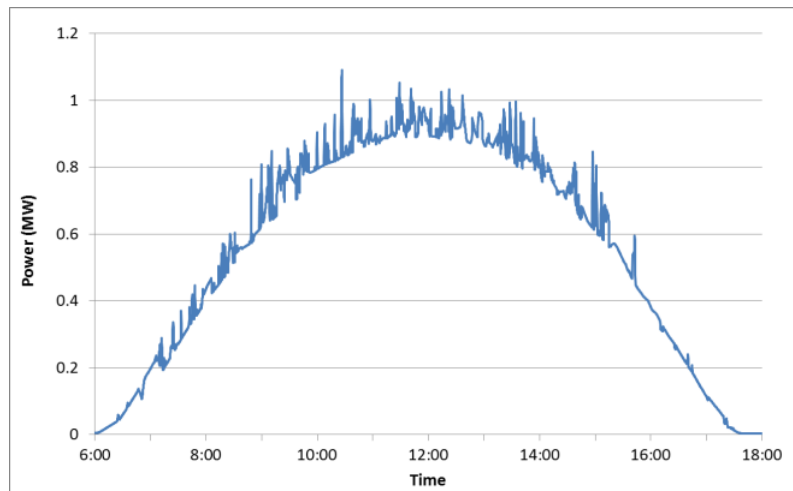


FIGURE 4.6 Characteristic Maximum Power Curve

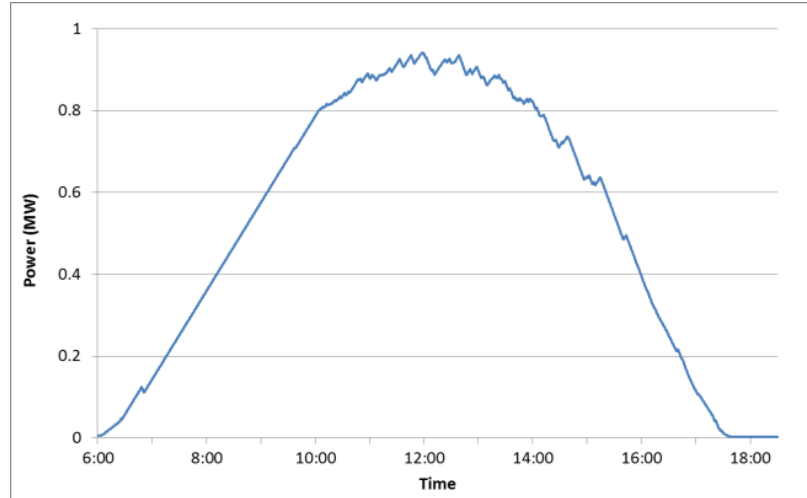


FIGURE 4.7: Smoothed Characteristic Maximum Power Curve (SCMP)

The goal is to attain a reference curve with which the PV output can be compared. During times of intermittent PV output, if the PV output is less than the reference value, the battery should discharge at the difference value. If the PV output is greater than the reference signal value, the battery will charge at the difference value also. In order to use the full range of our battery power (charge + discharge), a fraction of the (SCMP) curve is taken as the reference firming curve for times of power intermittency. The battery capacity ( $P_{Bmax}$ ) is 250kW so our maximum firming ability should be 500kW. Therefore, the multiplication factor is chosen such that it is 250kW below the maximum of the SCMP curve. This provides reachability to 250kW above and beneath the reference curve as shown in FIGURE 4.8. The area between the upper and lower firming limits represent the region where 100% of PV power swings can be theoretically eliminated.

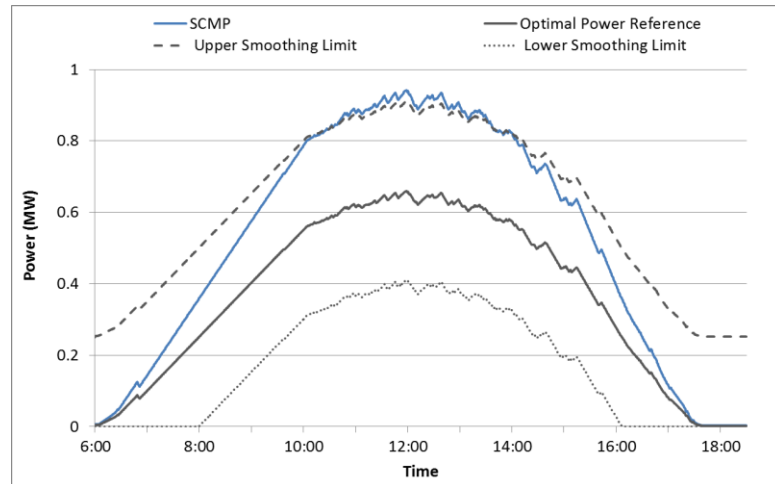


FIGURE 4.8: Optimal Power Reference Curve and the limits of PV firming (smoothing) region

The aim of the obtained optimal power reference curve (OPR) is to allow smoothing of PV output fluctuations that occur in the middle or close to middle of the day. These swings are the ones that cause noticeable transients on the connected circuit. These swings also cause distribution level feeder voltage regulators to operate. As shown in FIGURE 4.9, the range of PV firming of the reference curve offered by a 250 kW battery allows firming for almost the full range of power fluctuation of the 9<sup>th</sup> day of our sampled period.

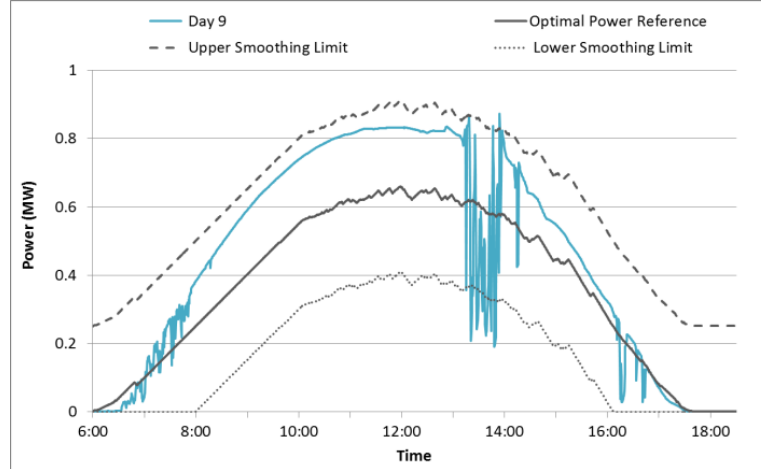


FIGURE 4.9: Firming range compared to day 9 output power

#### 4.2.2. Intermittency Detection

One of the most important battery operation priorities is battery life due to their expense. In order to increase battery lifetime, it is crucial to only use battery during times when it is truly needed. Intermittency detection allows the ability to idle the battery during times when PV output power is smooth and does not require any conditioning.

The intermittency detection algorithm relies on constantly tracking the rate of change of the difference ( $P_c$ ) between the output PV power and the OPF curve. The real time measured values of ( $P_c$ ) are passed through a low pass filter which rejects sudden power fluctuations to obtain ( $P_{cf}$ ). ( $P_{cf}$ ) is then subtracted from ( $P_c$ ) to obtain ( $D$ ). If the value of  $D$  violates an upper or lower limit, intermittency is then assumed to be present and firming is commenced. Firming continues till value of  $D$  is maintained within limits for a period  $T_d$ .

$$P_c(t) = P_{pv}(t) - P_{SCMP}(t) \quad (4.4)$$

$$P_{cf}(t) = \begin{cases} P_c(t) & \text{for } L_{l2} < \frac{\Delta P_c(t)}{\Delta t} < U_{l2} \\ U_l \Delta t + P_c(t - \Delta t) & \text{for } \frac{\Delta P_c(t)}{\Delta t} > U_{l2} \\ L_l \Delta t + P_c(t - \Delta t) & \text{for } \frac{\Delta P_c(t)}{\Delta t} < L_{l2} \end{cases} \quad (4.5)$$

$$D(t) = P_c(t) - P_{cf}(t) \quad (4.6)$$

As shown in FIGURE 4.10, if  $D(t)$  goes out of a predetermined band, PV station power fluctuations are assumed to be occurring and intermittency detection algorithm output (IDAOP) is set to the binary value (1). At this point, PV capacity firming is commenced. Firing dispatch is cleared if  $D(t)$  settles back within band for a period of time ( $T_d$ ). This triggers the IDAOP value back to a binary (0). This corresponds to the end of PV output fluctuations or in other words, clearing of clouds that were passing. So, no further firming would be required.

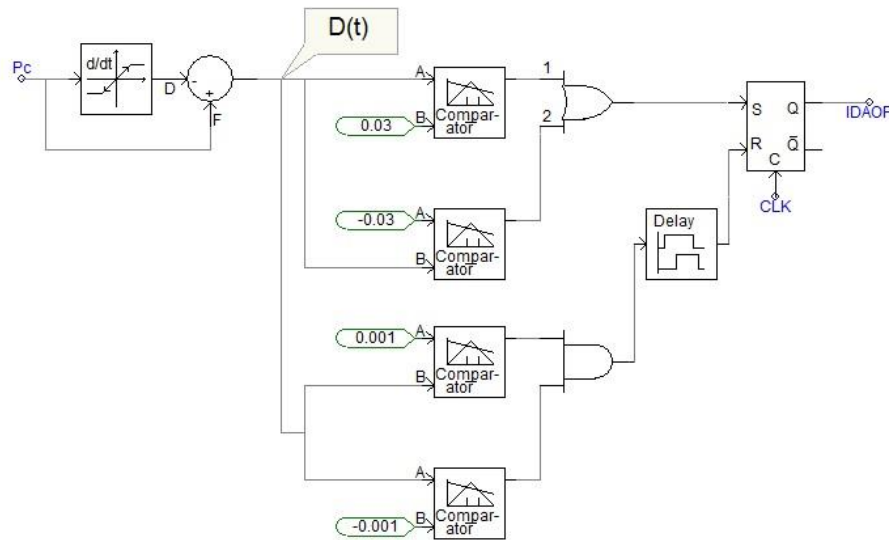


FIGURE 4.10 Intermittency detection algorithm PSCAD model

FIGURE 4.11 shows the response of the intermittency detection algorithm to a typical PV curve for a certain day. It can be noticed that the algorithm is effective at detecting the times of PV output intermittency. As soon as the measured output PV power fluctuated, the IDAOP value was set to a binary 1 and when the power fluctuations stopped, the IDAOP value returned to zero. This is suitable for the intended PV capacity firming application.

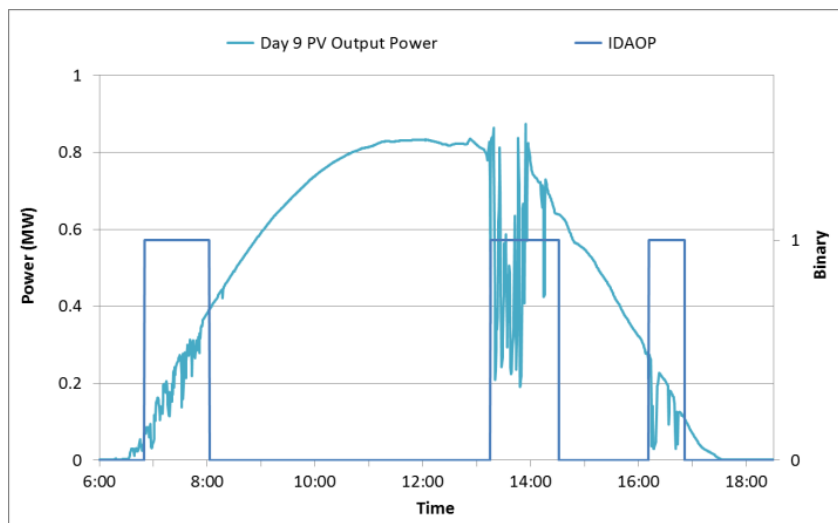


FIGURE 4.11: Intermittency detection algorithm output in response to power swing

#### 4.2.3. State of Charge Constraint

As can be inferred from the previous equations, the shape of the OPR controls the degree of firming attainable. Also, it dictates the extent to which the battery intervenes to firm PV power. So, we can infer that the factor ( $m$ ) in equation (4.3) can be used to control both the degree of firming and battery SOC.

Let us calculate the value of ( $m$ ) that corresponds to maximum PV firming. ( $R_u$ ) is defined as the upper firming limit of the battery for a determined OPR curve as shown in FIGURE 4.8.

$$R_u(t) = m P_{SCMP}(t) + P_{Bmax} \quad (4.7)$$

$$R_u(t_{noon}) = m P_{SCMP}(t_{noon}) + P_{Bmax} \quad (4.8)$$

Since maximum PV power firming is attained if  $R_u$  is equal to  $P_{SCMP}$  at noon (i.e. maximum PV power time), we get:-

$$R_u(t_{noon}) = P_{SCMP}(t_{noon}) \quad (4.9)$$

From equations (4.8) & (4.9), it can be deduced that the value of ( $m$ ) for maximum noon firming is as follows:-

$$m_i = 1 - \frac{P_{Bmax}}{P_{SCMP}(t_{noon})} \quad (4.10)$$

Looking at the energy side of the matter, it is required to attain a certain SoC at the end of the firming period to allow sufficient energy for various potential energy storage applications. For a certain time step ( $\Delta t$ ):-

$$\Delta SoC \times E_{cap} = (P_{pv}(t) - m_e(t)P_{scmp}(t))\Delta t \quad (4.11)$$

$$m_e(t + \Delta t) = \frac{P_{pv}(t)}{P_{scmp}(t)} - \frac{E_{cap}}{P_{scmp}(t)} \frac{\Delta SoC}{\Delta t} : \left| \frac{dm_e(t)}{dt} \right| < r_m \quad (4.12)$$

$$\frac{\Delta SOC}{\Delta t} = \frac{SOC_{targ} - SOC}{T_{targ} - t} \quad (4.13)$$

As shown from equations (4.12) & (4.13), the value of ( $m_e$ ) can be adjusted each time step ( $\Delta t$ ) to allow battery SoC to reach a target value ( $SOC_{targ}$ ) at a target time ( $T_{targ}$ ). The manner in which the SoC approaches its target value is shown in FIGURE 4.12. Not reaching the targeted SoC compromises the execution of further energy storage functions after PVCF.

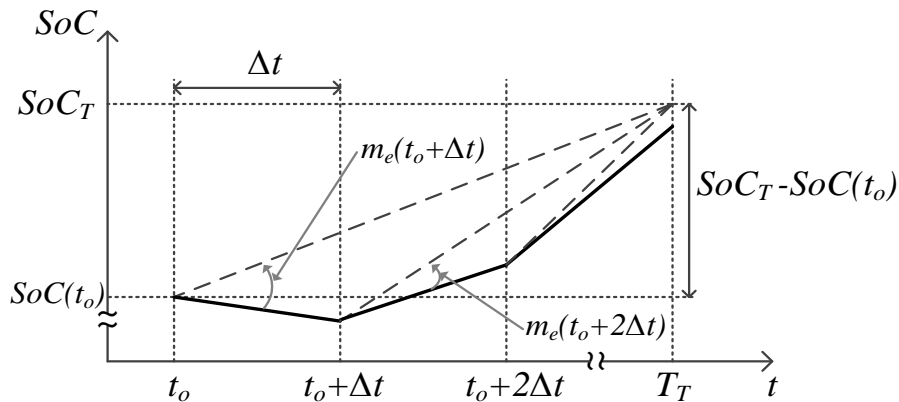


FIGURE 4.12:  $m_e$  calculation for energy oriented firming reference power

At this point, let us assume our target value is 100% SoC at a target time, end of daylight. This takes place under an inequality constraint for the value of ( $m$ ) to insure a minimal degree of firming.

Further, reaching the targeted SoC before the targeted time compromises PVCF performance till the targeted time. For our case, our target value is 95% SoC at a target time ( $T_{PVend}$ ).

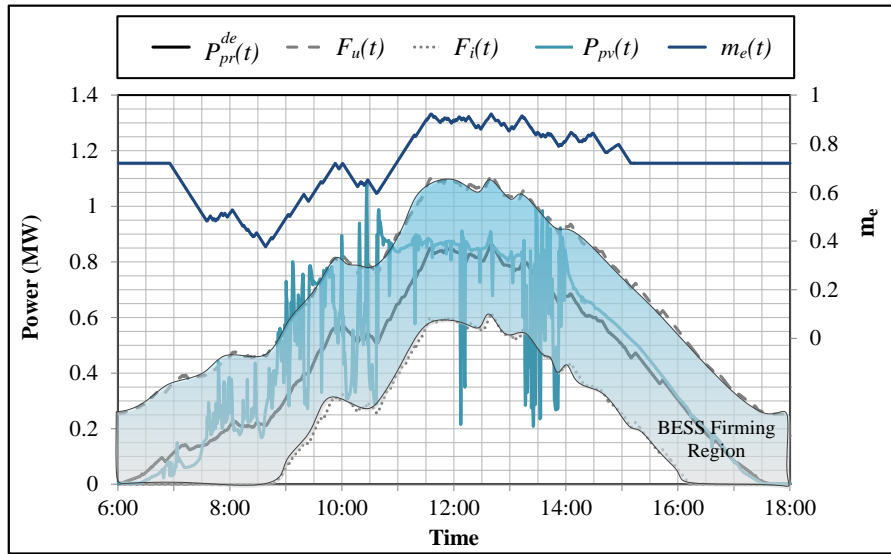


FIGURE 4.13: Dynamic BESS energy oriented reference power firming region

As shown in FIGURE 4.13, the change of the BESS firming region is in accordance with the fulfillment of the targeted SoC at the targeted time. This leads to greater PV power swings being outside the BESS firming region.

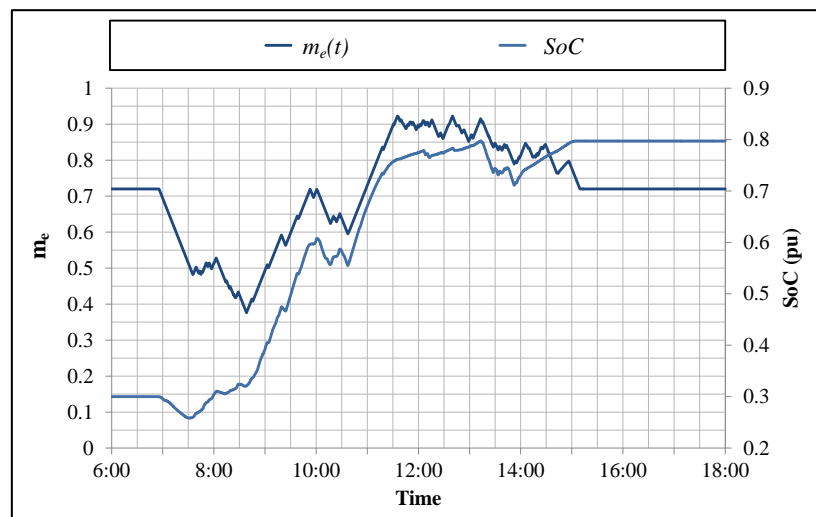


FIGURE 4.14: Weighing factor  $m_e(t)$  and SoC variation for example PV day  
However, the increase of the BESS SoC is apparent in FIGURE 4.17. Therefore, the

use of either power or energy oriented reference powers is based on the value priority in terms of maximizing firming or performing multiple functions.

### 4.3. Simulation Results

The described PV firming algorithm is applied to the circuit shown in Fig. 3. The PV output of the 8 days preceding the algorithm test day are known and are used to obtain the (OPR) curve. FIGURE 4.15 shows the output power of the PV station with the (OPR) curve calculated.

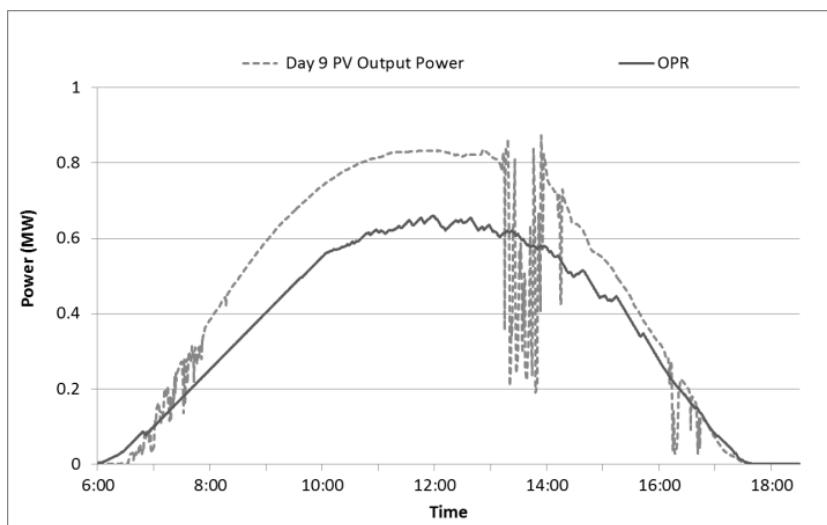


FIGURE 4.15: Day 9 PV power compared to algorithm firming optimal power reference

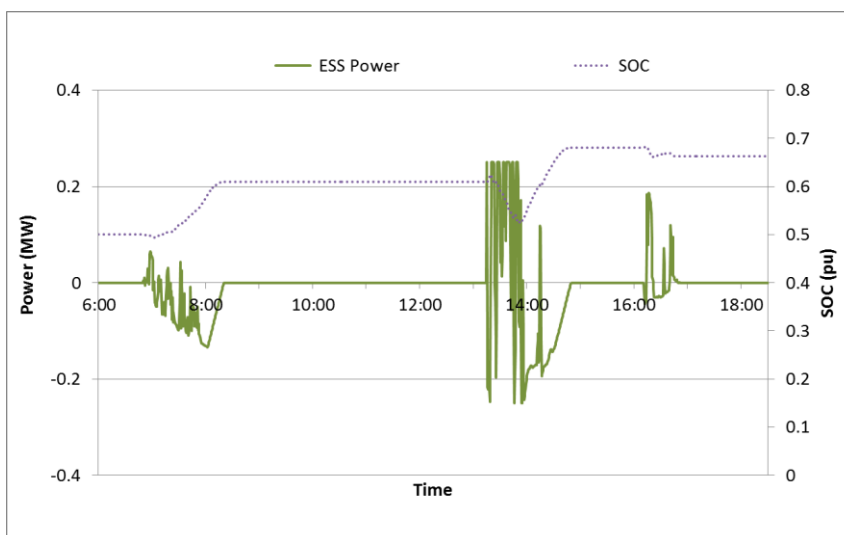


FIGURE 4.16: ESS power output for firming of day 9

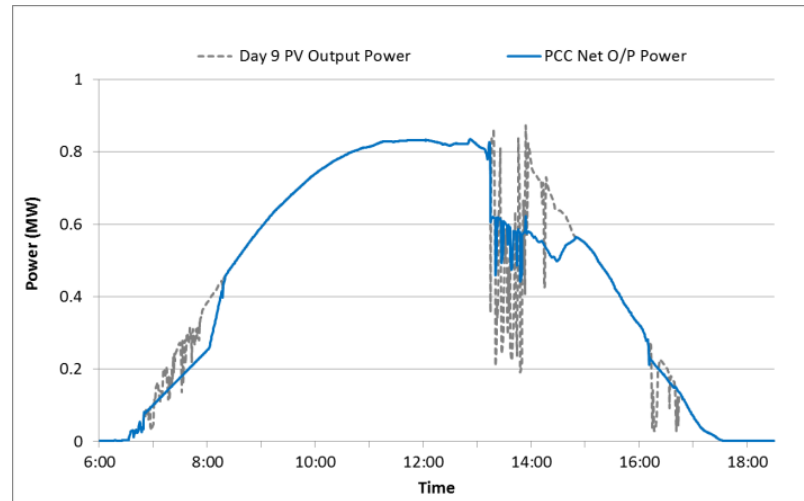


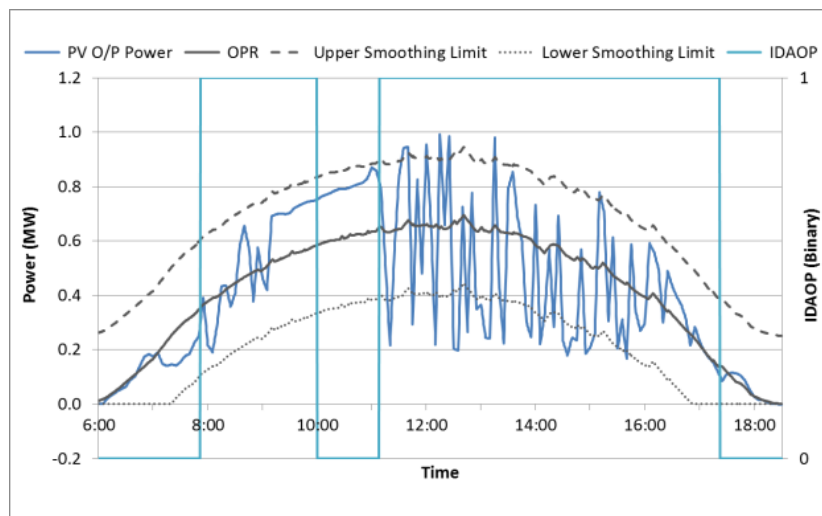
FIGURE 4.17: The point of common coupling output power compared to that of PV station

The ESS is operated during time of intermittent PV output at regions A, B and C shown. During these times, the ESS output power is as shown in FIGURE 4.16. Negative power represents battery charge while positive represents discharge. The battery state of charge (SoC) is set to 50% at the beginning of the day to allow sufficient energy charge and discharge capability for capacity firming. FIGURE 4.17 shows the PCC power which is the summation of ESS power and PV station power outputs. The figure shows efficient firming presented in a firmed PCC power output which will contribute to less voltage regulators' tap changes and transients at substation generators. The algorithm was capable of reducing the maximum PV power swing of this day from 650kW to 240kW (maximum power swings are reduced to 37% of previous values).

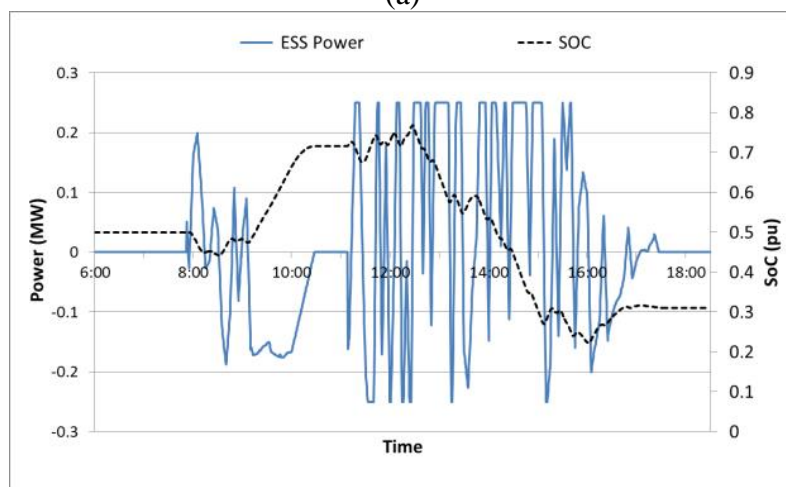
#### 4.3.1. Simulation Results without SoC Constraint

In this section we will present the firming simulation results for a certain day without SoC constraint. The PV output of the 8 days preceding the algorithm test day are

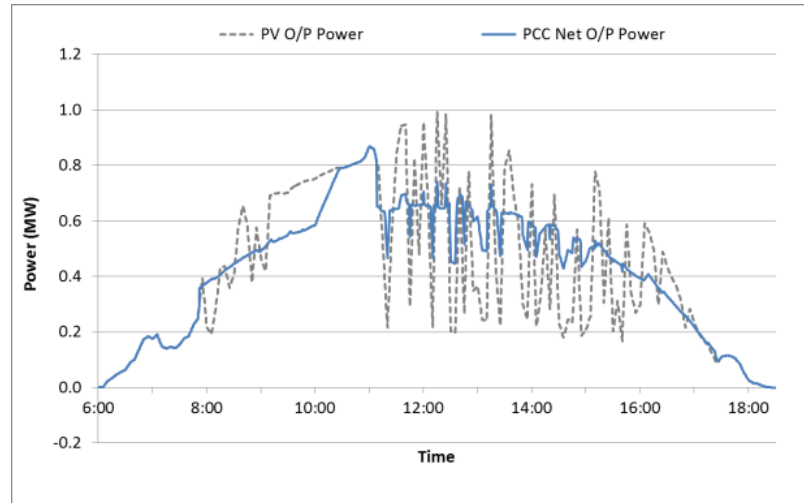
known and are used to obtain the SCMP curve. FIGURE 4.18 shows the output power of the PV station with the (OPR) curve calculated using  $m_i$  from equation (4.10).



(a)



(b)



(c)

FIGURE 4.18: PVCF simulation results without SoC constraint. (a) PV power output compared to OPR. (b) BESS output power with battery SoC plotted on the second y-axis. (c) PCC active power output after PVCF compared to PV power output.

The PV power intermittency is detected which allows the PVCF to commence.

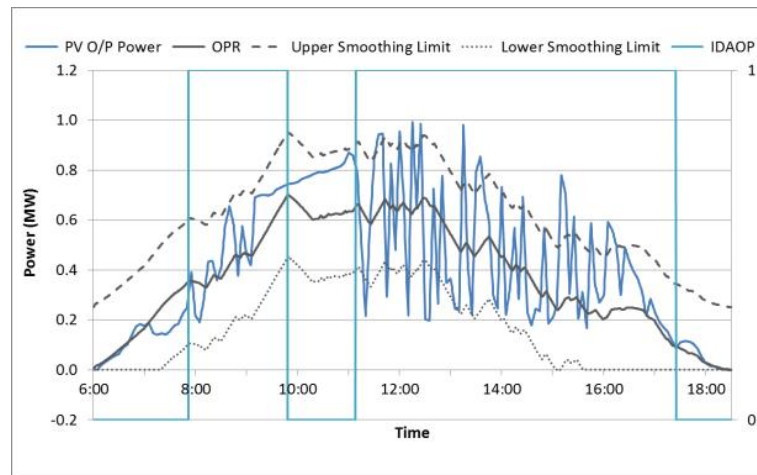
During firming times, the ESS output power is as shown in FIGURE 4.18 (b).

FIGURE 4.18(c) shows the PCC power which is the summation of ESS power and PV station power outputs. The figure shows efficient firming presented in a firmed PCC power output which will contribute to less voltage regulators' tap changes and transients in the feeder. The algorithm was capable of reducing the maximum PV power swing of this day from 800kW to 200kW (maximum power swings are reduced to 33% of previous values).

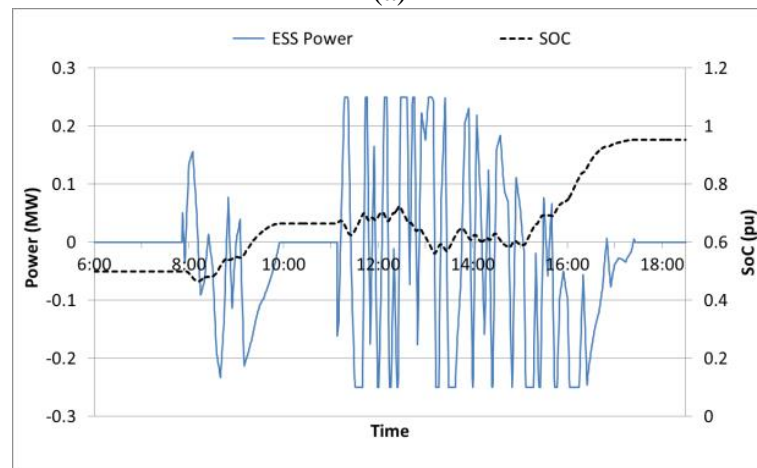
#### 4.3.2. Simulation Results with SoC Constraint

Although FIGURE 4.18 shows plausible firming results, the SoC remaining in the battery at the end of the firming application is 31%. This greatly hinders our ability to utilize the BESMS for any other potential application. For this reason, the maximization of SoC algorithm described is crucial. The results shown in FIGURE 4.18 show the same

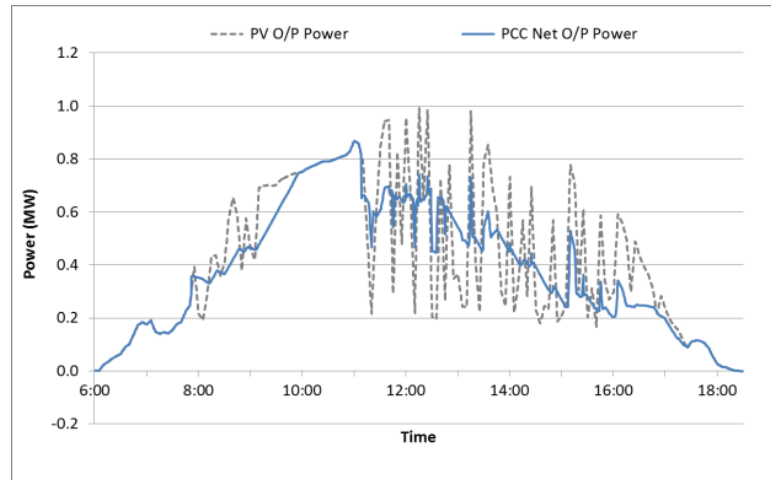
day firming cycle if SoC maximization was considered. As shown in FIGURE 4.19(b), The SoC at the end of the PVCF cycle is 95% which is suitable for the ESS to perform any other application at that time. But this was at the expense of the degree of firming. Nevertheless, firming was still efficient in decreasing the maximum PV power swings from 800kW to 230kW.



(a)



(b)



(c)

FIGURE 4.19: PVCF simulation results with SoC constraint. (a) PV power output compared to OPR. (b) BESS output power with battery SoC plotted on the second y-axis. (c) PCC active power output after PVCF compared to PV power output.

#### 4.4. PVCF Implementation

Field implementation of the designed algorithm was carried out through the communication infrastructure shown in FIGURE 4.20. A Java code is written to analyze streaming data from different points on the feeder and calculate the BESS reference values based on the algorithm discussed. This code resides physically on a computer in a remote lab. Messages are continuously published to the BESS. The time step for receiving and publishing messages is 1.7 seconds.

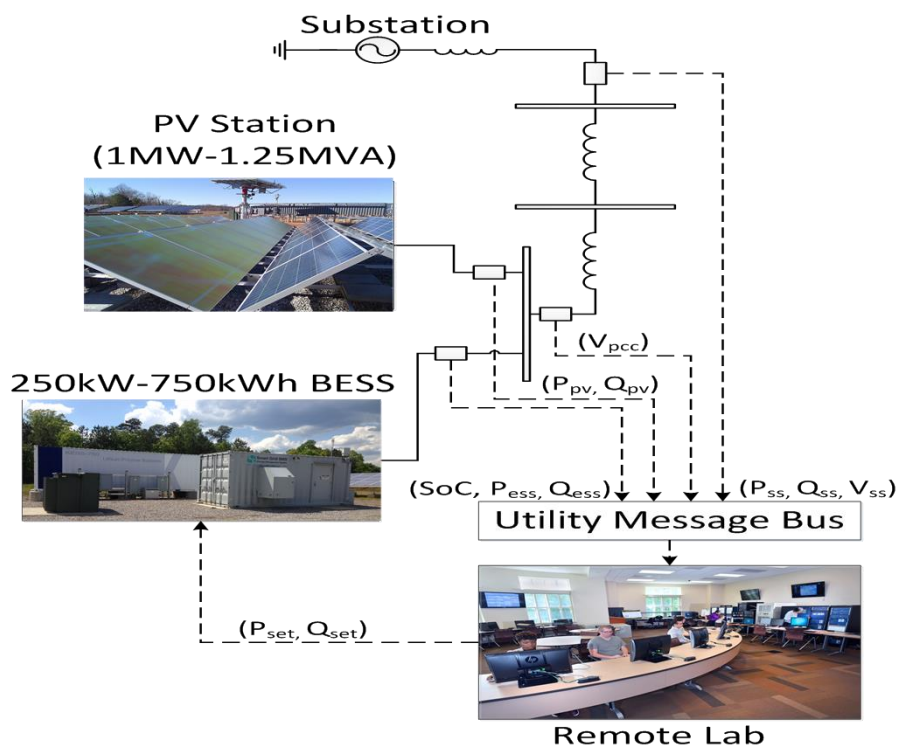


FIGURE 4.20: Field testing communication infrastructure

The following practical results reveal the operational characteristics of the described system after the designed algorithm was allowed to control the described BESMS. The implementation results of PVCF, with and without the SoC constraint are presented hereafter.

## 4.4.1. PVCF Implementation Results without SoC Constraint

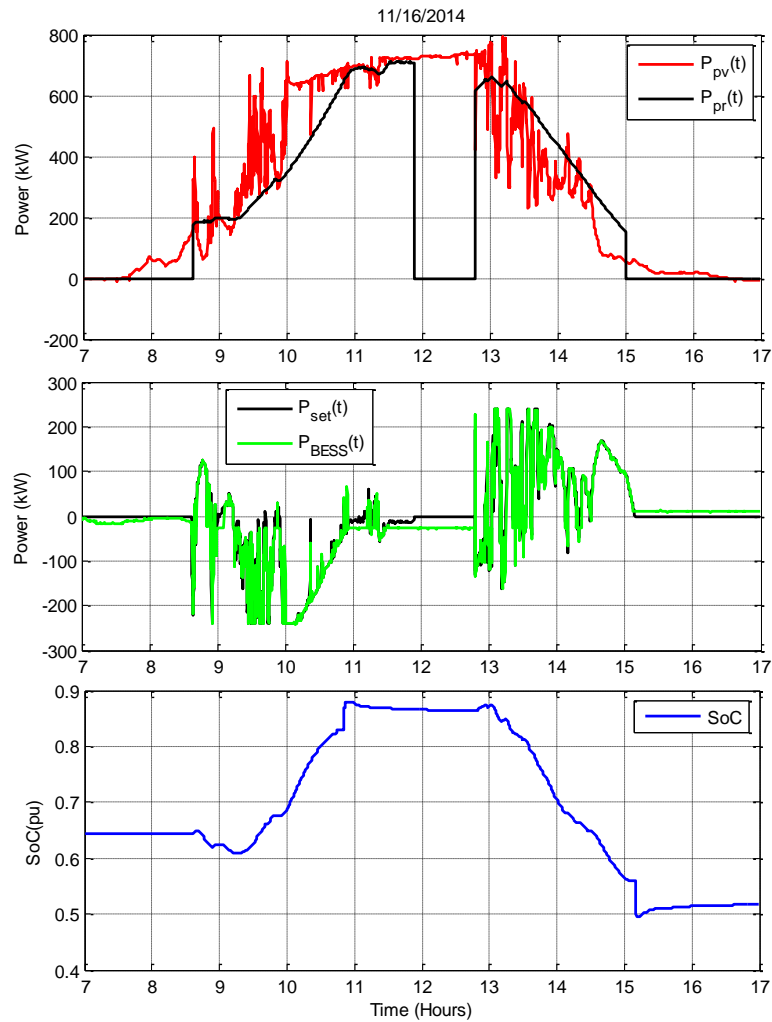


FIGURE 4.21: PV power compared to reference power, algorithm set-point compared to BESS dispatched power and SoC, respectively for November 16<sup>th</sup>, 2014 PVCF

FIGURE 4.21 shows the application of the main PVCF reference power curve (without SoC constraints) to a partially cloudy day. It can be seen that the reference power curve does not vary with the change in real time PV active power output as discussed. Also, it does not change with SoC variation. The reference power is equated to zero when the IDAOP is zero. Further, the algorithm's computed active power set points for the BESS ( $P_{set}(t)$ ) as well as the response of the BESS to such set points for the

operation of the controller on November 16<sup>th</sup>, 2014 are shown. It should be noted that differences between  $P_{set}(t)$  and  $P_{BESS}(t)$  are due to the simultaneous reactive power dispatch of the BESS during PVCF application. Practically, reactive power dispatch offsets active power due to the storage management system controller's non-ideality. Also, shown in FIGURE 4.21 is the variation of the SoC of the battery in response to the shown active power dispatch.

FIGURE 4.22 shows the operation of IDA in response to PV station output power. Further, FIGURE 4.23 shows the firmed PCC power compared to PV station power.

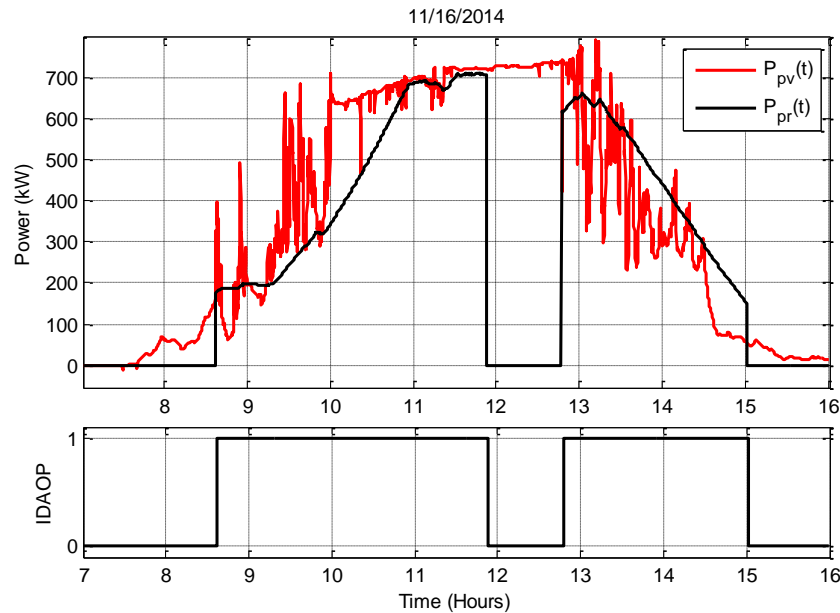


FIGURE 4.22: Intermittency detection algorithm output for November 16<sup>th</sup>, 2014 PVCF

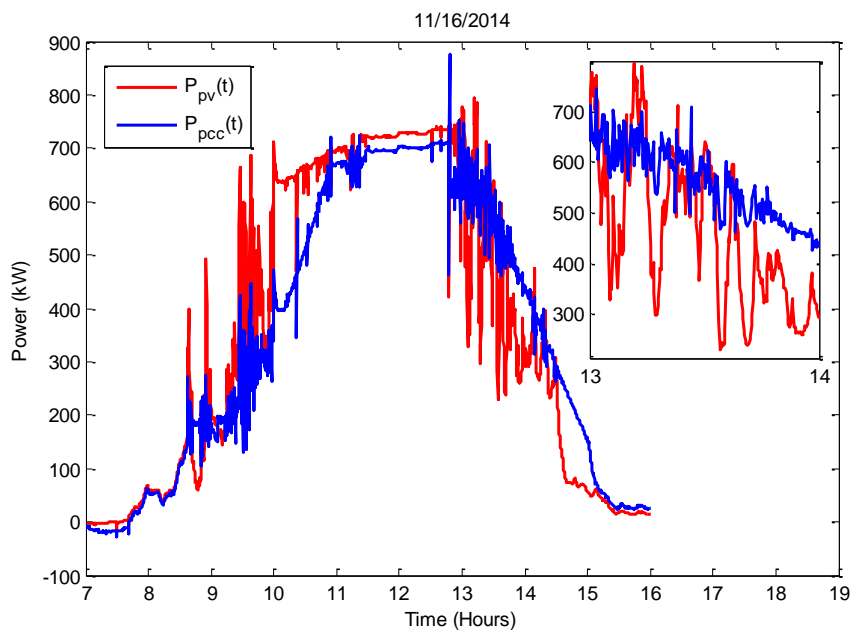


FIGURE 4.23: Result of PCCF application shown in the PCC power compared to that of the PV station for November 16<sup>th</sup>, 2014 PCCF

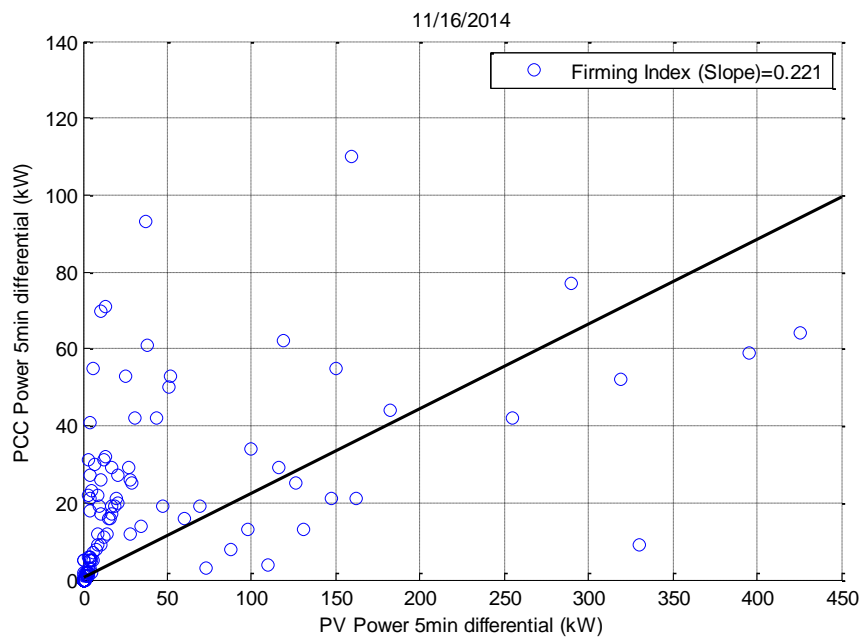


FIGURE 4.24: Firming index for November 16th, 2014 PCCF

In an effort to quantify our algorithm's PVCF efficiency, a similar firming index to that applied in [45] is shown in FIGURE 4.24. This firming index is defined as the slope of the least square line of the PCC power 5-minute differential plotted against that of the PV power. In other words, each point on the plot shown in has an x-axis value equal to the PV power differential over 5 minutes and a y-axis value equal to the PCC power differential over the same period. So, a point at (400, 60) implies that a 5 min power swing of 400 kW out of the PV station was reduced to 60 kW at the PCC, after BESS PVCF algorithm intervention. Now, taking the least square linear regression line's slope over the entire firming period gives an indication of how much firming was performed. Therefore, a unity slope implies no firming. On the other hand, a zero slope implies maximum firming.

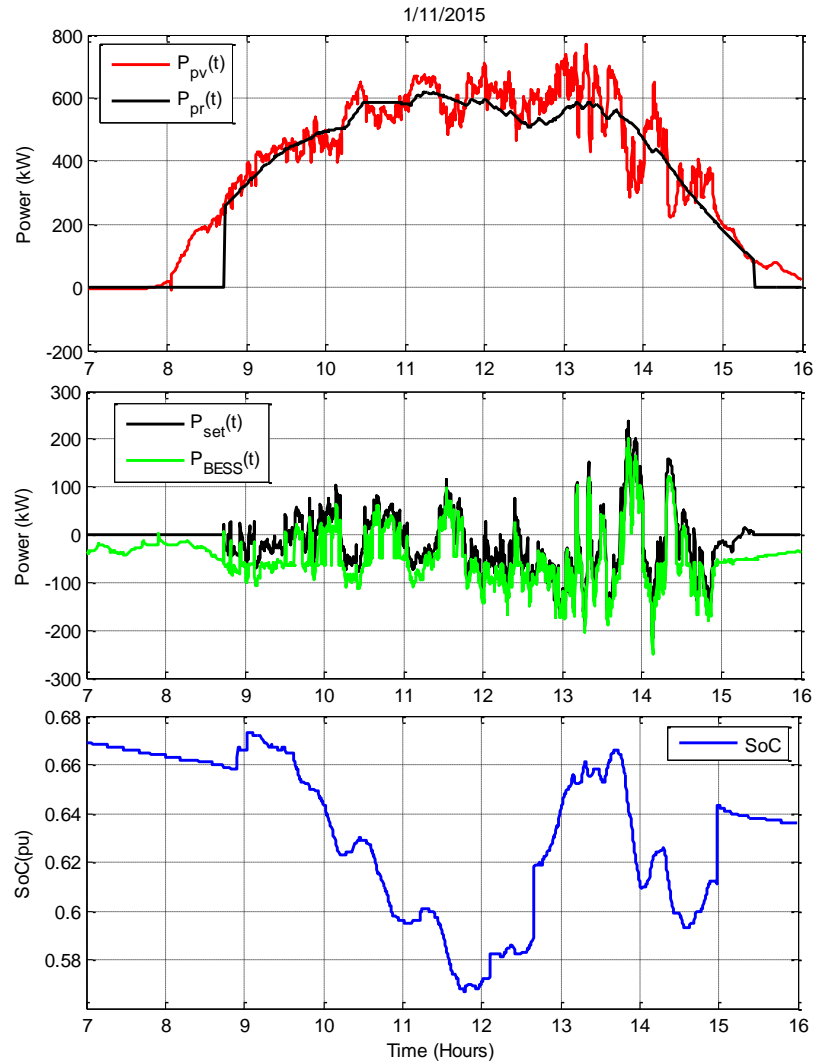


FIGURE 4.25: PV power compared to reference power, algorithm set-point compared to BESS dispatched power and SoC, respectively for January 11<sup>th</sup>, 2015 PVCF

FIGURE 4.25 shows the application of the unconstrained PVCF algorithm to an overcast day. It can be seen that the reference power curve varies with the change in real time PV active power output as discussed. This ensures that the BESS firming region covers most of PV output. Nevertheless, the reference power curve does not change with SoC variation. Also, Here the deviated values of  $P_{BESS}(t)$  from  $P_{set}(t)$  are also apparent since reactive power dispatch was also being simultaneously performed for this test date.

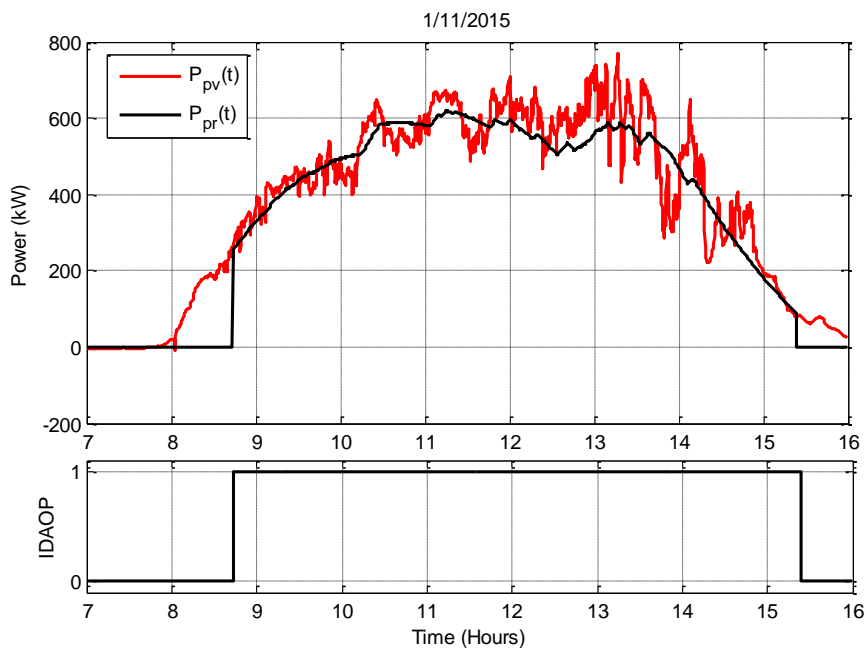


FIGURE 4.26: Intermittency detection algorithm output for January 11<sup>th</sup>, 2015 PVCF

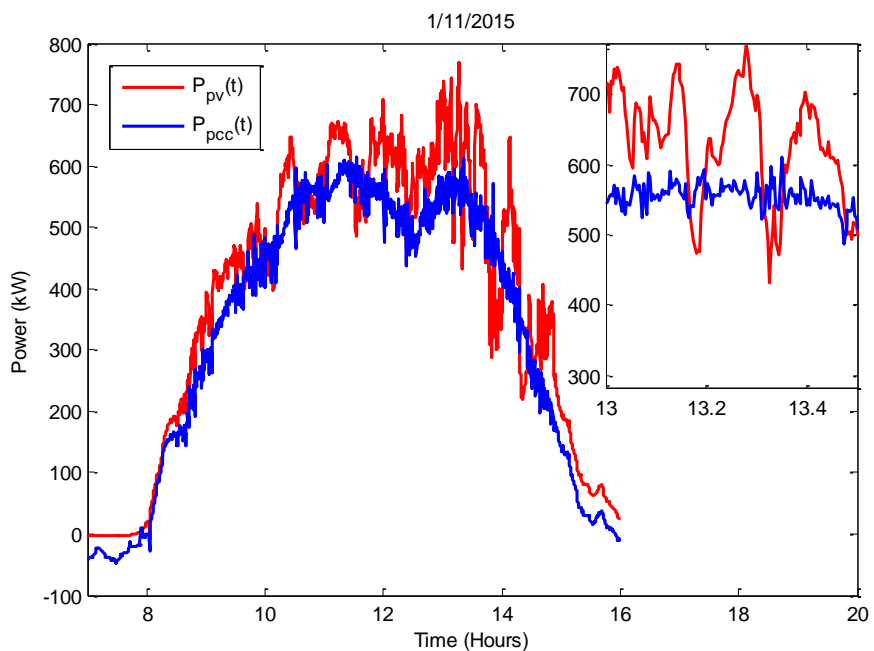


FIGURE 4.27: Result of PVCF application shown in the PCC power compared to that of the PV station for January 11<sup>th</sup>, 2015 PVCF

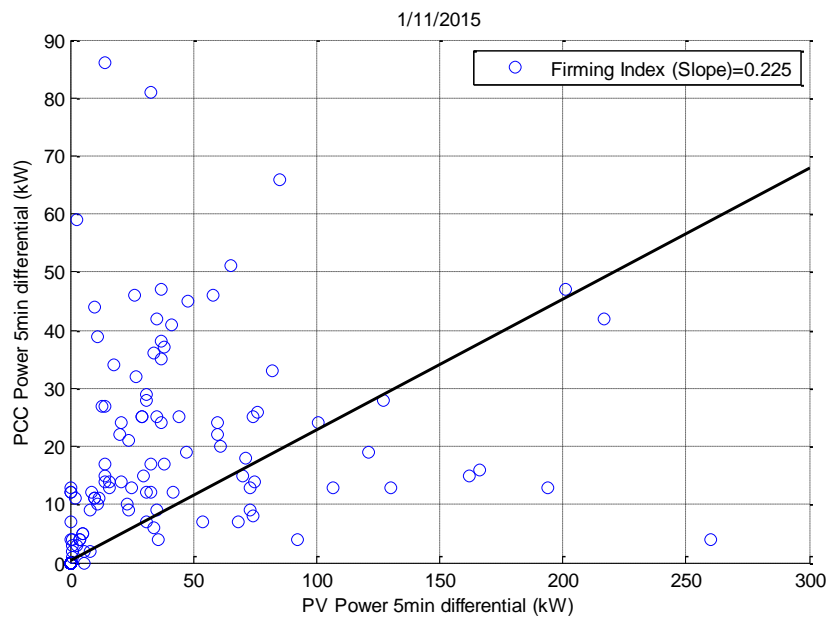


FIGURE 4.28: Firming index for January 11<sup>th</sup>, 2015 PVCF

As shown in FIGURE 4.26, FIGURE 4.27 & FIGURE 4.28, efficient firming was achieved. This is reflected in a firming index of 0.225

## 4.4.2. PVCF Implementation Results with SoC Constraint

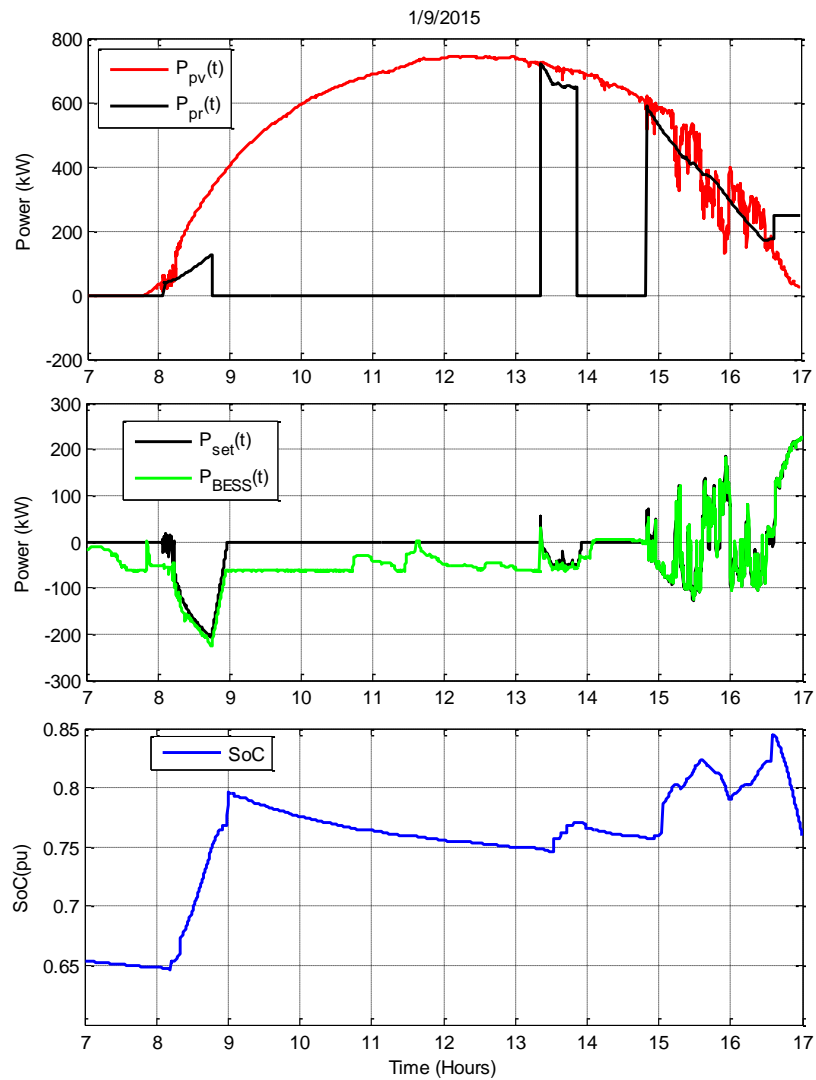


FIGURE 4.29: PV power compared to reference power, algorithm set-point compared to BESS dispatched power and SoC, respectively for January 9<sup>th</sup>, 2015 PVCF

FIGURE 4.29 shows the application of the SoC constrained PVCF algorithm to a clear day. It can be seen that the reference power curve varies according to SoC variation as discussed. Due to the stochastic nature of cloud passing, reaching the targeted SoC is not guaranteed. However, the real time modification of the weighing factor ( $m_e(t)$ ) increases the probability of approaching the targeted SoC at the targeted time. It is also

clear here that the values of  $P_{BESS}(t)$  are slightly deviated from that of  $P_{set}(t)$ . This is also attributed to the simultaneous reactive power dispatch of the SMS during the test time.

FIGURE 4.30 shows the IDAOP throughout the test day. It is clear that there was an instant where IDAOP assumed intermittency when there was no significant power fluctuation. This represents a case where both intermittency detection triggers were fired. After a certain clearing time, the IDAOP was cleared.

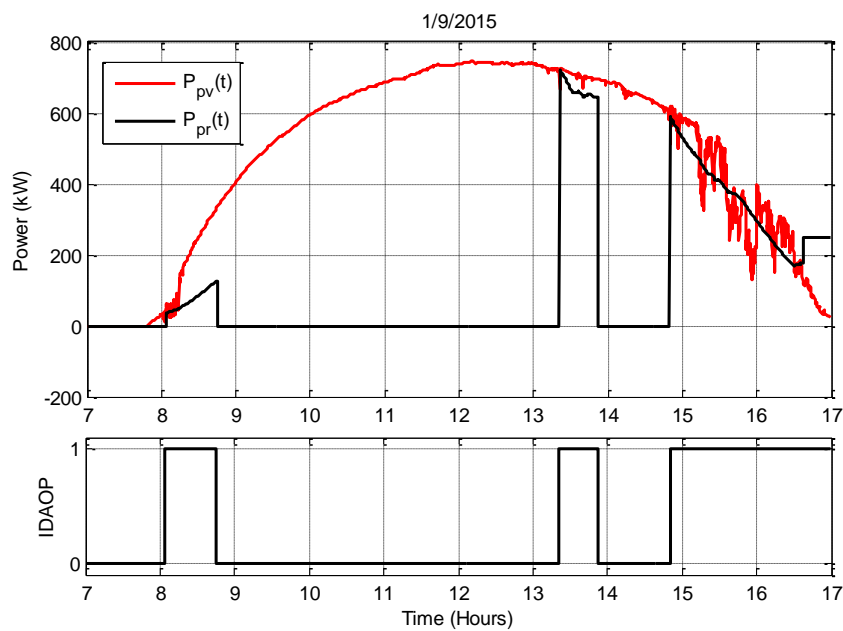


FIGURE 4.30: Intermittency detection algorithm output for January 9<sup>th</sup>, 2015 PVCF

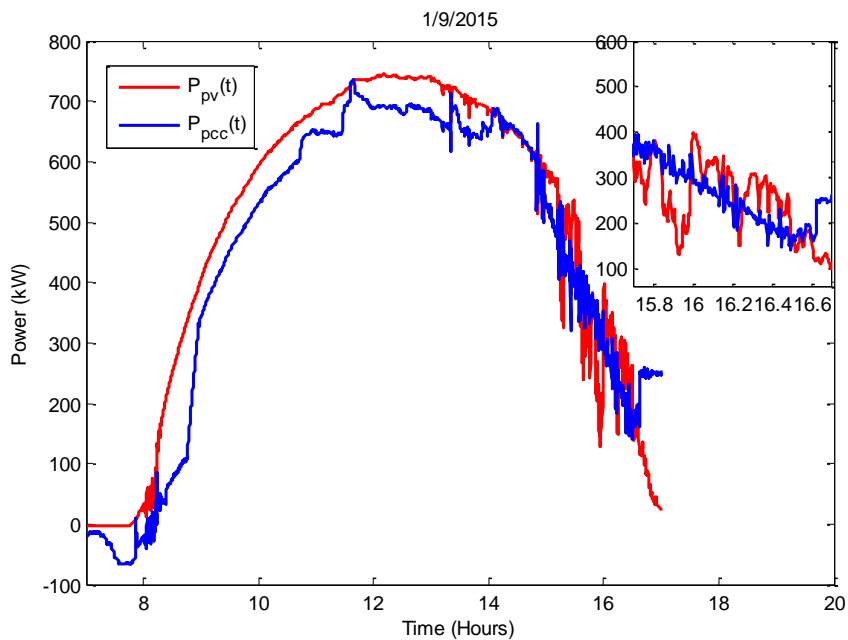


FIGURE 4.31: Result of PVCF application shown in the PCC power compared to that of the PV station for January 9<sup>th</sup>, 2015 PVCF

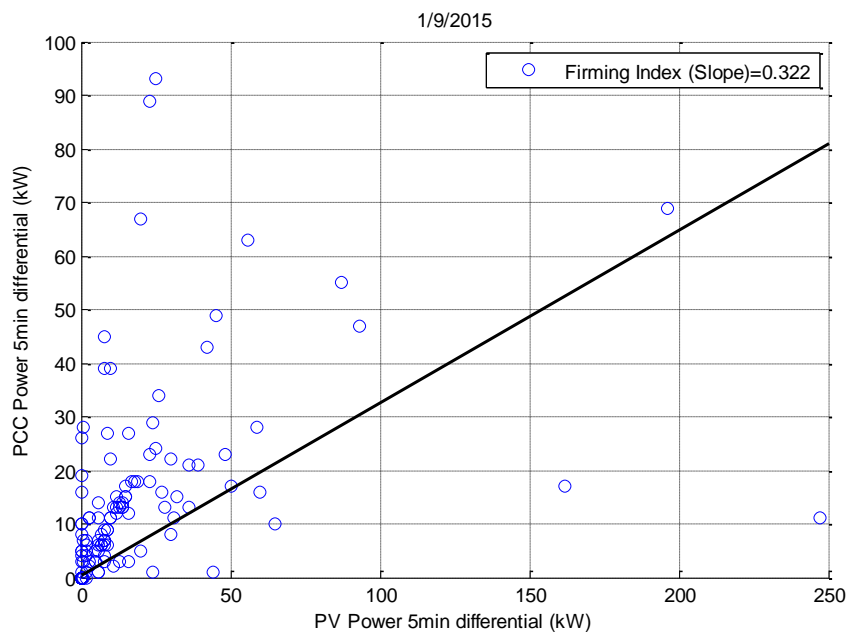


FIGURE 4.32: Firming index for January 9<sup>th</sup>, 2015 PVCF

#### 4.5. Conclusion

In this chapter a new control method for utilizing energy storage systems for PVCF is presented. PVCF using a BESS was found to be effective in firming power swings of double the capacity of the battery used. Consideration of SoC during PVCF application to allow proper coordination with other applications was found to be effective in setting battery SoC to a predetermined value at a predetermined time. In the next chapters we will study the addition of more battery energy storage applications and coordination between such applications and PVCF.

## CHAPTER 5: ENERGY TIME SHIFT APPLICATION

### 5.1. Introduction

In the previous chapters, the practical and model specifications of the BESMS and PV station connected to the same point of common coupling were thoroughly discussed. In this chapter we will study our second energy storage application, namely, Electric Energy Time Shift (ETS). ETS aims to minimize distribution feeder peak loads through utilizing battery energy stored during times of off peak loads. The prediction of feeder peak load value and time represents the most important aspect of ETS storage applications. An innovative prediction algorithm will be designed and tested in this chapter. Practical residential distribution feeder load curves will be used to validate the designed prediction algorithms.

Electric energy time-shift involves acquiring low-cost electric energy, available during minimal distribution feeder load, to charge the energy storage system in order to be able to use the stored energy during times of peak feeder load when price of energy is at its peak.

As stated in [1], “this application tends to involve purchase of inexpensive energy from the *wholesale* electric energy market for storage charging. When the energy is discharged, it could be resold via the wholesale market, or it may offset the need to purchase wholesale energy and/or to generate energy to serve end users’ needs.”

## 5.2. System Setup

The system model is setup as shown in

FIGURE 3.19. The designed aggregated PV station model is connected in conjunction with the BESMS. The load bus is where the total feeder load is assumed to be concentrated. PV station output power ( $P_{pv}$ ) and feeder load ( $P_{load}$ ) values of a 720 node, 12.475kV practical feeder are assumed to design and validate the ETS algorithm.

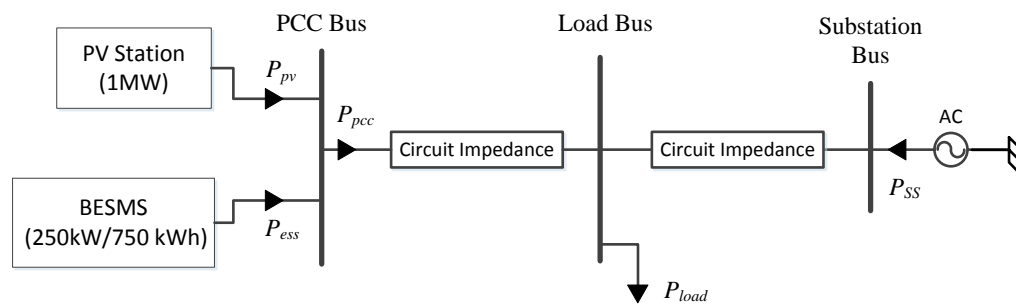


FIGURE 5.1: Distributed generation system setup

The practical feeder mentioned is aggregated into 3 main buses, The Point of Common Coupling bus (PCC), the substation bus and an intermediate load bus. Circuit impedances are the aggregated feeder impedances of the practical feeder studied.

## 5.3. Energy Time Shift Algorithm

The ETS algorithm designed here after aims to achieve the electricity market equivalent of financial arbitrage, a term widely used by utilities and storage system operators for ETS applications. The financial definition of arbitrage is the simultaneous purchase and sale of identical commodities across two or more markets in order to benefit from a discrepancy in their price relationship. In order to achieve this, the following parameters must be involved in the designed algorithm:-

- Prediction Algorithm Parameters:-
  - 1-  $P_{pl}$  :Feeder Peak load
  - 2-  $T_{pl}$  :Time of feeder peak load
  - 3-  $N_{lb}$  : Look back days, number of previous days' data used for prediction
- ESS Power Dispatch Algorithm Parameters:-
  - 1-  $SoC$  : ESS state of charge
  - 2-  $P_{ess}$  : Discharge Power
  - 3-  $T_{dur}$  : Discharge duration
  - 4-  $T_{start}$  : Discharge start time
  - 5- ESS current application running

### 5.3.1. Prediction Algorithm

The main goal of the prediction algorithm is to predict  $P_{pl}$  and  $T_{pl}$  values. This can be accomplished through storing and analyzing load curve data of a number of days ( $N_{lb}$ ) preceding the day for which these values are to be predicted.

#### 5.3.1.1. Weekend / Weekday discrepancy

In this section we define the range and specifics of data that is used for prediction of peak load power and time of peak load power values for a medium voltage distribution feeder aggregated in

FIGURE 3.19. The daily load curve data of three months is available. It is crucial to know the validity of usage of weekends for prediction of weekday's data and vice versa. The following matlab code is written to study visualize as well as calculate average values of weekend and weekday peaks. It is assumed that the day for which the ETS application is to be run is the 28<sup>th</sup> of October 2014.

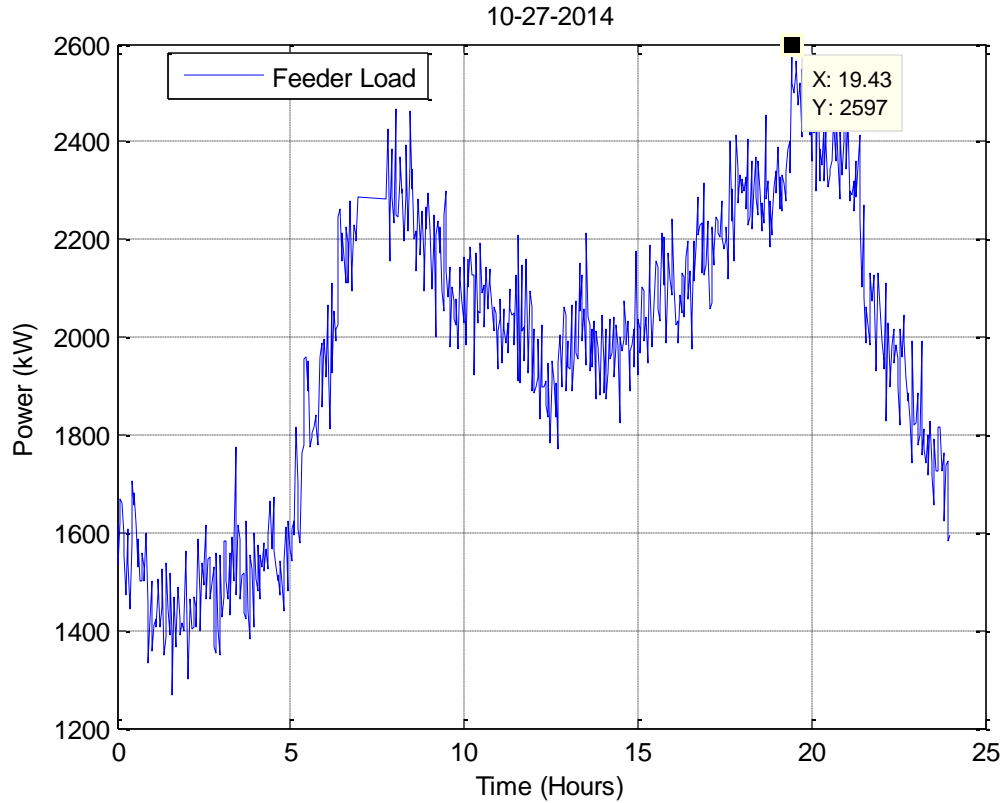


FIGURE 5.2: Feeder load curve of 27<sup>th</sup> of October 2014

We will analyze several days prior to the application run day. These days will be referred to hereafter as look-back days where “look-back day one” implies that said day is the one just prior to the application run day. i.e. the 27<sup>th</sup> of October is the 1<sup>st</sup> look-back day number (1) for the 26<sup>th</sup> of October.

As shown in FIGURE 5.2, the feeder peak load occurs at 7:26 pm and has a value of 2597 kW. Each look back day will be analyzed to attain these two values. The following matlab code is written to accomplish this through accessing historical data previously recorded.

```
clc
clear all
```

```

%% Historical Data Range & Run Day

Nlb=60;           % Number of look back days to be attempted
Sl=50;           % Number of skipped data lines to reduce run time

RunDay=28;
RunMonth=10;
RunYear=2014;

RunDateStr = sprintf('%d-%d-%d', RunMonth, RunDay, RunYear);
disp(RunDateStr)
formatIn = 'mm-dd-yyyy';
RunDayNum=datetime(RunDateStr, formatIn);

fid = fopen( 'APR_5Sep-28Oct.txt' );

while RUN

    Line=fgetl(fid);
    if Line==-1
        str=sprintf('End of File Reached');
        disp(str)
        break
    end

    if (rem(n,Sl)==0)

        cac = textscan( Line, '%s %s %f %f %f %f %f %f %f %f %f %s %f
%f %f %f', 'CollectOutput', true );

        %% Finding
        Date_num = datetime( char(cac{1,1}{1,1}), 'yyyy-mm-dd' );
        Date_Vec = datevec( char(cac{1,1}{1,1}), 'yyyy-mm-dd' );

        Day_Ins= Date_Vec(3);
        Month_Ins= Date_Vec(2);
        Year_Ins= Date_Vec(1);

        Time_num = datetime( char(cac{1,1}{1,2}), 'HH:MM:SS.FFF' );
        Time_Vec = datevec( char(cac{1,1}{1,2}), 'HH:MM:SS.FFF' );

        Second_Ins=Time_Vec(6);
        Minute_Ins=Time_Vec(5);
        Hour_Ins=Time_Vec(4);

```

```

        if Day_Ins==RunDay && Month_Ins==RunMonth &&
Year_Ins==RunYear

            V=1;
            % placing values we may plot in matlab vectors

            Time_Sec_Hd(i)=Second_Ins+60*Minute_Ins+3600*Hour_Ins;
            Time_Hrs(i)=(Second_Ins/3600)+(Minute_Ins/60)+Hour_Ins;
            APR(i)=cac{1,2}(1);
            P_pv(i)=cac{1,2}(2);
            OPR(i)=cac{1,2}(3);
            IDAOP(i)=cac{1,2}(4);

            if Battery_Online==0
                P_ess(i)=APR(i);
            else
                P_ess(i)=cac{1,2}(8);
            end

            SoC(i)=cac{1,2}(7);
            P_ss(i)=cac{1,2}(6);
            P_pcc(i)=P_ess(i)+P_pv(i);
            P_l(i)=cac{1,2}(6)+cac{1,2}(2);

            i=i+1;
        end

        if V==1 && Date_num>RunDayNum
            str=sprintf('Run Day Data Gathered');
            disp(str)
            break
        end

        if Date_num>=(RunDayNum-Nlb) && Date_num < RunDayNum

            LBday=RunDayNum-Date_num;
            if (m==1) P_pl(LBday)=0;end
            P_load=cac{1,2}(6)+cac{1,2}(2);

            if (P_load >P_pl(LBday) &
((Second_Ins+60*Minute_Ins+3600*Hour_Ins)/3600)>12 )

                P_pl(LBday)=P_load;

            T_pl(LBday)=(Second_Ins+60*Minute_Ins+3600*Hour_Ins)/3600;

            end
    
```

```

                                NumLBD(LBday)=Date_num;

                                m=m+1;
                                end

                                end

                                n=n+1;
                                end

```

The following section is to identify weekends, weekdays and missing days within that gathered data:-

```

%% Identifying which days of the look-back days are weekends and
which days are missing

WeekDay=weekday(NumLBD);
P_pl_we(length(NumLBD))=0;
T_pl_we(length(NumLBD))=0;
P_pl_wd(length(NumLBD))=0;
T_pl_wd(length(NumLBD))=0;

for(n=1:length(NumLBD))

    if ((WeekDay(n)==1 || WeekDay(n)==7) && NumLBD(n)~=0 &&
T_pl(n)>12)
        c=c+1;
        P_pl_we(n)=P_pl(n);
        T_pl_we(n)=T_pl(n);
        str=sprintf('Look-back day %d is a weekend',n);
        disp(str)
    end

    if (WeekDay(n)>=2 && WeekDay(n)<=6 && NumLBD(n)~=0 &&
T_pl(n)>12)
        d=d+1;
        P_pl_wd(n)=P_pl(n);
        T_pl_wd(n)=T_pl(n);
    end

    if P_pl(n)<=500
        b=b+1;
        str=sprintf('Look-back day %d data is missing',n);
        disp(str)
    end
end

```

```

end

end

%% Averaging Weekend and weekday values

P_pl_we_avg=sum(P_pl_we)/c;
T_pl_we_avg=sum(T_pl_we)/c;
P_pl_wd_avg=sum(P_pl_wd)/d;
T_pl_wd_avg=sum(T_pl_wd)/d;

str=sprintf('Average Peak Load of Week Days : %d',P_pl_wd_avg);
disp(str)
str=sprintf('Average Time of Peak Load of Week Days :
%d',T_pl_wd_avg);
disp(str)
str=sprintf('Average Peak Load of Week Ends : %d',P_pl_we_avg);
disp(str)
str=sprintf('Average Time of Peak Load of Week Ends :
%d',T_pl_we_avg);
disp(str)

```

The matlab code shown above outputs the following results summary:-

```

Historical Data Summary :-
Look-back day 2 is a weekend
Look-back day 3 is a weekend
Look-back day 4 data is missing
Look-back day 5 data is missing
Look-back day 6 data is missing
Look-back day 7 data is missing
Look-back day 9 is a weekend
Look-back day 10 is a weekend
Look-back day 12 data is missing
Look-back day 16 is a weekend
Look-back day 17 is a weekend
Look-back day 23 data is missing
Look-back day 24 is a weekend
Look-back day 29 data is missing
Look-back day 30 data is missing
Look-back day 31 data is missing
Look-back day 32 data is missing
Look-back day 37 is a weekend
Look-back day 38 is a weekend
Look-back day 44 is a weekend
Look-back day 45 data is missing
Look-back day 51 is a weekend

```

Look-back day 52 is a weekend

Number of Look back days attempted : 60  
 Number of Look back days out of available data range : 7  
 Number of Look back days within data range : 53  
 Number of missing Look back days : 11  
 Number of available Look back days : 42  
 Number of week days in data range : 30  
 Number of week ends in data range : 12

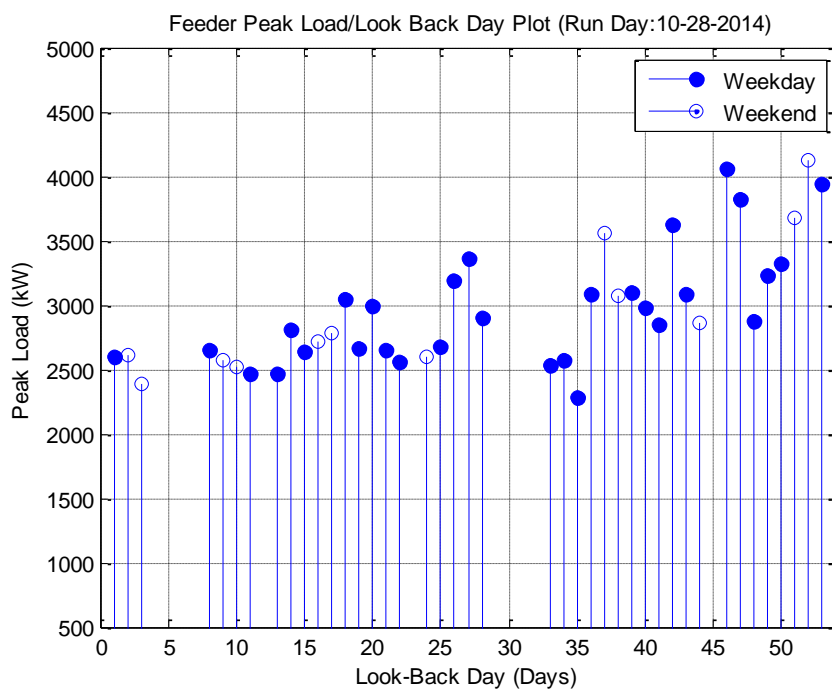


FIGURE 5.3: Feeder peak loads versus look-back days of October 28<sup>th</sup>, 2014

FIGURE 5.3 shows the value of feeder peak load for each look back day. Look back day number 1 represents that of October 27<sup>th</sup>, 2014. It can be noticed that there is no noticeable difference in weekend and weekday values of peak loads. This is also the case for the time of peak loads shown in FIGURE 5.4. Weekend time of peak values blend in unnoticeably with that of week days.

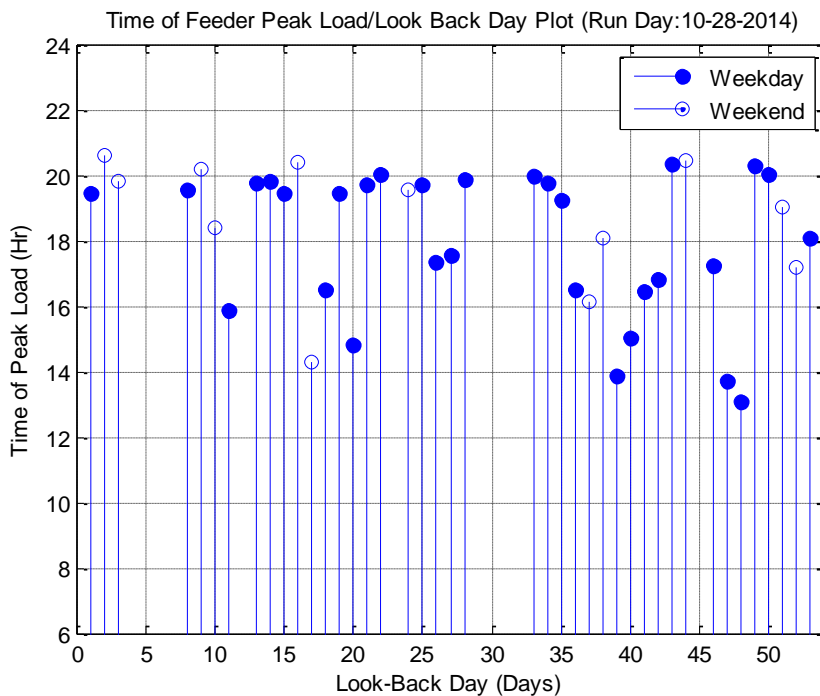
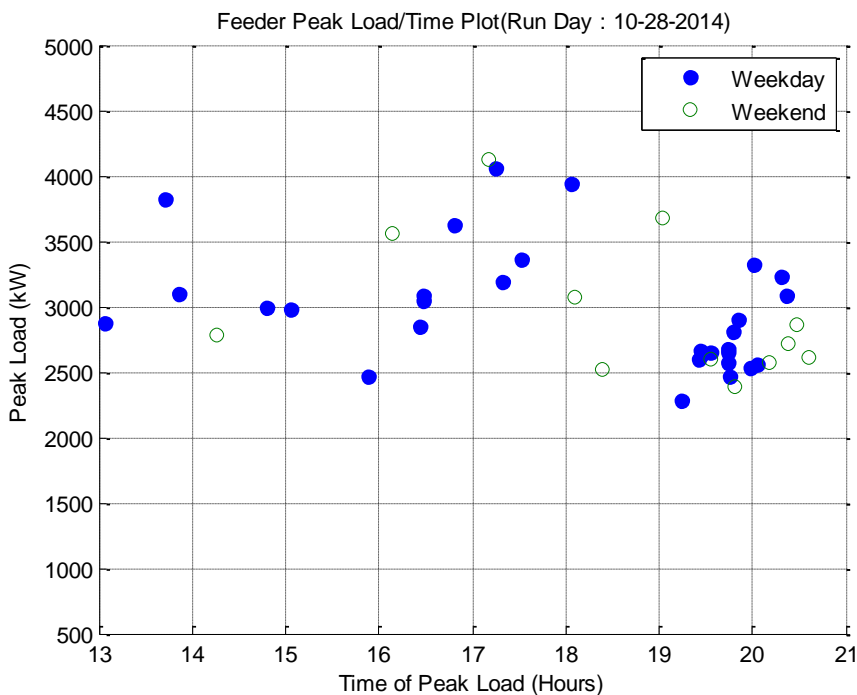


FIGURE 5.4: Time of feeder peak loads plotted against look-back days of October 28<sup>th</sup>, 2014



Averaging the peak feeder load and time of peak feeder load for both weekends and weekdays of the studied data pool gives the following results:-

Average Peak Load of Week Days : 2967.9 kW  
 Average Time of Peak Load of Week Days : 17.97  
 Average Peak Load of Week Ends : 2957.5 kW  
 Average Time of Peak Load of Week Ends : 18.67

The average values shown above imply that average peak feeder load difference between weekends and weekdays is 10.4kW. Further, the difference between average times of peaks of weekdays and that of weekends is 42 minutes.

Conclusively, the differences in averaged values above suggest that weekend and weekdays can be treated as a single data pool to predict application run day values.

#### 5.3.1.2. Averaged Historical Data Prediction Method

For this method, the historical data presented above is used to predict the magnitude and time of feeder peak power per day. Each day's recorded data set is added to the summation of recorded data available and divided by the number of days in said data period.

Equations (5.1) & (5.2) are used to find estimates for peak load magnitude and time, respectively.

$$P_{est}(n + 1) = \frac{\sum_{k=1}^n P_k(t)}{n} \quad (5.1)$$

$$T_{est}(n + 1) = \frac{\sum_{k=1}^n T_k(t)}{n} \quad (5.2)$$

The following matlab code is used:-

```

clc
%% Reversing look back day vectors to attain chronologically ordered
vectors
P=fliplr(P_pl);
T=fliplr(T_pl);
%% Initial Values
Psum=0;
Tsum=0;

%% Peak Load Magnitude & Time Prediction

for n = 1:(length(P_pl)-1)

    Psum=Psum+P(n);
    P_est1(n+1)=Psum/n;

    Tsum=Tsum+T(n);
    T_est1(n+1)=Tsum/n;

end

P_est1(1)=P(1); % Assuming we know the peak power of first day for
Averaged Historical Data Prediction Method
T_est1(1)=T(1); % Assuming we know the peak power time of first day
for Averaged Historical Data Prediction Method

for n=1:(length(P)) % Calculating absolute error for each prediction

    ErrorP_1(n)=abs(P(n)-P_est1(n));
    ErrorT_1(n)=abs(T(n)-T_est1(n));
end

%% Average Daily Prediction Absolute Error
Ep_avg1=sum(ErrorP_1)/length(P);
str=sprintf('Average Daily Peak Load Magnitude Error for Averaged
Historical Data Prediction Method: %d',Ep_avg1);
disp(str)

Et_avg1=sum(ErrorT_1)/length(P);
str=sprintf('Average Daily Peak Load Time Error for Averaged
Historical Data Prediction Method: %d',Et_avg1);
disp(str)

%% Average Daily Prediction Percentage Error
ep_avg1=sum(e_P_1)/length(P);
str=sprintf('Average Percent Magnitude Error for Averaged Historical
Data Prediction Method: %d %',ep_avg1);
disp(str)
et_avg1=sum(e_T_1)/length(P);

```

```

str=sprintf('Average Percent Time Error for Averaged Historical Data
Prediction Method: %d %',et_avg1);
disp(str)
et_avg2=sum(e_T_2)/length(P);

figure (11)
clf
plot(1:length(P),P,'-b')
hold on
plot(1:length(P), P_est1, '-g.',1:length(P), Error_1,'r')
grid on
xlabel('(Days)')
ylabel('Daily Peak Power Magnitude (kW)')
title('Averaged Historical Data Prediction Method');
legend('Actual Value','Predicted Value','Absolute Error')

figure (13)
clf
plot(1:length(T),T,'-b')
hold on
plot(1:length(T), T_est1, '-g.',1:length(T), ErrorT_1,'r')
grid on
xlabel('(Days)')
ylabel('Daily Peak Power Time (Hr)')
title('Averaged Historical Data Prediction Method');
legend('Actual Value','Predicted Value','Absolute Error')

```

This code gives the following results:-

```

Average Daily Peak Load Magnitude Error for Averaged Historical Data
Prediction Method: 366.4 (kW)

Average Daily Peak Load Time Error for Averaged Historical Data
Prediction Method: 1.59 (Hr)

Average Percent Magnitude Error for Averaged Historical Data
Prediction Method: 13.11 %

Average Percent Time Error for Averaged Historical Data Prediction
Method: 9.20 %

```

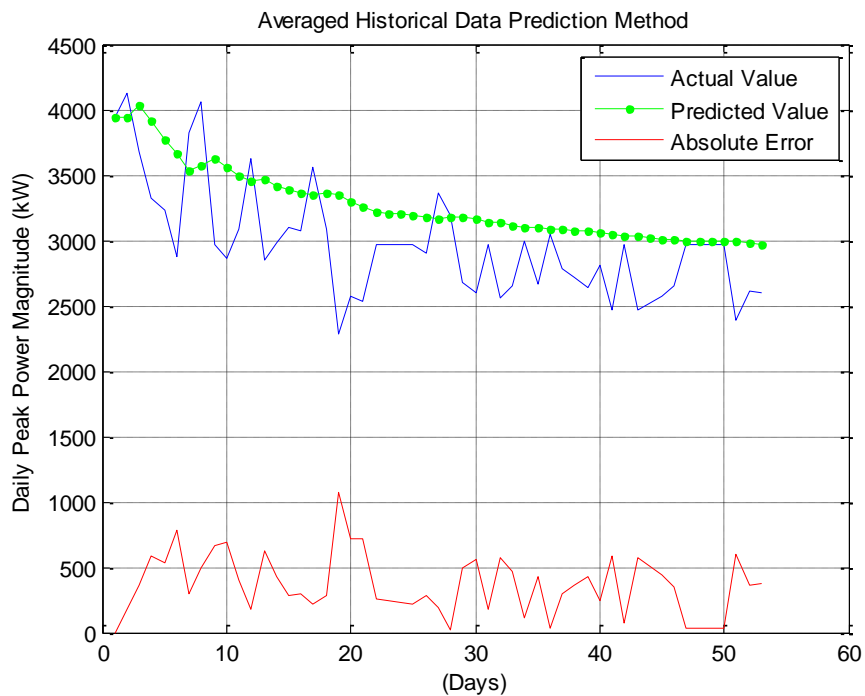


FIGURE 5.6: Daily peak load magnitude prediction using averaged historical data method

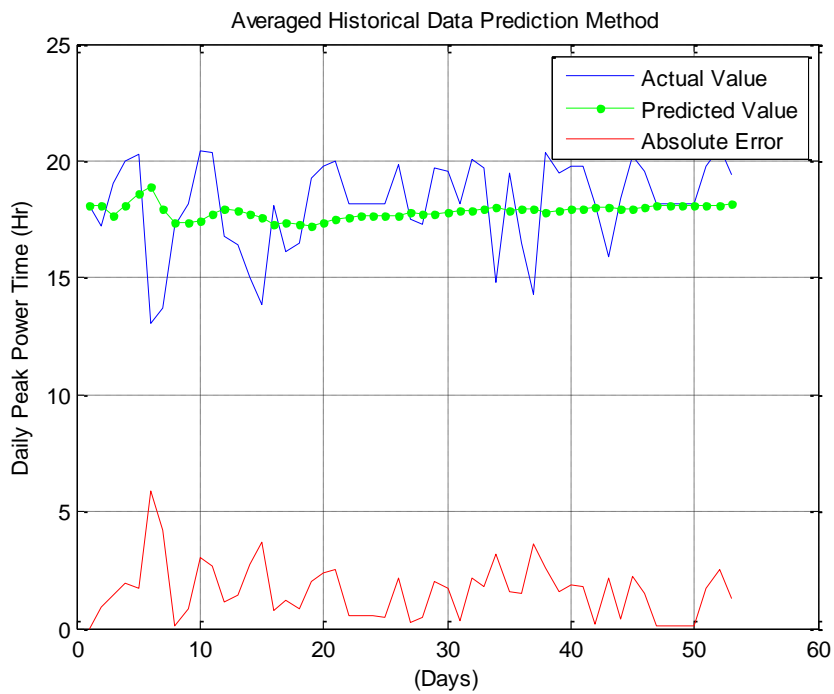


FIGURE 5.7: Daily peak load time prediction using averaged historical data method

As shown in FIGURE 5.6, the error in prediction for some days is relatively high. This is can be attributed to the fact that the impact of the first look back day on the prediction value is equal to that of the last one. However, the error in peak load time prediction shown in FIGURE 5.7 is relatively smaller than that of peak power magnitude. As shown in the matlab code output above, the average percentage error in time prediction for the studied data pool is 9.2 % where that of magnitude prediction is 13.11%. It is also clear in FIGURE 5.8 that time error are generally less than magnitude errors. This leads us to utilize a moving average prediction method and study the optimal time interval required to attain the least error for peak load magnitude and time individually.

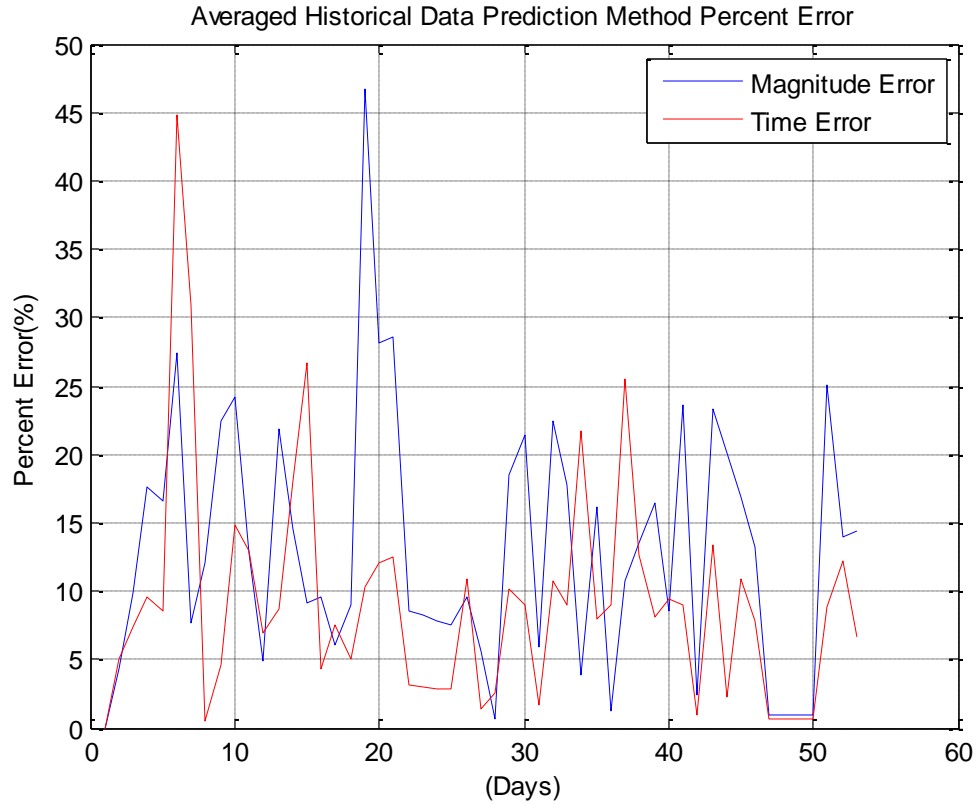


FIGURE 5.8: Averaged historical data prediction method percent errors

### 5.3.1.3. Moving Average Prediction Method

The moving average prediction method is governed by equations (5.3) & (5.4) are used to find estimates for peak load magnitude and time, respectively.

$$P_{est}(n+1) = \frac{\sum_{k=n-M+1}^n P_k(t)}{M} \quad (5.3)$$

$$T_{est}(n+1) = \frac{\sum_{k=n-M+1}^n T_k(t)}{M} \quad (5.4)$$

Where  $n$  and  $M$  represent the day number and the moving average interval, respectively. It is essential to specify the optimal value of the moving average interval ( $M$ ) to be used for each quantity individually.

We will initially assume a moving average interval ( $M=5$ ). The following matlab code is used to plot prediction and actual values:-

```

clc
%% Reversing look back day vectors to attain chronologically ordered
vectors
P=fliplr(P_pl);
T=fliplr(T_pl);

%% Peak Load Magnitude & Time Prediction

M=5; % Moving Average Interval

for n = 1:(length(P_pl)-1)

    Psum2(n)=0;
    Tsum2(n)=0;

    for k=n:-1:(n-M+1)
        if (k<=0) k=1; end
        Psum2(n)=Psum2(n)+P(k);
        Tsum2(n)=Tsum2(n)+T(k);
    end
    P_est2(n+1)=Psum2(n)/M;
    T_est2(n+1)=Tsum2(n)/M;
end

P_est2(1)=P(1); % Assuming we know the peak power of first day Moving
Average Prediction Method
T_est2(1)=T(1); % Assuming we know the peak power time of first day
Moving Average Prediction Method

for n=1:(length(P)) % Prediction Error

    ErrorP_2(n)=abs(P(n)-P_est2(n));
    ErrorT_2(n)=abs(T(n)-T_est2(n));

    e_P_2(n)=100*abs(P(n)-P_est2(n))/P(n);
    e_T_2(n)=100*abs(T(n)-T_est2(n))/T(n);
end

```

```

%% Average Daily Prediction Absolute Error

Ep_avg2=sum(ErrorP_2)/length(P);
str=sprintf('Average Daily Peak Load Magnitude Error for Moving
Average Method (M=%d): %d',M,Ep_avg2);
disp(str)

Et_avg2=sum(ErrorT_2)/length(P);
str=sprintf('Average Daily Peak Load Time Error for Moving Average
Method (M=%d): %d',M,Et_avg2);
disp(str)

%% Average Daily Prediction Percentage Error

ep_avg2=sum(e_P_2)/length(P);
str=sprintf('Average Percent Magnitude Error for Moving Average Method
(M=%d): %d %',M,ep_avg2);
disp(str)

et_avg2=sum(e_T_2)/length(T);
str=sprintf('Average Percent Time Error for Moving Average Method
(M=%d): %d %',M,et_avg2);
disp(str)

%% Plots

figure (11)
clf
plot(1:length(P),P,'-b')
hold on
plot(1:length(P), P_est2, '-g.',1:length(P), Error_2,'r')
grid on
xlabel('(Days)')
ylabel('Daily Peak Power Magnitude (kW)')
str=sprintf('Moving Average Peak Power Prediction Method (M=%d)',M);
title(str);
legend('Actual Value','Predicted Value','Absolute Error')

figure (12)
clf
plot(1:length(T),T,'-b')
hold on
plot(1:length(T), T_est2, '-g.',1:length(T), ErrorT_2,'r')
grid on
xlabel('(Days)')
ylabel('Daily Peak Power Time (Hr)')
str=sprintf('Moving Average Peak Power Time Prediction Method
(M=%d)',M);
title(str);
legend('Actual Value','Predicted Value','Absolute Error')

```

```
figure (13)
clf
plot(1:length(P), e_P_2, 'b',1:length(T), e_T_2,'r')
grid on
xlabel('(Days)')
ylabel('Percent Error(%)')
str=sprintf('Averaged Historical Data Prediction Method Percent
Error');
title(str);
legend('Magnitude Error','Time Error')
```

This code outputs the following:-

Average Daily Peak Load Magnitude Error for Moving Average Method (M=5):  
280.64

Average Daily Peak Load Time Error for Moving Average Method (M=5): 1.72 (Hr)

Average Percent Magnitude Error for Moving Average Method (M=5): 9.69 %

Average Percent Time Error for Moving Average Method (M=5): 10 %

As shown in the matlab code output above, the average magnitude error of the moving average method is 9.69% whereas that of the averaged historical prediction method is 13.11%. Nevertheless, the average time error of the moving average method is 10% whereas that of the averaged historical prediction method is 9.2%.

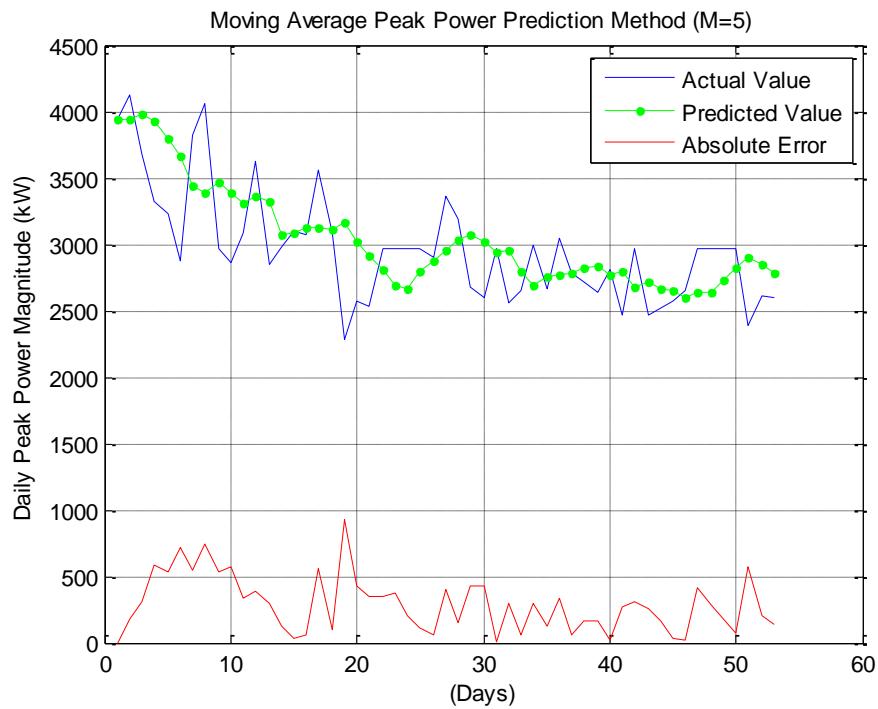


FIGURE 5.9: Daily peak load magnitude prediction using moving average method

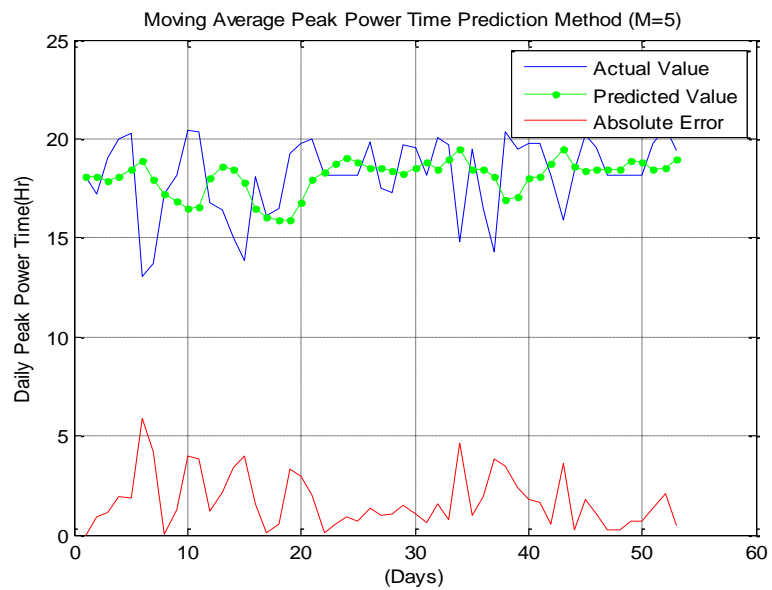


FIGURE 5.10: Daily peak load time prediction using moving average method

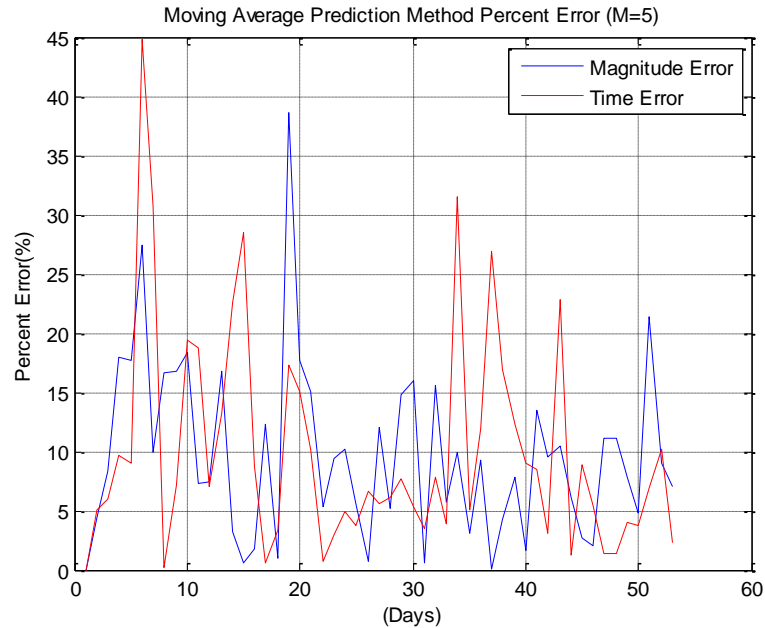


FIGURE 5.11: Moving average prediction method percent errors

It is now crucial to identify the optimal moving average time interval for the most accurate peak load magnitude and time prediction. The following matlab code is used:-

```

clc
%% Reversing look back day vectors to attain chronologically ordered
vectors
P=fliplr(P_pl);
T=fliplr(T_pl);

%% Initial Values
Emin_P=100;
Emin_T=100;

%% Peak Load Magnitude & Time Prediction

for M=1:(length(P_pl)) % Testing Moving Average Interval Values from 1
to the total number of available days

    for n = 1:(length(P_pl)-1)

        Psum2(n)=0;
        Tsum2(n)=0;

        for k=n:-1:(n-M+1)
            if (k<=0) k=1; end

```

```

        Psum2(n)=Psum2(n)+P(k);
        Tsum2(n)=Tsum2(n)+T(k);
    end
    P_est2(n+1)=Psum2(n)/M;
    T_est2(n+1)=Tsum2(n)/M;
end

P_est2(1)=P(1); % Assuming we know the peak power of first day
Moving Average Prediction Method
T_est2(1)=T(1); % Assuming we know the peak power time of first
day Moving Average Prediction Method

for n=1:(length(P)) % Prediction Error

    ErrorP_2(n)=abs(P(n)-P_est2(n));
    ErrorT_2(n)=abs(T(n)-T_est2(n));

    e_P_2(n)=100*abs(P(n)-P_est2(n))/P(n);
    e_T_2(n)=100*abs(T(n)-T_est2(n))/T(n);
end

%% Average Daily Prediction Percentage Error

ep_avg2(M)=sum(e_P_2)/length(P);
str=sprintf('Average Percent Magnitude Error for Moving Average
Method (M=%d): %d %',M,ep_avg2);
disp(str)

et_avg2(M)=sum(e_T_2)/length(T);
str=sprintf('Average Percent Time Error for Moving Average Method
(M=%d): %d %',M,et_avg2);
disp(str)

if (ep_avg2(M)<Emin_P) Emin_P=ep_avg2(M); M_minP=M; end
if (et_avg2(M)<Emin_T) Emin_T=et_avg2(M); M_minT=M; end

end

M_minP
Emin_P

M_minT
Emin_T

%% Plots
figure (14)
clf
plot(1:length(P), ep_avg2, 'b*',1:length(P), et_avg2, 'g.')
grid on
xlabel('Moving Average Interval (M)')
ylabel('Percent Error(%)')

```

```
str=sprintf('Average Daily Prediction Percent Error - Moving Average  
Interval Plot');  
title(str);  
legend('Average Magnitude Error',' Average Time Error')
```

This matlab code outputs the following:-

```
M_minP = 1 (Moving Average interval for minimum magnitude prediction  
error)  
  
Emin_P = 9.4157% (Average daily magnitude Prediction error using  
optimal moving average time interval)  
  
M_minT = 14 (Moving Average interval for minimum time prediction  
error)  
  
Emin_T = 8.8262% (Average daily time Prediction error using optimal  
moving average time interval)
```

According to the results shown above, the minimum average daily peak load magnitude prediction error is attained by utilizing a moving average interval of 1 day. Whereas the minimum average daily peak load time prediction error is attained by utilizing a moving average interval of 14 days.

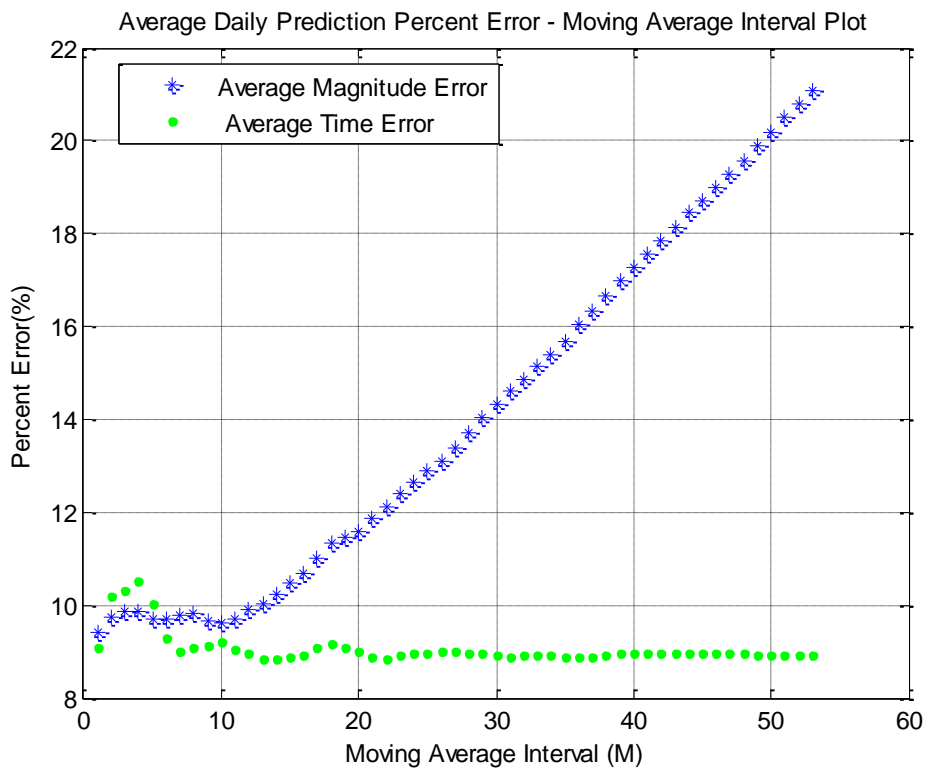


FIGURE 5.12: Average daily prediction percent error plotted versus the moving average time interval used

The results shown in FIGURE 5.12 reveal a very interesting trait about residential feeders' peak load magnitude and time prediction. It is clear that peak load magnitude prediction error almost linearly increases with the increase of moving average time interval beyond a certain threshold. In this case, the threshold is 10 days. It is also clear that the peak load time prediction error is vaguely affected by increase in moving average time interval. Nevertheless, in this case, the minimum error was achieved with a moving average time interval of 14 days.

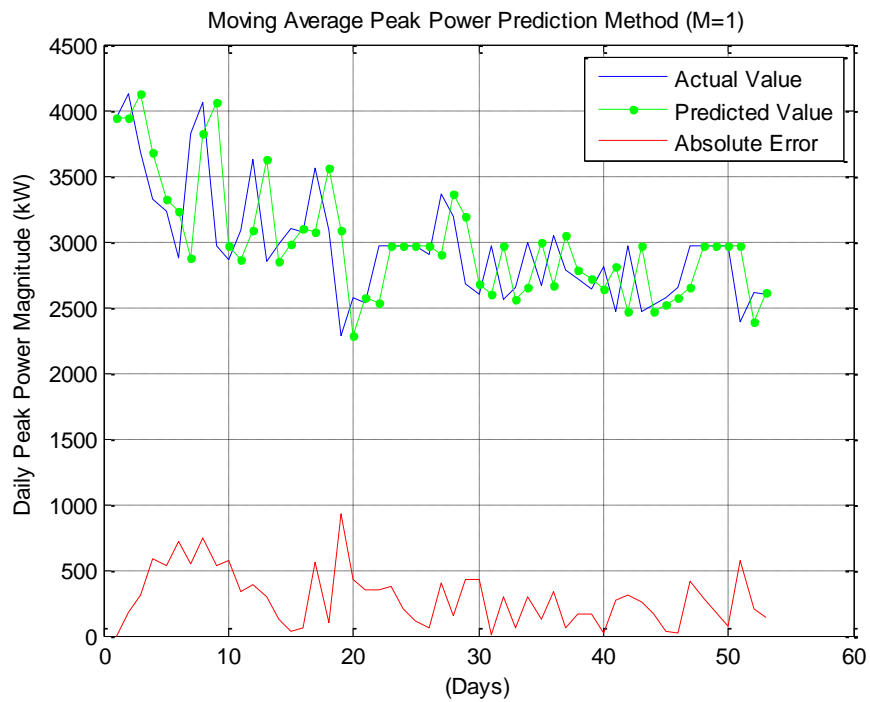


FIGURE 5.13: Moving average peak power magnitude prediction for M=1

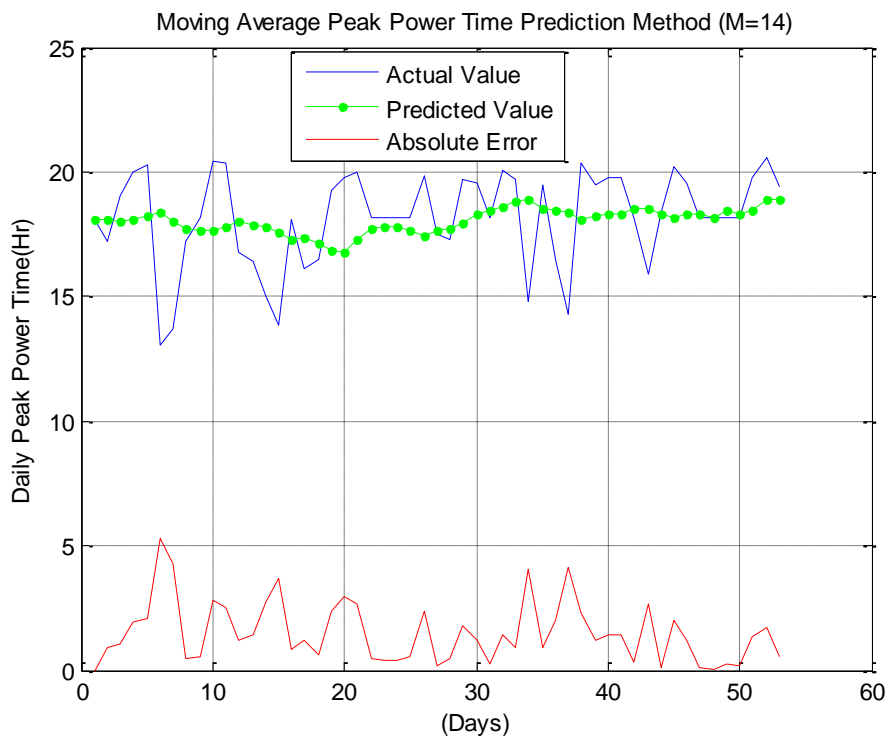


FIGURE 5.14: Moving average peak power time prediction for M=14

FIGURE 5.13 and FIGURE 5.14 show the results of utilizing a moving average interval of 1 and 14 for peak load magnitude and time prediction, respectively.

Conclusively, the ETS battery storage algorithm will use a moving average feeder peak load prediction algorithm with look back days intervals of 1 and 14 for peak load magnitude and time prediction respectively.

### 5.3.2. ESS Power Dispatch Algorithm

Studying the load curves of a practical feeder over several single week intervals time periods, it was found that the time difference between load peak maximums of two consecutive days was less than 40 minutes, whereas the maximum difference throughout the week was found to be 50 minutes as shown in FIGURE 5.15

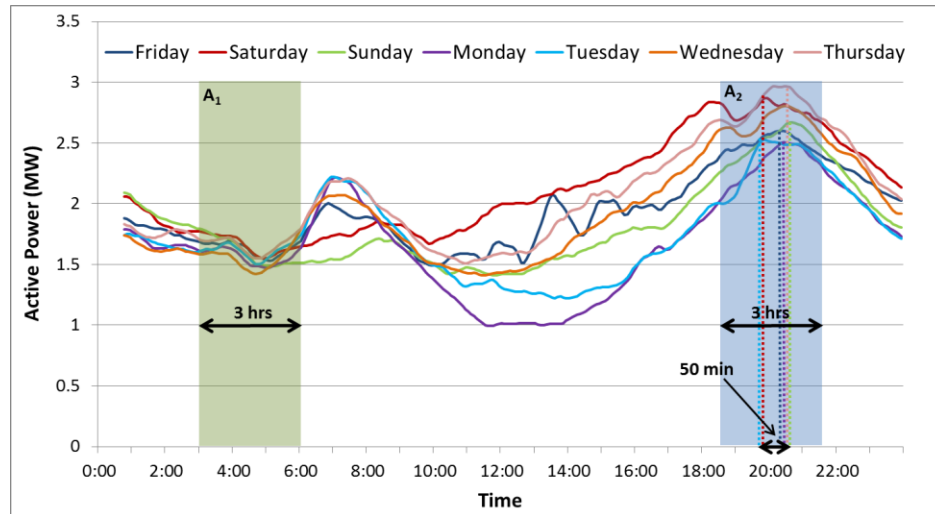


FIGURE 5.15 Load curves of a practical feeder in a residential area for the week of September 21<sup>st</sup>, 2012

Utilizing the prediction algorithm explained in the previous section, the ETS storage application is set to start discharge at a certain time ( $T_{Dstart}$ ) which is constrained by the concurrent ESS SoC, estimated time of feeder peak load ( $T_{est}$ ), ESS ETS discharge power ( $P_{ess}$ ) and desired ETS discharge duration ( $T_{dur}$ ). Let us assume that the battery is fully charged at the time of ETS discharge period (SoC=100%) and will perform ETS at maximum BESMS capacity (250kW). These assumptions set the total discharge duration to three hours. This covers the average peak load time prediction error calculated above (1.72 Hrs). Also, since load curves of most days show minimal load at 4:30am, the ETS algorithm is set to start charging the battery at 3 am to avoid the local maximum that occurs at 7:00am.

As shown in equation (5.5), the algorithm checks the battery state of charge (SoC) and calculates the time of day to commence battery discharge such that the predicted load curve peak lies in the middle of the discharge time interval.

$$T_{start} = T_{est} - \frac{(SoC) \times E_{cap}}{2 \times P_{ess}} \quad (5.5)$$

#### 5.4. ETS application Simulation Results

##### 5.4.1. Standalone ETS Application Simulation Results

The EMTP software was used to simulate the ETS algorithm for Tuesday of the mentioned week in FIGURE 5.15. the test feeder model shown in

FIGURE 3.19 was used to test the ETS algorithm. This test feeder represents the aggregated model of the feeder from which the load curves were recorded. As shown in FIGURE 5.16, the time of discharge start was calculated based on the predicted peak load time which is based on a 14 day interval moving average algorithm. It shows that the algorithm was successful in decreasing the peak load of Tuesday, September 21<sup>st</sup>.

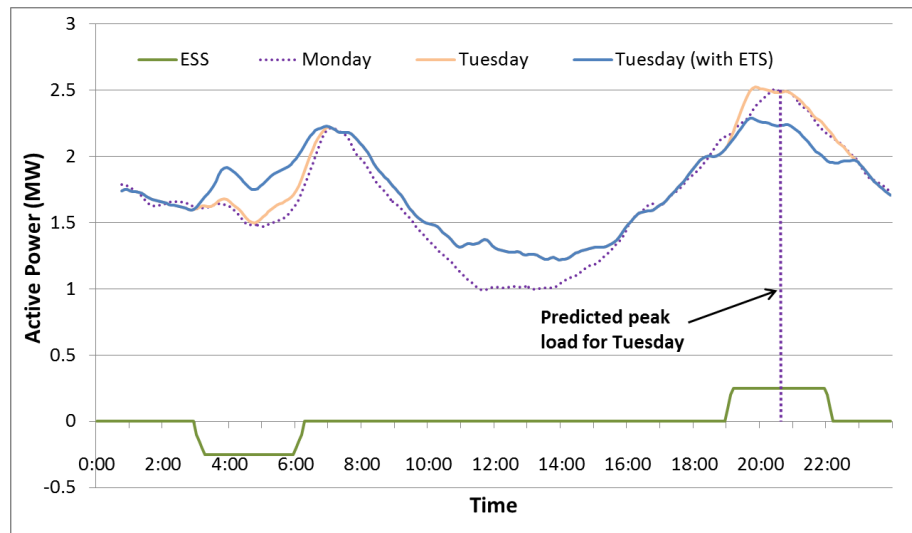


FIGURE 5.16: Energy time shift algorithm results for a residential feeder on Tuesday of the week of September 21<sup>st</sup>, 2012

#### 5.4.2. ETS Application Synergy with PVCF Application

As shown in FIGURE 5.27, after the conclusion of the PVCF application, the remaining energy in the battery (31% SoC) was not sufficient to perform the efficient energy time shifting. At the predicted feeder load maximum, the battery could only discharge for approximately 1 hour. This time could have been increased if optimized firming was performed.

#### 5.5. Combined ETS & PVCF (SoC Constrained) Implementation Results

The implementation results for combined PVCF and ETS is presented hereafter for three summer days. The practical operation of the devised algorithm is presented by showing four main figures. The first figure shows firming reference real time variation and associated parameters, namely, SoC and PV power output. The second figure presents operation of the intermittency detection algorithm. The third figure presents a firming index purposed to quantify the degree of firming performed is presented. Finally, the feeder load compared to the substation generation is presented to signify the effect of the ETS application in shaving feeder peak load. The percentage reduction in feeder peak load is calculated and shown within the figures.

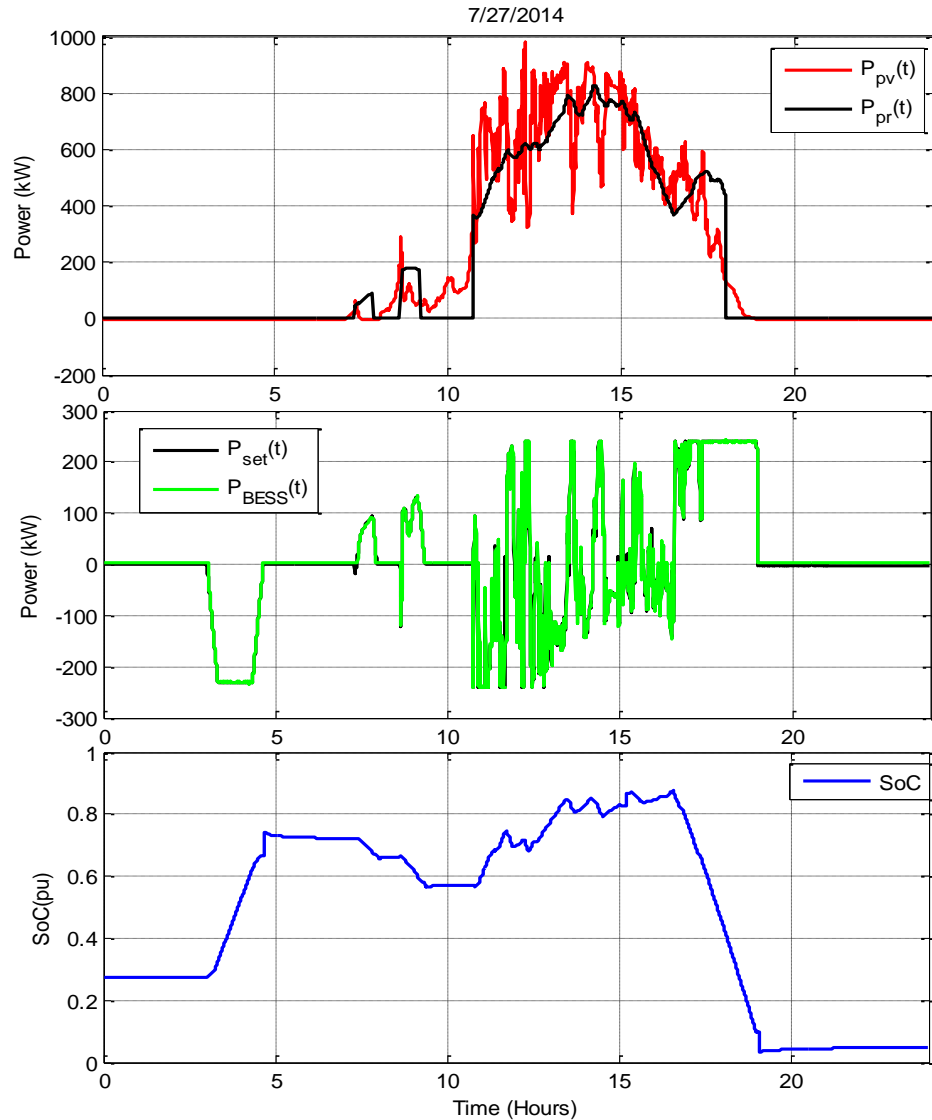


FIGURE 5.17: PV power compared to reference power, algorithm set-point compared to actual BESS dispatched power and SoC, respectively for July 27<sup>th</sup>, 2014 PVCF & ETS

FIGURE 5.17, FIGURE 5.21 and FIGURE 5.24 present in their first plot, the active PV power output for July 27<sup>th</sup>, July 29<sup>th</sup> and August 5<sup>th</sup>, respectively. Algorithm active power output set points ( $P_{set}(t)$ ) as well as actual BESS output is shown in the figure's second plot. Whereas the third plot illustrates the corresponding SoC variation. As presented in said figures, online calculation of  $P_{pr}(t)$  is governed by the current state

of charge, the time of predicted maximum feeder load and the PV power output to  $P_{scmp}(t)$  ratio.

FIGURE 5.18 shows the operation of intermittency detection algorithm in real time in response to real time PV output power variation.

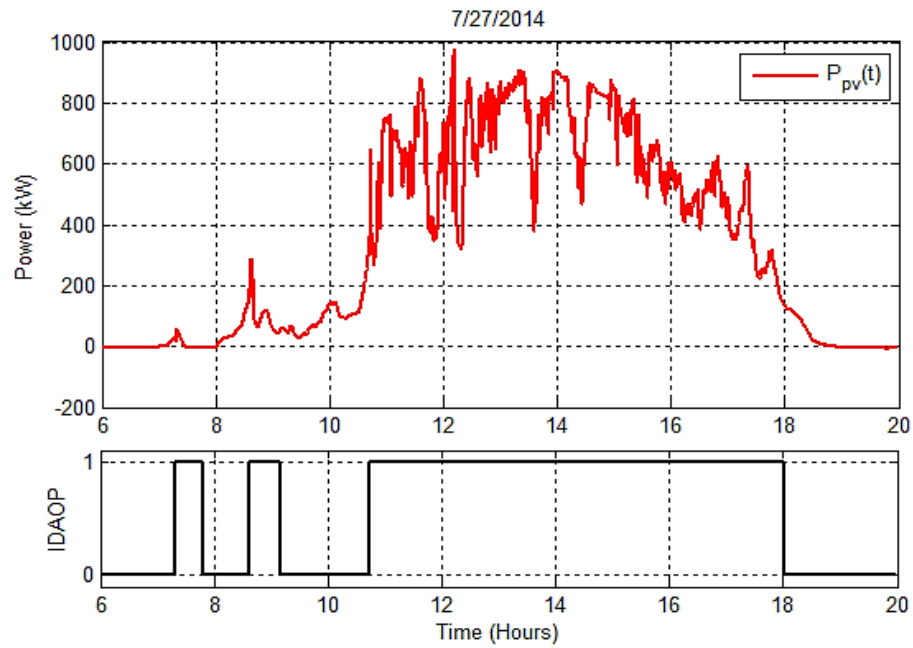


FIGURE 5.18: Intermittency detection algorithm output for July 27<sup>th</sup>, 2014 PVCF

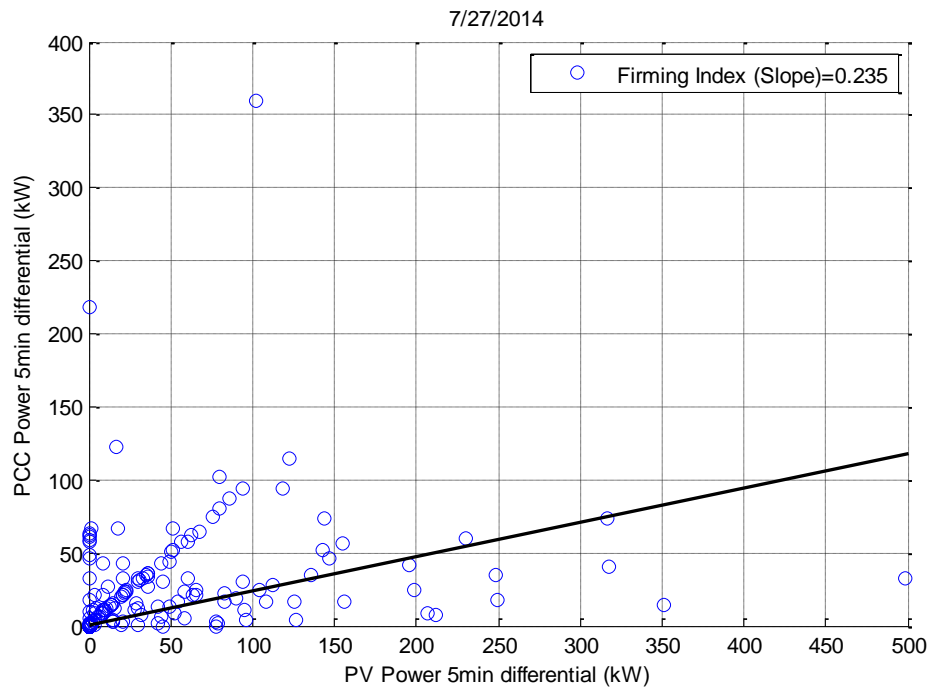


FIGURE 5.19: Firming index for July 27<sup>th</sup>, 2014 PVCF

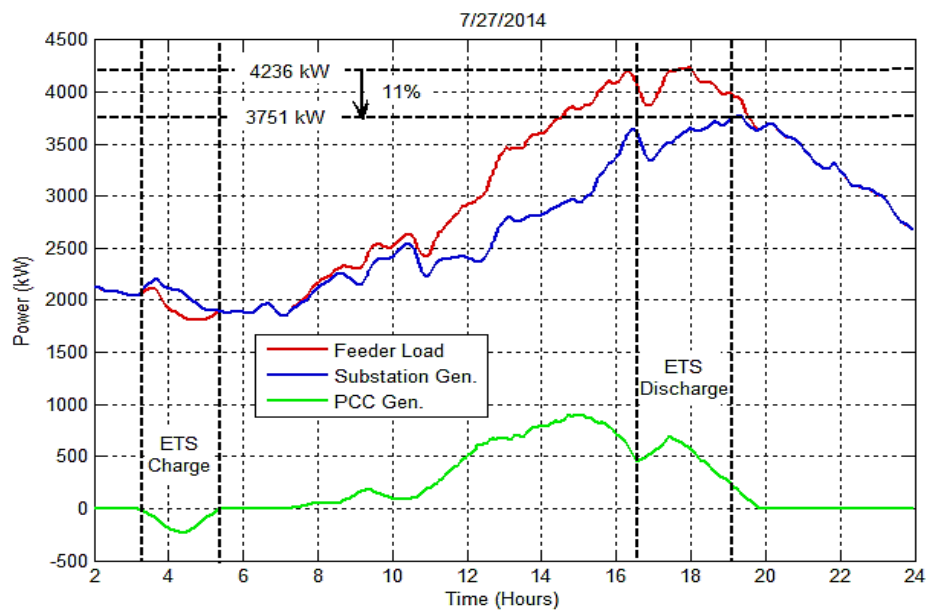


FIGURE 5.20: ETS application shown in the feeder active power load compared to substation generation for July 27<sup>th</sup>, 2014

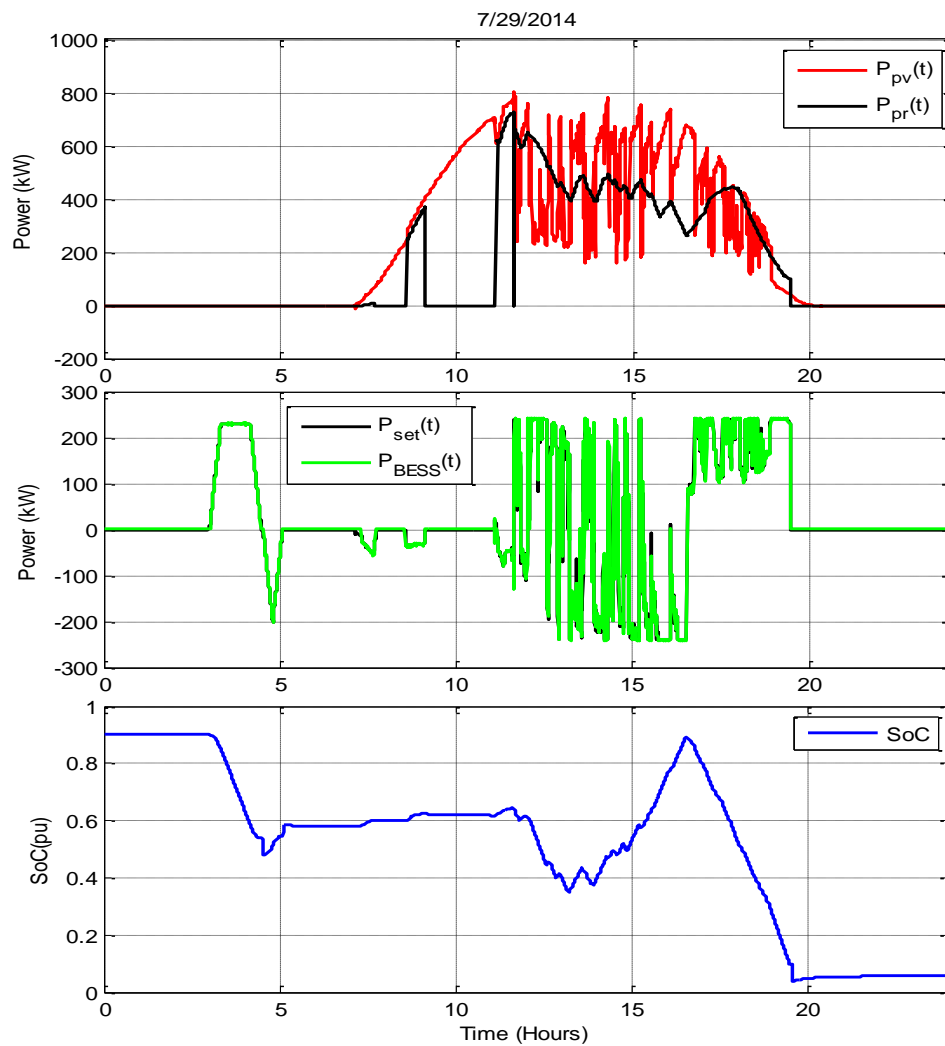


FIGURE 5.21: PV power compared to reference power, algorithm set-point compared to BESS dispatched power and SoC, respectively for July 29<sup>th</sup>, 2014 PVCF

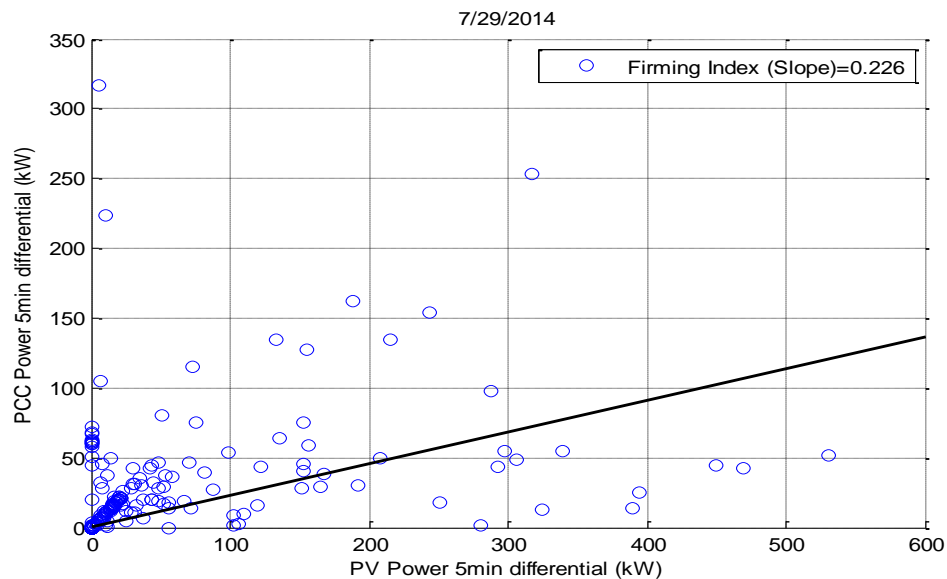


FIGURE 5.22: Firming index for July 29<sup>th</sup>, 2014 PVCF

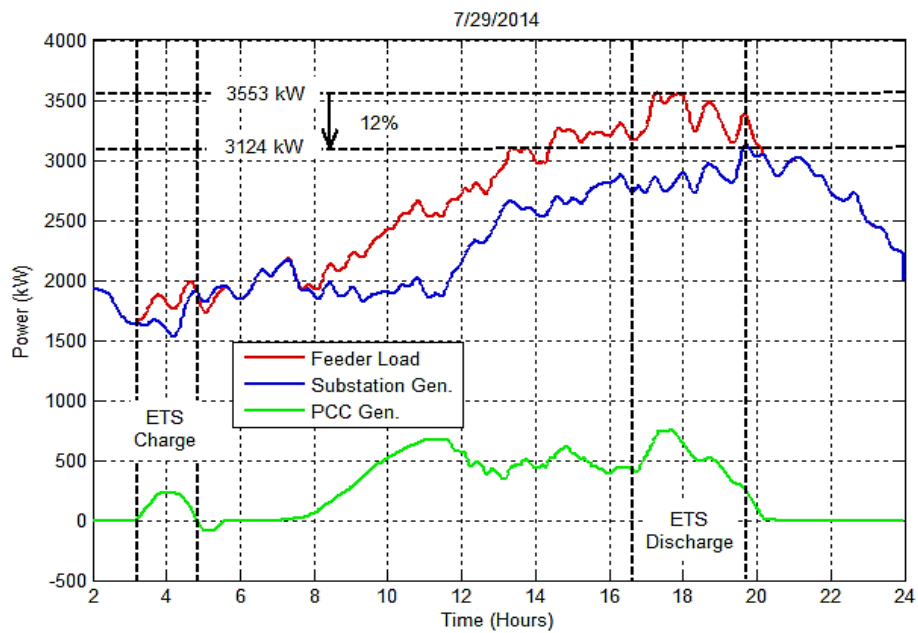


FIGURE 5.23: ETS application results shown in feeder active power load compared to substation generation for July 29<sup>th</sup>, 2014

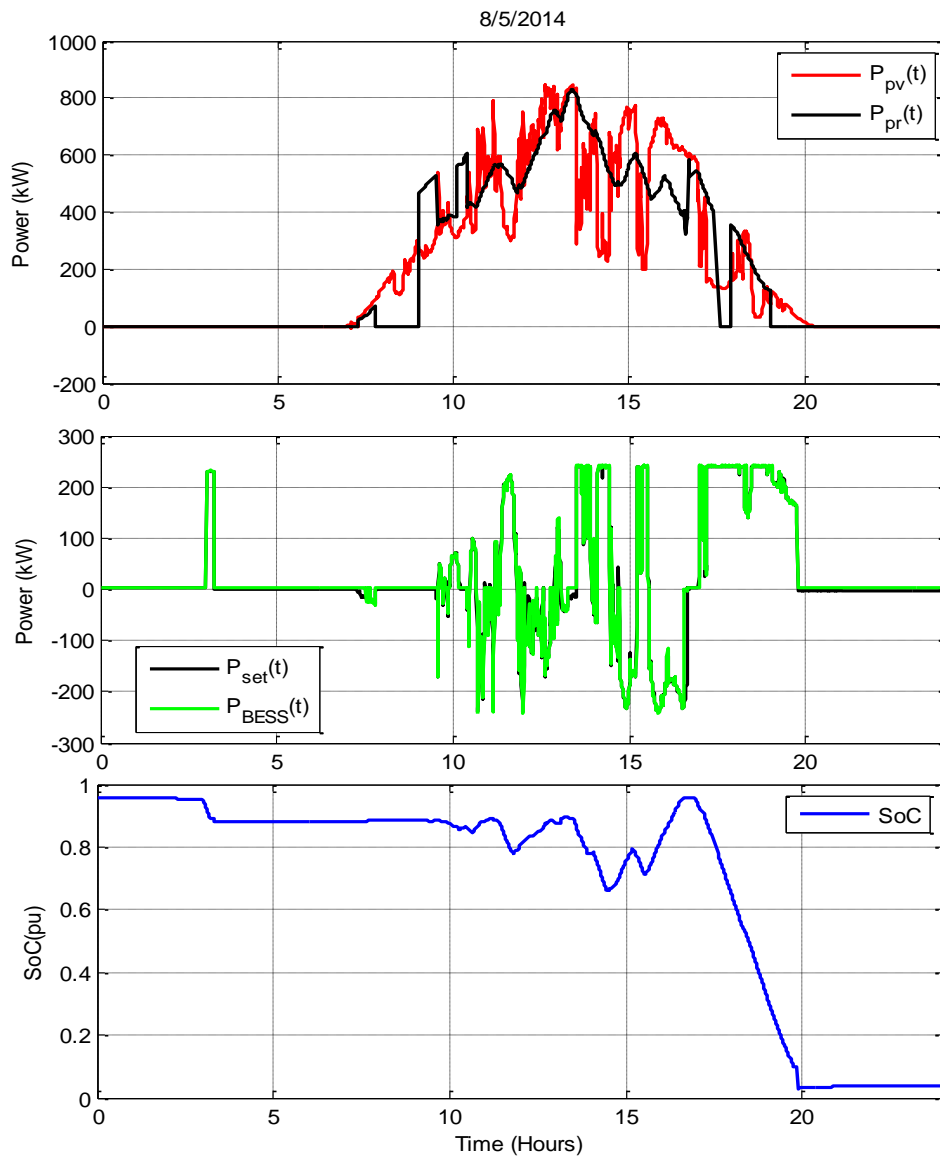


FIGURE 5.24: PV power compared to reference power, algorithm set-point compared to BESS dispatched power and SoC, respectively for August 5<sup>th</sup>, 2014 PVCF

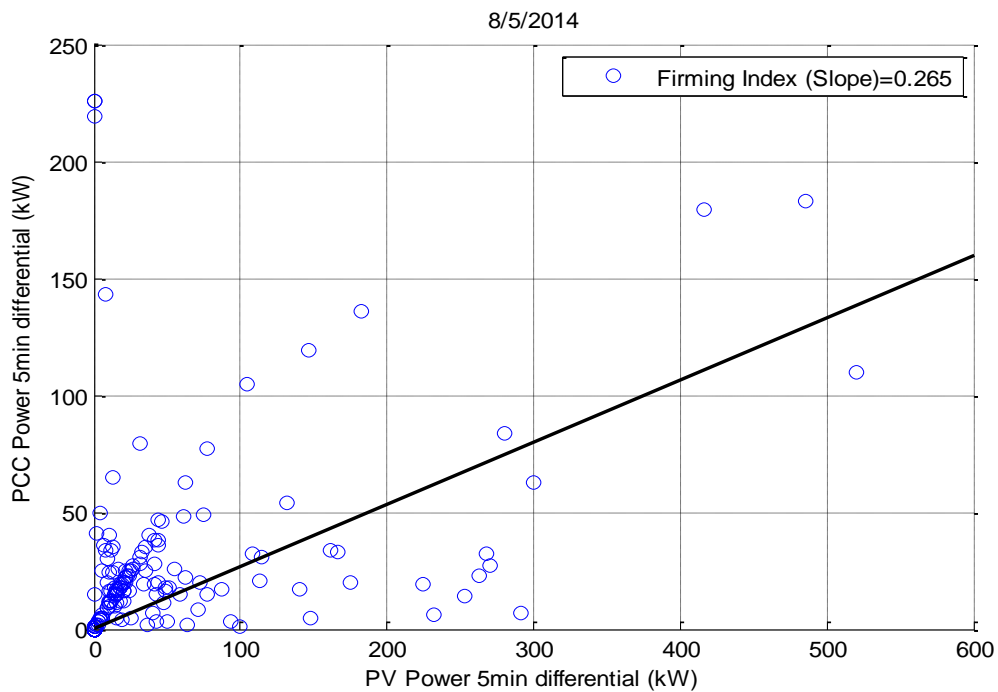


FIGURE 5.25: Firming index for August 5<sup>th</sup>, 2014 PVCF

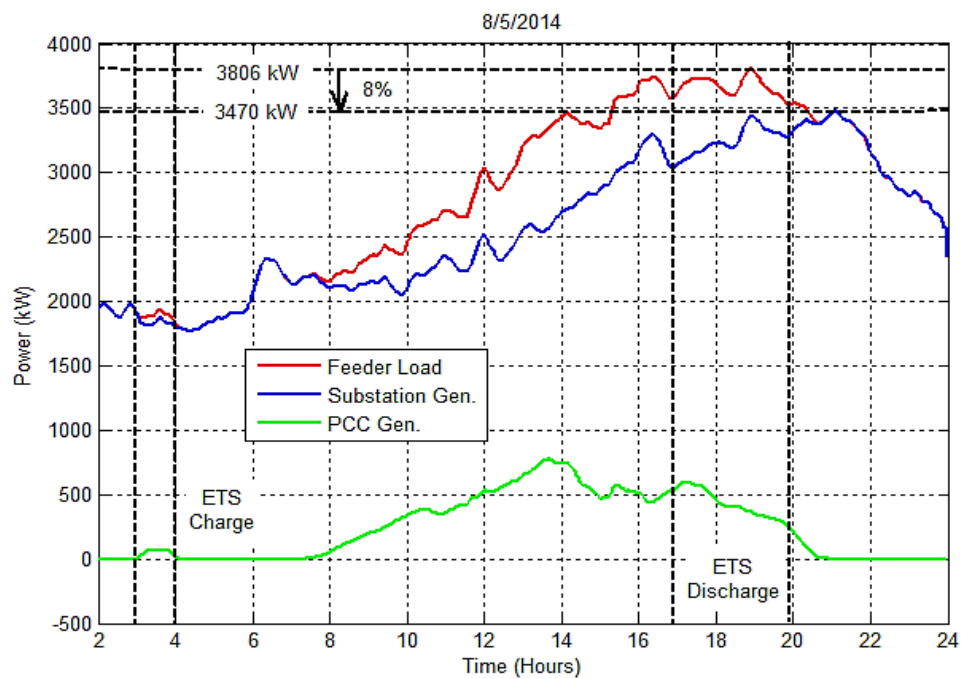


FIGURE 5.26: ETS application results shown in feeder active power load compared to substation generation for August 5<sup>th</sup>, 2014

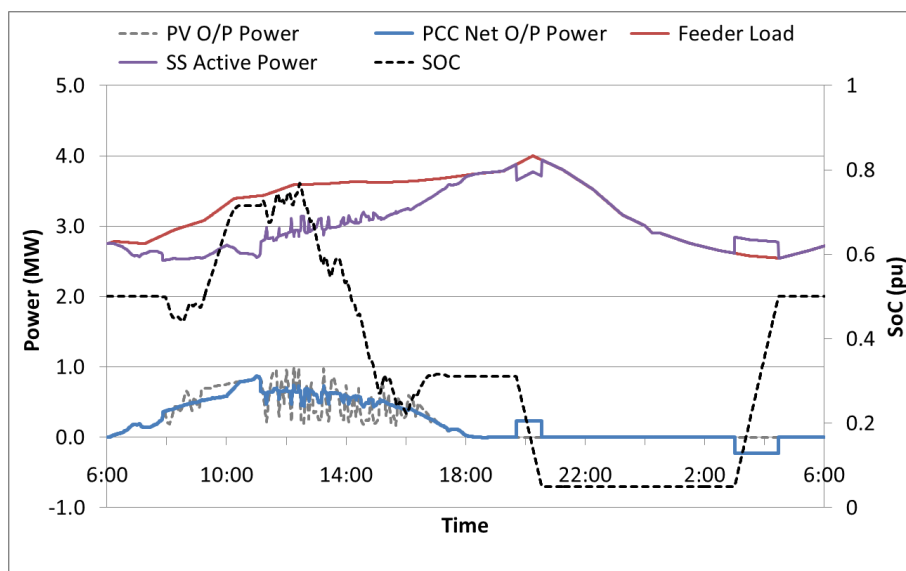


FIGURE 5.27: PVCF & ETS results without SoC optimization

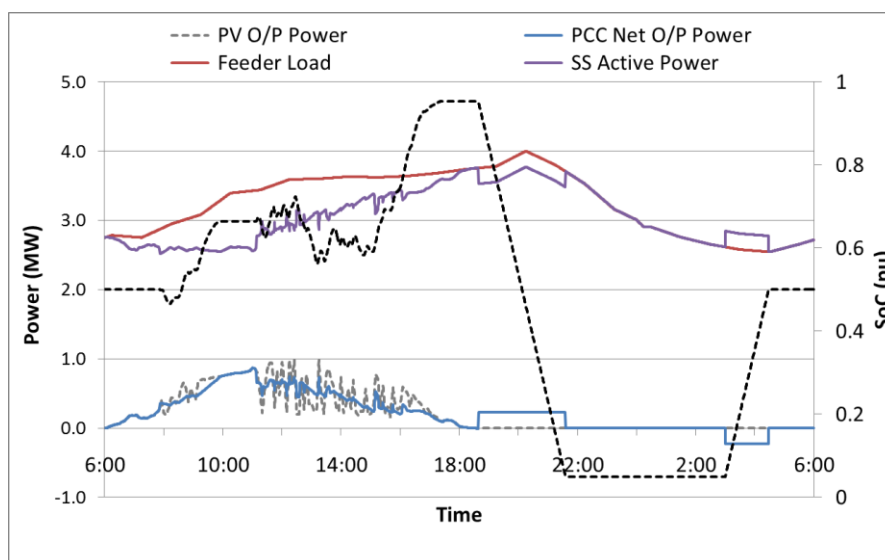


FIGURE 5.28: PVCF & ETS results with SoC optimization

As shown in FIGURE 5.28, after using the designed SoC optimization algorithm, the remaining energy in the battery (95% SoC) after conclusion of the PVCF application was sufficient to allow effective energy time shifting.

## 5.6. Conclusion

It was concluded in this chapter that weekend and weekday load curves could both be used for accurate peak load magnitude and time prediction. The optimal moving average algorithm time interval was deduced for each individual prediction parameter in order to minimize average error. The used energy time shift algorithm was found to be effective in covering the time of peak load. Optimization of the PVCF algorithm to allow proper coordination with ETS was found to be effective and greater peak load reduction was possible.

## CHAPTER 6: CLOUD STATE PATTERN RECOGNITION AIDED PV CAPACITY FIRMING OPTIMIZATION

### 6.1. Introduction

The proliferation of distributed renewable energy generation is causing increased utility concerns pertaining to issues like islanding, protection schemes, voltage stability and transients. Energy storage systems present a valuable solution to address such drawbacks. The utilization of BESSs for PV capacity firming can provide improved transient, dynamic and voltage stability. It also contributes to a decrease in the number of tap change operations of distribution feeders' voltage regulators due to sudden power swings.

Further, renewables capacity firming using energy storage units involves supplying (discharging) and consuming (Charging) power in a manner that will render the combined output of the renewable energy source and the energy storage system constant to some extent. As mentioned in [1], "The resulting firmed capacity offsets the need to purchase or 'rent' additional dispatchable (capacity) electric supply resources. Depending on location, firmed renewable energy output may also offset the need for transmission and/or distribution equipment. Renewables capacity firming is especially valuable when peak demand occurs." Reference [3] Discusses capacity firming for a large wind farm. It focuses on developing a control strategy for optimal use of BESS for wind capacity firming. It was concluded in that paper that capacity firming is achievable for the presence of a BESS with relatively high charge/discharge frequency and proper

size (20% to 30% of wind farm capacity). The case of PV station's output power also presents a clear example of intermittent power (due to clouds) that requires firming. Similar to [3]'s conclusion, PV capacity firming applications requires a power source capable of supplying power at rapidly changing pace to cope with intermittencies that are sudden in nature. Suitable energy storage technologies for firming include BESS and SCMESs.

Reference [43] proposes the implementation of multiple storage applications into a single storage system focusing in the process on maximizing value streams. However, insuring maximized individual value operation of each individual application was not performed. Here maximized PV station capacity firming is sought considering power and energy constraints of the utilized BESS. Further, [44] presents a moving average firming technique utilizing a 4 minute sliding centered window. The utilized micro-forecast method which is based on processing cloud pictures through a neural network prediction algorithm to anticipate power swings two minutes ahead of time proved to be efficient. However, this method only provides a two minute anticipation of PV power swings which is insufficient to condition the SoC of the BESS to avoid reaching system energy limits. The proposed method here utilizes cloud state forecasts, historical weather and PV data to identify optimal algorithm parameters, especially including daily starting SoC to avoid reaching system energy limits during firming. Evidently, PV capacity firming effectiveness is significantly affected by overall cloud conditions. State values of the PVCF algorithm like initial SoC amongst others must be considered in taking into account forecasted cloud states. Moreover, interrelating the day ahead weather forecast with PV/BESS power firming applications has not been discussed so far in the literature.

In this chapter, the BESS PVCF application presented in CHAPTER 3 is optimized utilizing weather forecasts. This method considers the daily general cloud state forecast with offline dynamic programming routines to attain the maximum possible firming given BESS power and energy limitations. The proposed method works with the Storage Management System (SMS) to enhance its active power capabilities while utilizing an innovative communication scheme to convey system data to the devised controller and return controller output to BESS.

## 6.2. PV Capacity Firming Methodology

The BESS PVCF application aims to minimize PV station power swings through targeting high scale power swings occurring throughout the day. Counteracting such swings is of the utmost importance to minimize transients caused by renewable distributed energy resources on feeders. A PV reference value is used to determine the optimal PV power output during power swings. This reference curve is deduced taking into account the PV station characteristics and BESS size. First, a characteristic PV curve is developed based on daily PV power output recorded throughout a number of days. Second, a reference curve is deduced in real time utilizing a time variant weighing factor ( $m$ ). This reference is compared with the instantaneous value of PV power output to deduce the required BESS power dispatch level to alleviate existing power swings. Third, an intermittency detection algorithm triggers the BESS to commence and halt firming based on PV station output ramp rates. The details of the algorithm are discussed next.

### 6.2.1. Characteristic PV Curve Calculation

The PVCF algorithm utilizes short term historical PV station output to develop a characteristic maximum PV curve for the PV station location at that time of year. This curve is used to ultimately deduce an optimal power reference which is compared with instantaneous PV output power to determine the manner in which the BESS active power should be dispatched to attain firmed PCC power. As shown in equation(6.1), the instantaneous value of the BESS active power reference ( $P_{set}(t)$ ) is equal to the difference between the power reference and the real-time output power of the PV station.

$$P_{set}(t) = P_{pr}(t) - P_{pv}(t) \quad (6.1)$$

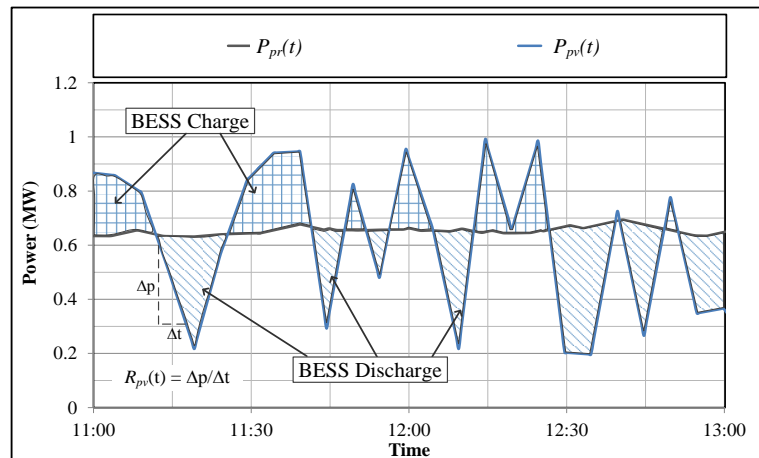


FIGURE 6.1: BESS operation in response to output PV power and reference power values

For a daily output power of PV station  $P_{pv}^k(t)$ . Where,  $k$  signifies the day number preceding the current day;  $k = 1, 2, 3, 4, \dots, n$ , the characteristic maximum PV curve is given by:

$$P_m(t) = \max(P_{pv}^1(t), P_{pv}^2(t), P_{pv}^3(t) \dots P_{pv}^n(t)) \quad (6.2)$$

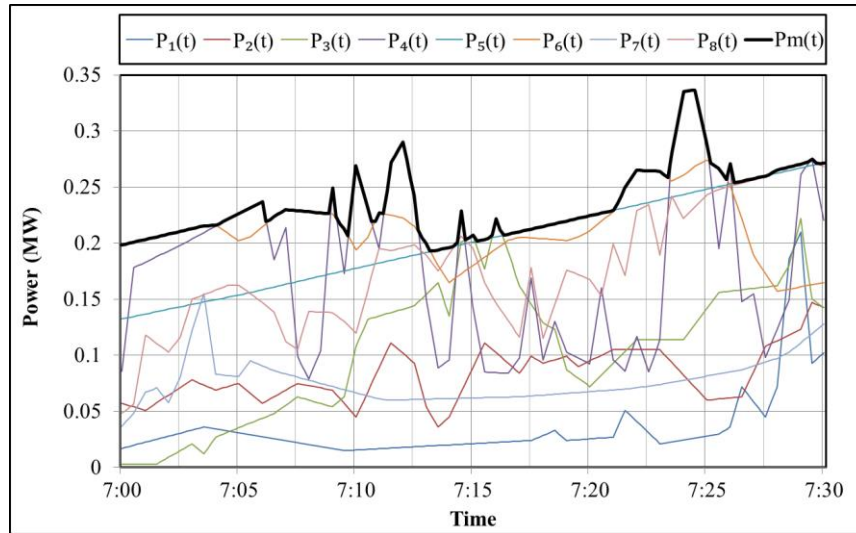


FIGURE 6.2: Characteristic maximum PV curve

The smoothed characteristic maximum power curve (SCMP) is defined as

$$P_{scmp}(t) = a P_m(t) + b (P_{scmp}(t - \Delta t) + R_m \Delta t) + c (P_{scmp}(t - \Delta t) + R_m \Delta t) \quad (6.3)$$

Where a, b and c are digits of a 3-bit binary number ( $\Psi$ ). 'a' being the most significant bit and 'c', the least significant. Let us define  $\lambda$  as:-

$$\lambda(t) = \frac{P_m(t) - P_{scmp}(t - \Delta t)}{\Delta t} \quad (6.4)$$

$$\Psi(t) = \begin{cases} 100 & \text{for } -R_m < \lambda(t) < R_m \\ 010 & \text{for } \lambda(t) > R_m \\ 001 & \text{for } \lambda(t) < -R_m \end{cases} \quad (6.5)$$

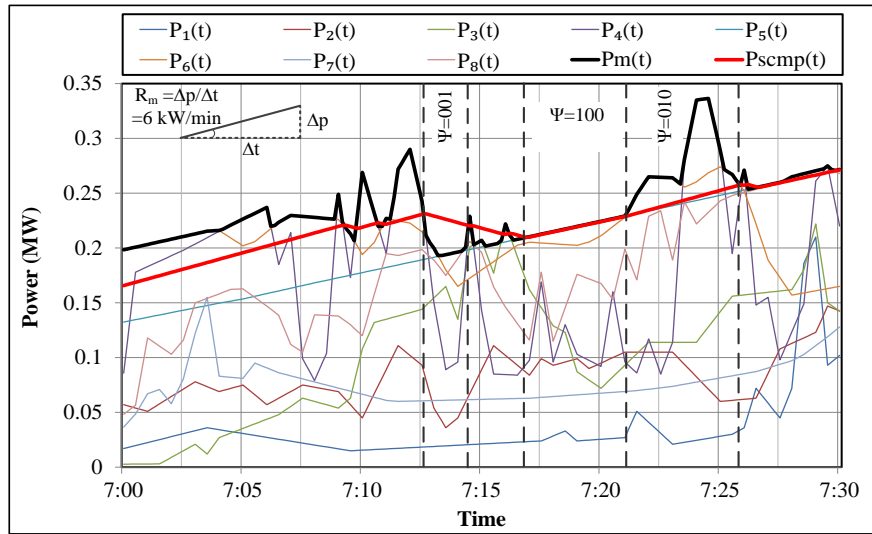


FIGURE 6.3: Smoothed characteristic maximum PV power

Where,  $R_m$  is defined as the maximum allowed rate of change of the smoothed characteristic maximum PV power with respect to time.  $R_m$  is directly related to  $R_n$  which is defined as the PV station's nominal characteristic rate of change of output active power. In other words, it can be described as the maximum rate of change of a PV station's output power with respect to time, in absence of clouds and any rapid power swings. The value of  $R_n$  is directly related to the size of the PV station in question. Assuming a 1MW PV station,  $P_m(t)$  is regressed to attain the sixth order polynomial shown below:-

$$\begin{aligned}
 p(t) = & 4.24 \times 10^{-13} t^6 - 8.98 \times 10^{-10} t^5 + 7.4 \times 10^{-7} t^4 \\
 & - 3 \times 10^{-4} t^3 + 0.05 t^2 + 0.24 t + 15.31
 \end{aligned} \tag{6.6}$$

The attained polynomial is differentiated with respect to time to attain  $(dp(t)/dt)$  as shown in FIGURE 6.4.

Since irradiance is approximately symmetrical across noon, single  $R_n$  and  $R_m$  values are defined for both increasing and decaying PV power output. Therefore, the maximum positive and negative rates of changes of the regressed 6<sup>th</sup> order polynomial are averaged to deduce  $R_n$  for a 1MW station.

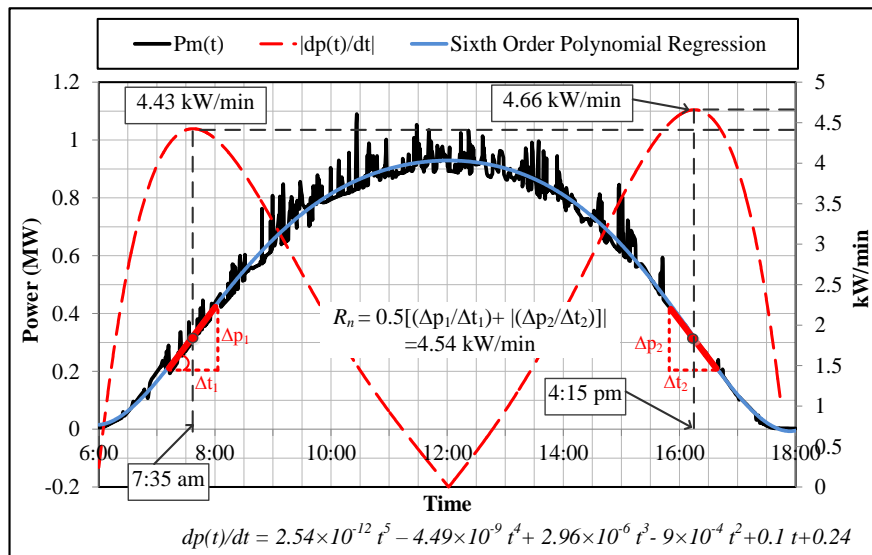


FIGURE 6.4: 1MW PV station sixth order polynomial rate of change and maximum ramp rate identification

The value of  $R_m$  is chosen to be 130% of  $R_n$  to allow for curve settling after fluctuations of  $P_m(t)$ . FIGURE 6.3 shows  $P_{scmp}(t)$  after utilizing an  $R_m$  value of 6kW/min.

Applying equations (6.2) to (6.5) to the short term historical data recorded from a 1MW PV station, we attain the smoothed characteristic maximum PV curve shown in FIGURE 6.5.

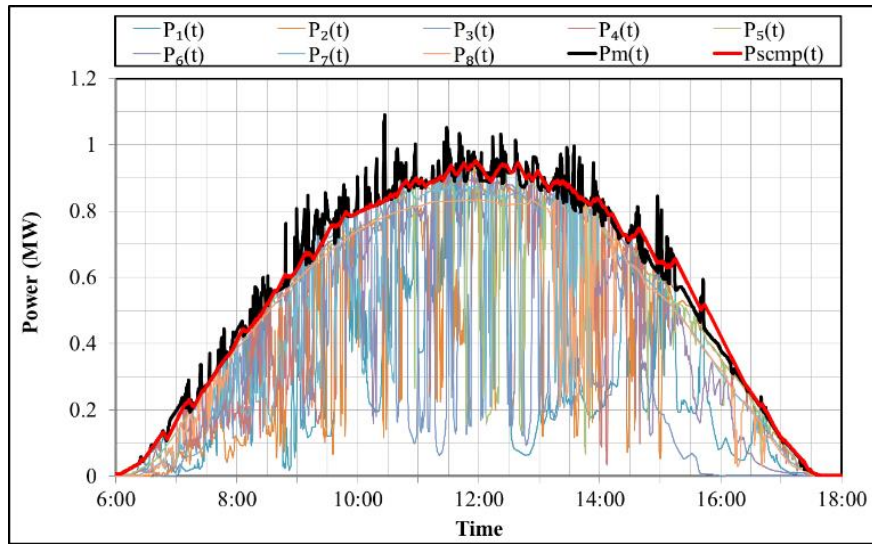


FIGURE 6.5: Smoothed characteristic maximum PV curve for a 1MW PV station

### 6.2.2. Firming Reference Calculation

As discussed, the second stage is to develop an optimal power reference considering the instantaneous PV station ramp rates. The PV Power Reference curve ( $P_{pr}(t)$ ) represents a weighted value of  $P_{scmp}(t)$ . This can be written as shown in (6.7).

$$P_{pr}(t) = m(t) \times P_{scmp}(t) \quad (6.7)$$

The weighting factor ( $m(t)$ ) should be chosen such that maximum power swing suppression is attained. As can be deduced from the previous equations, the power reference value dictates the degree of attainable firming. Also, it dictates the extent to which the BESS intervenes. Therefore, we can infer that the weighting factor ‘ $m$ ’ can be used to control both the degree of firming and, in turn, battery state of charge (SoC) throughout the firming period. A dynamic power reference weighing factor  $m_d(t)$  is defined here as a function of  $\tilde{F}_u(t)$ . The rate at which the angle of incidence of sun rays approaches and eludes perpendicularity is taken into consideration. Power output change

rates greater than these values are rendered as clouds passing. Before noon, angle of incidence of sun rays only approaches perpendicularity. Therefore,  $\tilde{F}_u(t)$  is only allowed to increase during that time. Whereas, in the afternoon, PV power output decrease could be either caused by the decrease in angle of incidence of sun rays, cloud passing or both. Therefore,  $\tilde{F}_u(t)$  is allowed to change according to a maximum rate of increase ( $R_h$ ) and decrease ( $R_l$ ). The corresponding weighing factor  $m_d$  in both cases is calculated according to equation (6.8).

$$m_d(t) = \frac{\tilde{F}_u(t) - P_{Bmax}}{P_{scmp}(t)} \quad (6.8)$$

Where, the inequality constraints shown in equation (6.9) apply to equation (6.8) and ensure that  $F_u(t)$  does not supersede  $P_{scmp}(t)$  and that the lower BESS firming limit  $F_l(t)$  does not fall below zero and the ramp rate  $m_d^*(t)$  is limited by a constant value ( $m_{dCap}^*$ ).

$$\begin{aligned} m_d(t) \leq m_s \quad , \quad \tilde{F}_u(t) \geq 2P_{Bmax} \\ \& \quad |m_d^*(t)| \leq m_{dCap}^* \end{aligned} \quad (6.9)$$

Where ( $m_s$ ) is defined as a constant weighing factor that would satisfy the case where the instantaneous value of the upper firming limit is equal to the that of  $P_{scmp}$  at noon as shown in equation (6.9). The constant  $m_{dCap}^*$  represents the maximum allowed rate of change of  $m_d(t)$  with respect to time (ramp rate limit).

$$m_s = 1 - \frac{P_{Bmax}}{P_{scmp}(t_{noon})} \quad (6.10)$$

The value of  $\tilde{F}_u(t)$  is a function of the instantaneous PV station output power as shown in equation (6.10):-

$$\tilde{F}_u(t) = \tilde{a}.P_{pv}^*(t) + \tilde{b}.P_{pv}^{**}(t) + 0.02 P_{pv}^r \quad (6.11)$$

Where,  $\tilde{a}$  and  $\tilde{b}$  are the most and least significant bits of a two bit binary number ( $\tilde{\Psi}(t)$ ), respectively. And  $P_{pv}^r$  is the PV station rated output power.

$$\tilde{\Psi}(t) = \begin{cases} 10 & \text{for } t \leq 12:00\text{pm} \\ 01 & \text{for } t > 12:00\text{pm} \end{cases} \quad (6.12)$$

$$P_{pv}^*(t) = x^*.P_{pv}(t) + y^*.P_{pv}^*(t - \Delta t) \quad (6.13)$$

Where  $x^*$  and  $y^*$  are the most and least significant bits of a two bit binary number ( $\Psi^*(t)$ ), respectively.

$$\lambda^*(t) = \frac{P_{pv}(t) - P_{pv}^*(t - \Delta t)}{\Delta t} \quad (6.14)$$

$$\Psi^*(t) = \begin{cases} 10 & \text{for } \lambda^*(t) \geq 0 \\ 01 & \text{for } \lambda^*(t) < 0 \end{cases} \quad (6.15)$$

$$P_{pv}^{**}(t) = x^{**}.P_{pv}(t) + y^{**}.(P_{pv}^{**}(t - \Delta t) + \Delta t R_h) \\ + z^{**}.(P_{pv}^{**}(t - \Delta t) - \Delta t R_l) \quad (6.16)$$

Where  $x^{**}$ ,  $y^{**}$  and  $z^{**}$  are the most to least significant bits of a three bit binary number ( $\Psi^{**}(t)$ ), respectively.

$$\lambda^{**}(t) = \frac{P_{pv}(t) - P_{pv}^{**}(t - \Delta t)}{\Delta t} \quad (6.17)$$

$$\Psi^{**}(t) = \begin{cases} 100 & \text{for } -R_l < \lambda^{**}(t) < R_h \\ 010 & \text{for } \lambda^{**}(t) > R_h \\ 001 & \text{for } \lambda^{**}(t) < -R_l \end{cases} \quad (6.18)$$

$$P_{pr}(t) = m_d(t) \times P_{scmp}(t) : \left| \frac{dP_{pr}(t)}{dt} \right| < R_m \quad (6.19)$$

Where the power reference indicated in (6.19) is constrained by its first time derivative not violating ( $R_m$ ).

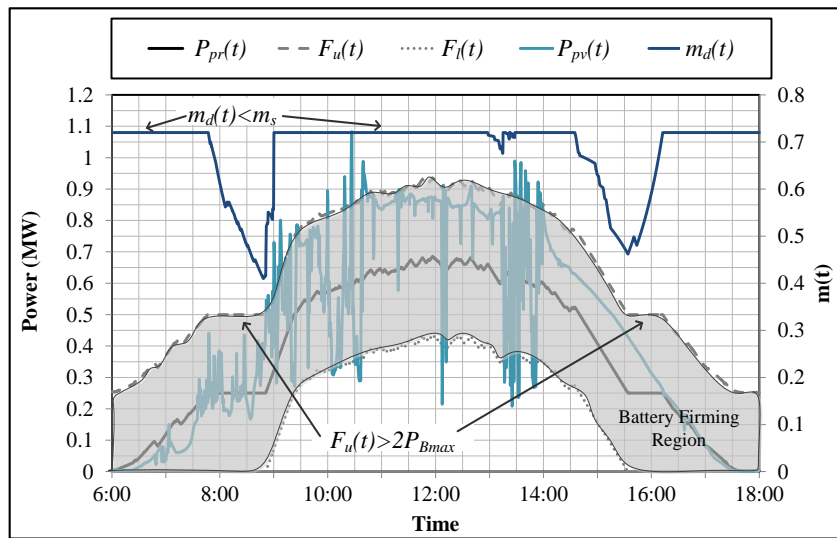


FIGURE 6.6: BESS firming region

The Battery Firing Region (BFR) shown in FIGURE 6.6 expresses maximum utilization of the BESS power spectrum with respect to the power swings of an average partially cloudy day. The extent to which the BFR covers power swings is constrained by  $m_{dCap}$ ,  $R_l$ ,  $R_h$  and  $R_m$  as shown in equations (6.8) to (6.19). Instances where  $P_{pv}(t)$  exceeds  $\tilde{F}_u(t)$  are regarded as PV station inverter transients since these values exceed the  $P_{scmp}(t)$  which expresses the maximum output of the PV station in absence of sudden changes in irradiance caused by cloud passing.

### 6.2.3. Intermittency Detection

Intermittency detection allows the idling of the battery during times when PV output power is naturally firmed and does not require conditioning. The Intermittency Detection Algorithm (IDA) contributes to conservation of battery life and decreases value degradation.

The intermittency detection algorithm relies on constantly tracking the rate of change of the difference  $P_c(t)$  between the output PV power and the power reference curve.  $P_{cf}(t)$  is equal to  $P_c(t)$  such that the first derivative with respect to time of  $P_c(t)$  is limited to a certain value ( $R_{sw}$ ). Equation (6.21) defines this relation.  $P_{cf}(t)$  is then subtracted from ( $P_c(t)$ ) to obtain ( $D$ ). If the value of  $D$  violates a certain threshold, PV power swings are identified and firming is commenced. Firming continues till value of  $D$  is maintained within limits for a period  $T_d$ .

$$P_c(t) = P_{pv}(t) - P_{pr}(t) \quad (6.20)$$

$$P_{cf}(t) = \begin{cases} P_c(t) & \text{for } -R_{sw} < \frac{P_c(t) - P_{cf}(t - \Delta t)}{\Delta t} < R_{sw} \\ R_{sw} \Delta t + P_{cf}(t - \Delta t) & \text{for } \frac{P_c(t) - P_{cf}(t - \Delta t)}{\Delta t} > R_{sw} \\ R_{sw} \Delta t + P_{cf}(t - \Delta t) & \text{for } \frac{P_c(t) - P_{cf}(t - \Delta t)}{\Delta t} < -R_{sw} \end{cases} \quad (6.21)$$

$$D(t) = P_c(t) - P_{cf}(t) \quad (6.22)$$

An important trait of the discussed IDA is the application of dual triggers to prevent premature setting of the Intermittency Detection Algorithm Output (IDAOP) which would cause unwanted BESS operation. The first threshold violation of  $D(t)$  is ignored

and used only to set the value of a SR flip-flop that in turn, sets the IDAOP provided that a secondary SR flip-flop is also set by a secondary threshold violation of  $D(t)$ .

FIGURE 6.7 shows the operation of the IDA for a sample day. It can be noticed that the algorithm is triggered only during the times of intermittent PV station output or in other words, during high scale power swings. It is also clear that the algorithm output is rested after the PV station output maintains a non-intermittent output state for the specified time period  $T_d$ .

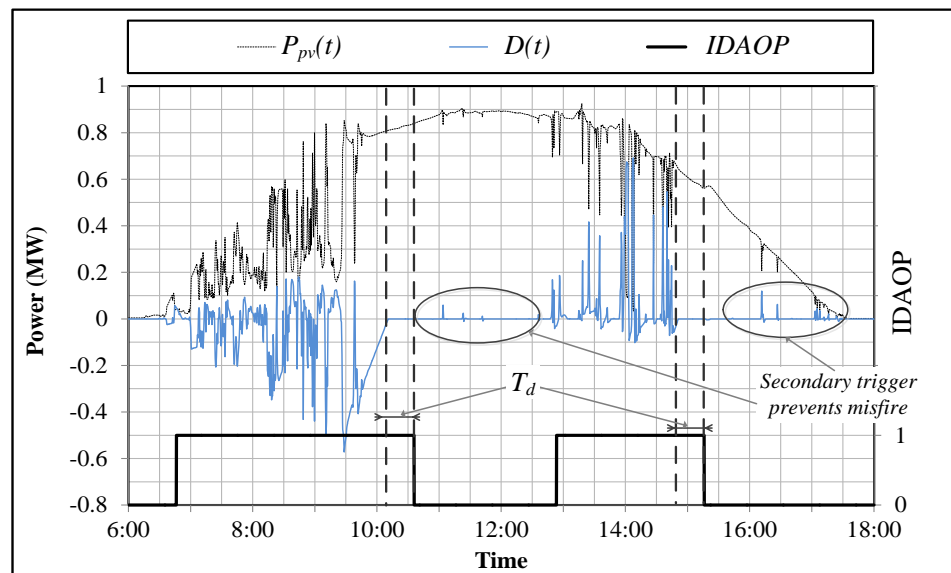


FIGURE 6.7: IDA operation for typical PV station output

### 6.3. Firming Maximization

Given the stochastic nature of PV station intermittencies, it is required to implement a dynamic programming optimization routine to determine optimal algorithm parameters to satisfy maximum firming. The optimization technique implemented here relies on the utilization of publicly available hourly weather forecasts for PV station location. Two main algorithm parameters are to be optimized, viz., initial BESS SoC ( $SoC_{st}$ ) and the limit applied for the first time derivative of the firming reference weighing factor ( $m_d(t)$ ). This is the constant expressed in equation (6.9) and namely,  $m_{dCap}^*$ . The following minimization function is to be considered

$$\min A_t = \int_{t_s}^{t_e} [P_{pv}(t) - P_{opr}(t) - P_{Bmax}]dt + \int_{t_s}^{t_e} [P_{opr}(t) - P_{Bmax} - P_{pv}(t)]dt \quad (6.23)$$

$$\forall P_{pv}(t) > P_{opr}(t) + P_{Bmax}, P_{opr}(t) - P_{Bmax} > P_{pv}(t) \ \& \ IDAOP(t) = 1$$

Where,  $t_s$  and  $t_e$  represent the time of start and end of PV station output, respectively.  $IDAOP(t)$  represents the instantaneous value of the intermittency detection algorithm output.  $J$  is the minimization function which represents the total unfirmed energy during a particular day. The constraints are

$$0.1 < SoC_{st} < 0.95 \quad (6.24)$$

$$10^{-5} < m_{dCap}^* < 10^{-3} \quad (6.25)$$

As expressed in equation (6.23), the minimization function applied here is the summation of unfirmed energy over the full day duration. Further, presented in FIGURE 6.8, unfirmed energy is the time integrated power differential between PV power and either the upper ( $F_u$ ) or lower ( $F_l$ ) firming limits dictated by the current value

of reference power  $P_{pr}(t)$ . This is the energy of the PV power swings that the BESS failed to firm due to its power or energy capacity. Therefore, the daily unfirmed energy could be regarded as a function of the BESS's current SoC and the instantaneous value of the reference power  $P_{pr}(t)$  which dictates the location of the BFR in reference to instantaneous PV output.

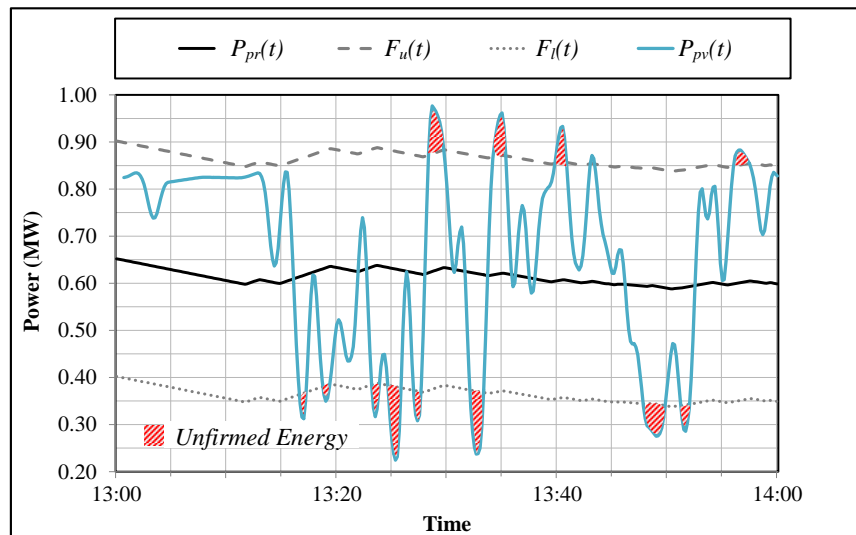


FIGURE 6.8: Unfirmed Energy for sample hour given reference power

### 6.3.1. Optimization Parameters

The PV capacity firming algorithm discussed in section 6.2 expresses an apparent correlation between the degree of firming and two main algorithm parameters, namely,  $SoC_{st}$  and  $m_{dcap}^{\bullet}$ . For instance, the simulation in FIGURE 6.9 clearly shows an unfirmed PV output for a time interval spanning from 12:30pm to 2:40 pm. This occurred due to the incapacity of the BESS to charge at that particular instant, due to the SoC reaching 95% (the maximum practically allowed SoC). This, in turn, resulted in the upper firming limit coinciding with the reference power ( $P_{pr}(t)$ ) during the mentioned time interval

which (by the description explained earlier) caused the upper firming limit's unfirmed energy ( $A_u$ ) to reach 400kWh as shown in FIGURE 6.10.

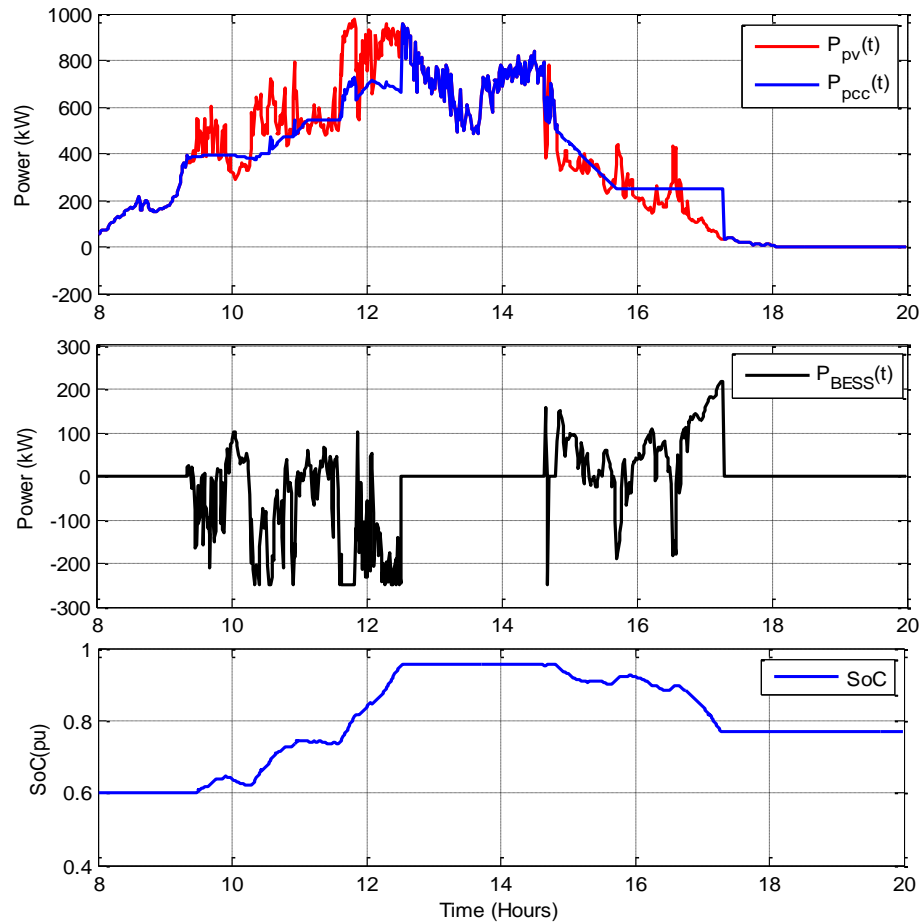


FIGURE 6.9: PVCF algorithm simulation result for sample day with arbitrarily chosen values for  $SoC_{st}$  and  $m_{dCap}$  (Feb 28<sup>th</sup>, 2015)

It is therefore, sought to identify the values of the optimizable parameters ( $SoC_{st}$  &  $m_{dCap}$ ) that would minimize the total unfirmed energy expressed in the minimization function in equation (6.23). In FIGURE 6.10, this is referred to as  $A_t$ , which is the summation of the upper and lower firming limits' unfirmed energy ( $A_u$  &  $A_l$ ).

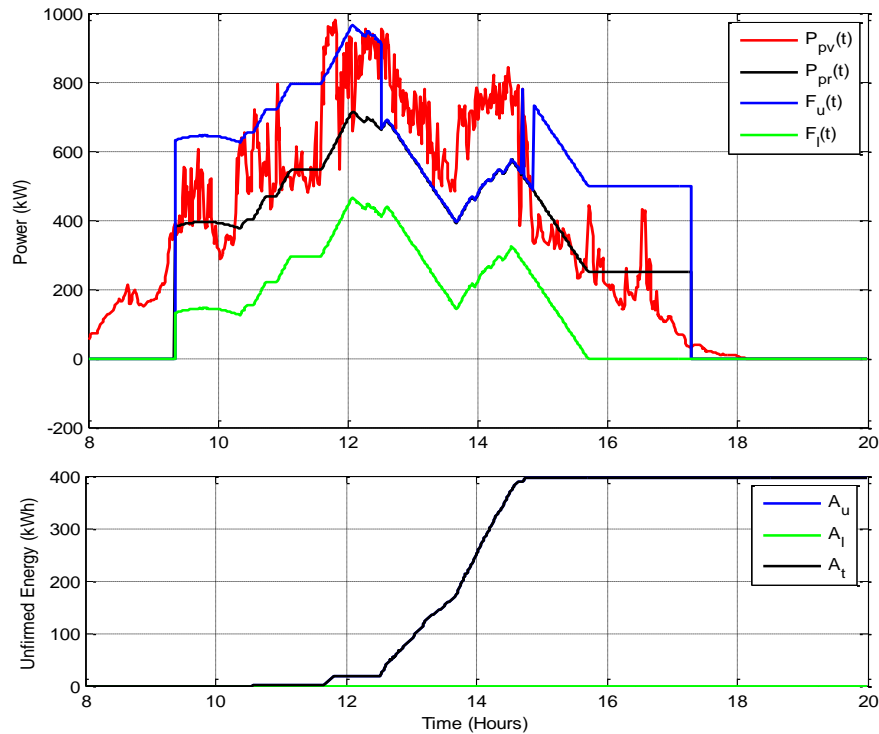


FIGURE 6.10: Upper and lower firming limits for deduced algorithm reference power and the resulting unfirming energy

### 6.3.2. Single Day Optimization Methodology

Maximum firming for a single day with known PV power output is achieved here through an offline dynamic programming optimization routine in which the chosen search range for each of the optimization parameters is fully exhausted in their application to the designed PVCF algorithm. This allows the identification of the optimal  $SoC_{st}$  &  $m_{dcap}^{\bullet}$  values, in addition to the minimum possible unfirming energy for the day in question. As shown in the flow chart presented in FIGURE 6.11, the search range and step values are initially specified for both  $SoC_{st}$  &  $m_{dcap}^{\bullet}$ . As dictated by the nested loop expressed in

the flow chart below, all the values of the “ $m_{dCap}^{\bullet}$ ” search range are applied with each new value of the “ $SoC_{st}$ ” search range to the PVCF algorithm, to, in turn, identify the total unfirmed energy and, consequently, opt to update the values of  $SoC_{stOpt}$  &  $m_{dCapOpt}^{\bullet}$  or not, based on the value of  $A_t(i,k)$  being a local minimum or not.

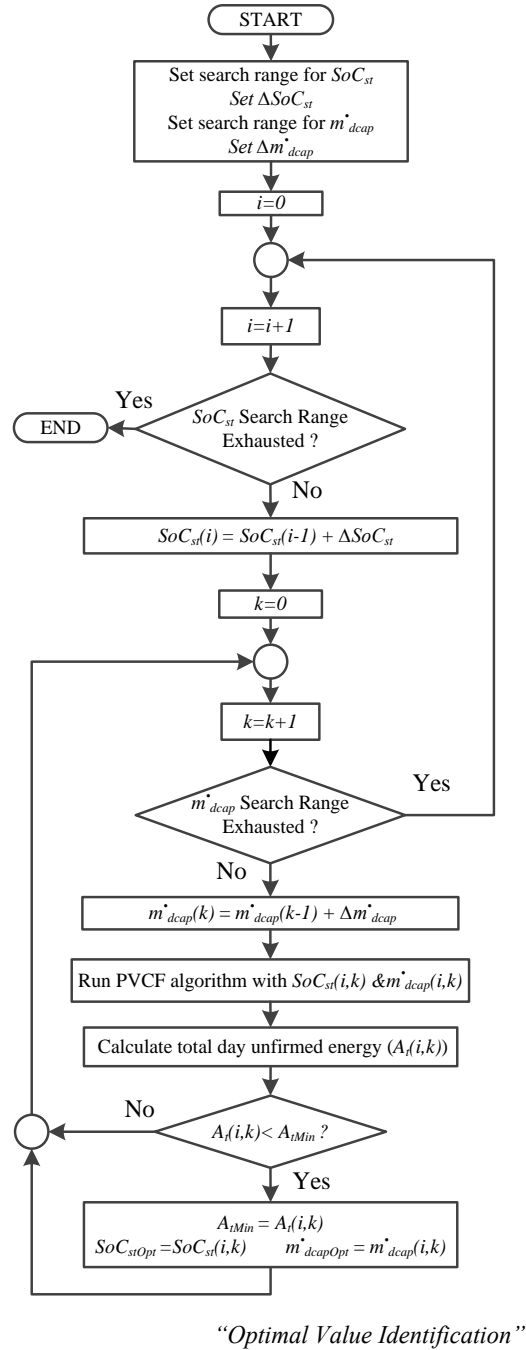


FIGURE 6.11: Dynamic programming optimization flow chart to identify optimal PVCF algorithm parameter values for single day

The described dynamic programming routine is applied to the sample day presented in FIGURE 6.9. The results are expressed in FIGURE 6.12, through graphing the

subsequent points, given by  $SoC_{st}(i,k)$ ,  $m_{dCap}^{\bullet}(i,k)$  and  $A_t(i,k)$ . The minimum value for unfirmed energy is found to be  $A_{tMin}=26$  kWh with a range of optimal values for both optimization parameters ( $SoC_{st}$  &  $m_{dCap}^{\bullet}$ ). This range is prescribed by the contour shown in FIGURE 6.13. The optimal values are chosen to be in the median of the minimum energy contour shown. This value is found to be at  $SoC_{st}=33.9\%$  &  $m_{dCap}^{\bullet} = 6.68 \times 10^{-5}$ .

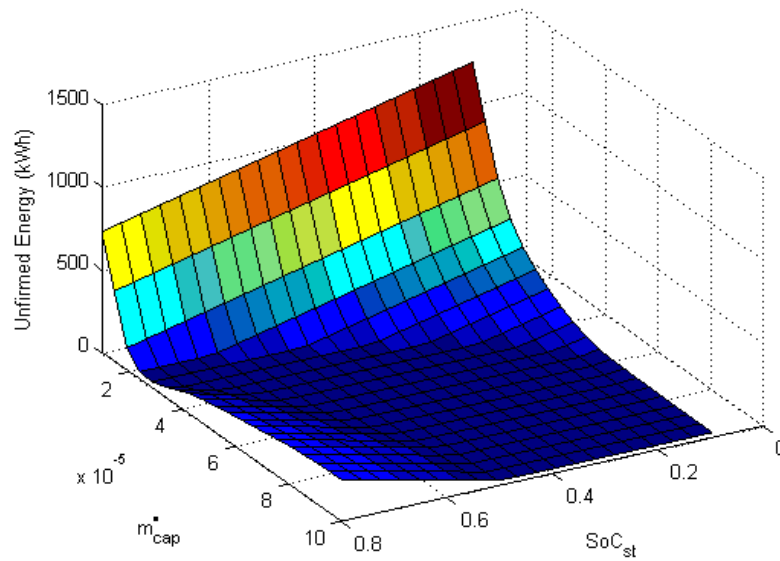


FIGURE 6.12: Surface plot for unfirmed energy ( $A_t$ ) plotted versus full search ranges of  $SoC_{st}$  &  $m_{dCap}^{\bullet}$

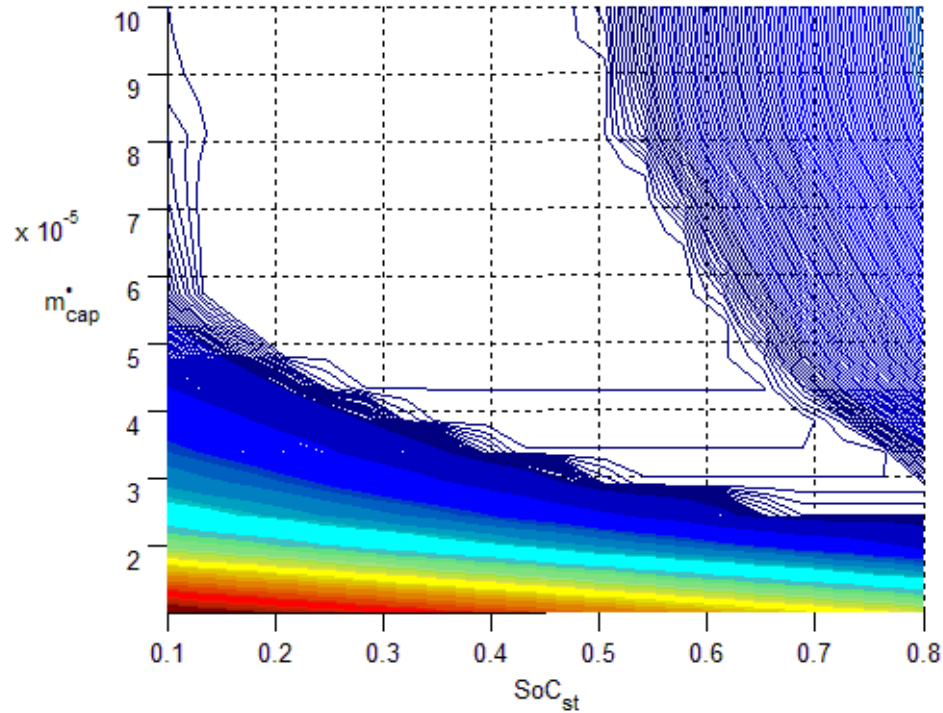


FIGURE 6.13: Contour plot showing the optimal values for  $SoC_{st}$  &  $m_{dCap}^*$ , satisfying maximum firming

Plugging the deduced optimal values for  $SoC_{st}$  &  $m_{dCap}^*$  into the PVCF algorithm and running the simulation gives the results shown in FIGURE 6.14. Comparison between firming results exhibited when utilizing averaged versus optimal parameter values reveals an apparent discrepancy when analyzing FIGURE 6.9 and FIGURE 6.14, respectively. The firming gap experienced when utilizing averaged values ceases to exist when adopting optimal values. Further, the battery SoC eludes reaching its upper and lower limits throughout the firming period. Also, most of PV power output lies within BFR.

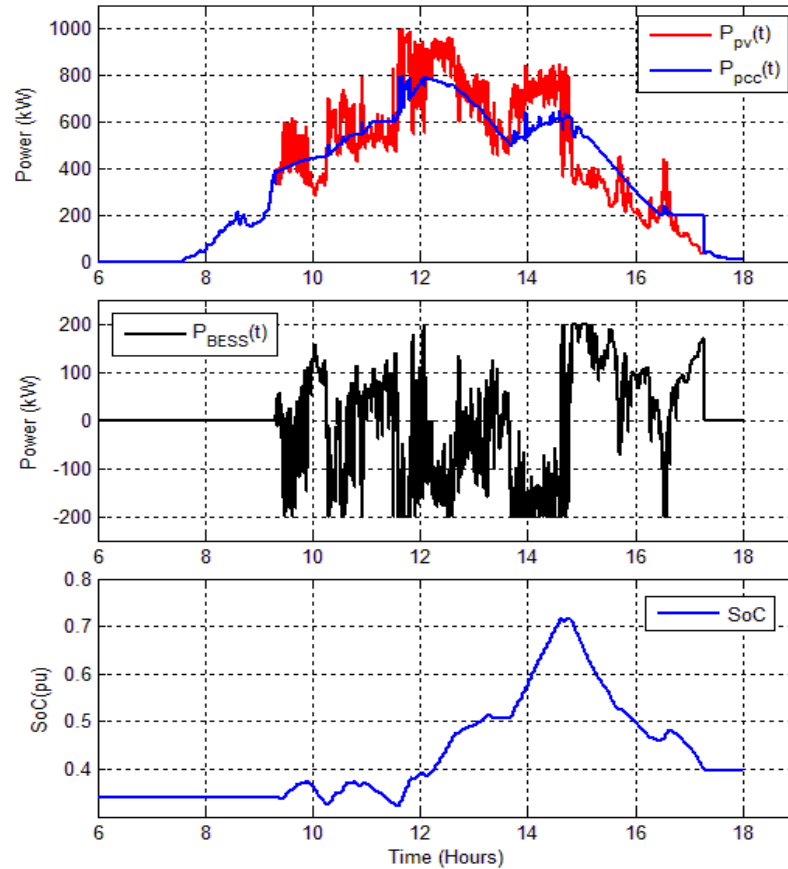


FIGURE 6.14: Firing results for sample day utilizing optimal algorithm parameters

#### 6.4. Multiple Day Optimization Framework

In the pursuit to design a full PVCF algorithm that ensures maximum daily firming, it is sought to utilize optimal values that were deduced offline for future days with similar PV output characteristics. The similarity between optimal values of the mentioned parameters for different days of similar PV output suggests a considerable degree of effectiveness. This leads to the presumption that the cloud state of a particular day could be a factor that dictates the value of the optimization parameters and thus allow the application of the concluded optimal values for days of similar cloud states. The framework would be as follows, first, a number of day types are defined based on their

cloud cover characteristics. Second, a criteria is built to identify each defined day type. Third, the optimization routine discussed is ran for mass historical data while identifying and recording day types and corresponding optimal values. Fourth, weather forecasts are utilized to identify next day cloud state and identify pattern and day type, to, in turn, adopt optimal values calculated offline for the identified day type.

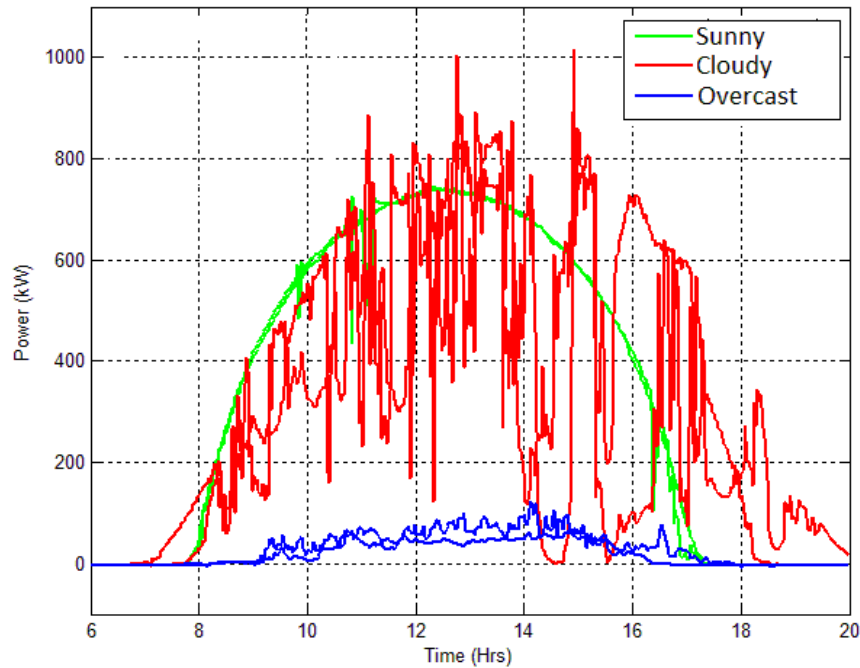


FIGURE 6.15: PV power output for two days for clear, partially cloudy and overcast cloud states

#### 6.4.1. Daily Cloud State Classification

Cross-referencing between several years of the practical PV power output and corresponding recorded cloud states for the described PV station, a strong correlation between PV output and hourly cloud state is concluded. Further, an apparent discrepancy in PV power output between days with sunny, cloudy and overcast cloud states is shown

in FIGURE 6.15. However, in order to accurately describe a day in terms of its cloud state, it is necessary to define intervals within a single day. Since most days exhibit more than one cloud state, each day here is divided into three main periods (Morning, Noon & Evening). Each of these periods can be described in terms of its cloud state as Sunny, Cloudy or Overcast. This yields twenty-seven combinations as shown in TABLE 6.1.

TABLE 6.1: Days types based on clouds states

Type	Morning	Noon	Evening
1	Sunny	Sunny	Sunny
2	Sunny	Sunny	Cloudy
3	Sunny	Sunny	Overcast
4	Sunny	Cloudy	Sunny
5	Sunny	Cloudy	Cloudy
6	Sunny	Cloudy	Overcast
7	Sunny	Overcast	Sunny
8	Sunny	Overcast	Cloudy
9	Sunny	Overcast	Overcast
10	Cloudy	Sunny	Sunny
11	Cloudy	Sunny	Cloudy
12	Cloudy	Sunny	Overcast
13	Cloudy	Cloudy	Sunny
14	Cloudy	Cloudy	Cloudy
15	Cloudy	Cloudy	Overcast
16	Cloudy	Overcast	Sunny
17	Cloudy	Overcast	Cloudy
18	Cloudy	Overcast	Overcast
19	Overcast	Sunny	Sunny
20	Overcast	Sunny	Cloudy
21	Overcast	Sunny	Overcast
22	Overcast	Cloudy	Sunny
23	Overcast	Cloudy	Cloudy
24	Overcast	Cloudy	Overcast
25	Overcast	Overcast	Sunny
26	Overcast	Overcast	Cloudy
27	Overcast	Overcast	Overcast

### 6.4.2. Day Type Identification Criteria

In order to correctly classify the optimal values for each day type, a certain criteria must be adopted to identify each day type when analyzing historical PV data. Therefore, each period within a certain day is sought to be identified. The adopted criteria will rely mainly on two parameters to identify periodical cloud states, namely, Period Energy (PE) and Period Euclidean Norm (PUN).

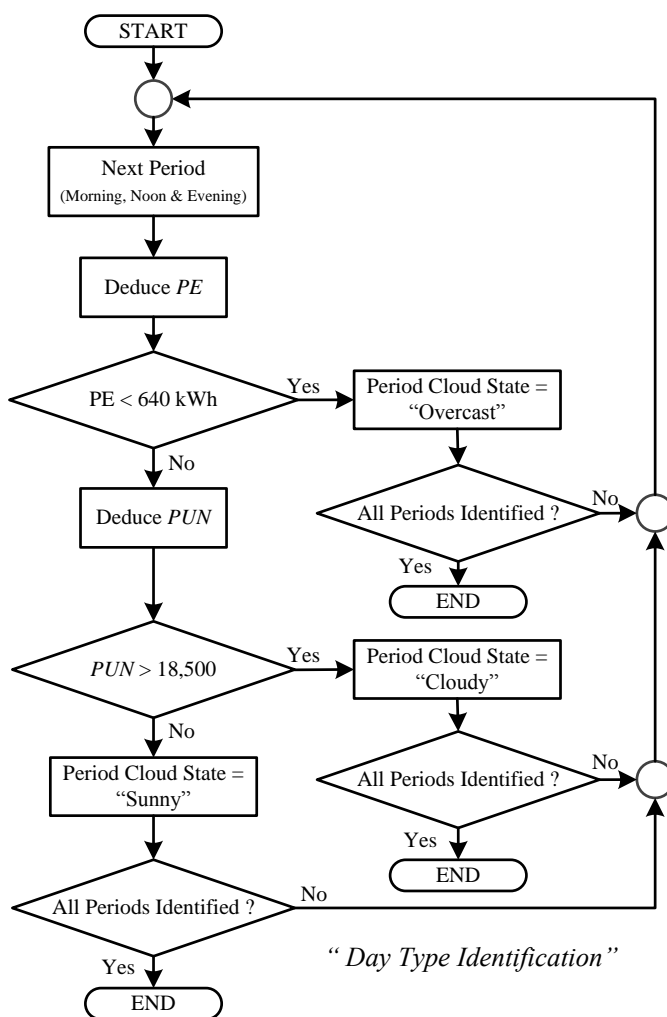


FIGURE 6.16: Flow chart to identify periodical cloud states based on PV station power output

Overcast days are readily identifiable since their PEs for morning, noon and evening are characterized by having a small value when compared to cloudy and sunny cloud states. Through analyzing historical weather data and cross-referencing with corresponding PV power output, it was found that overcast periods exhibit a maximum PE value of 640 kWh for all periods for the described 1MW PV station. Further, Sunny and Cloudy periods exhibit similar output energy levels. However, periodical Euclidean norms vastly differ between both. It was found that Cloudy periods experience elevated values of PUN, averaging in 25,000 units, whereas Sunny periods exhibit average values of 15,500 units with a maximum of 18,500 units. Therefore, PUNs are used to identify both Sunny and Cloudy periods. The flow chart in FIGURE 6.16 describes the full process used to identify periodical cloud states.

#### 6.4.3. Optimal Value Determination

After identifying the cloud state for each period, the day type is specified according to TABLE 6.1. Mass historical PV data is analyzed and optimal firming values are deduced for each identified day type according to the flow chart sequence shown in FIGURE 6.17.

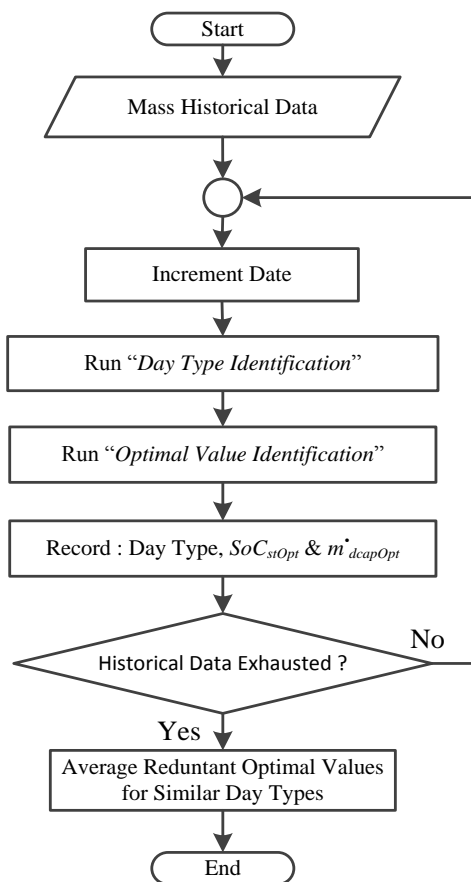


FIGURE 6.17: Flow chart showing to deduce average optimal values for different day types utilizing mass historical data

The described routine is allowed to process historical data yielding the optimal values for different sample day types shown in TABLE 6.2.

TABLE 6.2: Optimal value lookup table for sample day types

Day Type	Avg. Mor. PE (kWh)	Avg. Noon PE (kWh)	Avg. Ev. PE (kWh)	Avg. Mor. PUN ( $\times 10^4$ )	Avg. Noon PUN ( $\times 10^4$ )	Avg. Ev. PUN ( $\times 10^4$ )	Avg. $m_{dcapOpt}^{\bullet}$ ( $\times 10^{-4}$ )	Avg. $SoC_{stOpt}$ (%)
1	1549	2702	1310	1.14	1.36	1.34	3.020	43.4
14	1222	2917	1056	2.40	4.28	2.56	1.188	14.2
15	1205	2530	424	3.05	6.10	1.20	3.350	38.4
19	481	2322	1840	1.39	1.66	1.25	2.862	35.3
21	207	899	258	1.29	1.64	1.35	3.252	53.8
22	316	1768	1155	1.45	3.05	1.84	2.414	42.1
<b>23</b>	<b>174</b>	<b>1083</b>	<b>802</b>	<b>8.91</b>	<b>2.12</b>	<b>2.02</b>	<b>3.768</b>	<b>0.315</b>
24	356	1357	416	1.70	3.29	1.72	1.999	57.0
27	288	391	102	1.06	1.33	1.26	3.340	52.4

#### 6.4.4. Forecasting and Optimal Value Utilization

An Application Programming Interface (API) is set up to import daily, location specific cloud state forecasts from a host website (wunderground.com). The day type is identified according to the cloud state forecast and optimal algorithm values are imported from the recorded lookup table. Further, the BESS SoC is conditioned such that its value at the commencement of the firming period is equal to  $SoC_{stOpt}$ . The value of  $m_{dcap}^{\bullet}$  is set to the day type optimal value ( $m_{dcapOpt}^{\bullet}$ ).

### 6.5. Implementation Results

The described algorithm is ran on the 15<sup>th</sup> of May, 2015 on the practical system described in Section 2.4. Adopting the strategy applied in [43], generic values for the starting SoC as well as  $m_{dcap}^{\bullet}$  were utilized. As shown in FIGURE 6.18, The values are as follows;  $SoC_{st}=75\%$  &  $m_{dcap}^{\bullet} = 2 \times 10^{-4}$ . This however yielded poor result due to the unusual cloud pattern of the day at hand.

A firming index purposed to quantify the degree of firming performed is utilized here. This index is similar to that applied in [45]. Further, this index is defined as the slope of the least square line of the PCC power 5-minute differential plotted against that of the PV power. In other words, each point on the plot shown in FIGURE 6.19 has an x-axis value equal to the PV power differential over 5 minutes and a y-axis value equal to the PCC power differential over the same period. So, a point at (200, 50) implies that a 5 min power swing of 200kW out of the PV station was reduced to 50 kW at the PCC, after BESS PVCF algorithm intervention. Now, taking the least square linear regression line's slope over the entire firming period gives an indication of how much firming was performed. Therefore, a unity slope implies no firming. On the other hand, a zero slope implies theoretical maximum firming. To this point, the firming index concluded through utilizing generic values for the optimizable parameters is, as shown in FIGURE 6.19, 0.665, which implies relatively poor firming.

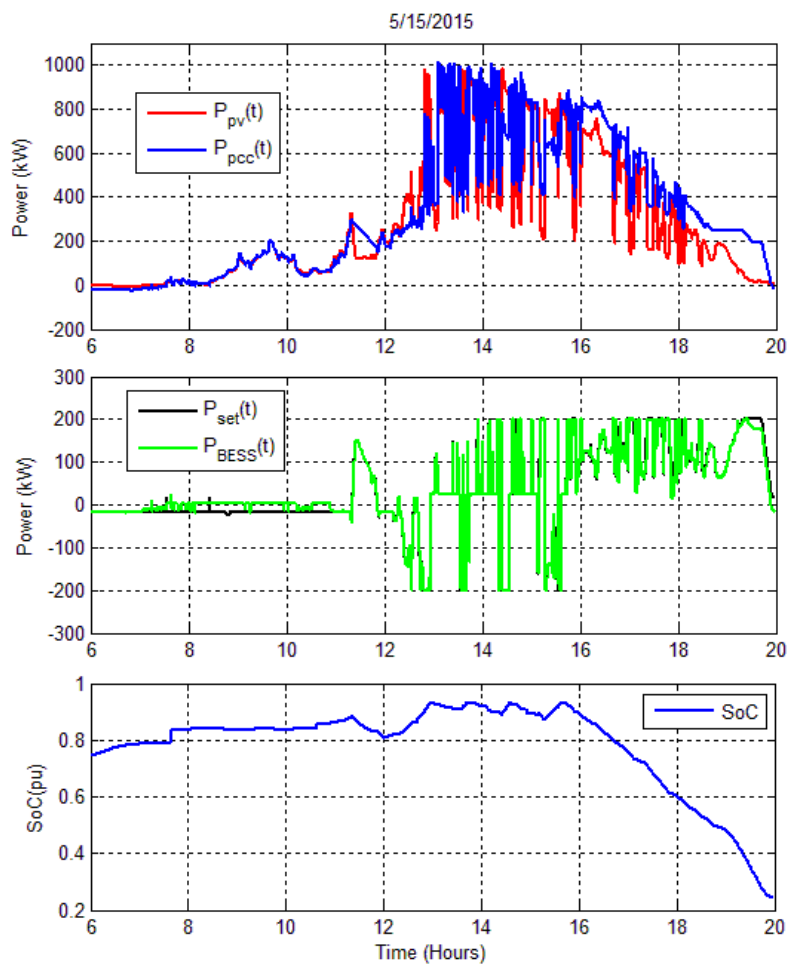


FIGURE 6.18: Practical firming results utilizing generic values for  $SoC_{st}$  &  $m_{dCap}$

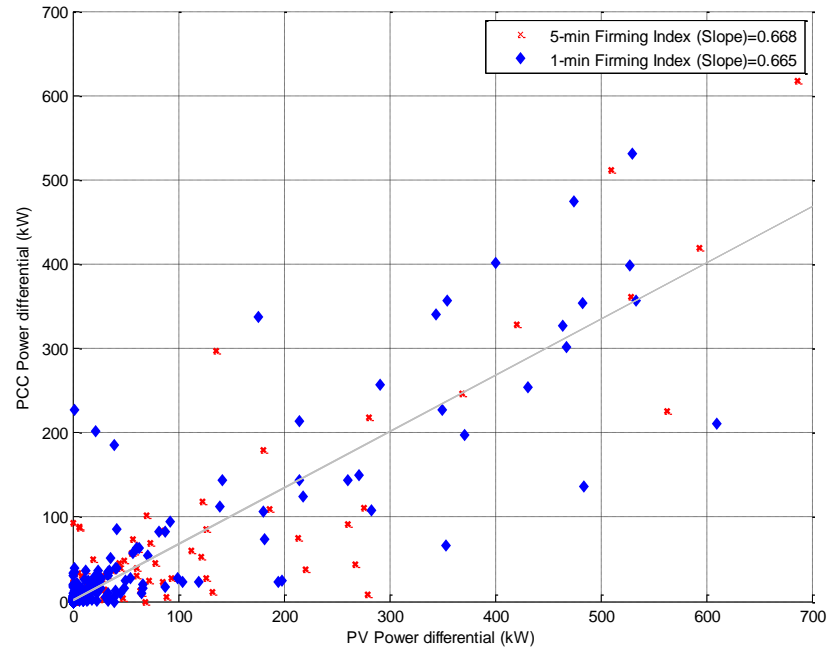


FIGURE 6.19: Firming index for practical firming case adopting generic values for  $SoC_{st}$  &  $m_{dCap}$

On the other hand, when utilizing the daily forecast for May 15<sup>th</sup>, 2015, to identify day type and utilize the corresponding optimal values ( $SoC_{stOpt}=31.4\%$  &  $m_{dCap} = 3.76 \times 10^{-4}$ ) from the lookup table in

TABLE 6.2, simulation results proved an obvious improvement in firming degree

as shown in FIGURE 6.20. This is substantially exhibited (in FIGURE 6.21) in the

improvement in the firming index to a value of 0.28 as compared to the earlier value of

0.665 when generic values were utilized.

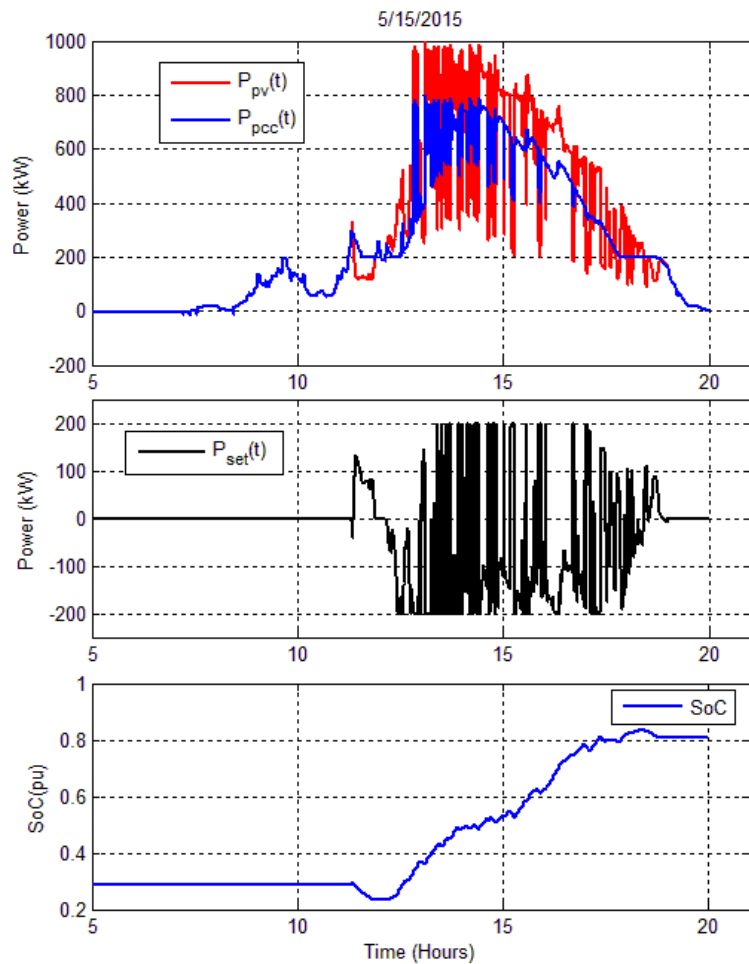


FIGURE 6.20: Simulation firming results utilizing optimal values for  $SoC_{st}$  &  $m_{dCap}^*$  as found in the lookup table

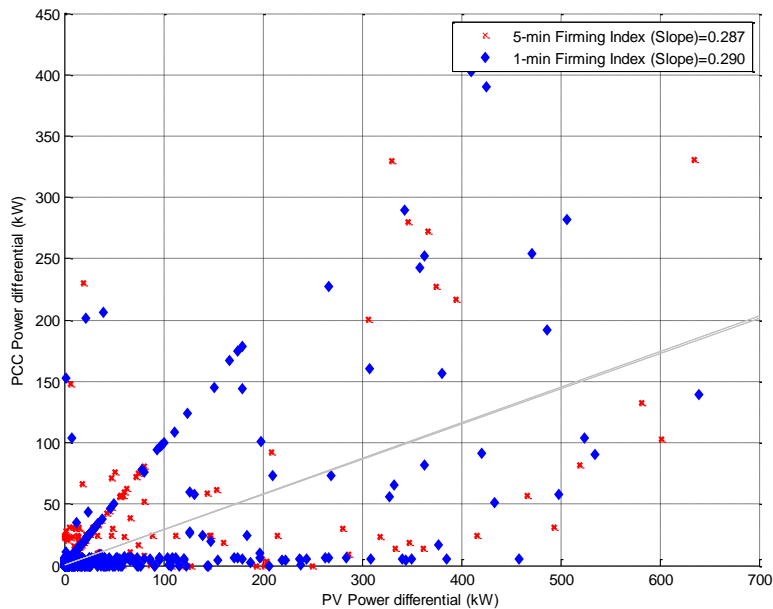


FIGURE 6.21: Firming index for optimized firming adopting optimal values of  $SoC_{st}$  &  $m_{dCap}$  as found in the lookup table

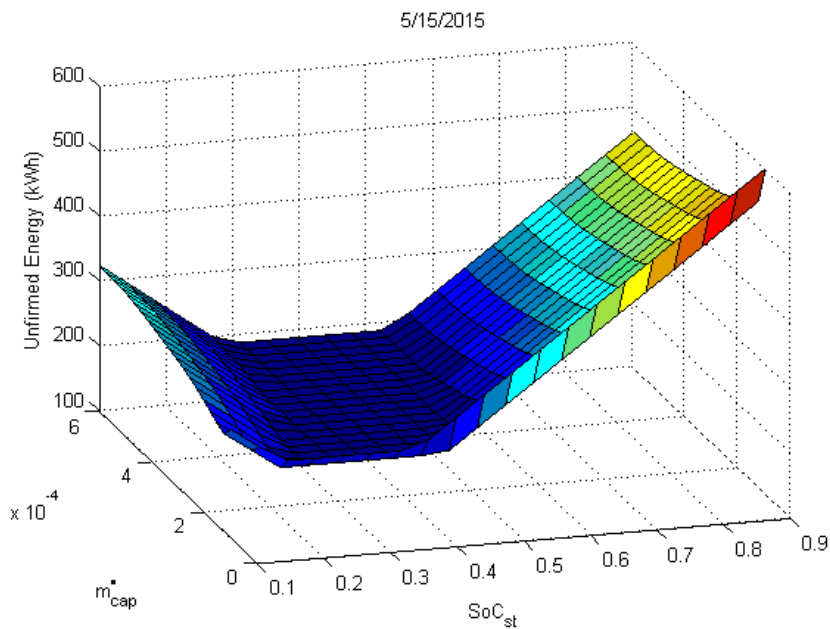


FIGURE 6.22: Optimization routine run for May 15<sup>th</sup> showing minimum attainable unfirming energy for search of  $SoC_{st}$  &  $m_{dCap}$

Further, in order to prove the validity of the assumed optimal values retrieved from the lookup table in TABLE 6.2, the optimization routine is ran for May 15<sup>th</sup> in order to find the minimum possible unfirmed energy and examine the corresponding optimal values for this specific day. Comparing the optimal values found, the look up table value were found as  $SoC_{stOpt}^T = 31.4\%$  &  $m_{dCapOpt}^* = 3.76 \times 10^{-4}$ . Whereas, the optimal values found specifically for May 15<sup>th</sup> are;  $SoC_{stOpt}^S = 36.29\%$  &  $m_{dCapOpt}^* = 3.93 \times 10^{-4}$ . The firming index corresponding to the specific values was found to be 0.26.

## 6.6. Conclusion

The implementation results displayed lead us to conclude that the devised weather pattern recognition aided optimized PVCF algorithm was successful in performing its purposed goal of maximizing firming under BESS capacity, ramp rate and energy constraints. Optimized PV firming was successful in improving firming references from 0.67 to 0.29 for the same test day. The applied communication infrastructure was successful in conveying controller inputs and outputs to and from the BESMS which allowed efficient control. It also provided a great environment for extended testing of the devised improved PVCF algorithm.

## CHAPTER 7: VOLTAGE SUPPORT APPLICATION

### 7.1. Introduction

One of the main and most important concerns for utilities and grid operators is maintaining voltage within permissible levels. Radial networks exhibit voltage depression as the distance from the substation increases. Utilities invest considerable amounts of money on capacitor banks and static VAR compensators to keep voltage levels steady within the permissible band. These devices generate reactive power to counter effect reactive power sinks represented in feeder lines and poor power factor loads connected to the grid like fans, air conditioning systems, washers and dryers. Utilities also invest in numerous voltage regulators (VRs) and load tap changers (LTCs) per feeder. These devices vary the number of turns connected to their primary or secondary winding in order either to buck or boost the voltage depending on the need. Unfortunately, each tap change for such devices decreases their remaining life time which forces utilities to invest in new VRs and LTCs after a shorter period of time. Since VRs and LTCs operate relatively slower than VAR compensators, BESS can be used to compensate for reactive power which in turn, will lead to a decreased total number of regulator operations and tap changes. As mentioned in [1, 27, 28], “BESS voltage support is an application for which distributed storage may be especially attractive because reactive power cannot be transmitted efficaciously over long distances. Notably, many major power outages are at least partially attributable to problems related to transmitting reactive power to load centers. So,

distributed storage – located within load centers where most reactance occurs – provides especially helpful voltage support.”

In our analysis to design a voltage support application, two main approaches were adopted. The first approach involves the continuous deduction of the amount of VARs to be absorbed from, or supplied to the distribution feeder in question, according to a model based analysis. The second approach involves the utilization of a sensor based approach where voltage levels at multiple points on the distribution feeder are monitored in real time. Based on these values, the amount of VARs, dispatched or absorbed, is deduced.

## 7.2. Model Based Voltage Support (MBVS)

The MBVS method utilizes a system model that was aggregated. The un-aggregated base model is the local Utility’s 720 node CYME model. This model was aggregated to a 16 bus system in PSCAD. The 16 bus PSCAD model was further aggregated to allow for real time reactive power support value calculation.

### 7.2.1. Methodology

The voltage support application relies on matching the PCC voltage and phase values to that of the substation. The required reactive power to be injected or drained to hold the voltage at the same value of the substation bus is calculated and set as a reference value ( $Q_{\text{essr}}$ ) for the BESS.

The reactive power ( $Q_{12}$ ) transmitted in a two bus system from bus 1 to bus 2 shown in FIGURE 7.1 is given by;

$$Q_{12} = \frac{|V_1|^2}{|Z|} \sin\gamma - \frac{|V_1||V_2|}{|Z|} \sin(\gamma + \delta_1 - \delta_2) \quad (7.1)$$

$\delta_1$  and  $\delta_2$  are the respective voltage angles at buses 1 and 2. Feeder resistance is relatively small compared to inductance. So, let us assume feeder lines to be fully reactive i.e. ( $R=0$ ,  $Z=jX$ ). Equation (7.1) Becomes:-

$$Q_{12} = \frac{|V_1|^2}{X} - \frac{|V_1||V_2|}{X} \cos(\delta_1 - \delta_2) \quad (7.2)$$

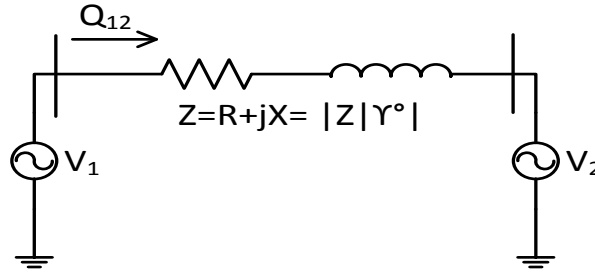


FIGURE 7.1: Two bus system to depict reactive power transmission.

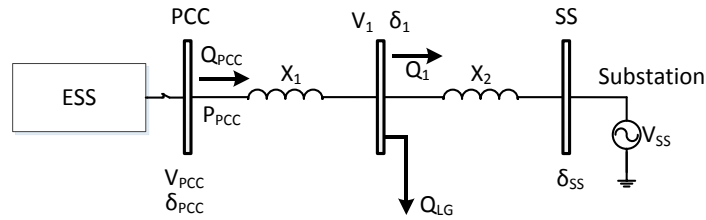


FIGURE 7.2: Aggregated model of a medium voltage feeder

Applying (7.2) to the system in FIGURE 7.2, we get;

$$Q_1 = \frac{|V_1|^2}{X_2} - \frac{|V_1||V_{ss}|}{X_2} \cos(\delta_1 - \delta_{ss}) + \frac{|V_1|^2}{X_1} - \frac{|V_1||V_{PCC}|}{X_1} \cos(\delta_1 - \delta_{PCC}) + Q_{LG} = 0 \quad (7.3)$$

$$Q_{PCC} = \frac{|V_{PCC}|^2}{X_1} - \frac{|V_{PCC}||V_1|}{X_1} \cos(\delta_{PCC} - \delta_1) \quad (7.4)$$

From equations (7.3) & (7.4), we get;

$$Q_{PCC} = \frac{|V_{PCC}|^2}{X_1} - \frac{|V_1||V_{SS}|}{X_2} \cos(\delta_1 - \delta_{SS}) + \frac{|V_1|^2}{X_2} + \frac{|V_1|^2}{X_1} + Q_{LG} \quad (7.5)$$

The goal is to calculate the reactive power to be injected at the PCC to attain a voltage equal to the voltage at the substation. So, we equate ( $V_{PCC}$ ) to ( $V_{SS}$ ) in equation (7.5). Under this condition, we assume the voltage at bus 1 to be 1pu. The active power injected at PCC is zero since active power supplied by the ESS is zero during voltage support. Equation (7.6) represents the approximate reactive power amount to be injected at the PCC to attain a voltage equal to that at the substation.

$$Q_{PCC} = \frac{|V_{SS}|^2}{X_1} - \frac{|V_{SS}|}{X_2} \cos(\delta_{PCC} - \delta_{SS}) + \frac{1}{X_1} + \frac{1}{X_2} + Q_{LG} \quad (7.6)$$

Voltage at the substation and the PCC is constantly monitored. ( $Q_{PCC}$ ) is calculated during operation and given to the BESS as a reference to support the voltage at the PCC. The reactance and reactive power load ( $Q_{LG}$ ) terms in (7.6) is considered as a constant in real time and is tuned till optimum reactive power support is attained.

### 7.2.2. Simulation Results

The methodology discussed is applied to the PSCAD model shown in FIGURE 7.3. Model input is a varying feeder load that was recorded from the actual load of the practical feeder. The real time calculated reactive power from equation (7.6) is given as the reference signal ( $Q_{ESSr}$ ) to the BESS.

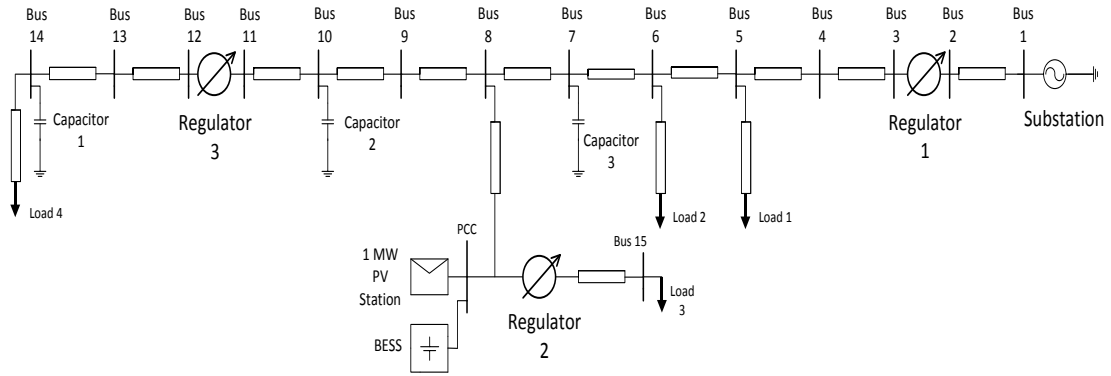
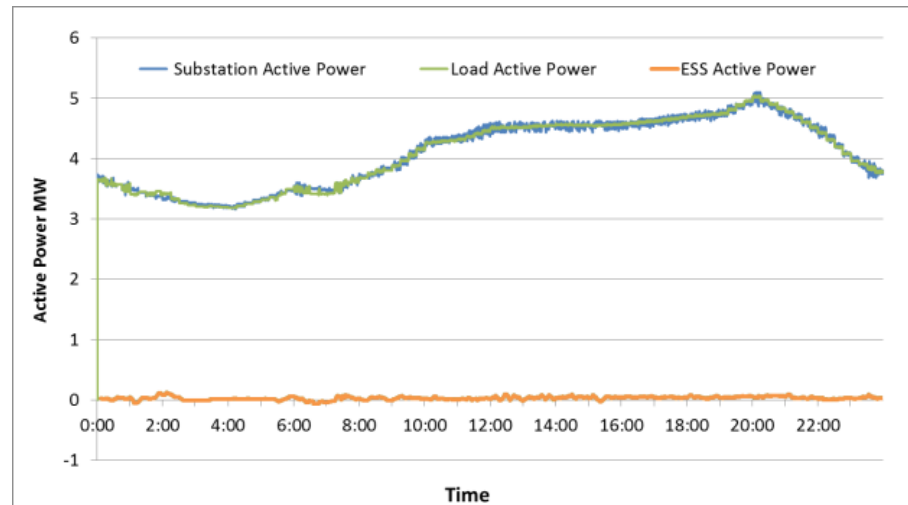
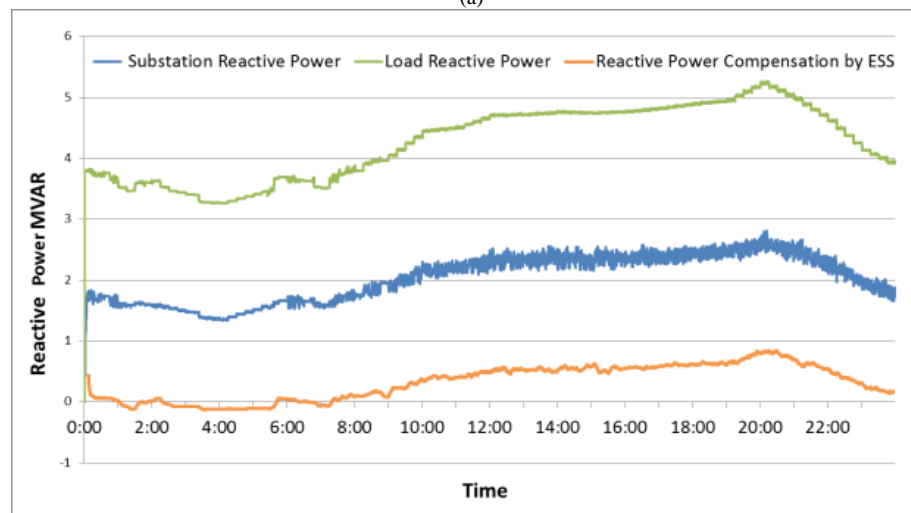


FIGURE 7.3: PSCAD distribution feeder model

Voltage at the substation and the PCC is monitored and compared for two main cases. The first case, is when the BESS is used for MBVS. The second case is when the BESS is operating at a unity power factor. During this simulation, the active and reactive power output of the PV station is zero. Feeder load is set to a typical load curve as shown in FIGURE 7.4(a&b).



(a)



(b)

FIGURE 7.4: Feeder loads and generation. (a)Active power output of substation & ESS, plotted with feeder active power load. (b)Reactive power output of substation & ESS, plotted with feeder reactive power load

FIGURE 7.5 and FIGURE 7.6 show the voltage profile of the PCC and the substation buses with and without MBVS BESS reactive power compensation. In both cases, feeder automatic voltage regulators are offline. It is clear that in the case of reactive power compensation by the ESS, voltage band is tighter and the BESS is effective in supporting voltage without the presence of voltage regulators on the feeder.

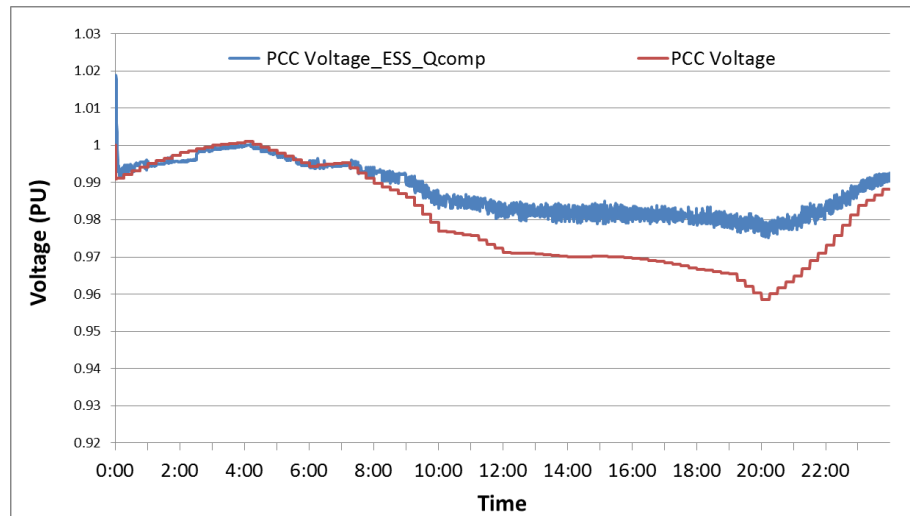


FIGURE 7.5: Voltage profile at PCC with and without MBVS

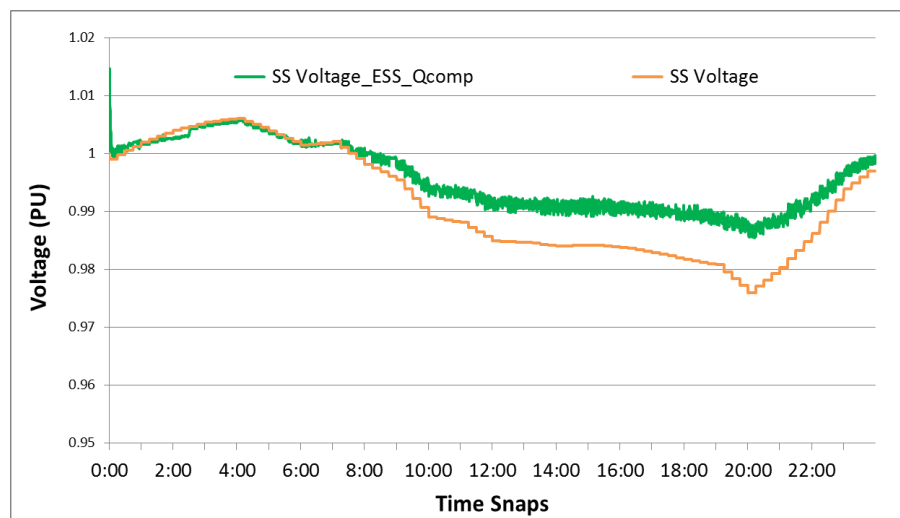


FIGURE 7.6: Voltage profile at substation with and without MBVS

Further, a second simulation is conducted seeking the identification of the effect MBVS has on feeder voltage regulators. Through this simulation, voltage regulators are operational and their performance is monitored for both cases, when BESS is running the MBVS function and when it is off. Figures 6.7, 6.8 and 6.9 show the operation of the

three feeder voltage regulators shown in FIGURE 7.3 for the case when MBVS is running and also, when it is not.

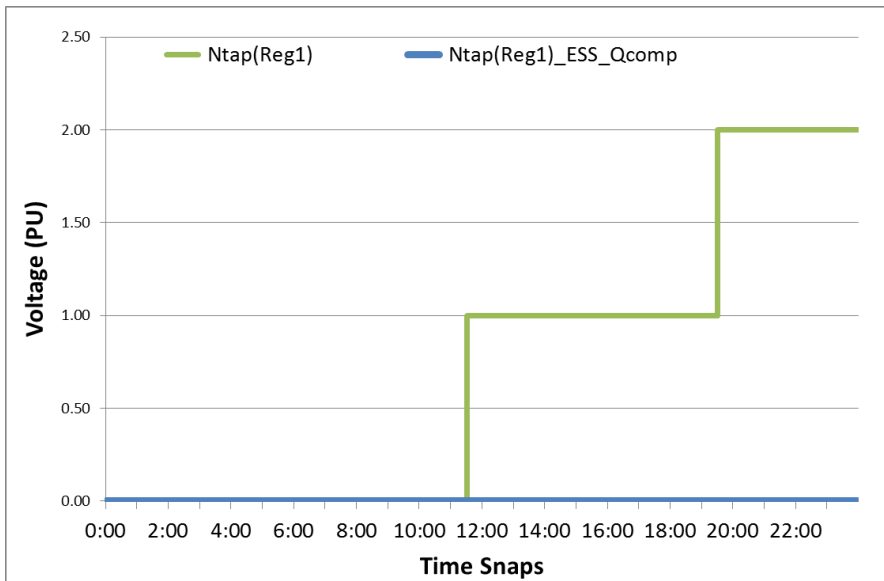


FIGURE 7.7: Voltage Regulator 1 tap operations

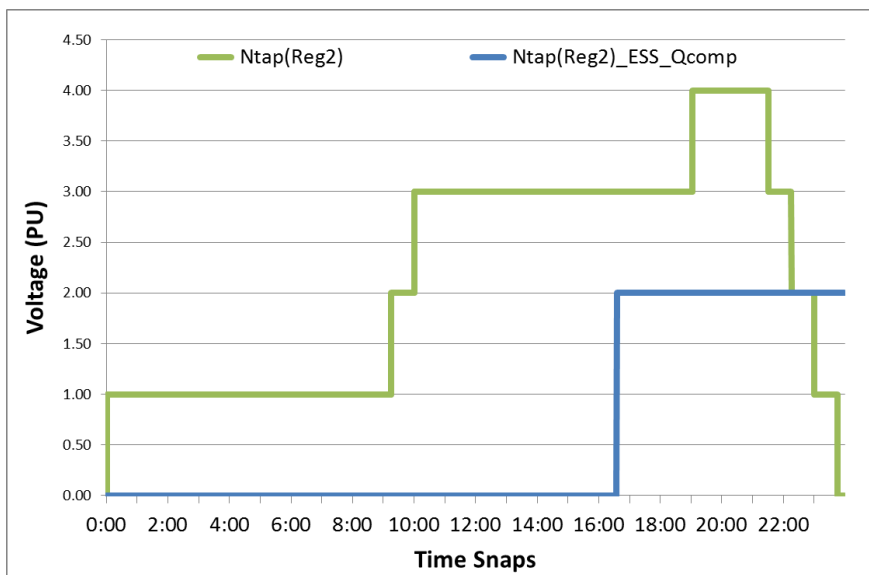


FIGURE 7.8: Voltage Regulator 2 tap operations

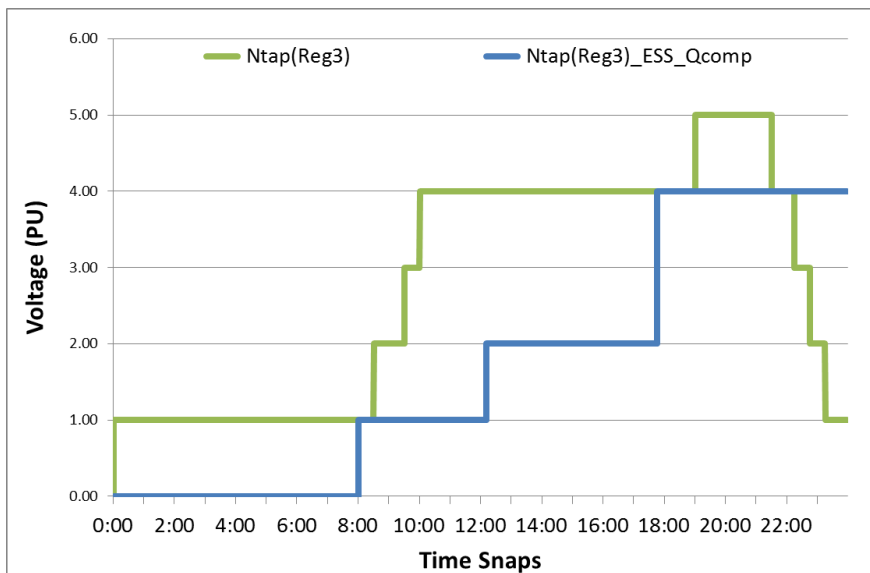


FIGURE 7.9: Voltage Regulator 3 tap operations

Results of both simulations conducted is summarized in TABLE 7.1

TABLE 7.1: MBVS Simulation results summary

	Case	PCC Voltage		SS Voltage		Reg1	Reg2	Reg3
		Min	Max	Min	Max			
Voltage Regulators: ON	<i>ESS: Off</i>	0.974	1.003	0.988	1.01	2	7	8
	<i>ESS Compensation</i>	0.978	1	0.986	1.0051	0	1	3
Voltage Regulators: OFF	<i>ESS: Off</i>	0.958	1.002	0.976	1.005	N/A	N/A	N/A
	<i>ESS Compensation</i>	0.976	1	0.986	1.005	N/A	N/A	N/A

### 7.2.3. Implementation Results

Field implementation of the designed MBVS algorithm was carried out through the communication infrastructure shown in FIGURE 7.10. A Java code is written to analyze streaming data from different points on the feeder and calculate the BESS

reference values based on the algorithm discussed. This code resides physically on a computer in a remote lab. Messages are continuously published to the BESS. The time step for receiving and publishing messages is 1.7 seconds.

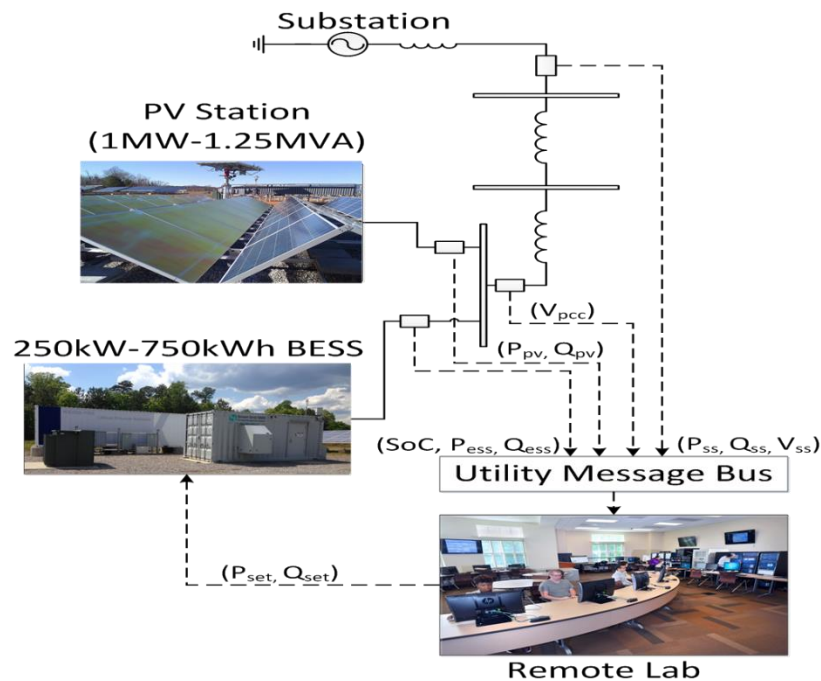


FIGURE 7.10: Field testing communication infrastructure

The following two figures show BESS reactive power dispatch, substation voltage, PCC voltage, feeder active and reactive power load for two day. These days are chosen such that the feeder load is greater in the case that the MBVS algorithm is chosen to be on. The thought is that the day in which the algorithm is chosen to be on, should be characterized by a feeder load profile that is, either similar to, or greater than that of the day in which the algorithm is off. This provides a fair basis of comparison. The first day, the BESS MBVS algorithm is off. So, reactive power dispatch is zero. This operation was

performed on the 26<sup>th</sup> of January, 2015. The second day, BESS MBVS algorithm is on.

This operation was performed on the 27<sup>th</sup> of January, 2015.

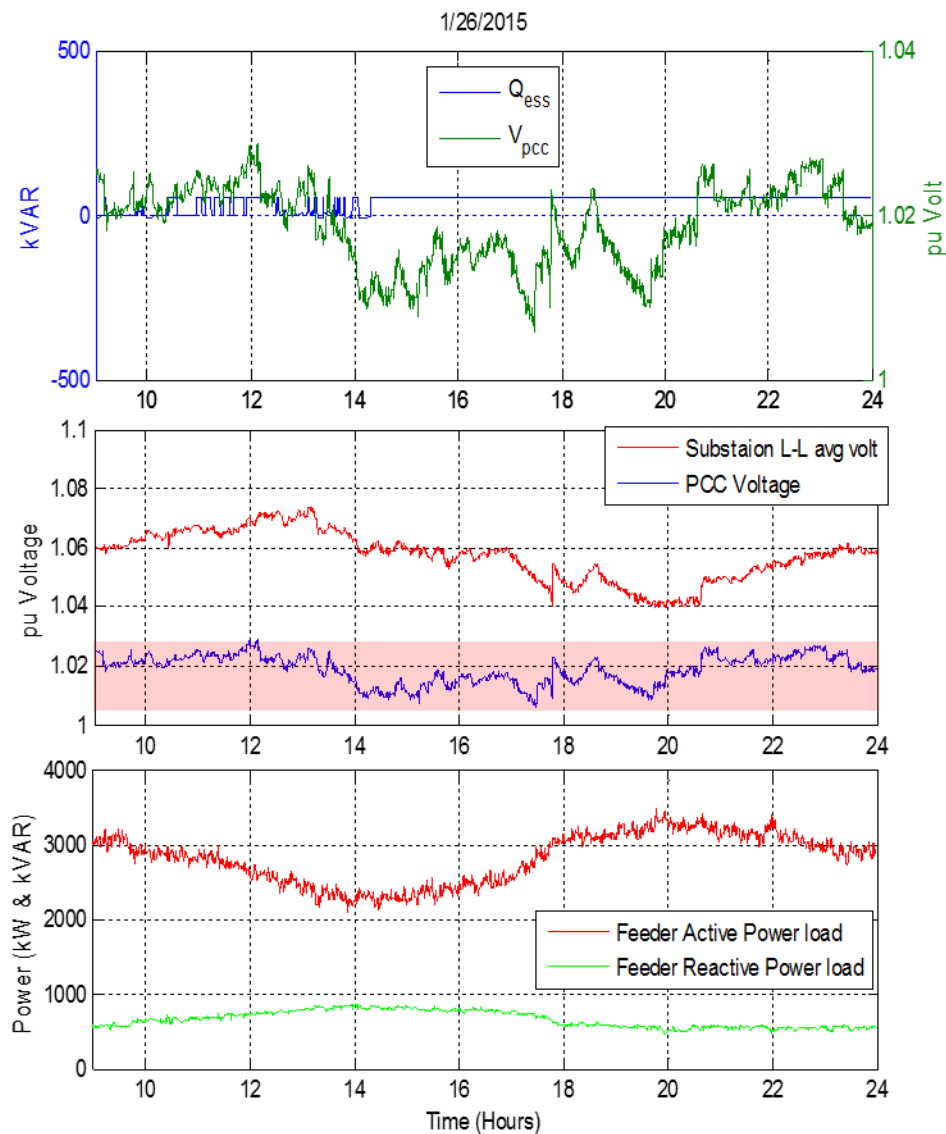


FIGURE 7.11: Voltage support parameters for day with MBVS application on (January 26<sup>th</sup>, 2015)

As shown through the first day in FIGURE 7.11, the voltage profile at the PCC varies more than 2% throughout the day. Whereas the second day in FIGURE 7.12,

shows that the PCC voltage profile variates approximately 0.5% throughout the day. This shows a clear suppression of voltage swings.

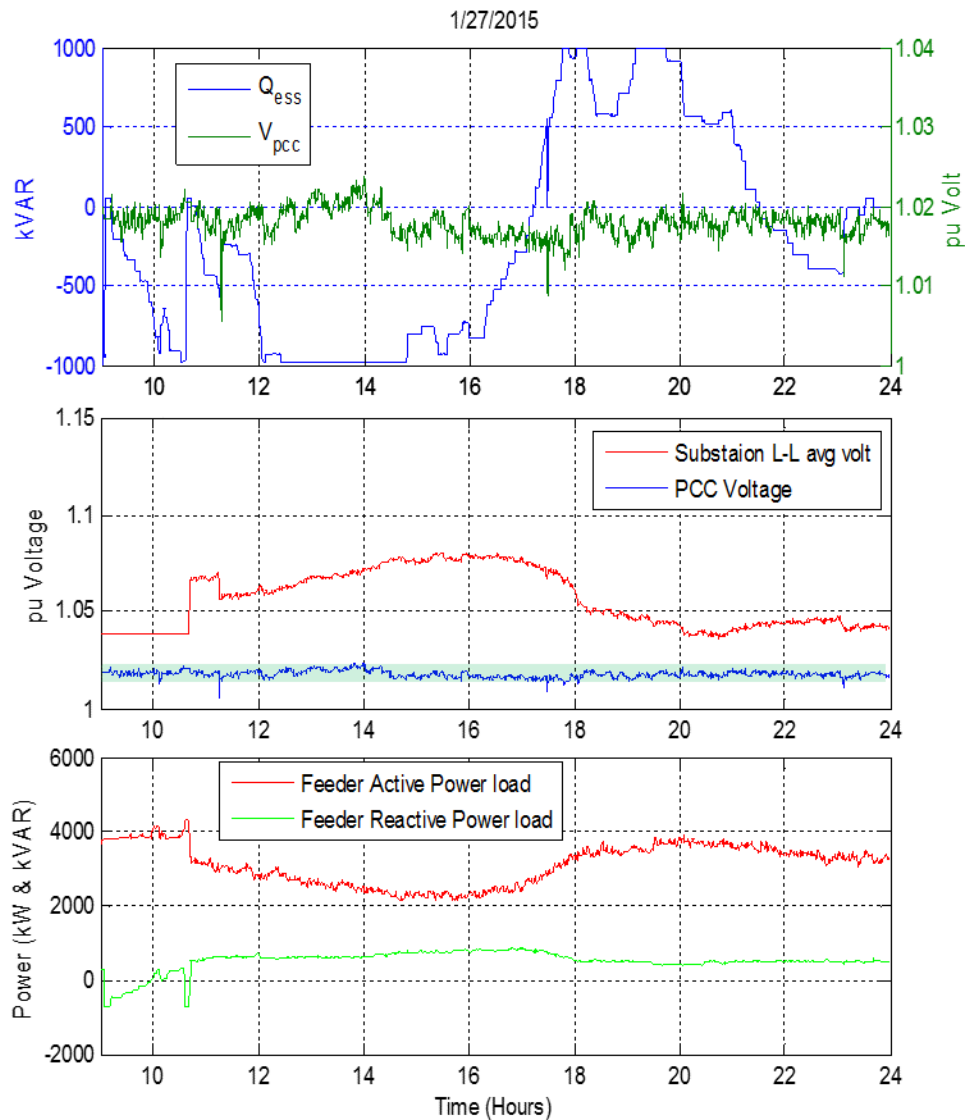


FIGURE 7.12: Voltage support parameters for day with MBVS application off (January 27<sup>th</sup>, 2015)

The operation of the MBVS algorithm results in an improvement in the number of voltage regulator tap operations as shown in FIGURE 7.13 & FIGURE 7.14.

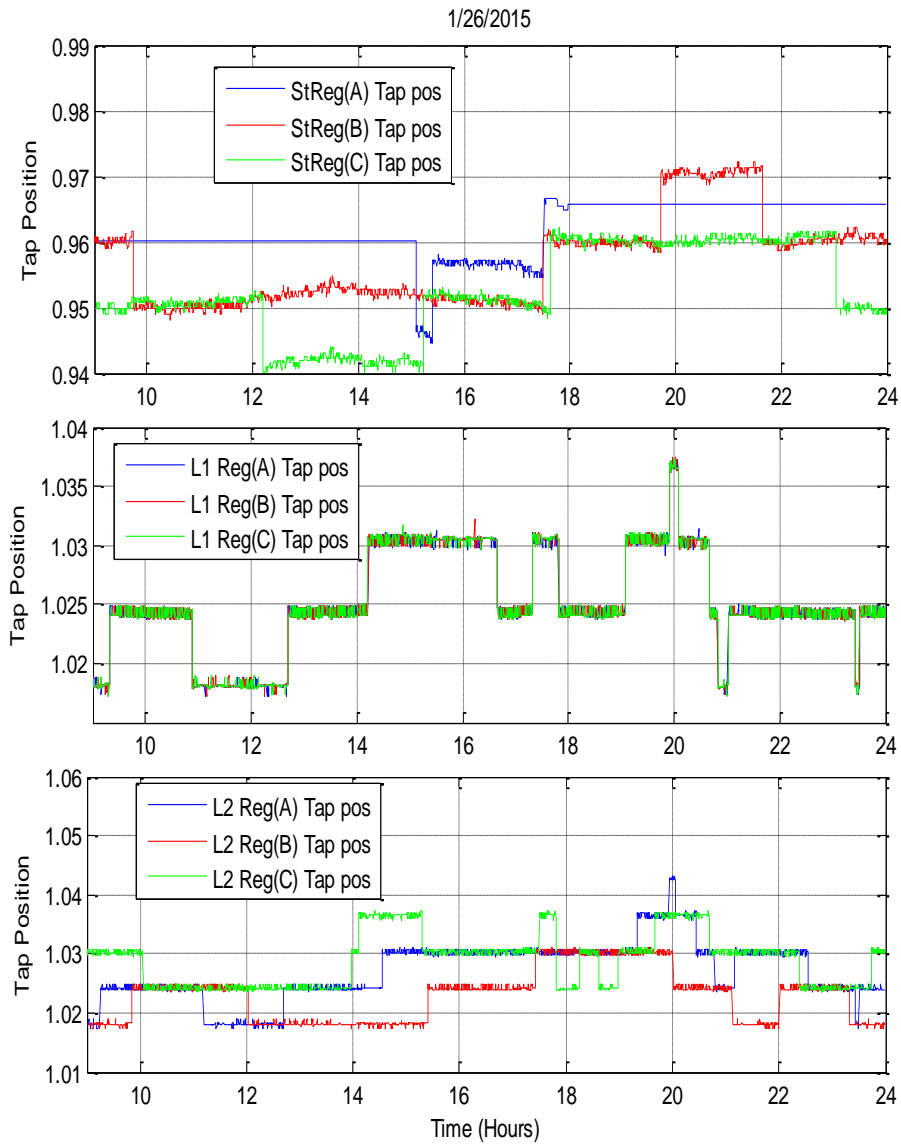


FIGURE 7.13: Feeder voltage regulators tap operations for day with MBVS application off (January 26<sup>th</sup>, 2015)

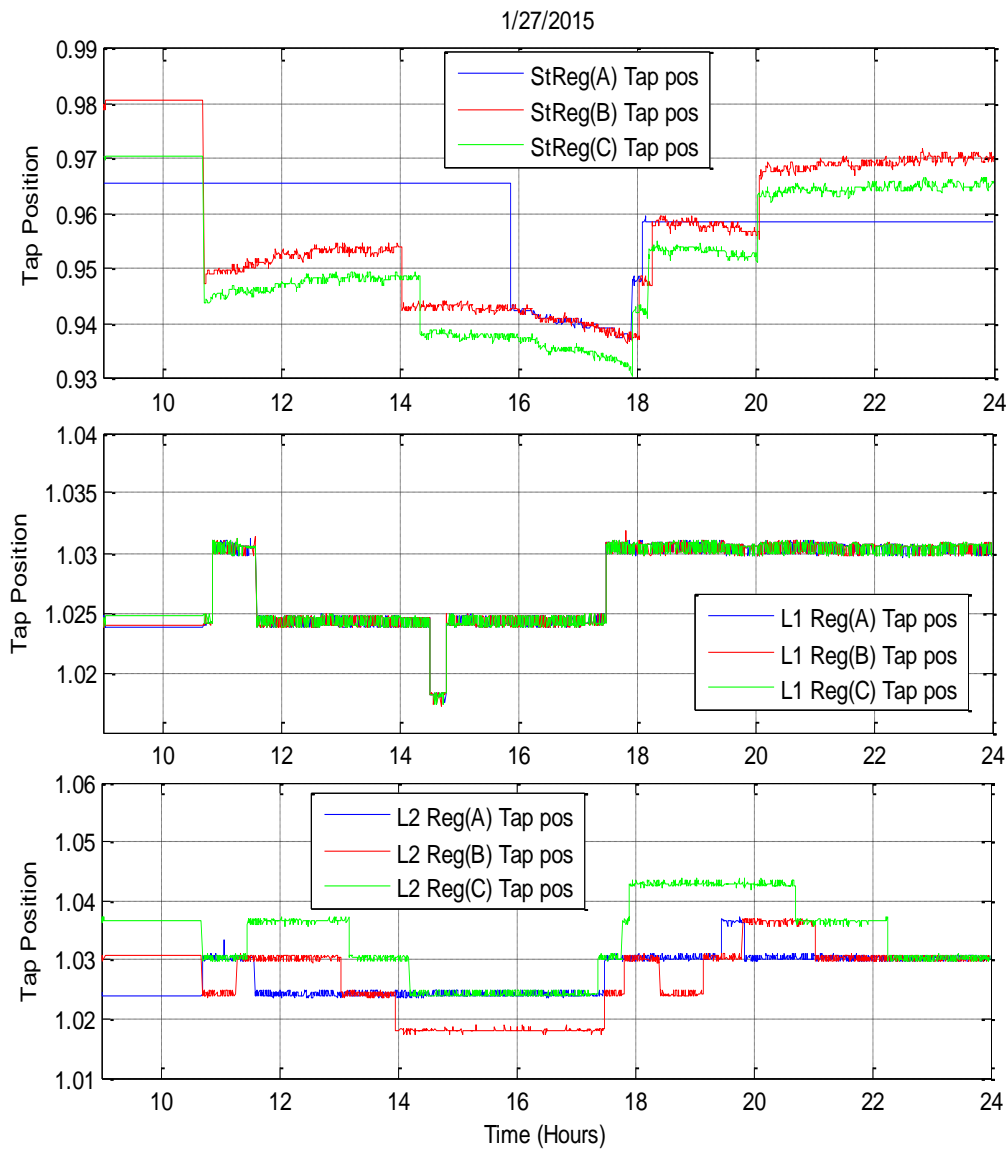


FIGURE 7.14: Feeder voltage regulators tap operations for day with MBVS application on (January 27<sup>th</sup>, 2015)

TABLE 7.2 indicates a clear reduction in number of tap operations when the MBVS was utilized. This comes with the exception of one case where the number of operations actually increased with the MBVS algorithm on.

TABLE 7.2: Voltage regulator tap operations comparison

Tap Operations				
	Phase	Station Regulator	Line Regulator 1	Line Regulator 2
No Voltage Support (1/26/2015)	A	3	15	14
	B	4	15	9
	C	4	15	14
BESS Voltage Support (1/27/2015)	A	2	5	6
	B	4	5	10
	C	4	5	10

### 7.3. Sensor Based Voltage Support (SBVS)

The MBVS algorithm presented plausible. However, it greatly relies on the feeder model which may not be as accurate as we think. Aggregations and approximations that are valid in nature may not be entirely suitable to for real time controller operation. Further, the intent of this controller is to rely on a sensor based operation scheme to allow for controller adaptability to different hosting systems. Therefore, a sensor based voltage support algorithm is pursued.

#### 7.3.1. Methodology

Operation of the sensor based voltage support algorithm relies on monitoring feeder line voltage regulators tap warnings. Tap warnings, as defined here, are signals that are issued by the voltage regulator and can be either a High Band (HB) or Low Band (LB) signal. These signals are binary values indicating a voltage violation when they maintain a value of “one” in binary. When the HB or LB is sustained at a binary “one” value for 45 seconds, a tap up or tap down operation is performed, respectively. If the voltage violation is cleared within these 45 seconds, the tap operation does not occur.

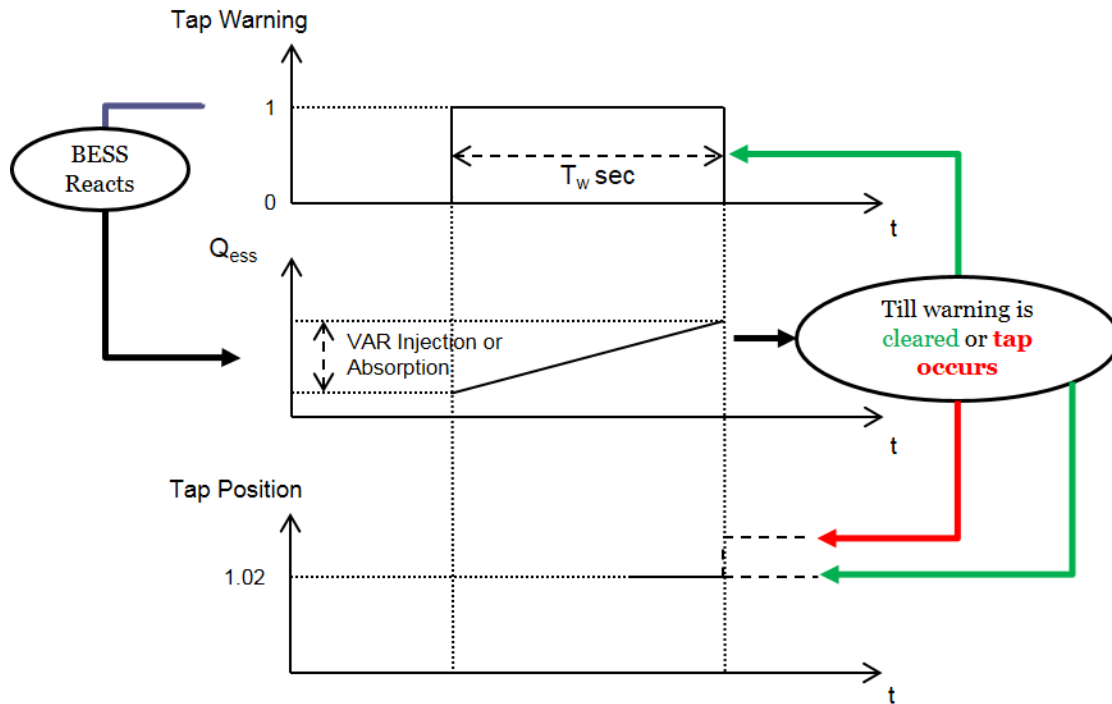


FIGURE 7.15: SBVS algorithm methodology

Tap warnings set immediately after a voltage violation and clear either after the voltage violation is cleared or the tap operation occurs, which usually clears the voltage violation and, in turn, the tap warning. Here, it is desired to utilize tap warnings to clear voltage violations and save tap operations.

Therefore, as indicated in FIGURE 7.15, the SBVS algorithm will operate as follows:-

- A warning is detected via MQTT messages
- BESS injects or absorbs VARS at a preset rate
- Either the tap warning is cleared or the voltage violation is too severe to be covered by BESS VAR capability at its distant location (VR1 and BESS site)

Further, a criteria is built to monitor the performance of the SBVS algorithm. This criteria aims to identify the number of unexecuted tap warnings. Which serves as a good indication of the number of saved tap changes. Furthermore, this index could be weighed versus averaged long term maintenance logs of VRs and be more accurately used to identify exact number of saved tap operations and in turn, monetize the performance of the algorithm through the deferred upgrade of the VR and decreased maintenance needs.

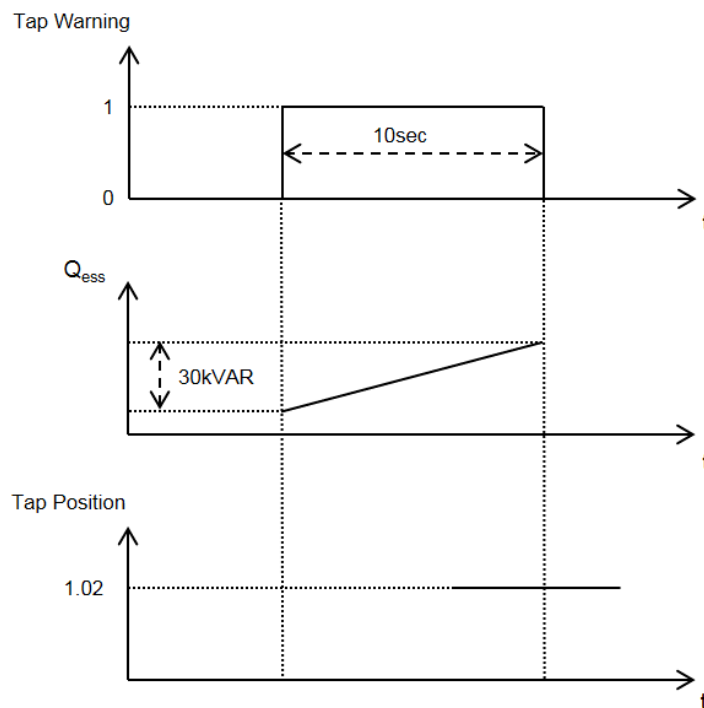


FIGURE 7.16: Unexecuted tap change identification criteria

As shown in FIGURE 7.16, this criteria sets the following rules to identify an Unexecuted Tap Warning (UTW):-

- Duration of high band or low band warning is greater than 10 sec

- BESS reactive power output changed by more than 30 kVAR during this band duration
- A tap change did not occur

### 7.3.2. Implementation Results

The discussed methodology is practically tested through the communication system shown in FIGURE 7.10. Actual voltage regulator tap operations, warnings and voltage levels are monitored, utilized and recorded for analysis. The following figures are presented to show SBVS operation targeting Line Regulator 2 (Reg 3 in FIGURE 7.3). FIGURE 7.17 shows substation regulator tap positions, tap warnings, BESS reactive power and PCC voltage. FIGURE 7.18 and FIGURE 7.19 show the same for Line Regulator 1 (Reg 2 in FIGURE 7.3) and Line Regulator 2 (Reg 3 in FIGURE 7.3), respectively.

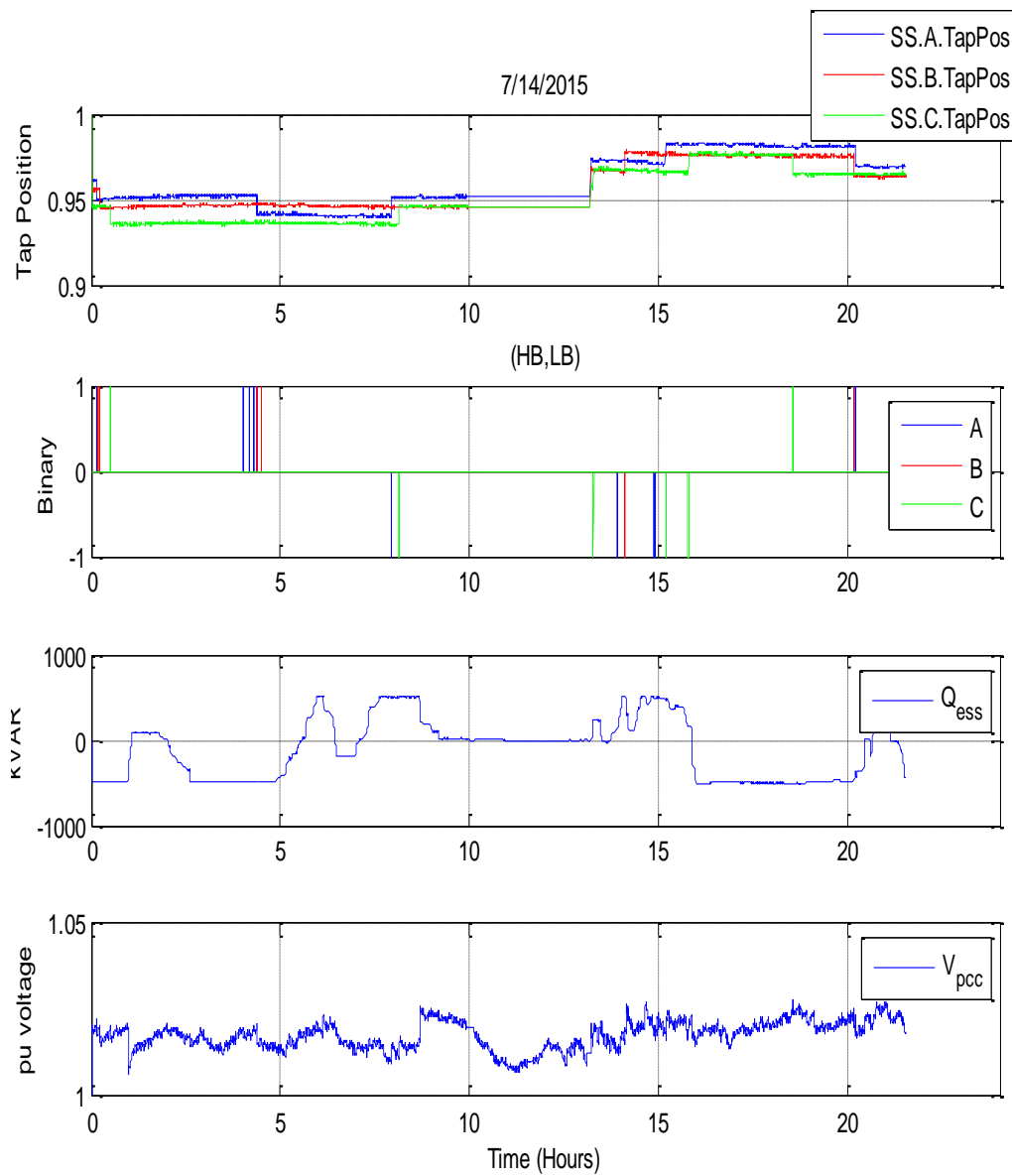


FIGURE 7.17: Substation Regulator (Reg 1) states during SBVS

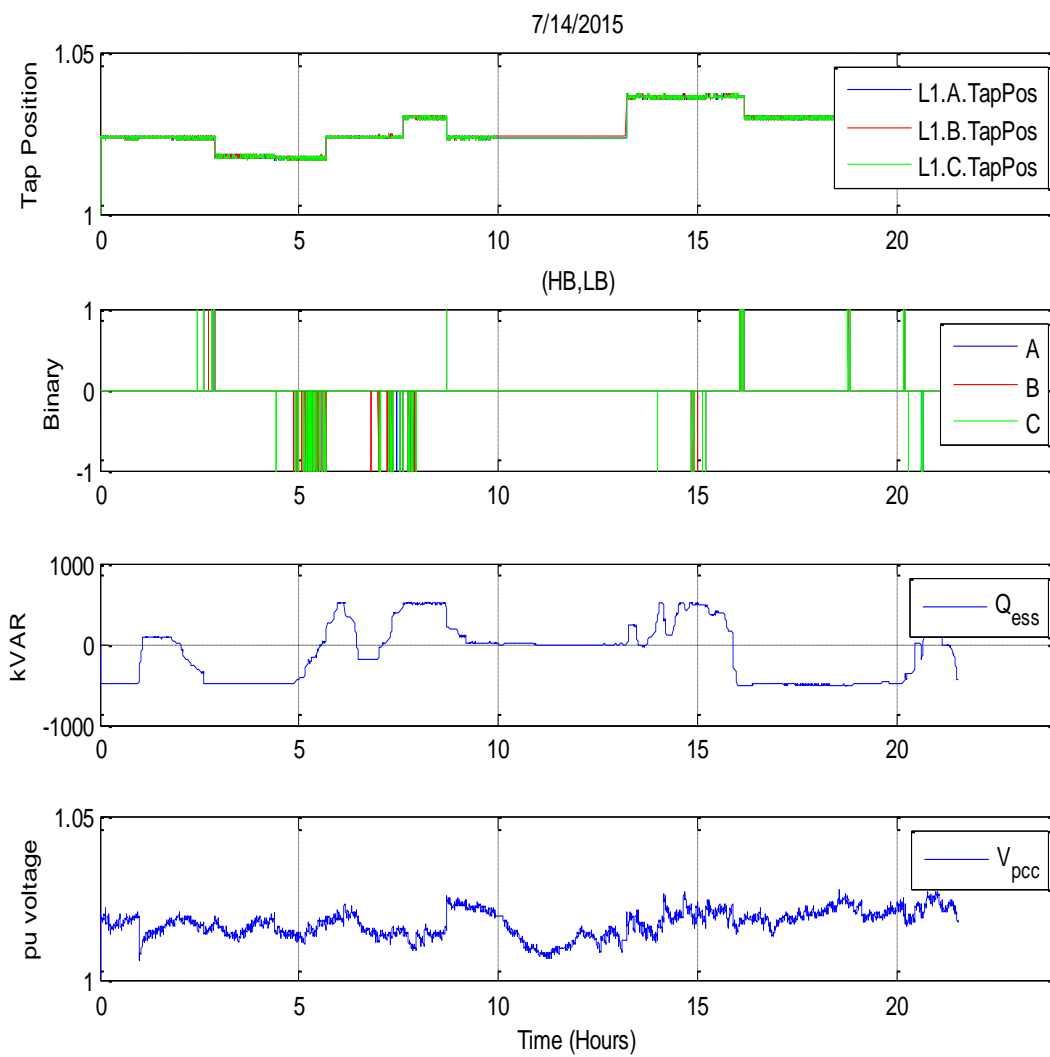


FIGURE 7.18: Line Regulator 1 (Reg 2) states during SBVS

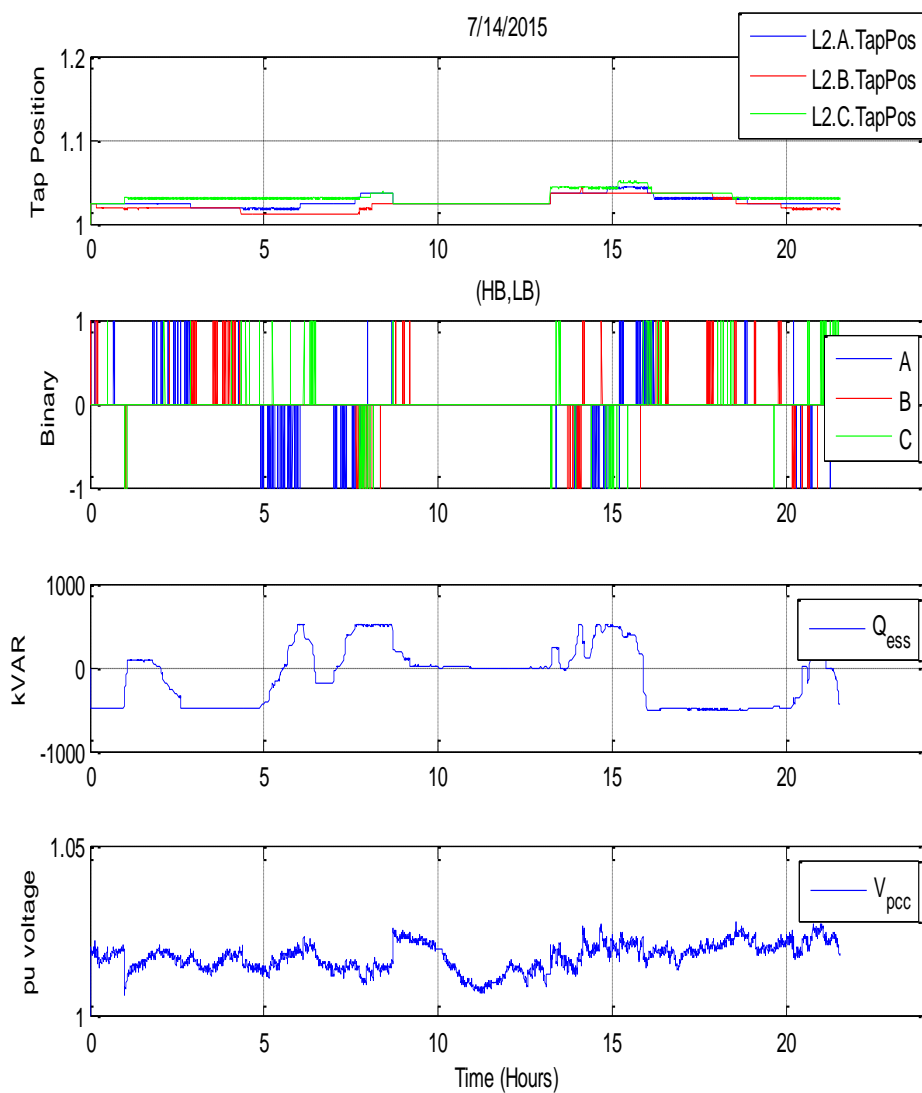


FIGURE 7.19: Line Regulator 2 (Reg 3) states during SBVS

Tap operations for July, 14<sup>th</sup>, 2015 are summarized in TABLE 7.3. It is clear that there is a significant number of UTWs for both line regulators when targeting Line Regulator 2. Also, comparing the number of tap operations (changes) between similar load curve days, with SBVS on and off, reveals an approximate 50% reduction in tap operations.

TABLE 7.3: Regulators operation summary targeting Line Regulator 2

Tap Changes Summary 14 July, 2015									
	Station Regulator A	Station Regulator B	Station Regulator C	Line Regulator 1 A	Line Regulator 1 B	Line Regulator 1 C	Line Regulator 2 A	Line Regulator 2 B	Line Regulator 2 C
Band Warnings	18	11	14	127	119	120	215	176	191
Tap Changes	6	4	4	7	7	7	11	10	9
Unexecuted Warnings due to BESS VS Alg.	0	0	2	10	6	8	39	4	12
							Targeted Regulator		

TABLE 7.4: Regulators operation summary targeting Line Regulator 2

Tap Changes Summary 28 May, 2015									
	Station Regulator A	Station Regulator B	Station Regulator C	Line Regulator 1 A	Line Regulator 1 B	Line Regulator 1 C	Line Regulator 2 A	Line Regulator 2 B	Line Regulator 2 C
Band Warnings	32	154	32	227	212	216	428	383	226
Tap Changes	11	0	9	15	15	15	16	22	20
Unexecuted Warnings due to BESS VS Alg.	2	N/A	1	34	29	31	26	6	5
							Targeted Regulator		

Tap operations for May, 28<sup>th</sup>, 2015 are summarized in TABLE 7.4. It is clear that there is a significant number of UTWs for both line regulators when targeting Line Regulator 1.

#### 7.4. Conclusion

In this chapter, two main voltage support methodologies were discussed, simulated and implemented. The MBVS algorithm presented plausible results and proved flexible for improvements. Since it is model based, optimization of different parameters can be performed offline and applied to the actual system based on simulation results. However, relying on a model allows room for errors and non-idealities which are attributed to the witnessed difference between operation of the practical and model system. Further, feeder adjustments (new circuits) which occur more than often by any

utility will be a certain cause for the practical system to deviate from its established model. This may cause the MBVS algorithm to fail. The SBVS algorithm proved efficient in minimizing feeder regulator tap operations. Unlike the MBVS method, it presented a flexible and adaptable solution for practical installations. However, relying on a model-less algorithm dictates various parameters based on a trial and error technique. Amongst these parameters is the reactive power ramp rate.

Conclusively, voltage support utilizing either methods proved effective in voltage profile improvement and tap operation reduction.

## CHAPTER 8: CONCLUSION

### 8.1. Introduction

In the previous chapters, the practical and model specifications of a battery energy storage system and PV station were thoroughly discussed. The integration of three main storage applications into one controller was studied in depth, simulated and implemented on a practical residential feeder in North Carolina. The designed PVCF application presented valuable results as presented in large PV power swing suppression and ramp rate control. The designed ETS algorithm was also successful in tracking expected feeder peak load magnitude and time which allowed efficient battery active power dispatch to allow peak load shaving. The optimization of PV power swings firming in light of the need to maximize battery SoC at a certain time was found to be crucial to allow for effective ETS performance. Reactive power compensation for voltage support presented valuable simulation and implementation results for both model based and sensor based voltage support.

## 8.2. Conclusion

Two main PVCF applications were designed and tested. Both applications were tested on an EMTP simulation platform (PSCAD). Promising simulation results, presented in suppression of PV power swings to 33% of previous values, was followed by practical implementation which provided substantial firming as indicated by 0.2 firming indexes. Integrating weather pattern recognition to the optimize PVCF proved to present significant firming improvements. Implementation results displayed, lead to the conclusion that the devised algorithm was successful in performing its purposed goal of maximizing firming under BESS capacity, ramp rate and energy constraints. Optimized PV firming was successful in improving firming indexes from 0.67 to 0.29 for the same test day. The applied communication infrastructure was successful in conveying controller inputs and outputs to and from the BESMS which allowed efficient control. It also provided a great environment for extended testing of the devised improved PVCF algorithm.

For the ETS application, simulation as well as implementation results proved that weekend and weekday load curves could both be used for accurate peak load magnitude and time prediction for the residential feeder in question. The optimal moving average algorithm time interval was deduced for each individual prediction parameter in order to minimize average error. The used energy time shift algorithm was found to be effective in covering the time of peak load. Optimization of the PVCF algorithm to allow proper coordination with ETS was found to be effective and greater peak load reduction was possible.

Voltage support utilizing either of the discussed methods (MBVS & SBVS) proved effective voltage profile improvement at several feeder nodes. Tap operation reduction at both of the line regulators and the station regulators was achievable with the VAR capabilities of the utilized BESS.

Communication infrastructure provided a great environment for extended testing of the devised algorithms. It was also successful in conveying controller inputs and outputs to and from the BESMS which allowed efficient control.

Conclusively, the implementation results displayed lead us to deduce that the designed controller, packaging its three main applications, could present a viable and valuable grid modernization solution to increase the penetration of renewable energy systems on distribution feeders. It also presented peak load shaving advantages which could lead to a direct reduction in the leveled cost of energy if implemented on a large scale. Further, this integrated controller proved to significantly improve voltage characteristics throughout the feeder while having a direct impact on the reduction of substation and line voltage regulator tap operations.

### 8.3. Future Work

In the future work, economic value, Productization of the designed controller and integrating forecasting methods to the developed battery energy storage applications should be studied. Further, the integration of a fourth application to address grid phenomena like “Load Duck Neck Curves” caused by large grid connected PV stations ramping down in the evening while residential loads are ramping up, is proposed to be sought.

### 8.3.1. Economic Value Evaluation

In the future, the evaluation of the economic benefits of the studied applications will be sought, in light of the individual value that each application provides. Further, each application operational priority is proposed to be set according to its real time economic revenue.

### 8.3.2. Controller Productization

The presentation of energy storage as a solution for distribution level renewables integration is predicted to flourish, especially with the price of battery energy storage technologies continuing to decrease. Therefore, controller source code is sought to be modified to allow for adaptability to new PV/BESS systems. This will allow the designed controller to be a general solution for similar system setups where the integration of new PV stations to the grid can be accompanied by a suitable BESS controlled by the designed controller. In that case, PV integration into distribution feeders will not be as impactful.

### 8.3.3. Grid Ramp Rate Control

The increased penetration of PV capacity on our grids causes several anomalies at the slack generation level. A perfect example is the increased generation ramp rate required from slack generation, resulting from grid generation decreasing while grid load is increasing. This occurs during the evenings in circuits with high PV penetration. It is proposed to integrate a storage application to counter act such ramp rates when they are most impactful.

#### 8.3.4. Forecast Integration

The effectiveness of the energy storage applications presented in this research can be greatly advanced if a forecasting method was to be integrated into each. The PV station capacity firming application designed could highly value a 2-4 minute forecast methodology. This is presumed to result in significant improvement in firming indexes. Also, it could allow for unavoidable communication delays to be overcome. The energy time shift application would also benefit from load forecasting if it were to provide lesser peak load time prediction errors. Further, a forecast based voltage support algorithm could presumably present a significant reduction in Voltage Regulators' tap operations.

(تم هذا العمل بحمد الله وعونه وتوفيقه)

## REFERENCES

- [1] Eyer, J. (2010). Energy Storage for the Electricity Grid: Benefits and Market Potential Assessment Guide A Study for the DOE Energy Storage Systems Program. Sandia Laboratories, 321, 232. doi:SAND2010-0815
- [2] Ribeiro, P. F., Johnson, B. K., Crow, M. L., Arsoy, A., & Liu, Y. (2001). Energy storage systems for advanced power applications. In Proceedings of the IEEE (Vol. 89, pp. 1744–1756). doi:10.1109/5.975900
- [3] Teleke, S.; Baran, M.E.; Huang, A.Q.; Bhattacharya, S.; Anderson, L., "Control Strategies for Battery Energy Storage for Wind Farm Dispatching," Energy Conversion, IEEE Transactions on , vol.24, no.3, pp.725,732, Sept. 2009
- [4] Karasik, V., Dixon, K., Weber, C., Batchelder, B., Campbell, G., & Ribeiro, P. (1999). SMES for power utility applications: a review of technical and cost considerations. IEEE Transactions on Applied Superconductivity, 9. doi:10.1109/77.783354
- [5] Lieurance, D., Kimball, F., Rix, C., & Luongo, C. (1995). Design and cost studies for small scale superconducting magnetic energy storage (SMES) systems. IEEE Transactions on Applied Superconductivity, 5. doi:10.1109/77.402561
- [6] McDowall, J. (2000). Conventional battery technologies-present and future. 2000 Power Engineering Society Summer Meeting (Cat. No.00CH37134), 3. doi:10.1109/PESS.2000.868757
- [7] W. V. Hassenzahl, Capacitors for Electric Utility Energy Storage: Electric Power Res. Inst., 1997, vol. WO-8812.
- [8] Boom, R., & Peterson, H. (1972). Superconductive energy storage for power systems. IEEE Transactions on Magnetics, 8. doi:10.1109/TMAG.1972.1067425
- [9] R. F. Giese, "Progress toward high temperature superconducting magnetic energy storage (SMES) systems—A second look," Argonne National Laboratory, 1998.
- [10] I. D. Hassan, R. M. Bucci, and K. T. Swe, "400 MW SMES power conditioning system development and simulation," Trans. Power Electron., vol. 8, pp. 237–249, July 1993.
- [11] Q. Jiang and M. F. Conlon, "The power regulation of a PWM type superconducting magnetic energy storage unit," IEEE Trans. EnergyConversion, vol. 11, pp. 168–174, Mar. 1996.
- [12] W. R. Lachs and D. Sutanto, "Battery storage plant within large load centers," IEEE Trans. Power Syst., vol. 7, pp. 762–769, May 1992.

- [13] M. A. Casacca, M. R. Capobianco, and Z. M. Salameh, "Lead-acid battery storage configurations for improved available capacity," *IEEE Trans. Energy Conversion*, vol. 11, pp. 139–145, Mar. 1996.
- [14] N.W. Miller, et.al., "Design and commissioning of a 5 MVA, 2.5 MWh battery energy storage," in *Proc. 1996 IEEE Power Engineering Society Transmission and Distribution Conf.*, 1996, pp. 339–345.
- [15] N. Abi-Samra, C. Neft, A. Sundaram, and W. Malcolm, "The distribution system dynamic voltage restorer and its applications at industrial facilities with sensitive loads," in *Proc. 8th Int. Power Quality Solutions '95*, Long Beach, CA, Sept. 9–15, 1995.
- [16] Grid Energy Storage, US Department of Energy Report, December 2013.
- [17] Akhil, A.A., Huff, G, Currier, A.B., Kaun, B.C, Rastler, D.M., Chen, S.B., Gauntlett, W.D. , DOE/EPRI 2013 Electricity Storage Handbook in Collaboration with NRECA. Sandia National Laboratories Report, SAND2013-5131.
- [18] Tremblay, O., & Dessaint, L. (2009). Experimental Validation of a Battery Dynamic Model for EV Applications. *World Electric Vehicle Journal*, 3, 1–10.
- [19] Corley, M.; Locker, J.; Dutton, S.; Spee, R., "Ultracapacitor-based ride-through system for adjustable speed drives," *Power Electronics Specialists Conference, 1999. PESC 99. 30th Annual IEEE* , vol.1, no., pp.26,31 vol.1, Aug 1999
- [20] Pillay, P.; Samudio, R.M.; Ahmed, M.; Patel, R.T., "A chopper-controlled SRM drive for reduced acoustic noise and improved ride-through capability using supercapacitors," *Industry Applications, IEEE Transactions on* , vol.31, no.5, pp.1029,1038, Sep/Oct 1995
- [21] Walker, Loren H., "10-MW GTO converter for battery peaking service," *Industry Applications, IEEE Transactions on* , vol.26, no.1, pp.63,72, Jan/Feb 1990
- [22] Leung, K.K.; Sutanto, D., "A storage power flow controller (SPFC) using battery storage," *Power Electronics and Drive Systems, 1999. PEDS '99. Proceedings of the IEEE 1999 International Conference on* , vol.2, no., pp.827,832 vol.2, 1999
- [23] Kyung-Hee Jung; Hoyong Kim; Daeseok Rho, "Determination of the installation site and optimal capacity of the battery energy storage system for load leveling," *Energy Conversion, IEEE Transactions on* , vol.11, no.1, pp.162,167, Mar 1996
- [24] Schempp, E.; Jackson, William D., "Systems considerations in capacitive energy storage," *Energy Conversion Engineering Conference, 1996. IECEC 96., Proceedings of the 31st Intersociety* , vol.2, no., pp.666,671 vol.2, 11-16 Aug 1996
- [25] Bullard, G.L.; Sierra-Alcazar, H.B.; Lee, H.L.; Morris, J.L., "Operating principles of the ultracapacitor," *Magnetics, IEEE Transactions on* , vol.25, no.1, pp.102,106, Jan 1989

- [26] Rastler, D. (2010) Electricity Energy Storage Technology Options: A White Paper Primer on Applications, Costs, and Benefits. Electric Power Research Institute (EPRI), Palo Alto.
- [27] Li, F. Fran. Kueck, John. Rizey, Tom. King, Tom. Evaluation of Distributed Energy Resources for Reactive Power Supply, First Quarterly Report for Fiscal Year 2006. Prepared for the U.S. Department of Energy by Oak Ridge National Laboratory and Energetics, Inc. November 2005.
- [28] Kirby, Brendan. Hirst, Eric. Ancillary Service Details: Voltage Control. Oak Ridge National Laboratory, Energy Division. Sponsored by The National Regulatory Research Institute. Oak Ridge National Laboratory Report #ORNL/CON-453. December 1997.
- [29] Electricity Storage Association "Technologies," 2009 [Online]. Available:<http://www.electricitystorage.org/site/technologies/>
- [30] <http://www.tva.gov/power/pumpstorart.htm>
- [31] Makansi J. Et Al: 'Energy Storage the Missing Link in the Electricity Value Chain.' An Esc White Paper/ Energy Storage Council 01 May 2002, Pages 1 - 23, Xp055105116 055105116
- [32] <https://share.sandia.gov/news/resources/releases/2008/caes.html>
- [33] Teleke, S. Energy Storage Overview: Applications, Technologies and Economical Evaluation. In Quanta Technology
- [34] Xiangjun Li; Dong Hui; Xiaokang Lai, "Battery Energy Storage Station (BESS)-Based Smoothing Control of Photovoltaic (PV) and Wind Power Generation Fluctuations," Sustainable Energy, IEEE Transactions on , vol.4, no.2, pp.464,473, April 2013
- [35] Guishi Wang; Ciobotaru, M.; Agelidis, V.G., "Power Smoothing of Large Solar PV Plant Using Hybrid Energy Storage," Sustainable Energy, IEEE Transactions on , vol.5, no.3, pp.834,842, July 2014
- [36] AEMC (May 2013). NationalElectricity RulesVersion 55 [Online].Available:<http://www.aemc.gov.au/Electricity/NationalElectricity-Rules/Current-Rules>.
- [37] Hassanzadeh, M.; Etezadi-Amoli, M.; Fadali, M.S., "Practical approach for sub-hourly and hourly prediction of PV power output," North American Power Symposium (NAPS), 2010 , vol., no., pp.1,5, 26-28 Sept. 2010
- [38] Robbins, B.A.; Hadjicostis, C.N.; Dominguez-Garcia, A.D., "A Two-Stage Distributed Architecture for Voltage Control in Power Distribution Systems," Power Systems, IEEE Transactions on , vol.28, no.2, pp.1470,1482, May 2013

- [39] Shengyi Liu and Roger A. Dougal, Dynamic Multiphysics Model for Solar Array, IEEE Transactions on Energy Conversion, Vol. 17(2), June 2002.
- [40] Abdelrazek, Sherif A.; Kamalasadana, Sukumar; Enslin, Johan, "An approach for control of battery energy storage management systems considering multiple functions," *PES General Meeting | Conference & Exposition, 2014 IEEE* , vol., no., pp.1,5, 27-31 July 2014
- [41] Capital Cost per Cycle of Current Storage Technologies (2008), [www.electricitystorage.org](http://www.electricitystorage.org).
- [42] H. Chen, T.N. Cong, W. Yang, C. Tan, Y. Li, and Y. Ding, Progress in Natural Science, 19 (3) (2009), pp. 291–312.
- [43] Abdelrazek, Sherif A.; Kamalasadana, Sukumar, "Battery energy storage management system control considering multiple functions," North American Power Symposium | Conference & Exposition, 2014 IEEE , vol., no., pp.1,5, 7-9 September 2014
- [44] Mammoli, A.; Menicucci, A.; Caudell, T.; Ellis, A.; Willard, S.; Simmins, J., "Low-cost solar micro-forecasts for PV smoothing," Technologies for Sustainability (SusTech), 2013 1st IEEE Conference on , vol., no., pp.238,243, 1-2 Aug. 2013
- [45] Sowder, Dan, "Mitigating solar intermittency using energy storage on a utility distribution system," Clemson University Power Systems Conference | Conference & Exposition, 2013 IEEE , February 13<sup>th</sup>, 2013
- [46] Abdelrazek, S.; Kamalasadana, S., "Integrated control of battery energy storage management system considering PV capacity firming and energy time shift applications," in *Industry Applications Society Annual Meeting, 2014 IEEE* , vol., no., pp.1-7, 5-9 Oct. 2014
- [47] M. J. E. Alam, K. M. Muttaqi, D. Sutanto, "A Novel Approach for Ramp-Rate Control of Solar PV Using Energy Storage to Mitigate Output Fluctuations Caused by Cloud Passing", IEEE Trans. Energy Conversion, vol. 29, No. 2, pp. 507–518, Apr. 2013.
- [48] Abdelrazek, Sherif; Kamalasadana, Sukumar; Enslin, Johan; Fenimore, Tom, "Integrated optimal control of battery energy storage management system for energy management and PV Capacity Firming," in *Energy Conversion Congress and Exposition (ECCE), 2015 IEEE* , vol., no., pp.62-69, 20-24 Sept. 2015
- [49] S. G. Tesfahunegn, Ø. Ulleberg, P. J. Vie, and T. M. Undeland, "PV fluctuation balancing using hydrogen storage—A smoothing method for integration of PV generation into the utility grid," Energy Procedia, vol. 12, pp. 1015–1022, 2011.

- [50] T. D. Hund, S. Gonzalez, and K. Barrett, “Grid-tied PV system energy smoothing,” in Proc. Photovoltaic Spec. Conf., Honolulu, HI, USA, Jun.20–25, 2010, pp. 2762–2766.
- [51] N. Kakimoto, H. Satoh, S. Takayama, and K. Nakamura, “Ramp-Rate control of photovoltaic generator with electric double-layer capacitor,”
- [52] <http://websphereknowledge.blogspot.com/2013/01/ssl-in-mq.html>